Author:
Cross, Jessica A A

Title:
Peptide disruptors and facilitators of protein-protein interactions for mediating intracellular transport

Peptide disruptors and facilitators of protein-protein interactions for mediating intracellular transport

Jessica A. A. Cross

A thesis submitted to the University of Bristol in accordance with the requirements for award of the degree of PhD in the Faculty of Science, School of Chemistry, December 2021

52 364 words
42 225 words (excluding appendices and bibliography)

Abstract

Kinesin-1 is an ATP-dependent motor protein that plays a key role in the spatial and temporal organisation of the cell by the anterograde transport of a diverse range of cargo including proteins and membrane bound organelles on microtubules. The motor complex is a heterotetramer of two heavy chains (KHCs) and two light chains (KLCs), built on a dimeric KHC coiled-coil scaffold. Understanding the structure and mechanisms of activation of this protein is important to gain insights into the normal and pathological roles it plays in intracellular transport. In addition, the development of new strategies to manipulate kinesin-1 and other motor proteins could allow us to target transport systems in human disease. To date, models of cargo transport have predominantly focussed on motor-microtubule interactions. The work described in this thesis sought to use peptide-design approaches to explore the mechanisms of cargo attachment and how this is linked to a transition from a regulated, autoinhibited state to an active form capable of motility on the cytoskeleton.

In Chapter 3, a new structure-guided, fragment-linking, peptide-design approach is developed to deliver a high-affinity peptide ligand that targets the kinesin-1:cargo interface through binding to tetratricopeptide repeat (TPR) domains of KLCs. In Chapter 4, the *de novo* peptide, KinTag, is shown to be effective in hijacking the transport function of endogenous kinesin motors in cells and can deliver cargo into axons of primary neurons with a high efficiency that correlates with its enhanced binding affinity. This demonstrates for the first time that the more tightly the motor holds onto its cargo adaptor, the more efficiently the cargo is transported. To enable inducible manipulation of transport in the cell, a *de novo* cell-penetrating peptide tag is described that delivers KinTag to the cytosol and dimerizes with a genetically encoded bait sequence, localized to an organelle of choice.

In Chapter 5, to understand better how conformational changes linked to cargo-binding in the KLCs are coupled to downstream activation of the motor domains, the interaction between the heavy and light chains in the tetrameric motor is investigated. The KHC-KLC interface is formed by a short region within the coiled-coil stalk of the KHCs and a purported coiled-coil region near the *N* terminus of the KLCs. This interaction is required for the autoinhibition and activity of kinesin-1, however, the structure and organisation remains unresolved. Solution-

phase biophysical characterisation alongside model building and X-ray crystallography is employed and reveals the KHC coils as a dynamic platform for protein-protein interactions.

In addition to its role in organelle transport, kinesin-1 performs a function in sliding pairs of microtubules relative to one another for regulation of the microtubule network. In Chapter 6, the organelle transport and microtubule remodelling activities are linked in a shared, acidification-induced activation mechanism. Mutations in full-length proteins in cells reveal that a Glu residue in the core of the KHC-KLC interface may play an important role in the pH sensing capacity of kinesin-1. This begins to develop a model for the long-unexplained pH dependence of kinesin-1 activity, opening the door for future studies using peptide design to target this interface.

This thesis is dedicated in loving memory to the late Jenny Cross who taught me to read, learn, laugh, and love. Mum, though you never got to read it, I couldn't have done it without you, I hope you would be proud.

Acknowledgements

Firstly, I am endlessly grateful to my supervisors for accepting me into their labs, proposing such an interesting, interdisciplinary project and for instructive and enthusiastic supervision, discussion and encouragement throughout. Dek, thank you for having confidence in me when I had little and for inspiring me to strive. Mark, thank you for having time for me, for taking a chemist into your lab and for the countless hours you have invested in re-training me and in this project. I have loved working as part of this team and am excited for our future pursuits, long may the collaboration continue.

I am grateful to the EPSRC Bristol Chemical Synthesis CDT for funding this work and to Kevin, Laura and Mar for accepting me onto the programme, allowing me to pursue a PhD project outside the realms of synthetic chemistry and their support throughout. In addition to Chris Willis, Paul Pringle and their research groups for the time I spent in their labs during research broadening sabbaticals. Thanks also to the staff of the Wolfson Bioimaging Facility (Dom, Alan, Katy and Mark) and our collaborators Roberto Steiner and Magda Chegkazi at Kings College London.

To the members of the Woolfson group, present and past, thank you for always making the lab a happy, busy place buzzing with science, ideas and smiling vegetables. I have benefited greatly from your help, support and friendships. In particular, Will, thank you for the endless time and patience you have invested in training me and in my work, and for all the fun we've had, I couldn't have done it without you. To Guto, Freddie and Prasun, thank you for your help with crystallography. Freddie, it's been a pleasure starting and ending this PhD with you, Frank, Georgia and Alex thank you for so many pub trips, and Debbie thank you for all the love and laughs, even in the deepest of lockdowns.

To the Dodding lab, I have loved being part of our little family. Thank you for the science, the moaning, the celebrations, the coffees, the cakes and the pints. Johannes and Zuri, it has been a blast learning from you and working with you on our favourite protein. Katy, through the highs and the lows you've been the best lab partner, thanks for everything. To all in EW8, thank you for the lab meetings, discussions, loaned reagents and all the socials, it has been a

pleasure. To Kirsty, thank you for your help with experiments in neurons. To Berni and Beth, thank you for brightening up my days.

To Eliza, thanks for living through it all with me, I couldn't have hoped for a better housemate. Eliza, Sbu, and Rachel, running the GCA with you was almost as much fun as all the holidays and nights out we've had, I'll never forget the lockdown quizzes. Imy and Lydia, thank you for making life in Bristol so much fun and reminding me of all the joys of life outside the ivory tower. Lorel and Katie, thank you for the happiest of times and our monthly weekend escapes.

To my Dad Charles, thank you for teaching me to be a scientist and for inspiring me to read, investigate and study from an early age. Thank you for believing in me, for often reminding me to work hard and more often reminding me not to work too hard. Without your emotional, intellectual and financial support none of this would have been possible. To my grandma Magda, thank you for always caring about my research and my happiness and to my uncles Rich, Jon and John thanks for your thesis writing empathy and support.

Finally, to my partner David, thank you for four wonderful years, for building a home with me in Bristol, surviving pandemic lockdowns, making the hard times liveable and the good times unforgettable. Your love and encouragement have made this thesis possible.

Author's declaration

I declare that the work in this dissertation was carried out in accordance with the requirements of the University of Bristol's Regulations and Code of Practice for Research Degree Programmes and that it has not been submitted for any other academic award.

Except where indicated by specific reference in the text, the work is my own work. Work done in collaboration with, or with the assistance of, others, is indicated as such.

Any views expressed in the dissertation are my own.

Signed: Jessica Cross

Date: 07.12.2021

Table of Contents

Abbreviations

ADP	Adenosine diphosphate
AIS	Axonal initial segment
ALS	Amyotrophic lateral sclerosis
Amp	Ampicillin
AP	Antiparallel
APP	Amalyoid precursor protein
ArmRP	Armadillo repeat protein
ATP	Adenosine triphosphate
AUC	Analytical ultracentrifugation
BLAST	Basic local alignment search tool
BME	Beta mecaptoethanol
BSA	Bovine serum albumin
BUDE	Bristol university docking engine
CC	Coiled coil
CD	Circular dichroism
Cl-HOBt	Chloro-1-hydroxybenzotriazole
CMT	Charcot-marie-tooth disease
CPP	Cell penetrating peptide
CRISPR	Clustered regularly interspaced short palindromic repeats
CSTN	Calsytenin-1
DCM	Dichloromethane
DIC	N,N′-Diisopropylcarbodiimide
DIPEA	N,N-Diisopropylethylamine
DMEM	Dulbecco's modified eagle medium
DMF	Dimethylformamide
DMSO	Dimethyl sulfoxide
DNA	Deoxyribonucleic acid
E.coli	Escherichia coli
EDTA	Ethylenediaminetetraacetic acid
ER	Endoplasmic reticulum
ESI-MS	Electrospray ionization mass spectrometry
FCS	Fetal calf serum

FCTM	Fragment-centric topographical mapping
FP	Fluorescent polarisation
FRET	Fluorescence resonance energy transfer
GFP	Green fluorescent protein
GTP	Guanosine-5'-triphosphate
GUI	Graphical user interface
HA	Hemagglutinin
HATU	(1-[Bis(dimethylamino)methylene]-1H-1,2,3-triazolo[4,5-b]pyridinium 3-oxid hexafluorophosphate)
HEPES	(4-(2-hydroxyethyl)-1-piperazineethanesulfonic acid)
HMM	Hidden markov models
HPLC	High-performance liquid chromatography
HTS	High-throughput screening
IMAC	Immobilized metal affinity chromatography
IPTG	Isopropyl ß-D-1-thiogalactopyranoside
ITC	Isothermal titration calorimetry
JIP1	JNK-interacting protein 1
JNK	c-Jun N-terminal kinases
Kan	Kanamycin
KD	Dissociation constant
KHC	Kinesin heavy chain
KIH	Knobs into holes
KLC	Kinesin light chain
LAMP	Lysosome associated membrane protein
LB	Lysogeny broth
LFP	Leucine-phenylalanine-proline
LLOME	L-leucyl-L-leucine methyl ester
MALDI-TOF	Matrix-assisted laser desorption ionization time-of-flight mass spectrometry
MAP	Microtubule-associated protein
MeCN	Acetonitrile
MOPS	3-(N-morpholino)propanesulfonic acid
MRE	Molar residue ellipticity

MS	Mass spectrometry
MT	Microtubule
MTOC	Microtubule organising centre
MUT	Mutant
NMR	Nuclear magnetic resonance
dNTP	Deoxynucleoside triphosphate
OD	Optical density
PBS	Phosphate-buffered saline
PCR	Polymerase chain reaction
PDB	Protein data bank
PEG	Polyethylene glycol
PEX	Peroxisome
PFA	Paraformaldehyde
PISA	Proteins, interfaces, structures and assemblies
PPI	Protein protein interaction
RAMP	Reversible association with motor proteins
RILP	Rab-interacting lysosomal protein
RNA	Ribonucleic acid
RP	Reverse phase
SBP	Streptavidin binding protein
SDS-PAGE	Sodium dodecyl sulphate–polyacrylamide gel electrophoresis
SEC	Size exclusion chromatography
TAMRA	Carboxy tetramethyl-rhodamine
TFA	Trifluoroacetic acid
TIPS	Triisopropyl silane
TPR	Tetratricopeptide repeat
UV	Ultraviolet
WT	Wildtype

List of Figures

List of Tables

1 Introduction

Ideas described in Section 1.1.3 of this chapter have been included in the publication

Motor-cargo adaptors at the organelle-cytoskeleton interface
Jessica A. Cross and Mark P. Dodding
Curr. Opin. Cell. Biol. **2019, 59,** 16-23 DOI: 10.1016/j.ceb.2019.02.010

1.1 Kinesin-1 is a cytoskeletal motor protein involved in intracellular transport

1.1.1 The cytoskeleton

Eukaryotic cells contain internal, membrane-bound compartments called organelles. These organelles allow different environments to exist within the cell, which facilitate specific functions effectively; for example, adenosine triphosphate (ATP) synthesis inside mitochondria and enzymatic degradation inside lysosomes.[1-3] The cell is organised further by a structural framework called the cytoskeleton. The cytoskeleton is a network of intracellular filaments essential for maintaining cell shape, internal organisation, and supporting many functions including cell motility and division. The eukaryotic cytoskeleton is composed of actin filaments, intermediate filaments and microtubules. Whilst previously thought to be unique to eukaryotes, research in the 1990s led to the discovery of actin[4] and tubulin[5-7] homologues in bacteria and archaea, revealing that prokaryotic cells also have active and dynamic cytoskeletons.[8] It is now hypothesised that the complex eukaryotic cytoskeleton, composed of filaments, motors and accessory proteins, may have evolved from simple prokaryotic origins.[9]

Microtubules are typically assembled from 13 protofilaments which align together to form a hollow, cylindrical structure. These protofilament polymers are assembled from α- and β-tubulin heterodimers (Fig. 1.1).[10] Microtubules are intrinsically polar structures that have a rapidly growing plus end that exposes β-tubulin and a minus end exposing α-tubulin. In most cases, cytoskeletal microtubule arrays are organised radially within the cell, with the minus ends anchored at the centrosome in many cell types (a microtubule organising centre (MTOC)) and the plus ends pointing towards the cell periphery. In addition, linear, non-centrosomal microtubule arrays are observed in polarized, nonmigratory cells such as neuronal, epithelial and skeletal muscle fibre cells.[11] Microtubules have a property known as dynamic instability, rapidly switching between phases of growth and depolymerisation. These dynamic properties

are essential for the remodelling of the cytoskeleton that occurs during mitosis and cell migration.[12] The rates of microtubule growth and depolymerisation depend on a number of factors including the availability of tubulin, tubulin post-translational modifications such as detyrosination or acetylation, the presence of microtubule-associated proteins (MAPs), which may play a stabilising or destabilising role, and the activity of motor proteins.[13]

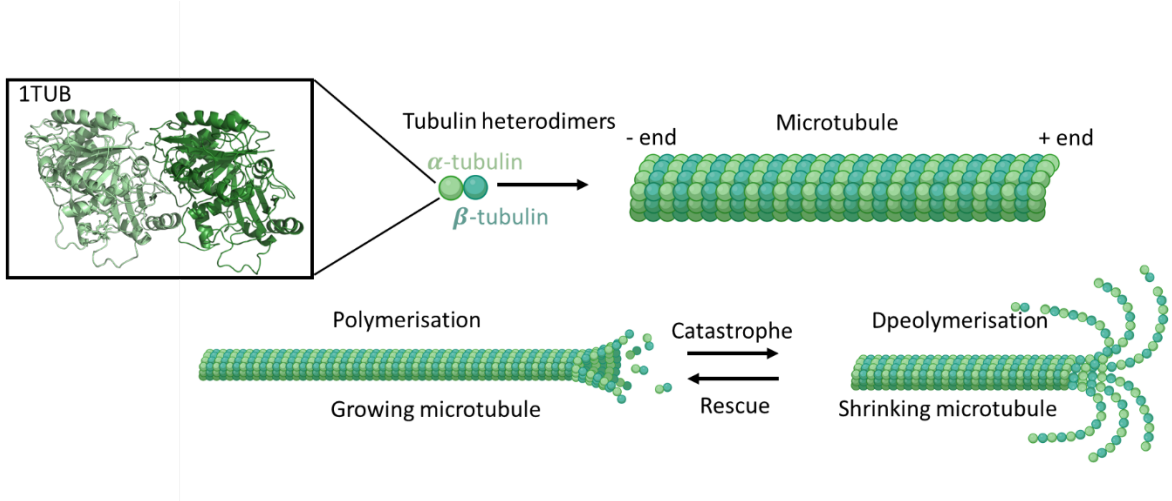

Fig. 1.1| Microtubule structure and dynamic instability. Microtubules are polarized polymers of α- and β-tubulin heterodimers which assemble to form hollow cylindrical filaments in the cytoskeleton of a cell. Usually, the minus end is anchored to nucleating material in the cell, while the plus end is free to bind and hydrolyse GTP during polymerisation. Microtubules show dynamic instability, rapidly switching between phases of growth (rescues) and depolymerisation (catastrophe), which are essential for their roles *in vivo*.

1.1.2 Cytoskeletal motors

Cytoskeletal motor proteins interact with the actin and microtubule cytoskeletons, generating mechanical energy from the hydrolysis of ATP. Motor proteins use this energy to produce force, allowing transport of cellular components along the cytoskeletal network. There are three classes of motor proteins: myosins interact with actin filaments; and kinesins and dyneins are microtubule motors that predominantly move towards the plus and minus ends, respectively (Fig 1.2).[14] Within these superfamilies there are further divisions into sub-classes of motors, performing different functions within the cell.

Within the myosin superfamily, there are 39 genes in the human genome which have been divided into 12 classes by phylogenetic sequence analysis.[15,16] These enzymes bind to actin filaments with affinities dependent on nucleotide-binding state. A subset of myosins are found

exclusively in muscle, where the molecules assemble into bipolar thick filaments, which slide relative to actin filaments during muscle contraction.[17] (Fig 1.2a) Non-muscle myosins can also assemble into filaments important for cell adhesion and migration.[18] Class V myosins are active in cargo transport. These proteins have two identical head domains with staggered ATPase cycles, allowing the motor to take steps along the filamentous track (Fig 1.2b).[19] Binding of ATP triggers dissociation of the rear head domain from the actin filament allowing the front head to undergo a lever-arm swing. This conformational change propels the rear head forward. Hydrolysis of ATP and release of phosphate then allows the head to reattach to the actin filament at a new site.[20]

Dynein was originally discovered as an axonemal ATPase in *Tetrahymena pyriformis* cilia[21]. Subsequently, cytoplasmic dynein-1 has been shown to be widely expressed in cells, driving intracellular transport of organelles, proteins, RNA and viruses towards the minus ends of microtubules.[22,23] Dynein motors assemble through homodimerization of two identical heavy chains composed of a globular head domain, microtubule-binding stalk and cargo binding tail. Dyneins also contain a variety of intermediate, light intermediate and light chains.[24] Cargo transport is mediated through a 23-subunit complex named dynactin, which interacts with cargo adaptor proteins through coiled-coil interactions.[25] Notably, in the cytoplasm of animal cells, there is only a single dynein in contrast to ~40 kinesins performing related functions.[26]

The kinesin superfamily can be subdivided into 14 sub-families.[27] All kinesins have a conserved motor domain for ATP hydrolysis and microtubule binding. Additionally, each family has specific variable domains for regulation and isoform-specific functions, including cargo binding and localization. In general, the position of the motor domain dictates function. *N*-terminal motor domains, which are the most common, direct motility towards the plus end of the microtubule. Conversely, *C*-terminal motor domains direct movement towards the minus end.[28] Kinesin motors with a central motor domain often depolymerise microtubules rather than moving along their surface.[29]

Historically, kinesins were given different names based on individual or systematic identification or the position of the motor domain.[30] At the 2003 meeting of the American Society for Cell biology, a standardised nomenclature system was adopted, naming kinesins by their subfamily kinesin 1-14. Within these subfamilies, individual sequences retained their originally described names.[27] In this thesis, the term kinesin-1 is used to refer to a

complete heterotetrameric holoenzyme of kinesin family 1, KHC refers to the heavy chain component from genes Kif5 A B or C and KLC the light chain component from genes KLC 1-4.

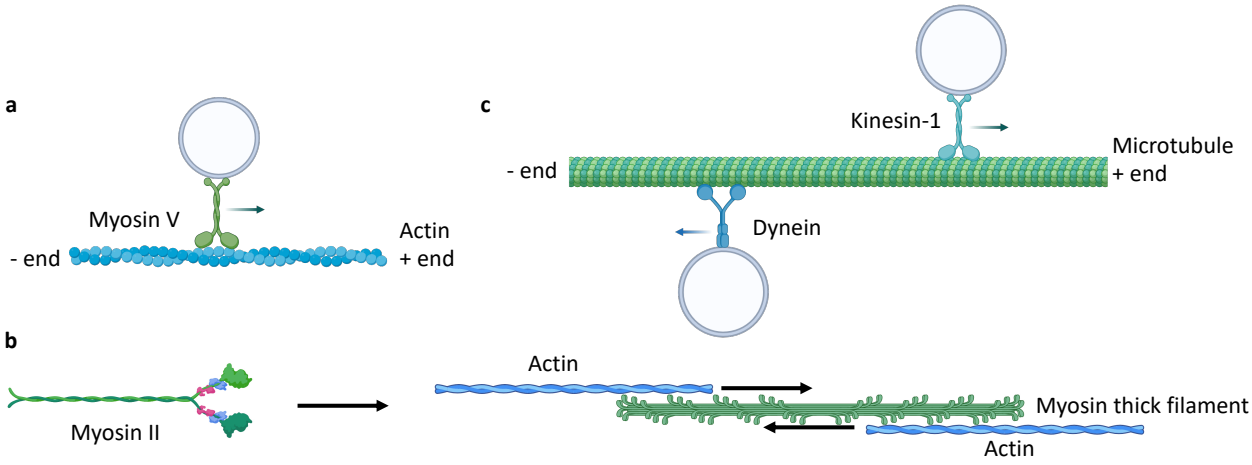

Fig. 1.2| Examples of cytoskeletal motor proteins of the kinesin, dynein and myosin families. **a**, Myosin-V proteins are important in cargo transport, two head domains with staggered ATPase cycles allow the motor to take steps along the actin track. **b**, Class II myosins assemble into bipolar thick filaments which slide relative to actin filaments. **c**, Kinesin-1 and dynein are microtubule motor proteins directed towards the plus and minus ends, respectively.

1.1.3 Kinesin-1

Kinesin-1 was the first family of kinesin motor proteins to be discovered, identified in giant squid axoplasm as a microtubule dependent ATPase by Vale *et al.* in 1985.[31] These microtubule motors play a key role in the spatial and temporal organisation of the cell by the anterograde transport of a diverse range of cargo, including proteins and membrane bound organelles.[29] Kinesin-1 is often hijacked by viruses and bacteria during their replication cycles and plays a role in several neurological diseases.[32-34] Therefore, understanding the structure and mechanisms by which kinesin-1 interacts with its cargo, and is activated, is important to gain insights into the normal and pathological roles it plays in intracellular transport.

Whilst myosin-V and kinesin-1 have no amino-acid sequence identity and exhibit distinct enzymatic[35,36] and motile[37,38] properties, the structural organisation of the proteins have similarities with the dimerization of coiled-coil domains bringing together a pair of motor domains for cargo transport. In addition, the two proteins share a common force-generating

mechanism with crystal structures revealing structural similarity between the motor domains. This suggests that myosins and kinesins may have evolved from a common ancestor.[39]

1.1.3.1 Structure of kinesin-1

Kinesin-1 exists predominantly as a heterotetramer comprising two heavy chains (KHCs) and two light chains (KLCs) (Fig.1.3).[40,41] There are three mammalian genes that encode KHCs: Kif5B is expressed ubiquitously while Kif5A and Kif5C are predominantly found in neuronal cells.[42] Notably, a search of the human gene mutation database reveals very few mutations in KHC genes Kif5B and Kif5C and KLC genes KLC1-4. In contrast, a large number of mutations have been identified in Kif5A and linked to diseases including spastic paraplegia, amyotrophic lateral sclerosis (ALS) and charcot-Marie-Tooth (CMT) disease.[43] These mutations are largely clustered in the motor domain in regions important for microtubule binding.[44]

ATP hydrolysis and microtubule binding occur at the *N*-terminal globular motor domains of the heavy chains (Fig. 1.4).[45] These motor domains are linked to an extended α-helical coiled-coil domain, which mediates heavy chain dimerization and contains a *C*-terminal region of four highly conserved heptad repeats, shown to interact with the light chains (Fig. 1.5).[46,47] This coiled-coil stalk plays a central role in the motility of kinesin-1 by coordinating intramolecular strain within the motor and facilitating the microtubule stepping mechanism.[48] In the inactive state, both head domains are complexed with ADP. Upon microtubule binding, one head releases ADP and binds ATP, triggering a conformational change in the neck linker.[49] This results in the docking of the 15 amino acid neck-linker into the catalytic core of the motor.[49] This induces internal strain between the two head domains to drive the movement of the unattached head to a forward microtubule-binding site, where it binds and subsequently releases ADP. Intramolecular strain prevents binding of a second ATP by the forward head until hydrolysis at the rear head has occurred.[50,51] In this way, the motor processes in a hand-over-hand stepping mechanism, taking 8 nm steps along the microtubule (Fig. 1.4).[38,52-54]

The *C*-terminal tail domain is involved in cargo binding and incorporates a second, ATP-independent, microtubule-binding site.[55] This second microtubule association is largely due to electrostatic interactions between the basic kinesin-1 tail and acidic *C*-terminus of tubulin.[56] The role of this microtubule binding site remains a topic of discussion but is likely to include a role in regulation of motor and microtubule function. It has been suggested that tethering of

inactive kinesin-1 to microtubules enhances processivity by keeping close proximity to microtubules in the event of motor-domain dissociation or that this interaction is important for pausing the motor in an inactive microtubule-bound state with high ADP affinity.[56,57] Microtubule association at this site may be prevented by the binding of regulatory proteins to overlapping cargo sites of the KHC tail.[56,57] Whilst a pool of homodimeric KHCs has been shown to exist in mammalian cells, the majority is complexed to KLCs in the form of tetrameric motors.[58]

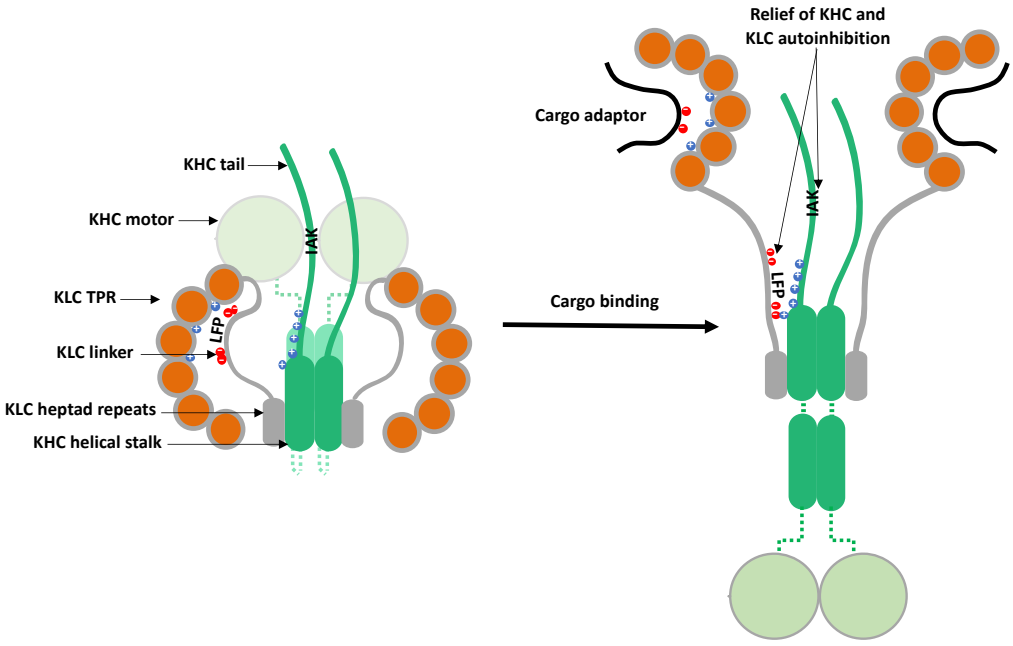

Fig. 1.3| Structure of kinesin-1 with a possible model for release of autoinhibition. Kinesin-1 is an autoinhibited heterotetramer of two heavy chains (KHCs) and two light chains (KLCs). KHCs (green) are composed of an *N*-terminal motor domain for ATP hydrolysis and microtubule binding, an extended helical-stalk region for dimerization and KLC binding and a *C*-terminal tail for cargo binding and regulation (IAK motif). KLCs (grey) interact with KHCs through an *N*-terminal helical domain connected by an unstructured linker to a TPR domain, important for regulation (LFP motif) and cargo binding. Organelle binding through cargo adaptor peptides triggers activation from a folded inhibited state to an extended structure, capable of motility on the microtubule cytoskeleton. Figure adapted from Yip *et al. PNAS*, 2016 with permission of the publishers.[59]

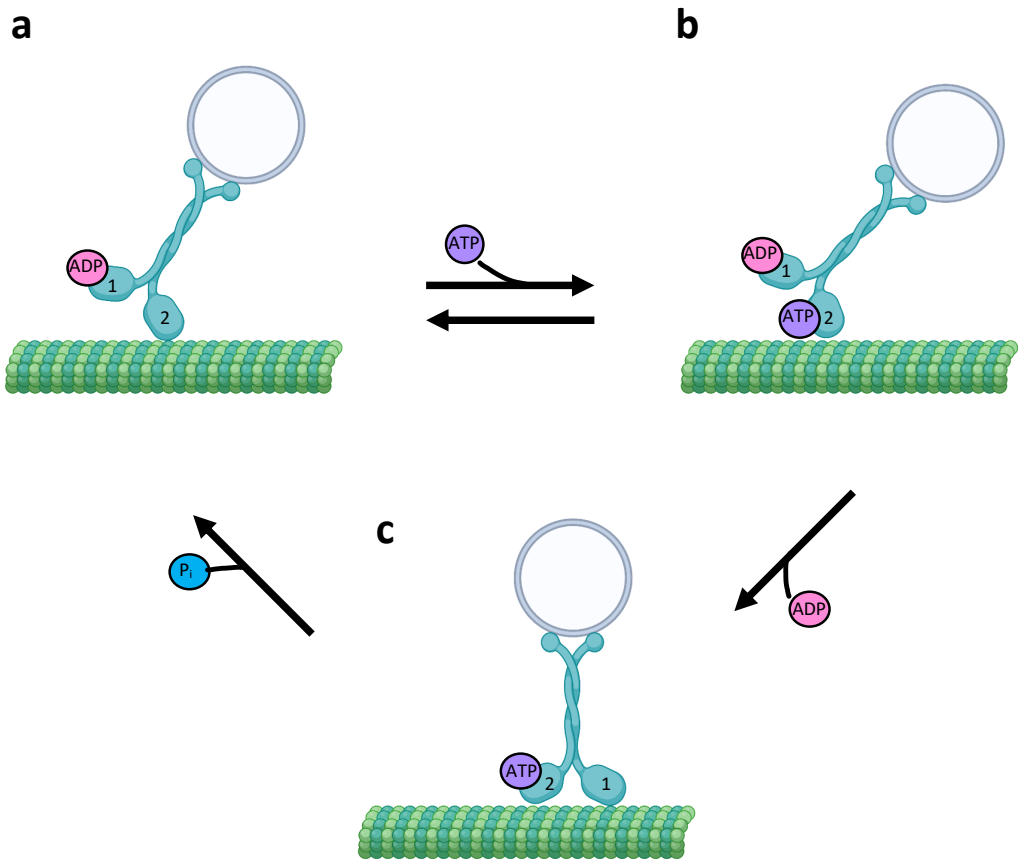

Fig. 1.4| Stepping mechanism of kinesin-1. a, Microtubule binding results in release of ADP from the motor domain. **b**, Binding of ATP to the microtubule bound motor domain results in conformational changes in the helical stalk domain, introducing intermolecular strain in the tetrameric motor. This leads to docking of the 15 amino acid neck-linker to the catalytic core of the motor. **c**, The associated strain facilitates microtubule binding of the second, unattached motor domain at a forward site, along with ADP release. ATP hydrolysis at the rear motor domain releases phosphate and microtubule binding, allowing the motor to cycle through these stages, processing along a microtubule in 8 nm hand-over-hand steps.

KLCs consist of an *N*-terminal α helical domain, thought to be a coiled coil, that binds to the conserved *C*-terminal region of the KHC stalk to form the heterotetrameric structure.[46] This is connected by a highly charged, unstructured linker to a conserved tetratricopeptide repeat (TPR) domain and a variable *C*-terminal domain, both of which are important for cargo binding (Fig. 1.5). Kinesin-1 TPR domains consist of 6 TPR repeats, which are made up of two anti-parallel α helices, 34 residues long.[60,61] TPR domains have been shown to mediate a diverse range of protein-protein interactions (PPIs), with targets binding in the concave groove of the domain or to loop regions connecting helices.[60,62-66] A range of kinesin-1 cargo interact with the concave groove of the TPR domains[25,67,68] and differences between these domains in KLC isoforms has been shown to confer selectivity for cargo binding.[68] Also, diversity of cargo

recognition is likely to be achieved through variability in the *C*-terminal region through four light chain genes (KLC1-4) and a multitude of splice isoforms. These *C*-terminal domains have been shown to contribute to targeting kinesin-1 to different cellular structures, in part through protein-lipid interactions of a KLC amphipathic helix with organelle membranes.[69-72] Potential diversity is also increased since different KLC isoforms can complex KHC dimers in cells to form asymmetric tetrameric complexes.[73]

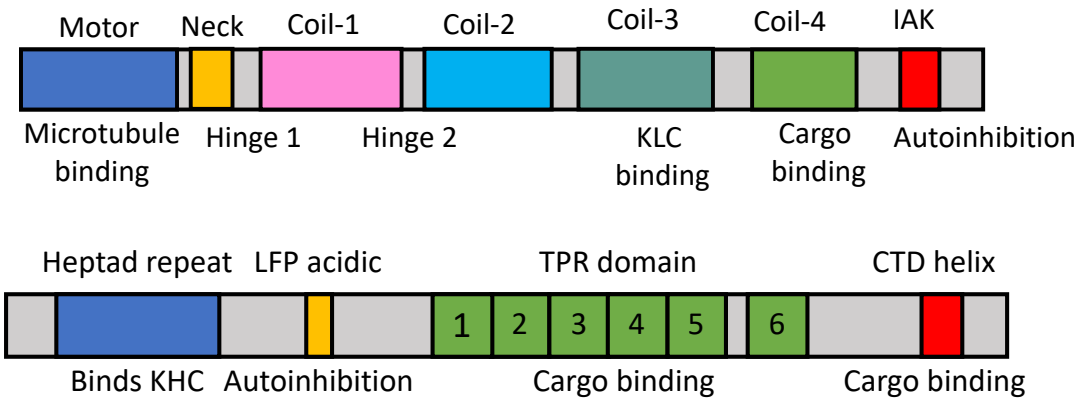

Fig. 1.5| Structure of KHCs and KLCs. Schematic showing the domain architecture of the KHC and KLCs. KHCs (top) have an *N*-terminal globular motor domain linked to an extended region of α-helical coiled-coil domains, important for heavy chain dimerization and interactions with cargo and the KLCs. A *C*-terminal isoleucine-alanine-lysine (IAK) motif binds to the motor domains and is important for autoinhibition. In the KLCs (bottom) an *N*-terminal α helical domain binds to the conserved *C*-terminal region of the KHC stalk in the tetrameric motor. A leucine-phenylalanine-proline (LFP) motif in an acidic unstructured linker region interacts with the TPR domain and is important for autoinhibition. Cargo binding is through the TPR domains and an amphipathic helix in the *C*-terminal tail domain (CTD).

1.1.3.2 Regulation of kinesin-1

When not involved in cargo transport, kinesin-1 exists in an autoinhibited conformation (Fig. 1.6). Initial evidence came from electron microscopy and sedimentation studies, showing that kinesin-1 can have an extended or folded conformation depending on salt concentration.[74,75] Further experiments concluded that this folded conformation is due to an interaction between the tail and motor domain of KHCs, inhibiting the motor.[76-80] This interaction has been mapped to a highly conserved isoleucine-alanine-lysine (IAK) motif in the KHC *C*-terminal tail, which binds to the homodimer interface of the *N*-terminal motor domain. This cross-links the motor

domains, preventing their stable association with microtubules and the corresponding movement required for ADP release, thus preventing unnecessary cycles of ATP hydrolysis.[57,79-81] Truncation of the tail domain encompassing this inhibitory motif results in increased motility compared to the full-length protein.[82] Whilst this inhibition is an intrinsic property of KHCs, KLCs also play a role in motor inhibition and regulation.[59,77,78,82-86]

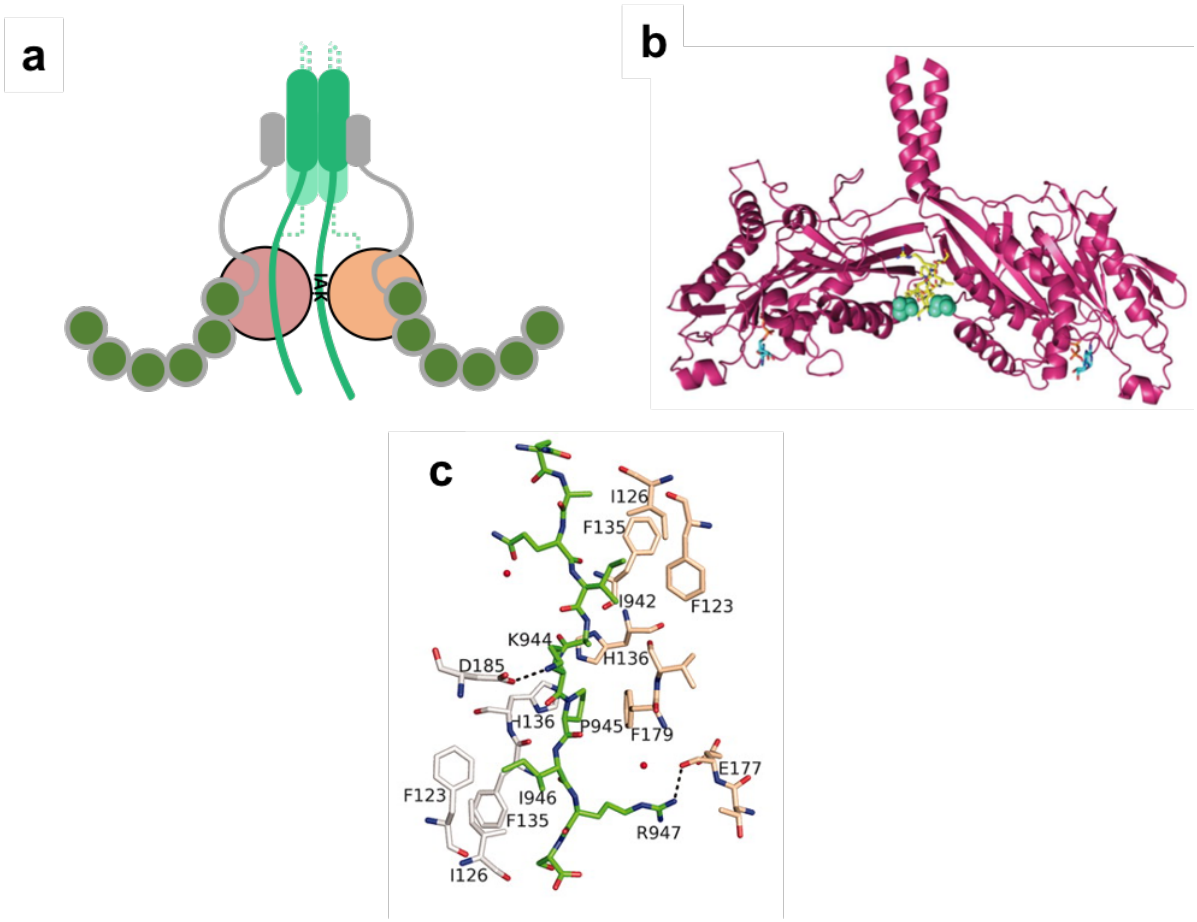

Fig. 1.6| Kinesin-1 is autoinhibited through head-tail interactions. a, Autoinhibition of kinesin-1 has been shown to be, in part, due to the interaction of the tail domain containing a conserved isoleucine, alanine, lysine (IAK) motif, with the motor head domains. **b**, A crystal structure of the inhibited *Drosophila* motor domain (PDB 2Y65) shows that a single IAK tail crosslinks the two motor domains, acting as a bridge and preventing the movement required for ADP release and thus microtubule binding. **c**, C–H-π and hydrogen bond interactions (dotted lines) between the tail (green) and motor domains (chain A, gray; B, beige). Fig. b and c adapted from Kaan et al. *Science* with permission from the publishers.[81]

Similar to KHCs, KLCs show dynamic conformational states regulated by autoinhibitory self-interactions and cargo binding.[59] A leucine-phenylalanine-proline (LFP) motif in the unstructured KLC linker region interacts with the TPR domain, occluding the cargo binding site.[59] Cargo adaptor peptides displace this LFP:TPR interaction, relieving autoinhibition and

causing a conformational shift within the TPR domain, increasing curvature via an induced-fit mechanism.[68] This structural change in the KLCs is thought to result in downstream conformational changes in the KHC motor domains, relieving heavy chain inhibition and resulting in the extended structure required for ATP hydrolysis and motility along microtubules.[77,86-88] Yip *et al*. speculate that activation may be due to electrostatic interactions between these autoinhibitory regions, whereby the KLC LFP containing linker, displaced from the TPR by bound cargo, interacts with the KHC tail, releasing inhibition of the motor domains (Fig. 1.3).[59]

1.1.3.3 Kinesin-1 cargo recognition

Like many other motor proteins, kinesin-1 is known to take part in a vast number of transport processes within the cell, highlighting the requirement for the selective recognition of multiple cargo by a single motor. New structural insights have shown this is, in part, due to the function of a class of proteins called "cargo-adaptors" acting as molecular bridges between specific organelles and the cytoskeleton.[25] Whilst the mechanisms underpinning motor activation are not fully understood, these cargo-adaptors play a role in relieving autoinhibition and driving an active conformation capable of motility on the cytoskeleton.

Cargo binding sites have been mapped to both the *C*-terminal tail of KHCs and the TPR domain of KLCs. There are many examples of KHC binding cargo reported in the literature, emerging from studies in fly, worm and mammalian systems.[89-100] Some examples including JIP3,[89] TRAK1 (OIP106/MILTON1)[98] and TRAK2 (GRIF-1/OIP98/Milt2)[96] are well established whilst others such as kinectin[101] and myosin Va,[102] identified through yeast two-hybrid experiments, are from single reports. Despite this wealth of literature, no common mechanisms of molecular recognition have been identified. In the absence of a common mechanism, identification and validation of these motor-cargo interactions remains a challenge. Interestingly, a recent study by Dimitrova-Paternoga *et al.* provides the first structural characterization of a direct cargo adaptor–KHC interface. An atypical tropomyosin, important for *oskar* mRNA transport in *Drosophila* oocytes, is shown to bind to the *C*-terminal region of the KHCs forming an antiparallel trimeric coiled-coil assembly. It will be interesting to see if this emerges as a common mechanism for KHC binding of other cargo.

In contrast, the mechanisms of cargo binding to KLCs have begun to be understood. KLC^{TPR} domains have been shown to accommodate ligand binding through distinct sites.[65,103]A recent structure reveals that a JIP3 coiled coil binds and cross-links two TPR domains via their TPR1s.[104] In addition, acidic peptide motifs that bind to the positively charged, concave surface of the KLC^{TPR} domain have been identified in a wide range of cargo. Pernigo *et al*. separate these into two distinct classes of cargo adaptor peptides.[67,68] The first, tryptophan acidic (W-acidic) motifs, include a tryptophan residue flanked by aspartic or glutamic acid within the consensus L/M-D/E-W-D/E. These W-acidic motifs are found in a growing list of well-validated adaptors including the lysosome adaptor SifA-kinesin interacting protein (SKIP), the neuronal protein calsyntenin-1 (CSTN-1), dynein intermediate chain (DIC), nesprin-2, gadkin, and cayman ataxia protein (BNIP-H).[67,88,103,105-111] W-acidic motifs have been shown to encode the capacity to both recruit and activate kinesin-1. Functional transport of cargo has been demonstrated when these motifs are substituted for homologous regions within the vaccinia virus KLC binding protein A36,[105] fused to the lysosome associated membrane protein 1 (LAMP1)[112] and in an artificial membrane protein containing two CSTN-1 W-acidic motifs.[88]

A second class, Y-acidic motifs (tyrosine flanked by acidic residues), has been shown to bind the TPR domain in a KLC-isoform specific manner. These motifs are present in both the c-Jun *N*-terminal kinase (JNK)-interacting protein 1 (JIP1), involved in the anterograde transport of the amyloid precursor protein (APP) and a key determinant in Alzheimer's disease[113,114]; and in TorsinA, a constitutively inactive AAA+ protein, whose gene is linked to early-onset dystonia type 1 (DYT1).[115] Unlike their W-acidic counterparts, Y-acidic motifs are sufficient for motor recruitment but apparently require secondary, KHC binding proteins such as FEZ1 or JIP3 for full activity.[65,85,86]

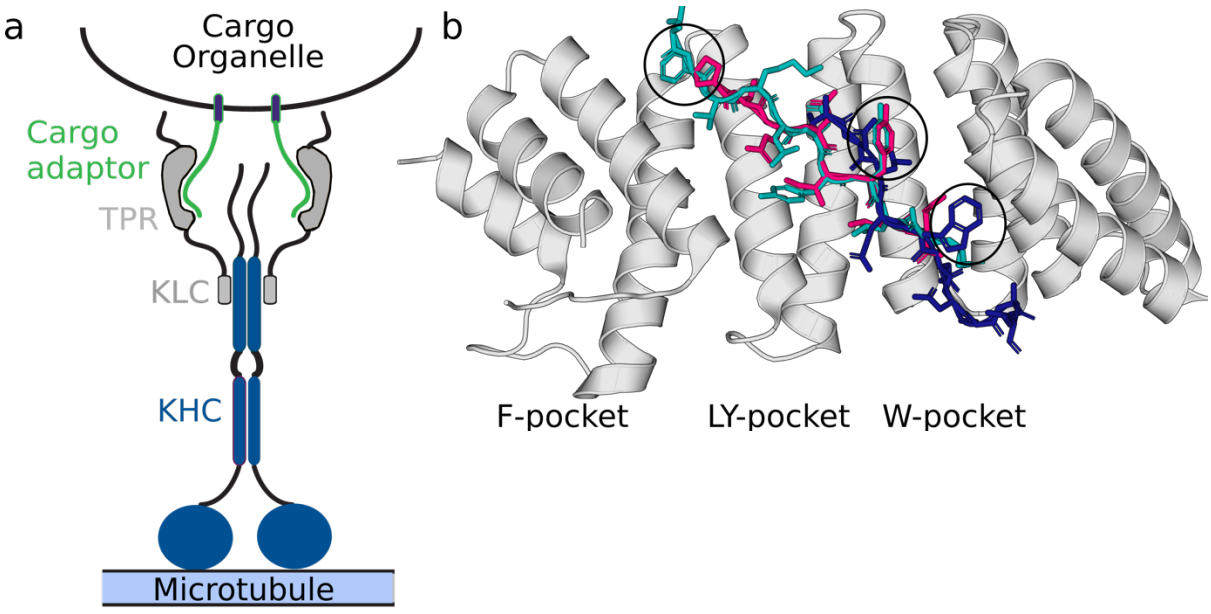

Fig. 1.7 | Structures of W and Y acidic cargo adaptor peptides bound to the TPR domain of kinesin light chains. a, Cartoon representation of kinesin-1 showing interaction of cargo adaptor W-acidic or Y-acidic peptides associated with the organelle surface (green) with KLC^{TPR} (grey). **b**, Crystal structures of W acidic cargo adaptor peptides from SKIP (dark blue; PDB code, 3ZFW) and Y acidic from JIP1, (pink; 6FUZ) and Torsin A (cyan; 6FV0) bound to the TPR domain of KLC1 (grey). *N.B.* SKIP is complexed with KLC2 and so $KLC1/2^{TPR}$ domains were aligned to produce the model. Hydrophobic W, Y and F residues occupy hydrophobic pockets and flanking acidic residues make electrostatic interactions with the positively charged surface of the TPR domain. These two classes of adaptor peptides bind to distinct but overlapping sites and induce curvature upon binding in an induced-fit mechanism.[67,68]

W- and Y-acidic motifs bind to distinct but partly overlapping sites on the concave surface of the TPR domain, increasing curvature via an induced fit mechanism (Fig. 1.7). Y-acidic cargo adaptor binding results in closure of the TPR receptor to a greater extent than W-acidic binding. This demonstrates the adaptive plasticity of these domains as platforms for PPIs. Yip *et al*. and Sanger *et al.* show that binding of W-acidic motifs displaces the autoinhibitory LFP interaction, causing global conformational changes in the KLCs, revealing an additional binding site on the KHC-tail and promoting motor activity.[59,87] Whilst inclusion of the LFP motif on the KLC^{TPR} significantly reduces the affinity for W-acidic peptides, it has little effect on the binding of Y-acidic peptides. The authors suggest that Y-acidic binding might co-exist with LFP-acidic binding, requiring cooperative interactions from a second binding partner to relieve autoinhibition. The model they propose begins to explain how two distinct classes of cargo adaptor peptides can bind to the TPR domains of KLCs with similar affinity (μM) but different functional ourtcomes.[68]

1.1.3.4 Microtubule sliding

A role for kinesin-1 has also been identified in microtubule remodelling through the sliding of microtubules against one another. Using microtubule binding sites in both the *N*-terminal motor domain and the *C*-terminal tail of the KHC, kinesin-1 can bridge two microtubules, allowing them to act as the cargo and track, respectively (Fig. 1.8). As the kinesin moves along the microtubule track it moves the "cargo" microtubule relative to the track.[116]

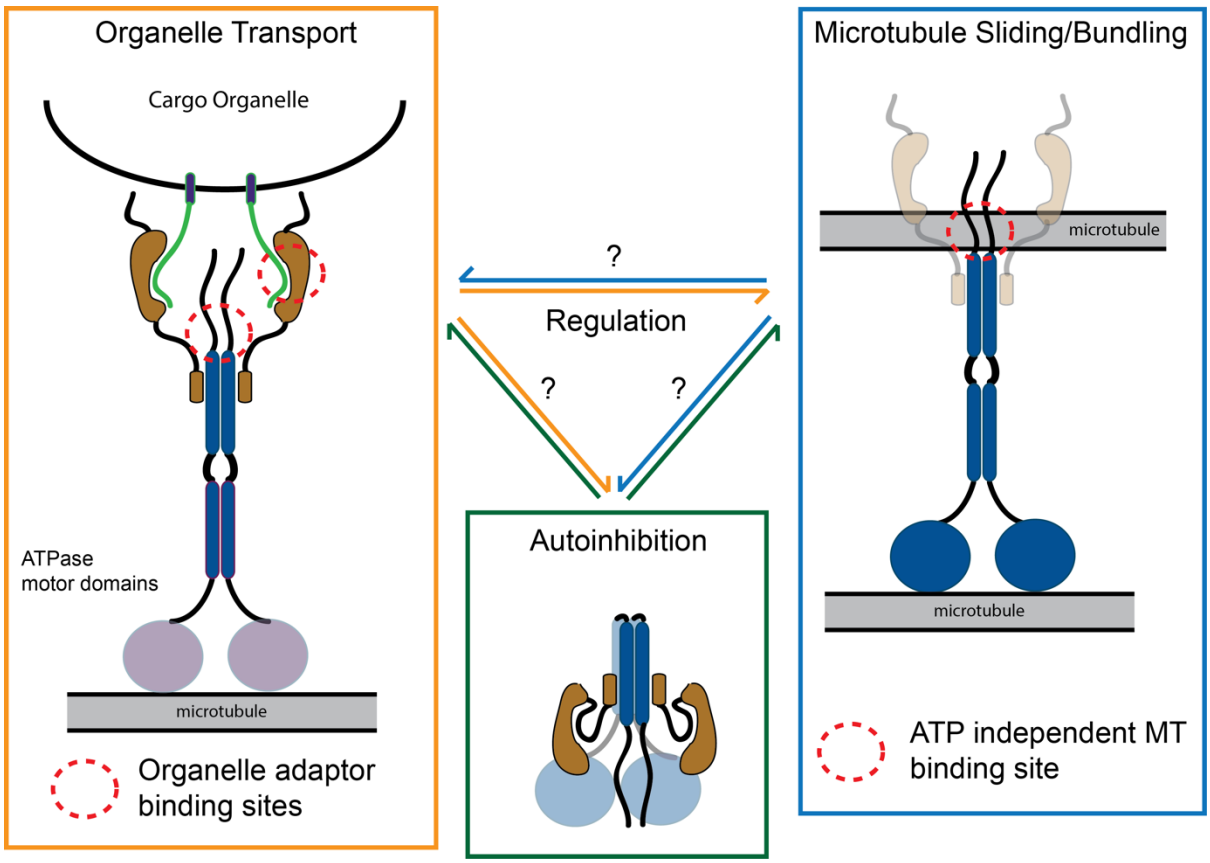

Fig. 1.8 | Cartoon representation of kinesin-1 activity. In addition to cargo transport, kinesin-1 can slide pairs of microtubules relative to one another by binding a second microtubule in the *C*-terminal region of the KHCs. These functions are linked by a shared activation mechanism.

An example of where this function is important is in *Drosophila* oogenesis, the process by which germ cells develop into an oocyte which then matures into an egg. During oogenesis, transport processes are essential to the define the asymmetries specifying the embryonic axes for patterning the egg.[117] The posterior pole of the future embryo is determined by local accumulation of *oskar* mRNA which requires transport by kinesin-1. This process has been shown to be KHC dependent, but independent of KLCs and dynein.[118,119] Lu *et al.* demonstrate

that a KHC mutant deficient in microtubule sliding but able to transport other cargo, reduces cytoplasmic streaming in *Drosophila* oocytes. This suggests that the function of the protein to slide microtubules relative to one another is important to generate force for cytoplasmic streaming. They propose that there are two populations of cellular microtubules, one immobilised network forming a stable assembly anchored to the actin network, and the other a cytoplasmic population moving in the ooplasm.[120]

Kinesin-1 microtubule sliding has also been shown to be important for neurite extension in young *Drosophila* neurons by pushing against the peripheral membrane.[121] Neuronal cells must transmit forces over long distances through axons, which are susceptible to mechanical damage as a result of their length. Microtubule sliding by kinesin-1 is also important in neuron regeneration following injury. Lu *et al*. demonstrate that calcium influx at the injury site triggers transient microtubule disassembly and reassembly of mixed-polarity arrays, allowing kinesin-1 driven microtubule sliding to regenerate axons.[122]

Microtubules have also been observed to buckle and loop in cultured cells, and this has been linked to the microtubule sliding capacity of kinesin-1.[123,124] This has direct links to cargo transport, with multiple peroxisomes shown to be transported alongside a moving microtubule. This shows that in addition to forming tracks for motors, microtubules demonstrate the capacity to transduce the force of distant motors onto cargo.[125] These studies suggest that microtubules are not limited to a rigid, structural role in the cell but form a dynamic network, responding to mechanical forces in the cell.[126,127]

1.1.3.5 Kinesin-1 activity in human disease

Loss of kinesin-1 cargo-transport function results in defects in intracellular transport leading to pathologies associated with human diseases. This is particularly apparent in neurons where proteins required for the axon and synapses must be transported long distances along the axon, requiring carefully controlled intracellular transport by kinesin and dynein motors. Disruption to transport has been associated with several neurodegenerative diseases including Alzheimer's, Huntington's, amyotrophic lateral sclerosis (ALS), and Charcot– Marie–Tooth (CMT) disease.[128-130] One example of a well-established kinesin-1 cargo thought to be involved in the development of Alzheimer's disease is the amyloid precursor protein (APP). Proteolysis of APP by β and γ-secretases gives rise to the amyloid-β peptide (aβ), which, in

turn, leads to formation of amyloid plaques.[131] Whilst some studies suggest that APP binds to KLCs and acts as a kinesin-1 cargo adaptor for axonal transport, other contrasting hypotheses are presented in the literature.[132-135] Both CSTN-1[136] and JIP1[113] have been shown to be important for mediating APP transport, and to bind to KLC^{TPR}s through W and Y- acidic adaptors respectively.[67,68] It is clear that the role of APP in kinesin-1 dependent axonal transport is a complex question that remains an active area of research. Future insights into the mechanisms of dysregulation may facilitate the development of cargo-adaptor tags to upregulate transport where it is impaired.

In addition to pathologies associated with transport defects, viruses and bacteria have been shown to recruit kinesin-1 and hijack intracellular transport mechanisms to facilitate their replication and spread in human infection.[32,33] A study from Dodding *et al.* reveals the mechanism of cargo attachment on viral hijack, in which a bipartite W-acidic motif, originally identified in CSTN-1 and present in A36 (a vaccinia integral membrane protein), is sufficient for the kinesin-1 dependent transport of the virus to the cell periphery.[105] Cargo adaptor interactions have also been shown to be important for the intracellular fate of *Salmonella enterica* bacteria, where interaction of the salmonella virulence factor SifA and cargo-adaptor SKIP are required for kinesin-1 dependent transport of vesicles that bud from the *Salmonella*-containing vacuole to the cell periphery.[137] In the future, increased understanding of the mechanisms of kinesin-1 recruitment by viruses and bacteria may allow the development of inhibitors as novel therapeutics.

The capacity of kinesin-1 to slide pairs of microtubules relative to one another, regulating the organisation of the microtubule network, suggests that it could also be a therapeutic target for indirect microtubule manipulation. Existing microtubule targeting agents are important drugs used for the treatment of cancers.[138] Examples include taxanes that bind directly to tubulin to stabilise microtubules, inhibiting cell division and vinca alkaloids which act to destabilise microtubules resulting in metaphase arrest.[139,140] Inhibition of mitotic kinesins such as kinesin-11 is also considered a potential cancer therapeutic strategy to block cell division.[141] Since neurological diseases are also associated with microtubule defects, recent work has also begun to investigate a role for microtubule-targeting chemotherapeutic agents in the treatment of these disorders.[142]

An exciting study from Randall *et al.* reports the discovery of a cell-permeable small molecule named kinesore (Fig. 1.9), capable of displacing the inhibitory interaction between the KLC LFP motif and TPR domain. This molecule also inhibits the binding of a W-acidic peptide from the lysosomal cargo-adaptor SKIP to the TPR domain of KLC2.[143] In contrast to the cargo-transport activity observed upon release of LFP-autoinhibition by adaptor peptides, treatment with kinesore results in dramatic remodelling of the microtubule network in cells. While control cells show a radial microtubule network with lysosomes distributed throughout the cytoplasm, when treated with kinesore the microtubule network reorganises into a series of loops and bundles with lysosomes clustered around the nucleus (Fig. 1.9). This is reversible, with a radial microtubule network re-established after kinesore washout, and kinesin-1 dependent since it is strongly supressed in Kif5B knockout cells, the major KHC isoform. The authors hypothesise that kinesore activation of kinesin-1 occurs in a similar manner to the binding of W-acidic cargo, by displacing the KLC LFP and KHC IAK autoinhibitory motifs.[57,59,67,80] This suggests that the organelle transport and microtubule sliding/bundling functions of the motor are coupled through a shared activation mechanism and that activation of kinsin-1 under conditions where a capacity to interact with organelles is limited, promotes its role in microtubule sliding.[143] Since kinesin-1 has no known function in mitosis and is likely strongly inhibited to avoid perturbation of spindle dynamics during cell division, chemically induced kinesin-1 dependent sliding of microtubules could act to disturb the delicate balance of motor activities required for chromosome alignment and segregation. This suggests the possibility that with improved affinity and specificity, kinesin-1 inhibitors could become a new class of indirect microtubule targeting agents as therapeutics for cancer or neurodegenerative diseases.

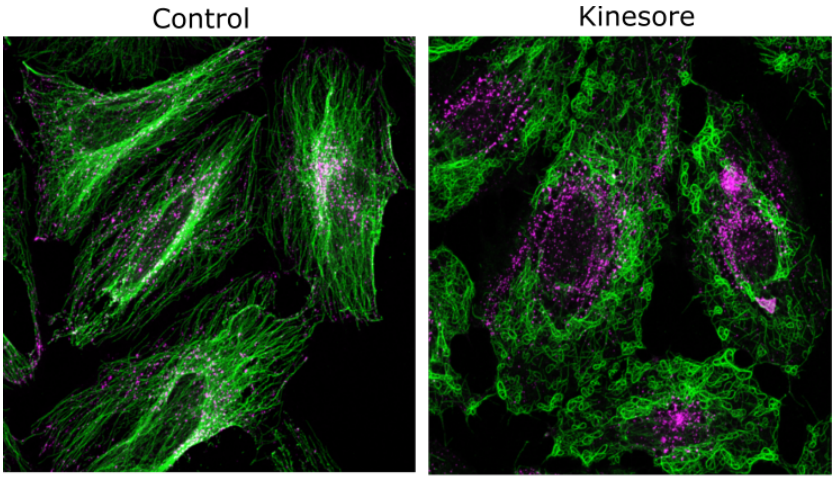

Fig. 1.9 | A small molecule displaces KLC autoinhibition and causes remodelling of the microtubule network. A cell permeable small molecule named kinesore causes kinesin-1 dependent remodelling of microtubules into loops and bundles. HeLa cells were treated with kinesore (50 μM) or vehicle control (0.1 % DMSO) for 1 h and immunostained for β-tubulin (green) and LAMP1 (magenta). This molecule is able to relieve KLC autoinhibition and compete for KLC^{TPR} binding with cargo adaptor peptides. This suggests the microtubule sliding and cargo transport functions of kinesin-1 are linked by a common activation mechanism. Fig. adapted from Randall *et al, PNAS,* 2017 with permission of the authors.[143]

1.1.4 Summary

Kinesin-1 is a ubiquitous microtubule-dependent motor protein that plays a key role in the spatial and temporal organisation of the cell through transport along microtubules of a diverse range of cargoes.[29,31] Kinesin-1 is a heterotetramer of two heavy chains (KHCs) and two light chains (KLCs).[14,41] A coiled-coil stalk domain mediates KHC dimerization and association with KLCs. The motor is autoinhibited and exists in a folded conformation when not transporting cargo. Autoinhibition is due to the interaction of KHC IAK and KLC LFP regulatory motifs in unstructured linker regions with the motor and TPR domains, respectively. Cargo recognition has been shown to be due, in part, to the binding of short, acidic, cargo-adaptor peptides on the surface of the cargo by TPR domains of the KLCs.[67,68] Cargo binding displaces autoinhibition through conformational changes in the motor and activates kinesin-1 transport activity. This cargo transport activity is linked to a second function of kinesin-1 in microtubule-microtubule sliding by a shared activation mechanism.[143] Kinesin-1 is hijacked by viruses and bacteria during their replication cycles and plays roles in several neurological diseases.[33,34,105,128-130] With improved affinity and specificity, kinesin-1 inhibitors could become a new class of indirect microtubule targeting agents or anti-virals/anti-bacterials. Additionally, developing tags for cargo transport may allow manipulation of motor-transport

for the orchestrated repositioning of organelles, upregulation where transport is impaired or the development of new classes of spatially targeted therapeutics.

1.2 Peptide design can be applied to manipulate protein-protein interactions to understand cell biology

PPIs underpin most biological processes and are an important novel therapeutic target for a wide range of diseases.[144,145] PPIs have been identified as playing important roles in signal transduction, metabolic pathways, enzyme activity, environmental sensing, cellular organisation and motor transport amongst many other cellular processes. These interactions form highly organised interactome networks allowing precise control of dynamic cellular systems.[145] Protein design offers the opportunity to manipulate natural PPIs to probe their function and develop new research tools and therapeutics. In the kinesin-1 complex, two classes of PPIs are key to the successful functioning of the motor protein in the cellular environment. The first is the interaction between autoinhibitory peptide motifs in unstructured regions of the polypeptide chain and the motor domains of the KHCs or TPR domains of the KLCs, to allow precise regulation of the motor. The second involves coiled-coil domains, mediating KHC dimerization and association with KLCs to form the heterotetrameric complex. In addition, motor-cargo PPIs between adaptor peptides and TPR domains are critical for motor activation and cargo transport. The application of protein design to target these interfaces may offer novel insights into the activity of the motor and facilitate manipulation of intracellular transport.

1.2.1 Protein design

The field of protein design seeks to use knowledge of protein folding to generate new protein folds and structures not observed in nature. The complexity of the protein-folding problem means that the design of new proteins remains a challenge, though significant progress has been made and a search of the PDB reveals an increasing number of examples of *de novo* designed proteins and peptides (Fig 1.10).[146,147] The field of protein design has promise to deliver structures with properties and functions that can be made to order, to solve important problems in cell biology.[148] In addition, successful protein design is a powerful way to test our understanding of protein function, after the maxim from Richard Feynman, "What I cannot create, I do not understand".[149]

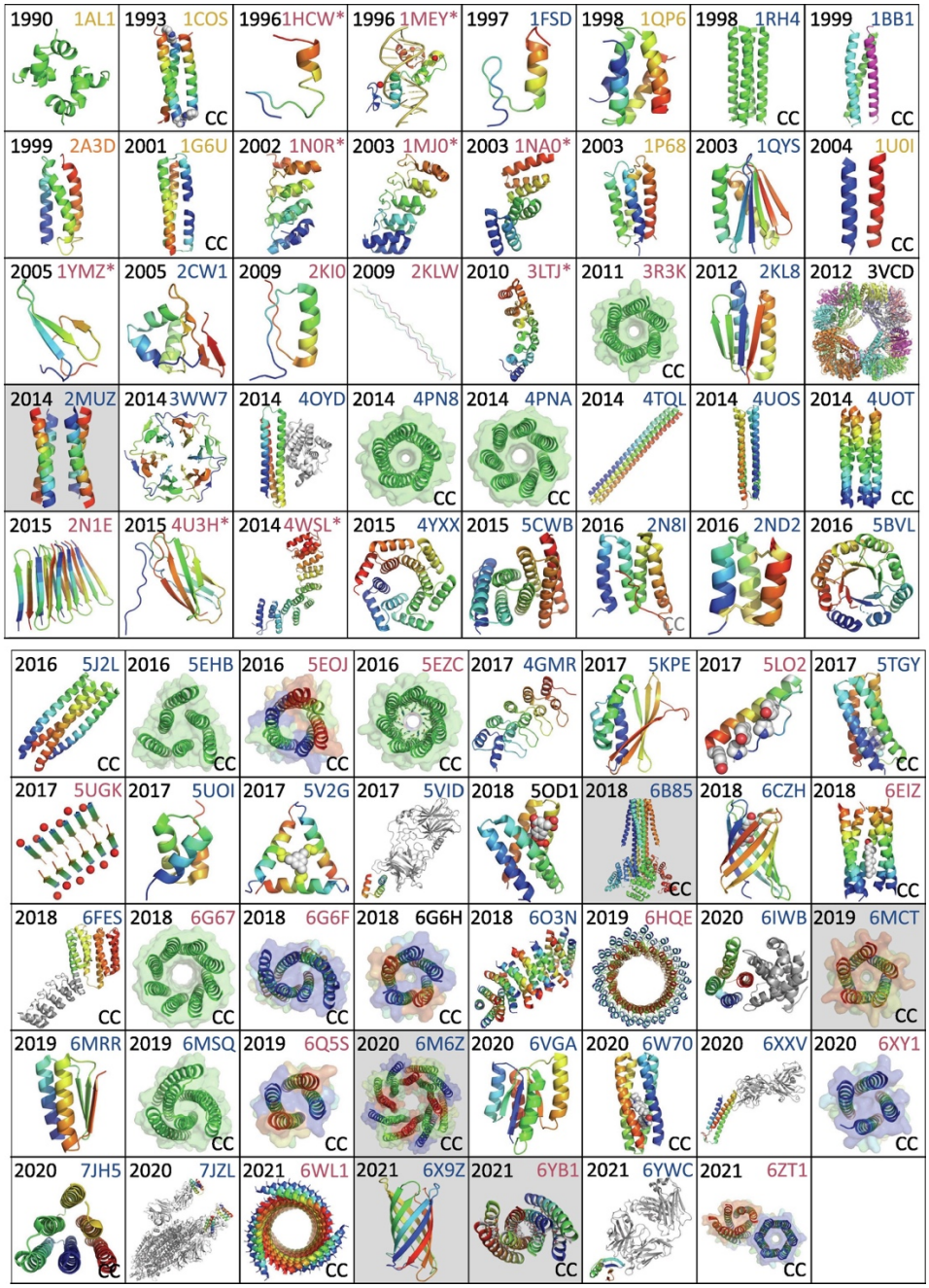

Fig. 1.10 | A gallery of *de novo* designed peptide and protein structures. Selected structures from the PDB labelled with publication dates and 4-letter codes.[150] Structures are represented as backbone cartoons, mostly coloured blue to red from the *N* to *C* terminus. Structures identified as positive for knobs-into-holes interactions by coiled coil structure identification programme SOCKET are labelled with CC.[151] This fig. is reproduced from a review by Derek Woolfson in the *Journal of Molecular Biology* with permission from the publisher.[147]

Protein design is distinct from protein engineering, which seeks to redesign natural proteins, to understand, alter or repurpose their functions. Protein engineering involves modification of a protein sequence through substitution, insertion or deletion of DNA nucleotides to generate

variants of the protein. Engineered proteins can be modified to increase efficiency in an existing function or have new functionality introduced.[152-155] In particular, there has been a great deal of research into engineering the active site of enzymes to generate novel biocatalysts.[156-158] In 2018 the Nobel prize in chemistry was awarded to Frances Arnold, George Smith and Gregory Winter for their work in the development of directed evolution and phage display for protein engineering.[157,159-165] Directed evolution mimics natural selection to select proteins best matching a chosen criterion through successive rounds of sequence diversification and selection. Engineered proteins have now been developed with both industrial and medical applications, demonstrating our ability to understand, harness and repurpose protein activity.[166,167] In addition to mutagenesis, it is now possible to incorporate unnatural amino acids into proteins to introduce a range of chemical functionalities not available to nature. Pioneering efforts to develop orthogonal aminoacyl-tRNA synthase/tRNA pairs has allowed incorporation of 70 unnatural amino acids in bacteria, yeast and mammalian cells.[168,169] Bio-orthogonal reactivity of these amino acids allows proteins to be modified with greater selectivity and efficiency, for example to covalently link other proteins or small molecules in antibody-drug complexes.[170,171]

In contrast to protein engineering, *de novo* protein design seeks to identify sequences to fold into a target protein shape or assembly to explore completely novel structures and functions. Due to the vast number of possible protein sequences, evolution has not yet had time to explore all possible structural space. In addition, since divergence occurs through random mutation, the structures that do exist are clustered in structural space.[172-174] *De novo* protein design seeks to create novel, unsampled structures by exploring the "dark matter" of protein fold space.[175,176] In comparison to directed evolution approaches, rational protein design relies on using sequence-to-structure relationships to develop rules for protein folding.[177] This approach can be considered the inverse of the protein-folding problem, in which a sequence of amino acids is determined to fit a target backbone structure.[178,179]

Both approaches can be used to modulate PPIs in cells for therapeutic purposes through the engineering of protein interfaces or the *de novo* design of peptide ligands for protein surfaces.

1.2.2 Interactions of linear peptides with α-helical repeat domains

Up to 40% of PPIs are now estimated to involve short, linear, adaptor peptide motifs that contain key binding residues and interact with larger protein domains.[180-184] Such interactions are important for signalling, gene expression and DNA replication as well as intracellular transport.[67,183,185-187] These linear motifs are difficult to identify as they occupy short stretches in often disordered regions of proteins, necessitating time-consuming experimental work for identification. It is likely that many undiscovered examples exist, and there is ongoing work into predicting and identifying these motifs.[182,183,188]

A subset of peptide-protein interactions involves the recognition of short linear motifs by α-solenoid structures of repeat proteins such as TPR domains, armadillo repeat proteins (ArmRPs) and HEAT proteins (Fig. 1.11).[189] In these proteins, repetitive tandem arrays of small helical domains stack together to form extended, stable structures. This results in a larger surface-area-to-volume ratio than the average globular protein, leading to a large binding surface.[190] TPR motifs are composed of highly degenerate 34-amino acid repeats that encode two anti-parallel α helices separated by a turn. Several of these motifs are arranged at regular angles in a right-handed superhelix. The large surface area and concave groove of these domains make them common targets for ligand binding. TPR domains have been shown to support variable peptide binding modes. Often, as described in kinesin-1 cargo recognition, peptides are accommodated in a concave groove formed by the assembly of pairs of antiparallel α helices. However, there have also been examples of peptides binding at alternative sites, for example to loop regions.[60,62,66] In general, these interactions occur with low micromolar affinity.[62,67,68] TPR domains are important for a diverse range of PPIs in the cell including cell-cycle regulation, chaperone activity, transcription and protein translocation.[60] It is becoming clear that these interactions are amenable to design, engineering and chemical manipulation.[154]

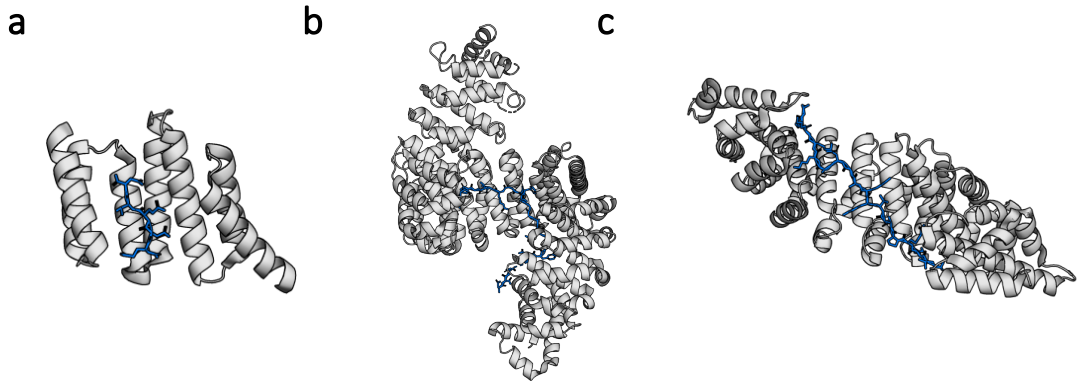

Fig. 1.11 | Peptide ligands bind to α-helical repeat proteins. Cartoon diagrams of structures of α-helical repeat proteins (grey) in association with their peptide ligands (blue). **a**, Hop (TPR2A) in complex with the C-terminal peptide of Hsp90 (PDB 1ELR). **b**, HEAT domain of karyopherinb2 in complex with the NLS of hnRNP A1 (2H4M) . **c**, ArmRP of yeast importin-a(karyopherina) binding to bipartite nuclearlocalization signal of *Xenopus* nucleoplasmin (1EE5).

1.2.3 Design of peptide inhibitors of natural PPIs

Until recently PPIs were considered "undruggable", largely due to the large, flat, interaction surfaces being incompatible with small-molecule-binding-pocket design strategies. A further challenge comes from the adaptive plasticity often observed between two complementary protein interfaces, meaning that available binding conformations may not be apparent within a single crystal structure.[191] The discovery of "hot-spot" residues, critical for binding and often clustered at the centre of the interface, gave hope to the small-molecule drug discovery approach.[192,193] These hot-spot residues can be identified by alanine-scanning mutagenesis in which each interface residue is sequentially mutated to alanine, to remove the side chain beyond the ß-carbon and the impact on binding affinity measured.[194] Examples of successfully engineered small-molecule PPI inhibitors include SP4206, which binds to the cytokine interleukin-2 (IL-2) with mid-nanomolar affinity; ABT-737, which binds to Bcl-X_L, a member of the B-cell lymphoma 2 family important for regulation of apoptosis with sub nanomolar affinity; and Nutlin-3, which binds the human protein double minute 2 (HDM2), an important cancer target.[195-198] Improvements in high throughput screening (HTS) have significantly accelerated the discovery of inhibitors for some categories of PPIs, while others, including multi-protein complexes, remain a significant challenge.[199]

An alternative approach is the use of peptides and peptidomimetics (modified peptides) to target these interfaces. Peptides are ideal candidates for inhibitors of protein-protein interactions since they can mimic the natural protein surface, compete for binding and are synthetically readily available and modified. Peptide inhibitors can be rationally designed based on the natural interface sequences and can be chemically modified with unnatural amino acids to generate peptidomimetics, mimicking the three-dimensional protein structure of the bioactive conformation and thus increasing affinity.

Peptide inhibitors are often identified by phage display HTS assays.[163-165] Bacteriophage that have been engineered to display a library of random-sequence peptides on their surface are screened against an immobilised target protein and phage that bind are isolated to identify the amino acid sequences that lead to binding.[200] This technique is faster and less expensive than the analogous HTS approaches for small-molecule libraries.[201] It is also possible to use similar display screens in yeast, bacteria or mammalian cells.[202-204] While these screens are an attractive approach where little structural information is known about a target PPI, screening a large random library remains time and cost intensive. Improved understanding of protein interfaces through X-ray crystal structures and *in silico* modelling enables the alternative approach of rationally designed peptides to target a specific interface.

High-resolution X-ray crystal structures, NMR structures and homology models allow *in silico* analysis of protein-protein interaction interfaces and structure-based rational design of inhibitors.[205] These approaches include the design of pre-organised structural mimics of the target interface such as stapled peptidomimetics and fragment-based approaches. Coupled with structural information, *in silico* alanine scanning and analysis of changes in solvent-accessible surface area facilitate the identification of residues that make important binding contributions.[206,207] Identification of these hot-spot residues gives an important starting point for such rational design approaches, with peptides that successfully recapitulate key binding interactions shown to act as potent inhibitors.[208,209]

PPIs often involve secondary and tertiary structural motifs such as α helices, β sheets and loops or turn regions.[210] While short peptides are often flexible and unstructured, inhibitor potency can be increased by stabilisation or induction of the desired secondary structure. Roughly 60% of PPIs feature a helix at the interface with most displaying hot spot residues on one helical

face.[209] Short α-helical peptidomimetics are common and can be stabilised by covalent *N*-terminal capping between the i and i+3 residue or incorporation of non-natural amino acids with high helical propensity.[211,212] Alternatively peptides can be stapled by incorporation of a hydrocarbon linker between two hydrophobic residues, which is often found to improve both affinity and proteolytic resistance.[213]

An alternative approach for the design of peptidomimetic or small molecule PPI inhibitors is the use of fragment-centric topographical mapping (FCTM) to characterise the large interaction interface as a set of localised fragment-targetable regions (Fig. 1.12).[214] Initial hits often bind with very low affinity due to reduced contact area but this can be overcome by a covalent 'tethering' approach in which fragments containing thiol moieties are utilized to form disulfide bonds with strategically located native or engineered cysteine residues.[215] Optimization of fragment-based inhibitors can be achieved by fragment linking; joining small fragment moieties after concurrent optimisation or fragment growing; progressively extending the fragment chain with successive optimization after each elongation step.[216,217]

Natural PPIs are often dynamic and transient in nature with synthetic inhibitors only mimicking a portion of the interface, leading to weaker affinity. An ongoing challenge in the design of peptide ligands for protein surfaces is to overcome this limitation in affinity by making additional binding interactions at the interface.[218]

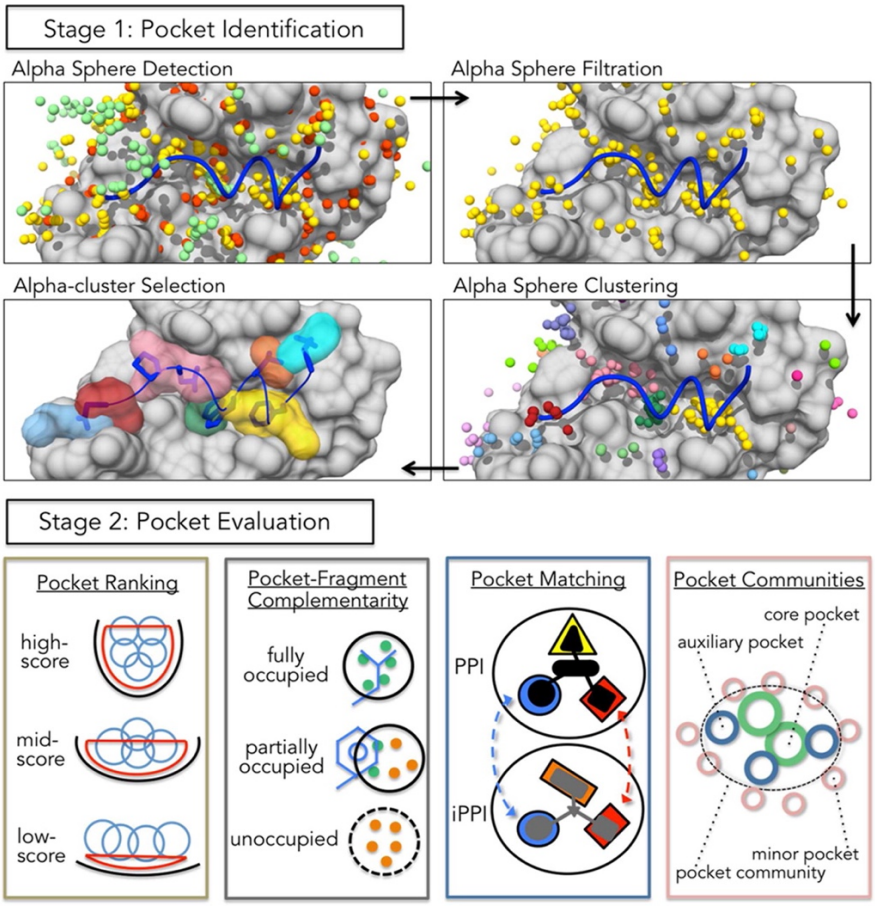

Fig. 1.12 | PPI inhibitors can be designed by fragment-centric topographical mapping. This approach builds on principles of fragment-based drug discovery to detect the fragment centric modularity of the protein surface and then characterize the PPI interface as a set of localized, fragment-targetable regions. AlphaSpace is a computational analysis tool that uses the alpha sphere construct, a geometric feature of a protein's Voronoi diagram, to map out concave interaction space at the protein surface. Stage 1 involves identifying pockets by detecting all alpha spheres, removing those outside the minimum or maximum radius cutoffs and clustering the remainder into fragment-centric pockets Only alpha-clusters in contact with the peptide or ligand are selected for evaluation. Evaluation of pockets involves ranking, calculation of the percentage occupation of each pocket, matching between different structures of the protein, and grouping of communities to identify potentially druggable surface regions. Image reproduced from Rooklin *et al*. *Journal of chemical information and modeling,* 2015.[214]

1.2.4 Coiled-coil interactions

Coiled-coil structural motifs occur ubiquitously in nature, occurring in approximately 3% of all protein sequences.[219] These domains act as both tight and dynamic protein-protein interaction sites allowing assembly and disassembly of multimeric protein complexes.[220] These highly specific interactions can be homomeric or heteromeric, have different oligomeric states and be orientated parallel or antiparallel.[221] In nature, these interaction domains show both

structural and functional diversity.[222-227] Examples include cytoskeletal,[228,229] transcription-factor,[230] signal-transduction,[231] and membrane proteins.[232]

Classical coiled coils have 2 - 4 amphipathic α helices with heptad sequence repeats of hydrophobic (**h**) and polar (**p**) residues ***hpphppp***, often denoted ***abcdefg***. [233] Coiled-coil formation is driven by the burial of hydrophobic ***a*** and ***d*** residues in the core of multi-helix assemblies (Fig.1.13). There is a mismatch between the periodicities of the 3.5 residue sequence repeat of the hydrophobic residues and the 3.6 residues per turn of the α helix, which results in the helices wrapping around one another to form a left-handed supercoil.[234,235] One consequence of this is that the side chains of adjacent helices interlock forming highly specific knobs-into-holes (KIH) interactions in the quaternary structure.[221,236] Side chains from one helix (knobs) dock into diamond-shaped holes formed by the side chains of four residues on the neighbouring helix. This highly regular assembly means that coiled coils can be described parametrically by a minimal number of parameters.[237-242]

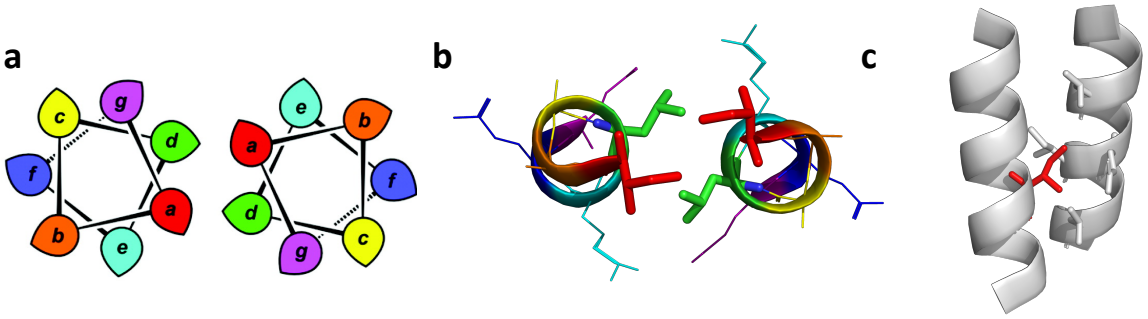

Fig. 1.13 | Coiled coils assemble from heptad repeats of hydrophobic (h) and polar (p) residues in a left handed supercoil. a, Helical wheel of a single heptad of a dimeric coiled coil showing assembly to bury hydrophobic residues at the ***a*** and ***d*** positions. **b**, View down the long axis of a single heptad of a *de novo* designed coiled-coil dimer showing burial of hydrophobic side chains in ***a*** and ***d*** residues (PDB 4DZM).[116] **c**, Highly specific knobs into holes (KIH) interactions are formed between the side chain of knob residues on one helix and diamond shaped holes formed by four residues on the adjacent helix.

The heptad repeat sequences, specific backbone geometry and side-chain KIH interactions can all be used to identify coiled coils in natural sequences and structures[243-246] A large number of algorithms are able to predict coiled-coil motifs in protein sequences. PCOILS detects regions of coiled coils in a protein sequence or multiple sequence alignment using profile-profile comparisons.[247] An alternative method is employed by MARCOIL, which is a windowless hidden Markov model (HMM) tool that calculates posterior probabilities to detect canonical

coiled coils.[248] The most recent software, DeepCoil, is a neural network based method, trained on over 10 400 coiled coils which can detect both canonical and noncanonical coiled coils, often missed by other approaches.[249] For validation of these structures, the development of programs such as SOCKET/iSOCKET has enabled automatic detection of coiled-coil structures in the Protein Data Bank (PDB) through identification of the specific geometry of KIH interactions.[146,151] These tools have allowed the development of coiled-coil databases such as CC+ and The Atlas of Coiled Coils.[250-252] Analysis of such databases has provided insights into the determinants of coiled-coil oligomeric state, which has been shown to be largely due to amino-acid composition of knob residues at the helical interface. Indeed, the oligomer state of classical coiled coils can now be predicted using bioinformatic tools, though these results are still prone to errors due to the relatively small set of training data of protein structures with complex coiled-coil arrangements.[253-259] One of these tools, LOGICOIL, uses an algorithm based on simultaneous use of Bayesian variable selection, and multinomial probit regression to deliver *ab initio* multi-state classification of coiled-coil oligomers.[256]

1.2.5 Designing coiled-coil peptides

The well-established sequence-to-structure relationships that determine coiled-coil assembly makes them attractive targets for both rational and computational protein design.[237,260] In addition, their ubiquitous occurrence in nature means there are many therapeutically relevant PPI targets centred around coiled coils.[223,261,262] Parameterisation of these structures has allowed the development of bioinformatic tools for *de novo* design. The first of these was described by Parry in 1982, utilizing residue frequency at each position of the ***abcdefg*** heptad repeat.[246] More recently, software such as CCCP, CCBuilder, ISAMBARD and Rosetta have been developed to allow the design, optimisation, modelling and analysis of coiled-coil assemblies.[238-240,263,264] These tools have allowed the design of a diverse range of coiled coils of varying oligomeric state and orientation (parallel/antiparallel) in both homomeric and heteromeric systems, with structures selected for the desired applications. Examples include highly stable helical bundles,[265] pore-forming barrels,[266] self-assembling coiled coils,[267] a transmembrane zinc transporting tetramer,[268] a lanthanide binding assembly for imaging,[269] a synthetic bacterial cytoscaffold[270] and a molecular motor.[271]

Robust understanding of the design parameters required for formation of coiled-coil dimers, timers and tetramers has facilitated the development of a ‘basis set’ of coiled coils in the

Woolfson group, for use as scaffolds in synthetic biology (Fig. 1.14).[265] Recent and ongoing work to expand this set introduces larger oligomeric assemblies in addition to heteromeric and antiparallel systems.[266,272,273] The high thermostability of these *de novo* coiled coils gives them potential to interfere with natural PPIs. In these designed assemblies, the side chains of residues in the ***b, c*** and ***f*** positions of the heptad repeats are not involved in the coiled-coil interface and therefore have scope to be decorated with residues of choice. Fletcher *et al*. demonstrate that these positions can be used to incorporate hot-spot binding residues in the MCL-1/NOXA-B interface to generate a synthetic peptide to inhibit this natural PPI (Fig. 1.15).[270] The designed coiled coil stabilises the helical conformation required for interaction of key binding residues at the interface. Design knowledge can be applied to manipulate natural coiled-coil interfaces to probe function through mutations to disrupt interactions or increase affinity.[262,274] *De novo* coiled coils can also be used as templates for protein folding and to introduce PPIs for new biological activity in living systems.[275-277] These approaches have potential to offer structural insights into kinesin-1 tetramer assembly and the role of the KHC coiled-coil stalk in motor activation and motility.

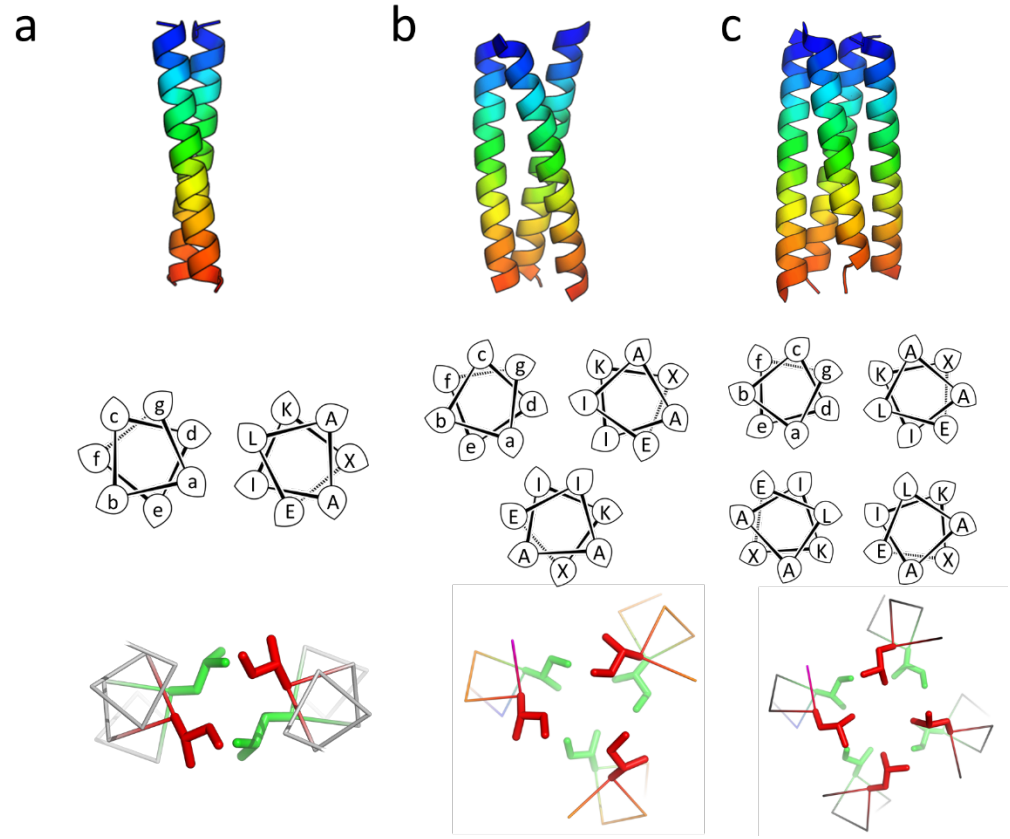

Fig. 1.14 | A basis set of designed hyperstable coiled coils can be used as templates and scaffolds to disrupt natural PPIs and introduce new interactions in cells. Crystal structures, helical-wheel diagrams and KIH packing for basis set *de novo* coiled coils **a**, CC-Di (PDB ID 3R4A), **b**, CC-Tri (E4DZL), and **c**, CC-Tet (3R4A).

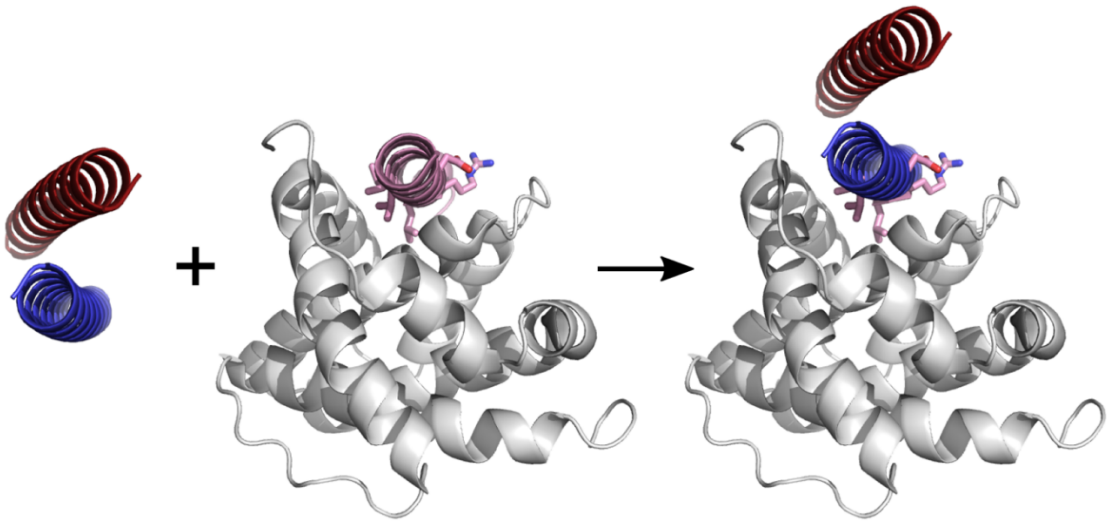

Fig.1.15 | *De novo* coiled coils can be used as scaffolds to disrupt natural PPIs. Hot spot binding residues in the MCL-1/NOXA-B PPI were identified by computational alanine scanning. These residues were grafted onto the solvent exposed surfaces of a designed heterodimeric coiled-coil peptide. The peptides selectively inhibited a cognate MCL-1/BID complex in the mid-nM range. Image reproduced from an Fletcher *et al*., *Chem. Sci*, 2018 with permission from the publisher.[278]

1.2.6 Summary

PPIs are critical for most biochemical processes and, when dysregulated, can result in disease.[144,145] In addition to globular interactions between protein subunits, common classes of PPIs include those directed through peptide-protein interactions and coiled-coil domains.[180-182,223,261,262] An important subclass involve recognition of short linear motifs by repeat proteins such as TPR domains, where helices stack together to form extended, binding surfaces.[190] TPR-peptide binding is observed in cell-cycle regulation, chaperone activity, transcription and protein translocation.[60] Examples in kinesin-1 include cargo recognition by the binding of acidic adaptor peptides to the KLC^{TPR} domains and the association of the LFP regulatory motif involved in KLC autoinhibition.[59,67,68] Coiled coils are formed by the assembly of amphipathic α helices**,** which wrap around one another in a left-handed supercoil to form a hydrophobic core.[233,234,235] These assemblies are found in a wide range PPIs, allowing dynamic assembly and disassembly of multimeric protein complexes.[220,222-227] One example is in the assembly of the tetrameric motor protein kinesin-1. Coiled-coil domains mediate both KHC dimerization and association with KLCs.[46,47] In addition, coiled coils are essential for mediating the intramolecular strain that drives microtubule-based motility.[48]

Understanding of sequence-to-structure relationships has allowed the field of protein design to generate new assemblies, not seen in nature.[148] These design approaches can be used to manipulate natural PPIs, to probe their function and develop new research tools and therapeutics. Peptide design to disrupt or augment PPIs involved in kinesin-1 cargo recognition and autoinhibition could increase our molecular understanding of motor activity and regulation and may allow us to hijack the motor to manipulate intracellular transport. In addition, applying coiled-coil design knowledge to kinesin-1 has the potential to offer structural insights into how KHCs and KLCs assemble in the heterotetramer, how this is linked to motor regulation and the role of the KHC coiled-coil stalk in motor activation and motility.

1.3 Scope of this thesis

Kinesin-1 activity and regulation is critical for healthy cell function. Current structural understanding of the motor protein demonstrates the importance of PPIs, through binding of short peptide motifs to TPR and motor domains in cargo recognition and autoinhibition and between coiled-coil domains in tetramer assembly, regulation and motility. Protein design has

been used to manipulate natural PPIs in cells to inhibit, augment and hijack biological activities and answer new questions in cell biology. This thesis aims to use protein design to investigate kinesin-1 structure and activity, probing the roles it plays in healthy and disease states by targeting PPIs within the motor and between the motor and its cargo. New peptide tools were developed to disrupt and facilitate kinesin-1 activity, offering new insights into the mechanisms of motor activity and regulation in both organelle transport and microtubule sliding. Chapter 3 describes the design of *de novo* cargo-adaptor peptides that bind KLC^{TPR} domains *in vitro* with high affinity. Chapter 4 investigates the capacity of a *de novo* cargo adaptor to hijack kinesin-1 activity within cells. Chapter 5 applies coiled coil-design principles to probe the nature of the KHC-KLC interaction. Chapter 6 considers a role for pH dependence in regulation of PPIs involved in motor activation. Together, these studies offer new insights into the structure and function of kinesin-1 motors in the cell.

2 Methods

2.1 Materials

2.1.1 Peptide synthesis and characterisation

Fluorenylmethyloxycarbonyl (Fmoc) protected amino acids, dimethylformamide (DMF) and 6-Chloro-1-hydroxybenzotriazole (Cl-HOBt) were purchased from Cambridge Reagents. Rink amide supporting resin (100-200 mesh) and 5-Carboxytetramethylrhodamine (TAMRA) were purchased from Novabiochem® and ChemMatrix solid support from PCAS BioMatris Inc. N, N′-Diisopropylcarbodiimide (DIC) was purchased from Carbosynth, morpholine from Merck Millipore, formic acid, Triisopropyl silane (TIPS), and Trifluoroacetic acid (TFA) from Acros Organics, pyridine and dichloromethane (DCM) from Fisher, acetic anhydride from BDH Laboratories, diethyl ether from Honeywell, and HPLC-grade acetonitrile (MeCN) from VWR Chemicals. (1-[Bis(dimethylamino)methylene]-1H-1,2,3-triazolo[4,5-b]pyridinium 3-oxide hexafluorophosphate (HATU), N,N- Diisopropylethylamine (DIPEA), methanol, ammonium bicarbonate and biotin were purchased from Sigma Aldrich. All chemicals were used as supplied. Synthesis-grade ultra-pure DMF (Cambridge Reagents) was used exclusively during peptide synthesis. Commercial crystallisation screens JCSG, Structure Screen 1+2,ProPlex and PACT Premier™ were from Molecular Dimensions.

2.1.2 Molecular biology

Restriction enzymes, T4 DNA ligase, the corresponding buffers, purple DNA loading dye and chemically competent *E.coli* BL21(DE3) cells were supplied by New England Biolabs. Chemically competent *E.coli* TOP10 cells were purchased from Invitrogen. Lysogeny broth (LB), LB-agar, ampicillin (Amp), kanamycin (Kan), isopropyl β-D-1-thiogalactopyranoside (IPTG), 4-(2-hydroxyethyl)-1-piperazineethanesulfonic acid (HEPES), imidazole, hydrochlodic acid (HCl) β-mercaptoethanol (BME), sodium chloride (NaCl), ethylenediaminetetraacetic acid (EDTA), tris(hydroxymethyl)aminomethane hydrochloride (Tris HCl), 2-amino-2-(hydroxymethyl)-1,3-propanediol (Tris base), agarose, and Vivaspin® sample concentrators were purchased from Sigma Aldrich. QIAprep spin miniprep, plasmid plus midi and QIAquick gel extraction kits were from Qiagen. SYBR® Safe stain, NuPAGE® Novex® Bis-Tris gels, NuPAGE® MOPS Running Buffer and NeutrAvidin Agarose Resin, were purchased from Thermo Fischer Scientific. Taq plus precision polymerase was from Agilent. Protease inhibitor cocktail tablets were from Roche.

His-trap HP columns and 16⁄60 HiLoad Superdex 75 columns were from GE Healthcare. Protein Marker V PeqGOLD, was from VWR. Oligonucleotide synthesis, PCR primer synthesis and DNA sequencing was from Eurofins Genomics. Plasmids were purchased from Genscript, Novagen and Addgene or donated by other researchers.

2.1.3 Cell culture

Dulbecco's Modified Eagle's Medium (DMEM), phosphate buffered saline (PBS), Neurobasal media, GlutaMAX and B27 were from Gibco Invitrogen. Lipofectamine LTX was from Invitrogen. Foetal calf serum (FCS), Bovine Serum Albumin (BSA), potassium chloride (KCl), calcium chloride ($CaCl_2$) magnesium chloride ($MgCl_2$), monosodium phosphate (NaH_2PO_4), glucose, dimethyl sulfoxide (DMSO), glycine, Triton X-100, polyethylene glycol sorbitan monolaurate (Tween-20), horse serum and poly-lysine were from Sigma-Aldrich. Effectene transfection reagent was purchased from Qiagen. Penicillin and streptomycin were from PAA. Paraformaldehyde 16% solution and NP-40 were from Thermo Fischer Scientific. Skimmed milk powder and FluorSave reagent was purchased from Merck and PVDF membranes were from Immobilon-P, Millipore. Kinesore was from Tocris Bioscience. Anti-HA monoclonal antibody (HA-7) used for Western blot, anti-HA polyclonal antibody (H6908) used for immunofluoresence, and anti–β-tubulin (B-5-1- 2) were supplied by Sigma-Aldrich. Anti-LAMP1, rabbit monoclonal, was from Cell Signalling Technologies. Anti-Ankyrin-G was from NeuroMab. Alexa 488-, 568-, and 633-conjugated anti-mouse or anti- rabbit secondary antibodies were from Thermoscientific. GFPTrap beads were from ChromoTek.

2.1.4 Figure preparation

All structures included in the manuscript were created using educational-use PyMOL software (https://www.pymol.org/). Exact peptide masses were calculated using Peptide Synthetic's online Peptide Mass Calculator tool (**http://www.peptidesynthetics.co.uk/tools/**). Data analysis was performed using the Prism (GraphPad Software Inc., San Diego CA, USA) package. Confocal images were collected using a Leica SP5II system with a 40× or 60× objective running Leica LAS X and are presented as maximum intensity projections. Figures were assembled using ImageJ in conjunction with Inkscape and Biorender.

2.2 Peptide synthesis and purification

2.2.1 Peptide synthesis

Standard Fmoc solid-phase peptide synthesis was performed on a 0.1 mM scale using CEM Liberty Blue automated peptide synthesis apparatus with inline UV monitoring. Activation was achieved with DIC/Cl-HOBt. Fmoc deprotection was performed with 20% v/v morpholine/DMF with addition of 5% formic acid to prevent aspartimide formation where DG, DA, DS, DD or DN appeared in the sequence. Double couplings were used for β-branched residues and the subsequent amino acid. All peptides were synthesised from C to N terminus as the *C*-terminal amide on Rink amide resin or, in the case of challenging synthesis, ChemMatrix solid support. *N*-terminally acetylated peptides were produced by addition of acetic anhydride (0.25 mL) and pyridine (0.3 mL) in DMF (5 mL) for 30 minutes at room temperature (rt). Fluorescently labelled peptides were produced by addition of TAMRA (0.1 mM, 2 eq.), HATU (0.095 mM, 1.9 eq.) and DIPEA (0.225 mM, 4.5 eq) in DMF (3 mL) to DMF washed peptide resin (0.05 mM) with agitation for 3 hours. Resin was washed with 20% piperidine in DMF (5 mL) for 2 x 30 minutes to remove any excess dye. All manipulations were carried out under foil to exclude light. Biotinylated peptides were produced by addition of Cl-HOBt (1 ml, 0.5 M) to a solution of biotin (0.25 mM, 5 eq.) and DIC (1 ml, 1 M) in DMF and the mixture added to DMF washed peptide resin with agitation at rt for 2 hours. Peptides were cleaved from the solid support by addition of TFA (9.5 mL), TIPS (0.25 mL) and water (0.25 mL) for 3 hours with shaking at rt. The cleavage solution was reduced to approximately 1 mL under a flow of nitrogen. Crude peptide was precipitated upon addition of ice-cold diethyl ether (40 mL) and recovered via centrifugation. The resulting precipitant was dissolved in 1:1 acetonitrile and water (≈ 15 mL) and lyophilised to yield crude peptide as a solid.

2.2.2 Peptide purification

Peptides were purified by reverse phase HPLC on a Phenomenex Luna C18 stationary phase column (150 x 10 mm, 5 μM particle size, 100 A pore size) using a preparative JASCO HPLC system. A linear gradient of 20-80% acetonitrile and water (with 0.1% TFA) was typically applied over 30 minutes with gradient adjusted for each peptide to optimise separation. For acidic peptides, a linear gradient of 10-60% ammonium bicarbonate (25 mM) and water was typically applied over 30 minutes with gradient adjusted for each peptide to optimise separation. Where peptides were insoluble in HPLC solvents, DMSO was added to improve solubility. Chromatograms were monitored at wavelengths of 220 and 280 nm. The identities

of the peptides were confirmed using MALDI-TOF mass spectrometry using a Bruker ultrafleXtreme II instrument in reflector mode. Peptides were spotted on a groundsteel target plate using dihydroxybenzoic acid or α-Cyano-4-hydroxycinnamic acid (CHCA) as the matrix. Masses quoted are for the monoisotopic mass as the singly protonated species. Masses were measured to 0.1% accuracy. Peptide purities were determined using a JASCO analytical HPLC system, fitted with a reverse-phase Kinetex® C18 analytical column (100 x 4.6 mm, 5 µm particle size, 100 Å pore size). Fractions containing pure peptide were pooled and lyophilised. Peptides were dissolved in buffer, typically PBS or FP assay buffer (25 mM pH 7.4 HEPES buffer with 150mM NaCl, 5mM BME) and their concentrations determined by UV-Vis at 280 nm on a ThermoScientific Nanodrop 2000 spectrophotometer using the known extinction coefficients for Tyrosine (ε_{280} = 1280 M^{-1} cm^{-1}) and Tryptophan (ε_{280} = 5690 M^{-1} cm^{-1}). The total extinction coefficients for a sequence was calculated by adding the extinction coefficient for each chromophore. For TAMRA coupled peptides concentration was calculated by measurement of UV absorbance at 555 nm (ε_{555}(TAMRA) = 85 000 mol^{-1} cm^{-1}).

2.3 Recombinant protein expression

2.3.1 Molecular genetics

The TPR domain of KLC1 alone (His-KLC1^{TPR}, amino acids A211–S495), a longer version containing the conserved LFP motif (His-KLC1^{extTPR}, K173–S495), and equivalent constructs for KLC2 (His-KLC2^{TPR}, A196–S480 and His-KLC2^{extTPR}, K161–S480) cloned in the bacterial expression vector pET28His-Thrombin have been described previously.[59] A codon-optimized DNA sequence encoding the TPR domain of mouse KLC1 (residues 205 – 496, Uniprot Q5UE59, KLC1^{TPR}) fused *N*-terminally to the KinTag peptide via a (Thr-Gly-Ser)$_{10}$-Gly flexible connector was purchased from Genscript and subcloned between the NdeI/XhoI sites of a pET28 vector (Novagen). This strategy allowed for the expression of a chimeric protein KLC1^{TPR}-(TGS)$_{10}$-G-KinTag (His-KLC1^{TPR}:KinTag) bearing a thrombin-cleavable *N*-terminal hexa-histidine tag.

For mammalian cell expression rat kinesin-1 heavy chain (KHC, Kif5C) was obtained as an *N*-terminally mCit-tagged clone.[77] Full-length, wild-type mouse kinesin light chain 1 and 2 (KLC1, KLC2) and rat KIF5C were cloned into the cytomegalovirus-driven mammalian expression vector CB6-HA and CB6-GFP. Plasmids for LAMP1-mGFP plasmid number 34831,[279] for mCherry-Peroxisomes plasmid number 254520,[280] mCherry-TOMM20-N-10,

plasmid number 55146,[281] and pMito-GBPen, plasmid number 128269[282] were obtained from Addgene. SKIP or Kin-Tag sequences followed by a $(TGS)_2$ linker were introduced by annealing of the relevant oligonucleotides and cloned between LAMP1 and mGFP in Sal1-BamH1 restriction enzyme sites, between mCherry and TOMM20 in BamH1 and AgeI sites and at the N termius of mCherry-PEX in EcoRI and AgeI sites (Table 2.1). The KinTag and CC-AP-Di-A sequences followed by a $(TGS)_2$ linker were cloned to the *C*-terminus of CB6-GFP between Not1 and EcoR1 restriction sites by annealing of the relevant oligonucleotides (Table 2.1). A $(TGS)_2$ linker followed by the CC-AP-Di-A sequence was cloned C terminal to LAMP1-GFP through Golden Gate assembly using Sap1type II restriction sites (Table 2.1). All plasmids were verified by DNA sequencing by Eurofins Genomics.

Table 2.1 | Oligonucleotide sequences used for sub-cloning, 5'-3'

LAMP1-SKIP-GFP-For:	TCGACGGCAGCACCAACCTGGAGTGGGATGATAGCGCGATTACCGGCA GCACTGGATCAG
LAMP1-SKIP-GFP-Rev:	GCCGTCGTGGTTGGACCTCACCCTACTATCGCGCTAATGGCCGTCGTG ACCTAGTCCTAG
LAMP1-KinTag-GFP-For:	TCGACGGCACCGTGTTTACCACCGAAGATATCTATGAATGGGATGATA GCGCGATTACCGGCAGCACTGGATCAG
LAMP1-KinTag-GFP-Rev:	GCCGTGGCACAAATGGTGGCTTCTATAGATACTTACCCTACTATCGCG CTAATGGCCGTCGTGACCTAGTCCTAG
KinTag-mCherry-PEX-For:	AATTCATGGGCACCGTGTTTACCACCGAAGATATCTATGAATGGGATG ATAGCGCGATTACCGGCAGCACCGGCAGCGGA
KinTag-mCherry-PEX-Rev:	CCGGTCCGCTGCCGGTGCTGCCGGTAATCGCGCTATCATCCCATTCAT AGATATCTTCGGTGGTAAACACGGTGCCCATG
mCherry-KinTag-TOMM20-For:	GATCCAGGCACCGTGTTTACCACCGAAGATATCTATGAATGGGATGAT AGCGCGATTACCGGCAGCACCGGCAGCGGA
mCherry-KinTag-TOMM20Rev:	CCGGTCCGCTGCCGGTGCTGCCGGTAATCGCGCTATCATCCCATTCAT AGATATCTTCGGTGGTAAACACGGTGCCTG
GFP-KinTag-For:	GGCCGCACCGGCAGCACTGGATCAACAGGGTCTGGCACCGTGTTTACC ACCGAAGATATCTATGAATGGGATGATAGCGCGATTTGAG
GFP-KinTag-Rev:	AATTCTCAAATCGCGCTATCATCCCATTCATAGATATCTTCGGTGGTA AACACGGTGCCAGACCCTGTTGATCCAGTGCTGCCGGTGC
GFP-CC-Di-A-For:	GGCCGCACCGGCTCTACCGGCAGCGGCCAGCTGGAACAAGAACTGGCC GCTCTGGATCAGGAGATCGCCGCCGCCGAGCAGGAGCTGGCTGCCCTG GACTGGCAGATCCAGGGCTGAG
GFP-CC-Di-A-Rev:	AATTCTCAGCCCTGGATCTGCCAGTCCAGGGCAGCCAGCTCCTGCTCG GCGGCGGCGATCTCCTGATCCAGAGCGGCCAGTTCTTGTTCC AGCTGGCCGCTGCCGGTAGAGCCGGTGC
LAMP1-GFP-CC-Di-A-For:	AGTAGCTCTTCAGCCGCGGCTGAACAGGAATTGGCCGCGCTTGATTGG CAAATTCAAGGCTAAAGCGGCCGCGACTC
LAMP1-GFP-CC-Di-A-For:	AGTAGCTCTTCAGGCTATCTCCTGGTCCAGCGCTGCAAGTTCTTGTTC CAATTGACCGGATCCTGTGGAACCGGTCTTGTACAGCTCGTCCATGCC

For site directed mutagenesis, complementary oligonucleotides incorporating one or more nucleotide changes were designed to target the region of interest (Table 2.2). The IAK/AAA and LFP/AAA constructs have been described previosuly.[59,87] Typically, reactions were in a final volume of 100µl and contained 100 ng template plasmid DNA, 125 ng of forward and reverse primer, 1µl 10µM dNTP's, 1µl (2.5U) Native Pfu Polymerase, and 10µl 10x polymerase buffer. In a BioRad C1000 thermal cycler, reactions were subject to a 2 minute denaturing step at 95 °C followed by 18 cycles of 1 minute at 95 °C, 1 minute at 55 °C and 15 minutes at 68 °C. Reactions were completed by a 15 minute incubation at 68 °C and then cooled

to 4°C. Reaction mixtures were incubated with 1µl Dpn1 for 1 hour at 37°C to digest methylated template DNA before transformation.

Table 2.2 | Oligonucleotide sequences used for site-directed mutagenesis, 5'-3'

E794L-For:	GTGTCCAGACTTCTCCAGACTCTTCACAAC
E794L-Rev:	AGTCTGGAGAAGTCTGGACACAGTCTCTTC
KIF5C-WT-H918R-For	GAACATGGCCAGGAGGGCAAGATCGGCTCAGATCGCCAAG
KIF5C-WT-H918R-Rev	CTTGGCGATCTGAGCCGATCTTGCCCTCCTGGCCATGTTC
KIF5C-WT-H930R-For	CATCCGCCCAGGACGATATCCTGCATCATC
KIF5C-WT-H930R-Rev	GATGATGCAGGATATCGTCCTGGGCGGATG
KIF5C-IAK/AAA-H918R-For	GGCCAGGAGGGCAAGATCGGCTGCAGCAG
KIF5C-IAK/AAA -H918R-Rev	CTGCTGCAGCCGATCTTGCCCTCCTGGCC
KIF5C-IAK/AAA -H930R-For	GCCGCCGCCGCACGATATCCTGCATCATC
KIF5C-IAK/AAA -H930R-Rev	GATGATGCAGGATATCGTGCGGCGGCGGC

Genes for CC-Di-G_5-Kif5B and CC-Di-G_5-KLC1were purchased from Twist Bioscience and cloned between BglII and XhoI sites in pET-21(+) and NdeI and XhoI sites in pET-28a(+) respectively (Table 2.3).

Table 2.3 | Gene sequences for CC-Di fusion proteins

CC-Di-G_5-Kif5B	CGATCCCGCGAAATTAATACGACTCACTATAGGGGAATTGTGAGCGGATAACAATTCCCCTCTA GAAATAATTTTGTTTAACTTTAAGAAGGAGATATACCATGGGTTCCAGTCACCACCACCACCAC CATTCTTCAGGACTCGTTCCCCGTGGGTCCCACATGGAAATTGCAGCGTTGAAGCAGGAGATT GCAGCTCTGAAGAAGGAGAATGCCGCGTTGAAGTGGGAAATCGCTGCGCTCAAGCAAGAAG GTGGTGGGGGGGGTCTGACGGTGATGCAAGACCGCCGTGAACAGGCGCGCCAGGATCTTAA GGGGCTCGAAGAGACCGTCGCCAAGGAGCTGCAGACTCTGCATAACTTACGTAAGCTGTTTGT TCAAGACCTCGCCACGTGATAA
CC-Di-G_5-KLC1	GAGATTGCGGCCCTTAAGCAAGAGATCGCGGCGTTGAAGAAGGAGAATGCGGCGTTAAAGT GGGAAATCGCAGCCCTGAAGCAGGAAGGCGGAGGAGGTGGCATGGCATTAAGCAACCATTT GAACGCGGTGGAAAGCGAGAAGCAGAAATTACGTGCGCAAGTGCGCCGTCTTTGCCAAGAG AACCAGTGGTTACGCGATGAGCTTGCCAATACACAGCAGAAGTTGCAAAAGAGCGAACAAAG TGTTGCACAGCTTGAAGAGGAAAAGAAACATTTAGAGTTTATGTGATGATAATGA

For sub-cloning, or to confirm the identity of plasmids according to restriction digest profile, plasmid DNA was digested with the relevant restriction enzymes in buffers recommended by the manufacturer. A typical reaction made up to 50 µl with H_2O contained DNA (2 µg), 10x digestion buffer (5 µl) and restriction enzymes (1 µl), incubated at 37°C for 2 hours. Reactions were analysed by agarose gel electrophoresis. For sub-cloning, oligonucleotides were resuspended in H_2O to give a concentration of 1 µg/µl. Forward and reverse oligonucleotides (2 µl each) were annealed in 46 µl of annealing buffer (10 mM Tris pH 7.8, 50 mM NaCl, 1mM EDTA) at 95°C for 5 minutes and gradually cooled to room temperature over 45 minutes. Ligation reactions were carried out at 16°C overnight using T4 DNA ligase in 1x T4 DNA ligase buffer. A typical reaction consisted of vector (2 µl), insert (10 µl), buffer (2 µl) and ligase (1µl) made up to 20 µl with H_2O.

Chemically competent *E.coli* TOP10 cells (typically 20 µl) and DNA (typically 1 µl) were incubated on ice for 30 minutes. Transformation was achieved by heat-shock at 42 °C for 45 seconds followed by incubation on ice for 10 minutes. S.O.C medium (250 µl) was added and the transformation reaction incubated at 37°C with agitation at 180 rpm for 1 hour. Transformed bacteria (100 µl) were spread onto LB-agar plates containing appropriate antibiotics ampicillin or kanamycin (50 µg/ml) and incubated overnight at 37°C. A single bacterial colony of E.coli TOP10 cells was picked and grown overnight in LB (5 ml or 100 ml) supplemented with either ampicillin or kanamycin (50 µg/ml). The DNA was purified using QIAprep spin miniprep or Plasmid Plus Midi kits according to manufacturer's protocol. DNA was added to 6x purple loading dye and loaded onto a 1% (W/V) agarose gel containing 1X SYBR® Safe gel stain. A 1 kb plus ladder was used as a DNA marker. DNA bands were visualised and excised on an Odyssey Sa (LI-COR) imaging system and DNA extracted using the QIAquick Gel Extraction Kit according to the manufacturers guidelines.

Polymerase chain reactions with Taq plus precision polymerase were used to amplify fragments of DNA from plasmids. Reaction mixtures were made up to 100 µl with H_2O and contained template DNA (100 ng), forward and reverse primers (0.5 µl, 100 µM), dNTP's (1 µl,10 mM), 10X Polymerase buffer (10µl), and polymerase (1µl). In a BioRad C1000 thermal cycler, reactions were subject to a 2 minute denaturing step at 95°C followed by 25 cycles of 30 seconds at 95°C, 1 minute at 55°C and 1 minute per kb of sequence to be amplified at 72°C. Reactions were completed by a 10 minute incubation at 72°C and then cooled to 4°C.

2.3.2 Protein expression and purification

Chemically competent *E.coli* BL21(DE3) cells were transformed as above. Single bacterial colonies of *E.coli* BL21(DE3) cells were picked and grown overnight in 5 ml LB supplemented with ampicillin or kanamycin (50 µg/ml) at 37°C, 180 rpm. Small scale overnight bacterial cultures (5 ml) were used to inoculate larger cultures (1 L) which were incubated at 37°C until they reached an OD600 of 0.8. Protein expression was induced by the addition of 300 µM Isopropyl β-D-1-thiogalactopyranoside (IPTG) and the cultures incubated at 16°C, 180 rpm for 16 hours. Cells were harvested in a Beckman Counter Avanti J-25 centrifuge with J-10 rotor at 2824 x g for 30 minutes at 4°C and resuspended in 35 ml lysis buffer (25 mM HEPES pH 7.4, 500 mM NaCl, 20mM imidazole, 5mM β-mercaptoethanol supplemented with protease inhibitor cocktail (Roche)). Cell lysis was accomplished by sonication for 3 minutes (SONICS,

Vibra Cell, Pulses of 5 seconds on, 10 seconds off, 70% amplitude). Insoluble material was sedimented in a Beckman Counter Avanti J-25 centrifuge with J-20 rotor at 20 388 x g for 30 minutes at 4°C and the supernatant loaded onto a His-trap HP column preequilibrated with lysis buffer. The protein was eluted with an imidazole gradient (20 mM to 500 mM imidazole) and fractions containing the target protein identified by SDS polyacrylamide gel electrophoresis. Samples were resuspended in1 x SDS loading buffer (10% glycerol, 2% SDS (w/v) 60mM Tris pH 6.8, 0.001% bromophenol blue, 100 mM DTT) and denatured at 95 °C for 5 minutes. Samples were run alongside a protein marker ladder in 12% acrylamide Bis-Tris gels at 180 V for 1 hour in 1 x MOPS Running Buffer (20X = 50 mM MOPS, 50 mM Tris Base, 0.1% SDS, 1 mM EDTA, pH 7.7). Fractions containing the target protein were further purified by size exclusion chromatography (SEC) on a HiLoad 16⁄600 Superdex 75 prep grade column preequilibrated with sample buffer (25 mM HEPES pH 7.4, 500mM NaCl, 5mM β-mercaptoethanol) and 2 ml fractions collected using an AKTA prime plus. Fractions containing pure protein were identified by SDS polyacrylamide gel electrophoresis, pooled and concentrated using spin sample concentrators. Protein concentration was determined using a UV/Vis spectrometer.

A collaboration with the Steiner lab, Kings College London was established for crystallization of KLC1^{TPR}:KinTag. In the Steiner lab, protein eluted from the immobilized metal affinity chromatography step was buffer exchanged in lysis buffer and was further incubated overnight at room temperature with thrombin conjugated beads (Thrombin CleanCleave Kit, Sigma-Aldrich). The protein-bead mixture was filtered using a gravitational column and non-tagged protein was collected utilizing reverse IMAC on a HisTrap HP column, followed by size exclusion chromatography on a HiLoad 16/600 Superdex 75 column (GE Healthcare) pre-equilibrated with 25 mM HEPES pH 7.5, 150 mM NaCl and 5mM β-mercaptoethanol. Crystallization conditions are reported in Cross et al.[283]

2.4 Cell culture

HeLa cells were maintained in high glucose Dulbecco's Modified Eagle's Medium with 10% (v/v) FCS and 5% penicillin/streptomycin (herein referred to as DMEM) at 37 °C and 5% CO_2. For transfection, cells were seeded in 6-well plates on fibronectin coated 13 mm coverslips, generally at a density of 1 x 10^5 cells per well and incubated at 37 °C and 5% CO_2 for 16 h prior to transfection. Cells were transfected with 0.4 µg DNA using Effectene transfection reagent as per the manufacturer's instructions. For transfection of GFP and GFP nanobody (GBPen) constructs a ratio of DNA of 1:2 was used. For confocal imaging, cells were generally left for 24 hours before fixation by addition of 4% (v/v) paraformaldehyde in PBS at room temperature for 10 minutes (2 ml per well for 6-well plate) and washed 3 x with PBS. For preservation of microtubules, instead cells were fixed with ice cold methanol at – 20 °C and then permeabilised with 0.1% Triton X-100 in PBS for 10 minutes. For immunofluorescence, fixed cells were incubated in blocking buffer at (1% BSA, 3% FCS) rt for 10 minutes before probing with primary and secondary antibodies, each for 1 hour, with 3 x washes in blocking buffer following each antibody incubation. Coverslips were mounted on microscope slides using FluorSave mounting media.

Primary hippocampal neuron cultures were prepared from embryonic day E18 Wistar rats as previously described.[284] Dissociated neurons, gifted from Dr Kevin Wilkinson and Dr Kirsty McMillan, were grown on 22 mm glass coverslips coated in poly-L-lysine (1 mg/mL). Cells were plated at 150,000 cells/coverslip in 2 ml plating medium (Neurobasal supplemented with 5% horse serum, 1% GlutaMAX and 2% B27). Media was changed to feeding medium (Neurobasal supplemented with 0.4 % GlutaMAX and 2% B27) 2 h after plating. Cells were fed with an additional 1 ml of feeding medium 7 days after plating. Cells were cultured in a humidified incubator at 37 °C and 5% CO_2. Animal care and procedures were carried out in accordance with the UK Animals Scientific Procedures Act (1986) and University of Bristol guidelines. Transfection of neuronal cultures was carried out at DIV 12 using Lipofectamine LTX according to the manufacturer's instructions. Cells were left for 48 h before fixation with 4 % (v/v) paraformaldehyde in PBS at room temperature for 15 minutes and washed 3 x with PBS. Paraformaldehyde was quenched with the addition of 100 mM glycine.

2.4.1 Cell treatments

For acidification treatments, as described by Heuser, cells were incubated in Ringer's buffer (150 mM NaCl, 5 mM KCl, 2 mM $CaCl_2$, 1 mM $MgCl_2$, 2 mM NaH_2PO_4, 10 mM glucose, 10 mM HEPES, pH 7.4) or Ringer's acetate buffer (80 mM NaCI, 70 mM Na acetate, 5 mM KCl, 2 mM $CaCl_2$, 1 mM $MgCl_2$, 2 mM NaH_2PO_4, 10 mM glucose, 10 mM HEPES, pH 6.8) for 1 h at 37 °C in an incubator without CO_2.[285]

For kinesore treatment, stocks were prepared by solubilization of dry powder from Tocris Bioscience, confirmed by electrospray ionisation mass spectrometry (ESI-MS), at a concentration of 50 mM in 100% DMSO and stored at −20 °C before use. Stocks were then diluted to 50 µM in Ringer's buffer to give a final concentration of DMSO of 0.1% and added directly to cells. Cells were incubated in for 1 h at 37 °C in an incubator without CO_2. Vehicle control experiments refer to cells treated with 0.1% DMSO in buffer.

For peptide treatments, stocks were prepared by solubilization of dry powder at a concentration of 1 mM in 100% DMSO or H_2O (determined by solubility) and stored at −20 °C before use. Stocks were then diluted to 20 µM in DMEM to give a final concentration of DMSO or H_2O of 2% and added directly to cells. Cells were incubated for 1 h at 37 °C in a 5% CO_2 incubator. Vehicle control experiments refer to cells treated with 2% DMSO or H_2O in DMEM. For lower-concentration treatments, stocks were first diluted in DMSO or H_2O to yield a 50× solution that was subsequently added to DMEM. For Chariot reagent treatments were carried out as per the manufacturer's instructions.

For transfected cells, treatments were 24 h after transfection.

2.4.2 Cell imaging

Confocal images were collected using a Leica SP5II Multi-laser confocal laser scanning microscope system attached to a Leica DMI 6000 inverted epifluorescence microscope with a 40 × or 60 × objective lens running Leica LAS X and are presented as maximum intensity projections. Figures were assembled using ImageJ in conjunction with Inkscape.

2.4.3 Quantification of organelle positioning

To quantify organelle distribution in an unbiased fashion, confocal images of cells were acquired at 40× magnification, with an open pinhole (1 Airy unit). In HeLa cells, as described previously, the cell perimeter was defined by thresholding equivalent saturated images and the cell area was scaled in 10% decrements. After background subtraction, cumulative integrated fluorescence intensity of the chosen organelle (relative to the whole cell) was then plotted for increasing incremental deciles.[286] For analysis of the resulting data, a nonlinear regression function in was used to fit a centred 6th order polynomial. To compare models to assess the statistical significance of differences in distribution profiles, the extra sum of F-squares test was applied. P-values for particular comparisons are indicated on the graphs. In addition, the cumulative integrated fluorescence intensity in the central 50% of the cell plotted for the different constructs and compared using an unpaired T-test. In HeLa cells where altered cell shape made this approach challenging, an alternative approach was employed. For this, the cell perimeter was defined by thresholding equivalent saturated images and after background subtraction, integrated fluorescence intensity of the perinuclear cluster was compared to the whole cell to give a measure of proportion of dispersed fluorescence.[69] In neuronal cells the soma perimeter was defined by thresholding equivalent saturated images. The axonal initial segment (AIS) was defined by thresholding equivalent images stained for ankyrin G. After background subtraction, mean fluorescence intensity for the two areas was plotted. Data sets were compared by an unpaired T-test.

2.5 Protein interaction assays

2.5.1 Fluorescence polarisation assays

TAMRA conjugated peptides were diluted to 150 nM and incubated with increasing concentrations of the protein of choice (typically 0 – 10 μM) in assay buffer (25mM HEPES pH 7.4, 5 mM β-mercaptoethanol and 150mM NaCl) using an EpMotion liquid handling robot (Eppendorf). Measurements were performed on a CLARIOstar (BMG Labtech) microplate reader at room temperature. Data were fitted to a quadratic one-site tight binding equation to account to calculate a value for K_d accounting for ligand depletion (Equation 4).[287]

Binding of a fluorescent peptide to the protein reduces the rate of tumbling of peptide in solution. Light is polarized by a polarizing filter and excites fluorescently labelled molecules that are oriented in the plane of the polarized light. The emitted light is then measured

perpendicular and parallel to the plane of the excitation beam. Polarization is a measure of the extent of molecular rotation between excitation and emission. Smaller molecules tumble more quickly and have low polarization values while larger molecules retain polarization longer. The polarization value, P, is a ratio of light intensities expressed in millipolarization units, calculated by equation [1] where F1= fluorescence intensity parallel to the excitation plane and F2= fluorescence intensity perpendicular to the excitation plane. An increase in the polarisation of emitted light can therefore be used as a measure of binding of the fluorescently labelled peptide to the target protein. This can be fitted to a binding curve to obtain a value for the dissociation constant, K_D.

$$P = \frac{F1-F2}{F1+F2} \qquad \text{Equation 1}$$

In a single site binding model, the fractional saturation of the receptor, R, (the fraction of protein molecules that are saturated with peptide) is the same as the ratio of bound ligand, L, to receptor and can be calculated using the Langmuir isotherm equation [2].

$$R + L \rightleftharpoons \mathrm{RL}$$

$$K_{eq} = \frac{[RL]}{[R][L]}$$

$$[RL] = K_{eq}[R][L]$$

$$K_d = \frac{1}{K_{eq}} = \frac{[R][L]}{[RL]}$$

$$\frac{[RL]}{[L]_{Tot}} = \frac{[RL]}{[L]+[RL]} = \frac{K_{eq}[R][L]}{[L]+K_{eq}[R][L]} = \frac{K_{eq}[R]}{1+K_{eq}[R]} = \frac{[R]}{K_d+[R]} \qquad \text{Equation 2}$$

This binding model assumes that the peptide is at very low concentration and therefore that the concentration of free protein remains approximately constant throughout the experiment. It is generally accepted that, providing the concentration of peptide is 10 x lower than the value or K_D, this is a valid approximation.[287] Since the designed cargo adaptor peptides bind KLC^{TPR}s with high affinity, a major fraction of the protein will be bound to the peptide and a tight binding model should be considered instead. In a tight binding model, it is no longer assumed that the concentration of free ligand, L, is equal to the total concentration of L. An additional calculation can be used to determine the concentration of free protein [3] and data fitted to the resulting quadratic equation [4] to calculate a value for K_D accounting for ligand depletion.[287]

$$K_d = \frac{([R] - [RL])([L] - [RL])}{[RL]}$$ Equation 3

$$0 = ([R] - [RL])([L] - [RL]) - K_d[RL]$$
$$0 = [RL]^2 - ([R] + [L] + K_d)[RL] + 4[R][L]$$
$$[RL] = \frac{([R] + [L] + K_d) - \sqrt{([R] + [L] + K_d)^2 - 4[R][L]}}{2}$$
$$\frac{[RL]}{[L]_{Tot}} = \frac{([R] + [L] + K_d) - \sqrt{([R] + [L] + K_d)^2 - 4[R][L]}}{2[L]}$$ Equation 4

2.5.2 Immunoprecipitation and pulldown assays

For biotin-neutravidin pull downs, biotinylated peptides (1 mg) were dissolved in PBS (1.5 ml). Pierce™ NeutrAvidin™ Agarose resin slurry (300 μl) was diluted in PBS (1 ml) and centrifuged for 2 minutes at 358 x g, 4°C followed by washing (2 x 1 ml PBS). The resin was resuspended in PBS (3 x 100 μl) and dissolved peptide added (0.5 ml, 0.33 mg). The resin-peptide mixtures were incubated at 4°C overnight with agitation before centrifugation, 2 minutes at 358 x g, 4°C followed by washing (2 x 1 ml PBS). HeLa cells were plated at a density of 2 x 10^6 per 10 cm dish 4 hours prior to transfection. Cells incubated on ice and washed in 2 x 5 ml wash buffer (25 mM HEPES pH 7.4, 150 mM NaCl) followed by 1 ml lysis buffer (25 mM HEPES pH 7.4, 150 mM NaCl, 0.1% NP-40, 0.1% Trition-X 100 and protease inhibitor cocktail) for 10 minutes. Cells were centrifuged at 15 115 x g for 10 minutes at 4°C and the supernatant incubated with 30 µl of prewashed (3 x 800 µl wash buffer, 2000 rpm) NeutrAvidin™ Agarose resin slurry for 120 minutes at 4°C. 50µl of supernatant was retained for analysis of cell lysate. Beads were centrifuged at 358 x g for 2 minutes, the supernatant removed and washed (3 x 800 µl wash buffer, 358 x g). Samples were analysed by gel electrophoresis and western blotting.

For GFP immunoprecipitation, HeLa cells were plated at a density of 2 x 10^6 per 10 cm dish 4 hours prior to transfection and peptide treatment. Cells were incubated on ice and washed in 2 x 5 ml wash buffer (25 mM HEPES pH 7.4, 150 mM NaCl) followed by 1 ml lysis buffer (25 mM HEPES pH 7.4, 150 mM NaCl, 0.1% NP-40, 0.1% Trition-X 100 and protease inhibitor

cocktail) for 10 minutes. Cells were centrifuged at 15 115 x g for 10 minutes at 4 °C and the supernatant incubated with 30 µl of prewashed (3 x 800 µl wash buffer, 2000 rpm) GFPTrap beads for 120 minutes at 4 °C. 50 µl of supernatant was retained for analysis of cell lysate. Beads were centrifuged at 358 x g for 2 minutes, the supernatant removed and washed (3 x 800 µl wash buffer, 358 x g). Samples were analysed for GFP expression by gel electrophoresis and western blotting. Elution from beads was achieved by addition of 1% SDS at 95 °C for 10 minutes. TAMRA fluorescence intensity measurements of eluents were performed at 555 nm on a CLARIOstar (BMG Labtech) microplate reader at room temperature.

2.5.3 Western blotting

Protein samples separated on SDS-PAGE gels were transferred to a PVDF membrane for 1 hour at 100 volts. Membranes were prepared by wetting for 1 minute in methanol followed by 5 minutes in transfer buffer (2 5mM Tris, 192 mM glycine, 10% methanol). The membrane was blocked for 1 h at 4 °C in 5% milk in TBS-T (20 mM Tris, 0.25 M NaCl, 0.1% Tween-20, pH 7.5 with HCl) and probed with the appropriate antibodies overnight at 4 °C in 5% milk. Membranes were washed 3 x in TBS-T prior to incubation with fluorescently labelled secondary antibodies. followed by another 3 washes in TBS-T. Secondary antibodies were visualised using an Odyssey CLx (LI-COR) infrared imaging system.

2.6 Biophysical characterisation

2.6.1 Circular dichroism spectroscopy

Circular dichroism (CD) spectroscopy was used to determine the secondary structure of the peptide. In this experiment, differences in absorbance of right- and left- circularly polarised light are measured between 260 and 190 nm. Different peptide secondary structures have been shown to give characteristic spectra, with minima at 208 and 222 nm indicating α-helicity of the peptide in solution. CD spectra were collected on a Jasco J-815 or J-810 spectropolarimeter fitted with a Peltier temperature controller. Unless otherwise specified, CD spectra were measured at 50 µM total peptide concentration in PBS (8.2 mM sodium phosphate, 1.8 mM potassium phosphate, 137 mM sodium chloride, 2.7 mM potassium chloride at pH 7.4) or phosphate buffer (50 mM sodium phosphate, 50 mM NaCl, pH 7.4 or 5.8). For interaction experiments, peptides were mixed in buffer by vortexing. Spectra were recorded at 5 °C or 20 °C in a 1 mm or 5 mm quartz cuvette between 260 and 200 nm with a scan rate of 100 nm min^{-}

[1], 1 nm interval, 1 nm bandwidth and 1 s response time. For each sample an average of 8 recorded scans was taken. Thermal denaturation spectra were collected at 222 nm between 5 and 95°C, with the settings as above and a ramping rate of 40 °C hour^{-1}. Baseline measurements from the same buffer, cuvette and settings were subtracted from each data set before processing. Spectra were converted from ellipticities (deg) to molar ellipticities (MRE; deg.cm^2 .dmol^{-1} .res^{-1}) by normalising for concentration of peptide bonds and path length of the cuvette, using equation 5 where θ is the measured difference in absorbed circularly polarised light in millidegrees, c is the concentration in mM, l is the pathlength of the cuvette in cm and b is the number of amide bonds in the polypeptide. For calculation of b, the *N*-terminal acetyl bond was included but not the *C*-terminal amide.

$$MRE\ (deg.cm^2.dmol^{-1}res^{-1}) = \frac{\theta*100}{c*l*b} \qquad \text{Equation 5}$$

Fraction helicity (%) was calculated by equation 6 where $[\theta]_{222}$ is the blanked MRE at 222nm in cm^2 dmol^{-1} res^{-1}, T is the temperature in °C and n is the number of peptide bonds.

$$\% = 100 * \frac{[\theta]_{222} - [\theta]_{Coil}}{[\theta]_{Helix} - [\theta]_{Coil}} \qquad \text{Equation 6}$$

$$[\theta]_{Coil} = 640 - 45 * T$$

$$[\theta]_{Helix} = -42{,}000 * (1 - \frac{3}{n})$$

2.6.2 Analytical ultracentrifugation

The oligomeric state of coiled-coil peptides was measured by sedimentation equilibrium analytical ultracentrifugation (SE AUC). In this experiment the sample is spun at high speeds so that a centrifugal force pushes the protein towards the outside of the rotor, diffusion acts to oppose this concentration gradient. At equilibrium a balance between sedimentation and diffusion is reached and the concentration distribution across the cell is measured, giving a measure of molecular mass and thus oligomeric state.[288] AUC experiments were performed at 20 °C on a Beckman Optima XL-A or XL-I analytical ultracentrifuge with either an An-50 (Ti) or An-60 (Ti) rotor. The buffer density and partial specific volume (v) for each peptide at 20 °C was calculated using Sednterp (http://rasmb.org/sednterp/). AUC sedimentation equilibrium experiments were conducted in a sedimentation equilibrium cell in triplicate, with a 6-channel epon centre piece and quartz windows. Unless otherwise specified, peptide (110 µL, 100 µM,

PBS) was placed in the sample channels, and PBS (120 µL) in the reference channels. Absorbance scans (280 nm) were taken every 8 hours at speeds between 15 – 48 krpm, with scans at each speed duplicated. Data was fitted to single ideal species model using SEDPHAT.[289] 95% confidence limits were obtained following Monte Carlo analysis of the obtained fits.

2.6.3 Structural analysis and model building

For crystallography, freeze-dried peptides were dissolved in deionized water to a concentration of 10 mg ml^{-1} for vapour-diffusion crystallization trials using standard commercial screens (JCSG, Structure Screen 1+2, ProPlex and PACT PremierTM) at 19 °C with 0.3 µl of the peptide solution equilibrated with 0.3 µl of the screen solution. To aid with cryoprotection, crystals were soaked in their respective reservoir solutions containing 25% glycerol prior to data collection. X-ray diffraction data were collected at the Diamond Light Source (Didcot, UK) on beamline I24 at a wavelength of 0.98 Å. Data were processed with the Xia2 pipeline and AIMLESS,[290] as implemented in the CCP4 suite.[291] Structures were solved via molecular replacement using PHASER.[292] Model building and crystallographic refinement was performed using COOT[293,294] and PHENIX Refine or Refmac 5.[295]

2.7 Computational tools

Sequence alignments were done using BLAST.[296]
https://blast.ncbi.nlm.nih.gov/Blast.cgi

In silico alanine scanning was done using BUDE Alanine Scanning.[297]
https://pragmaticproteindesign.bio.ed.ac.uk/balas/

Buried surface area of interface residues was calculated using the Protein Interfaces, Surfaces and Assemblies (PISA) algorithm[298]
https://www.ebi.ac.uk/pdbe/pisa/pistart.html

In silico mutagenesis was done using Predictive Saturation Variation Scanning.[299]

Prediction of regions of coiled coils was done with MARCOIL.[248]
https://toolkit.tuebingen.mpg.de/tools/marcoil

Prediction of coiled coil oligomeric state was done with LOGICOIL.[256]
http://coiledcoils.chm.bris.ac.uk/LOGICOIL/

Models of homomeric coiled coils were built and optimised using CCBuilder v2.[240]
http://coiledcoils.chm.bris.ac.uk/ccbuilder2/builder

Models of heteromeric coiled coils were built and optimised using ISAMBARD with code written by Dr William Dawson.[263]
https://github.com/woolfson-group/isambard

Protein structure prediction was done using Alphafold Colab notebooks.[300]
https://colab.research.google.com/github/deepmind/alphafold/blob/main/notebooks/AlphaFold.ipynb

3 Fragment-linking design of *de novo* cargo adaptor peptides for kinesin-1

Results described in this chapter have been included in the publication:

Fragment-linking peptide design yields a high-affinity ligand for microtubule-based transport
Jessica A. Cross, Magda S. Chegkazi, Roberto A. Steiner, Derek N. Woolfson, Mark P. Dodding *Cell Chemical Biology* **2021, 28,** 1-8 DOI:10.1016/j.chembiol.2021.03.010

Some of the text in this chapter resembles the manuscript, for which I am first author. Under guidance from my supervisors, this work is my own, with the exception of the crystal structure, which was determined and solved by Dr. Magda Chegkazi and Prof. Roberto Steiner, Kings College London. Figures 3.2, 3.4, 3.7-3.9 are their work (as published in Cross et al. 2021).

3.1 Background

Recent studies exploring the molecular basis for the attachment and recognition of cargo by motor proteins have identified a new class of proteins termed cargo-adaptors. One class of these have peptide motifs, displayed on the surface of cargo, which bind to recognition domains on motor proteins, acting as molecular bridges between specific organelles and the cytoskeletal transport system (Fig. 3.1).[25] A number of kinesin-1 cargo-adaptor peptides have been shown to bind to the tetratricopeptide repeat (TPR) domains of kinesin light chains (KLC^{TPR}s) and have been structurally characterised (Fig 3.1-2), including a region of the lysosomal cargo adaptor SKIP and peptides from the *C* termini of JIP1 and Torsin A.[67,68] These studies have identified two distinct sequence classes of cargo-adaptor peptides: tryptophan-acidic (W-acidic) motifs have a tryptophan (W) residue flanked by aspartic or glutamic acid in the consensus L/M-D/E-W-D/E; and tyrosine-acidic (Y-acidic) motifs have tyrosine (Y) flanked by acidic residues. These two classes bind to distinct but overlapping sites on the concave surface of the KLC^{TPR}s, with μM affinities measured *in vitro*.[67,68] Presumably, tighter interactions are achieved in the cell through avidity, as multiple copies of the adaptor peptides are expressed on the surfaces of organelles and the kinesin-1 heterotetramer presents a pair of KLCs.[67,68] Several reports indicate an important role for co-operative interactions with the KHCs, again generally in the μM range.[86,87,301] Taken together, these studies support the notion that a network of medium-affinity interactions between cargo adaptor peptides and KHCs and KLCs co-operate to effect cargo recognition. Evidence that appending multiple copies of W-acidic sequences in tandem or triplicate enhances the efficiency of transport, suggests that μM binding is a limiting factor, and thus that increased cargo adaptor affinity could augment

transport.[112] Nonetheless, the hypothesis that adaptor-motor binding affinity *per se* is a limiting factor in transport is yet to be formally tested.

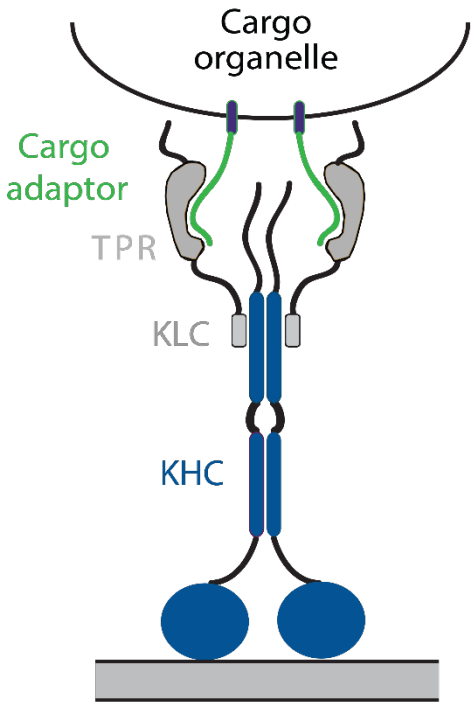

Fig. 3.1 | Acidic cargo adaptor peptides bind to TPR domains of KLCs. Cartoon representation of the kinesin-1 tetramer showing interaction of cargo adaptor peptide associated with the organelle surface (green) with KLC^{TPR} (grey).

More broadly, up to 40% of protein-protein interactions (PPIs) in the cell are thought to be directed by the recognition of short linear peptide motifs (SLiMs) by larger protein domains,[183,184] with a significant subset of these involving α-solenoid architectures such as armadillo repeat proteins (ArmRPs), HEAT proteins, and TPR domains.[189,302] In these α-solenoid proteins, tandem arrays of α-helices are stacked together to form extended superhelical structures. This arrangement results in high surface-area-to-volume ratios compared with typical globular proteins and, thus, larger binding surfaces.[190] In addition to kinesin-1 cargo transport, TPR domains are important for a diverse range of PPIs in the cell including cell-cycle regulation, chaperone activity, transcription, protein translocation and membrane trafficking.[60] It is becoming clear generally that α-solenoid domain-peptide interactions are amenable to design, engineering and chemical manipulation, making them potential therapeutic targets for a range of diseases and the development of research tools.[143,154,303]

Adaptable and synthetically accessible peptides are attractive candidates for targeting protein-protein interactions in the cell as they mimic the natural interactions to compete for binding.[205] However, protein-peptide interactions are often dynamic and weak due to the conformational flexibility of linear peptides. Therefore, a challenge is to design peptide ligands that overcome this limitation by making additional or improved interactions with the target.[218]

This chapter describes the rational design of high-affinity peptide ligands to target kinesin-1:cargo interfaces *in vitro*. Synthetic peptides are designed to mimic KLC^{TPR} interactions from natural sequences, but to make additional interactions at the interface to deliver increased binding affinities. These designs deliver high affinity *de novo* cargo adaptor peptides to answer a long-standing question in kinesin-1 biology; namely, *is adaptor-motor binding affinity a limiting factor in transport?* In addition, this work aims to explore a new strategy of peptide design for structurally defined peptide-protein interfaces, a fragment-linking approach combining functional elements from multiple natural sequences into a single peptide design.

3.2 *Mash-up* design of *de novo* cargo adaptor peptides

Analysis of structural data of natural cargo adaptor-TPR interactions was used to guide design of novel peptides. In previous studies, mutagenesis analysis of natural cargo-adaptor peptides has revealed that W and Y residues in W-acidic and Y-acidic motifs, respectively, are essential for binding.[67,304] Furthermore, the X-ray crystal structures of W- and Y-acidic cargo-adaptor peptides from SKIP, JIP1 and Torsin A complexed with KLC^{TPR} domains have identified how these residues interact with their receptor. These reveal overlapping but distinct binding sites in the groove formed by the TPRs (Fig. 3.2). Specifically, the SKIP- $KLC2^{TPR}$ complex shows that the W-acidic site is largely defined by residues on TPRs 2, 3 and 4, where the central W residue of the peptide occupies a hydrophobic pocket formed between the internal helices of TPRs 2 and 3 (W-pocket, p^{+2}). At the p^{0} position, a leucine (L) residue occupies a second hydrophobic pocket formed by residues from TPRs 3 and 4 (LY-pocket). In contrast, Y-acidic peptides are shifted along the KLC^{TPR} superhelix such that key interactions are specified by TPRs 3-5, with TPR2 playing only a minor role. In structures of JIP1 and Torsin A in complex with $KLC1^{TPR}$, the W-pocket is not involved but the LY-pocket (p^{0}) is occupied by the central Y residue. For Torsin A, an additional phenylalanine (F) at the p^{-6} position occupies a third pocket (F-pocket) formed by the internal helices of TPRs 5 and 6. In all cases, these sequence

specific elements are stabilized by a network of salt bridges and electrostatic interactions between the positively charged TPR groove and negatively charged peptides. Key to peptide stabilization within the concave surface of KLC^{TPR}s is an induced-fit closure of the receptors' solenoid-shaped architecture upon peptide binding that also enables several hydrogen bonds.

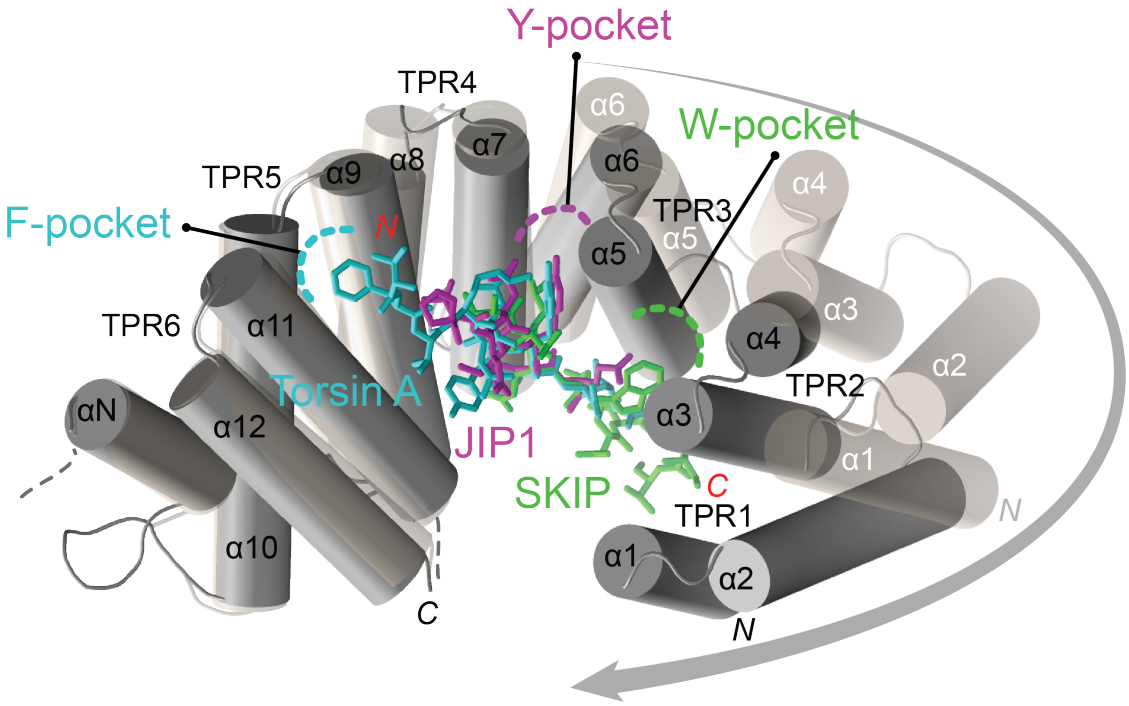

Fig. 3.2 | Structures of kinesin-1 cargo adaptor peptides bound to the TPR domain of kinesin light chains. Cartoon representation of crystal structures of natural cargo adaptor peptides from SKIP (green; PDB code, 3ZFW), JIP1, (magenta; 6FUZ) and Torsin A (cyan; 6FV0) bound to the TPR domain of KLC1 (6FUZ, grey). *N.B.* SKIP is complexed with KLC2 and so KLC1/2^{TPR} domains were aligned to produce the model. For simplicity, only one peptide bound KLC^{TPR} is shown. The peptide-free KLC^{TPR} (PDB: 3NF1) is shown as transparent cylinders and an the arrow represents the domain closure upon peptide binding. Key binding pockets (F, Y, and W pockets) on KLC^{TPR} are highlighted.

To evaluate the contribution of each residue to binding, an *in silico* alanine scan of the SKIP, JIP1 and Torsin A cargo adaptor sequences was performed using the Bristol University Docking Engine (BUDE) Alanine Scanning software (BAlaS) (Fig. 3.3).[297] Residues with a high value of ΔΔG are predicted to be hot-spot residues that make major contributions to binding, since the modelled binding affinity decreases significantly when the residue is mutated to alanine. Mutation to alanine is used to mimic deletion of the side chain beyond the β carbon as it does not impose electrostatic or significant steric effects or alter the main-chain conformation (as glycine or proline can).[305] In comparison to previous mutagenesis

experiments, which show that the W residue is essential for W-acidic motif binding,[67,304] this prediction likely under-estimates the contribution of the W to binding but highlights the importance of hydrophobic interactions formed by L/Y/F residues and the electrostatic contribution of charged acidic residues. BAlaS modelling predicted that tyrosine (from JIP1 and Torsin A) contributed more to binding than the corresponding leucine in SKIP. In addition, whilst none of the highest affinity residues are found in the *N*-terminal fragments of JIP1 and Torsin A, these made multiple positive interactions suggesting that an extended interface could increase affinity.

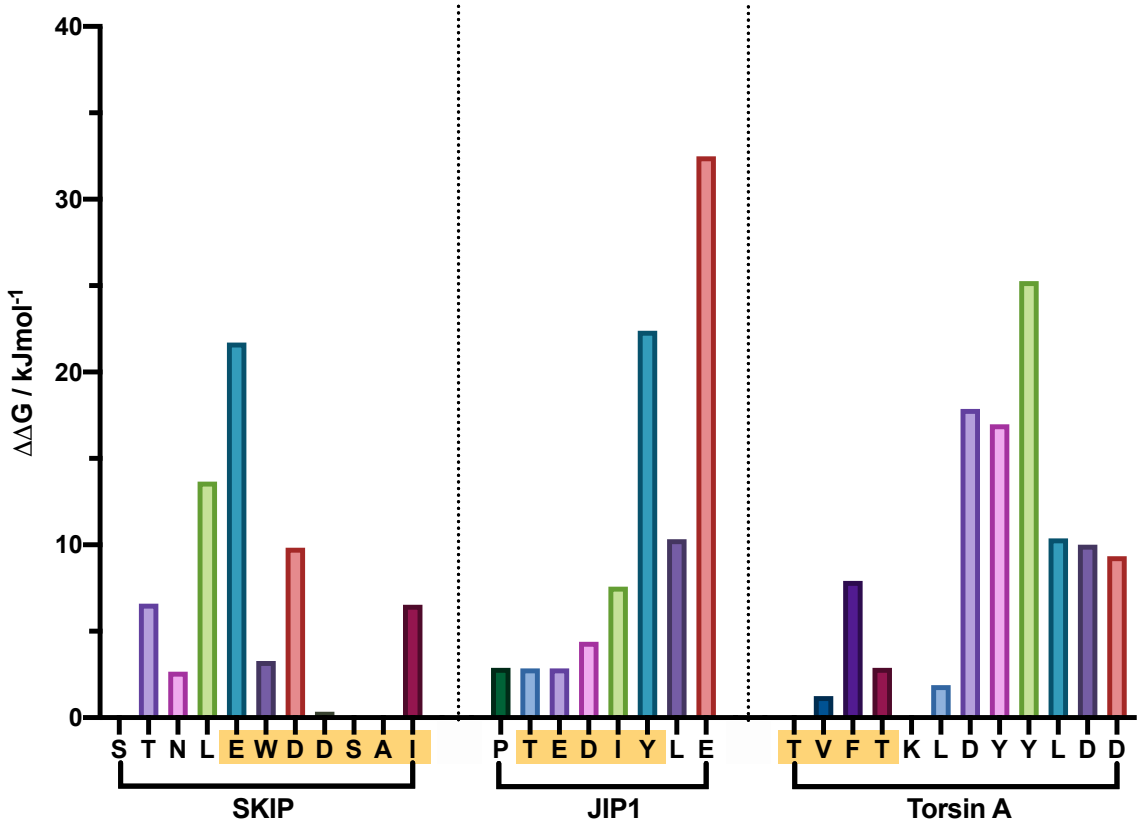

Fig. 3.3 | *In silico* alanine scanning of natural adaptor sequences using BUDE force field identifies *"hot spot"* binding residues. ΔΔG values from an *in silico* alanine scan of W-acidic SKIP and Y-acidic JIP1 and TorsinA in cargo adaptor peptides in complex with KLC^{TPR}s performed using the Bristol University Docking Engine (BUDE) Alanine Scanning software (BAlaS).[297] Residues were sequentially mutated to alanine and the change in binding free energy (ΔΔG) calculated using the BUDE force field. Residues included in design of the eventual KinTag sequence are highlighted in yellow.

An overlay of the three TPR-bound peptide structures revealed the potential to design a contiguous peptide backbone to span the F, LY and W pockets of KLC^{TPR} (Fig. 3.4). Fragment

based drug-discovery is a common approach for developing new therapeutics and involves identifying small chemical fragments that bind weakly to a target and linking or growing them to increase affinity. A similar approach was applied to this design challenge: *i.e.,* low affinity binding interactions from SKIP, JIP1 and TorsinA were linked in a single peptide sequence. This new design approach, termed '*mash-up*' design, aimed to link fragments from multiple sequences to deliver an extended chimeric peptide, capturing key interactions from all three peptides, to improve binding affinity. The approach borrows from consensus design, which identifies key amino acids for a protein structure from multiple-sequence alignments.[306,307] However, it builds on this by incorporating offset fragments, analogous to fragment-based small-molecule drug design.[208,216]

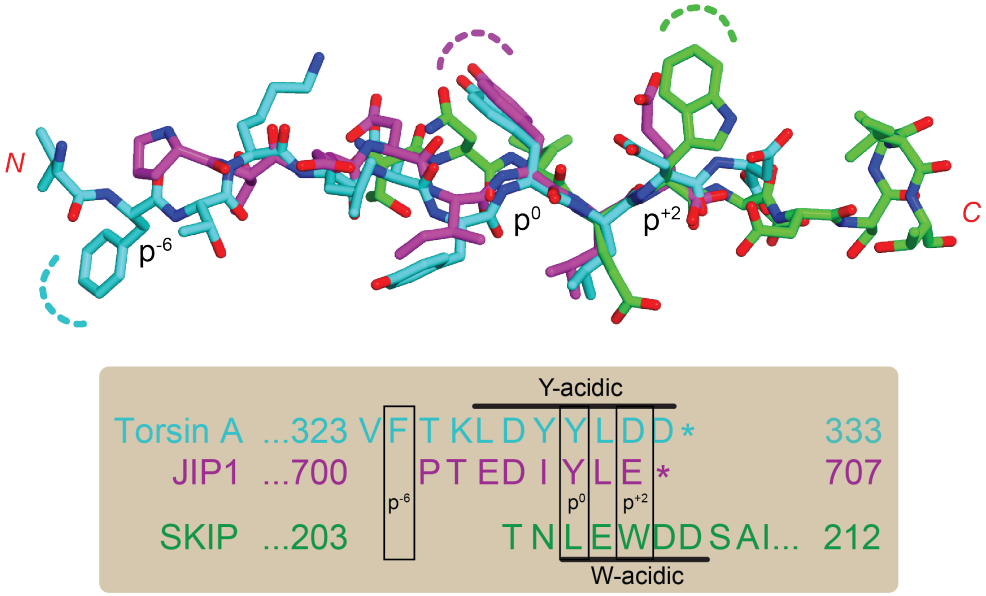

Fig. 3.4 | An overlay of three natural TPR-bound peptide structures revealing the potential to design a contiguous peptide backbone to span the F, LY and W pockets of KLC^{TPR}. Structure based sequence alignment of the three cargo adaptor peptides, overlaid showing a contiguous peptide backbone with the potential to span the F, LY and W pockets of KLC^{TPR}. Nitrogen and oxygen atoms in blue and red, respectively. The labels p^{+2}, p^{0}, and p^{-6} refer to the relative positions of peptide residues buried in the W, Y, and F pockets of KLC^{TPR} with the Y residue of the Y-acidic motif as reference (p^{0}). Figure by Dr Magda Chegkazi and Prof. Roberto Steiner, Kings College London.

In addition to acting as molecular bridges between cargo and kinesin-1, cargo-adapter peptides are also important for activation of kinesin-motor activity. Downstream, adaptor peptide-KLC^{TPR} interactions trigger, or stabilize, larger-scale conformational changes in the kinesin-1

tetrameric motor, resulting in a shift from a compact autoinhibited state to an extended, active form capable of hydrolyzing ATP and generating motile force to transport cargo on the microtubule cytoskeleton.[57,59,80,81] One important change is the displacement of an autoinhibitory peptide (LFP-acidic motif) that binds to a KLC^{TPR} site overlapping that of W-acidic peptides. Binding of W-acidic peptides displaces this interaction and consequently, when targeted to the cytosolic face of an organelle membrane, these sequences are sufficient to drive kinesin-1 dependent transport.[88,105,308] Interestingly, binding of Y-acidic peptides at the adjacent site does not relieve KLC^{TPR} autoinhibition and requires additional interactions to support efficient transport.[68]

The designed peptides aimed to integrate the transport-activating capacity of W-acidic sequences with the extended binding interfaces from Y-acidic sequences. The designs extend the *N* terminus of the SKIP W-acidic motif with residues from JIP1 (J-S peptides), or from both JIP1 and Torsin A (T-J-S peptides). Since the leucine of SKIP and tyrosine from JIP1 and Torsin A bind to the same LY-pocket, two peptides were designed for each of the J-S and T-J-S constructs (Table 3.1).[67,68]

Table 3.1 | Sequences of natural and designed cargo adaptor peptides

Peptide name	Sequence
Peptides from natural cargo adaptors	
SKIP (S)	STNLEWDDSAI
JIP1 (J)	PTEDIYLE
Torsin A (T)	TVFTKLDYYLDD
De novo cargo adaptor peptides from mash-up design	
J-S(L)	GTEDILEWDDSAI
J-S(Y)	GTEDIYEWDDSAI
T-J-S(L)	GTVFTTEDILEWDDSAI
T-J-S(Y) *'KinTag'*	GTVFTTEDIYEWDDSAI

The designs were made by solid-phase peptide synthesis with the 5-carboxytetramethylrhodamine (TAMRA) fluorophore appended *N* terminally, purified by high performance liquid chromatography, and confirmed by MALDI-TOF mass spectrometry (Appendix 8.1). Challenges were encountered during purification due to the insolubility of the

acidic peptides in the standard HPLC solvent system of water/acetonitrile with 0.1% trifluoracetic acid (TFA). To improve solubility, the peptides were dissolved first in DMSO and then diluted to a final concentration of 20 % DMSO in an ammonium bicarbonate buffered system, pH 8.8.

3.3 Synthetic peptides bind KLC^{TPR}s in vitro with high affinities

The binding affinities of the designed peptides for KLC^{TPR} proteins comprising TPRs 1 – 6 were determined *in vitro* using fluorescence polarization (FP) assays. For protein expression, constructs of two paralogs, KLC1$^{TPR\text{-}211\text{-}495}$ and KLC2$^{TPR\text{-}196\text{-}480}$, were used. [67,103] TPR domains were expressed in *E. coli* as *N*-terminally His_6-tagged proteins and purified by Ni^{2+}-affinity chromatography followed by size exclusion chromatography (SEC) (Appendix 8.2). TAMRA-labelled peptides (150 nM) were incubated with increasing concentrations of KLC^{TPR} proteins in saturation-binding experiments[68] to obtain dissociation constants, K_D, (Fig. 3.5, Table 3.2). The designed peptides had increased affinities over the natural sequences for both proteins. Peptides J-S(L) and J-S(Y) bound with moderately increased affinities, with the tyrosine variant as the tighter binder. Interestingly, this result matches the prediction from the *in silico* BAlaS modelling (Fig 3.3). Increasing the *N*-terminal extension in the T-J-S(Y) peptide led to a further increase in affinity, but this was not observed for the leucine variant. Thus, peptide T-J-S(Y) had the highest affinities for KLC^{TPR}s with K_Ds of tens of nM to KLC1^{TPR} and hundreds of nM to KLC2^{TPR} (Table 3.2). This KLC^{TPR} isoform selectivity is akin to that of natural Y-acidic motifs, which bind to KLC1^{TPR} with higher affinity than KLC2^{TPR}.[68] The highest affinity peptide, T-J-S(Y), was renamed ‘KinTag’.

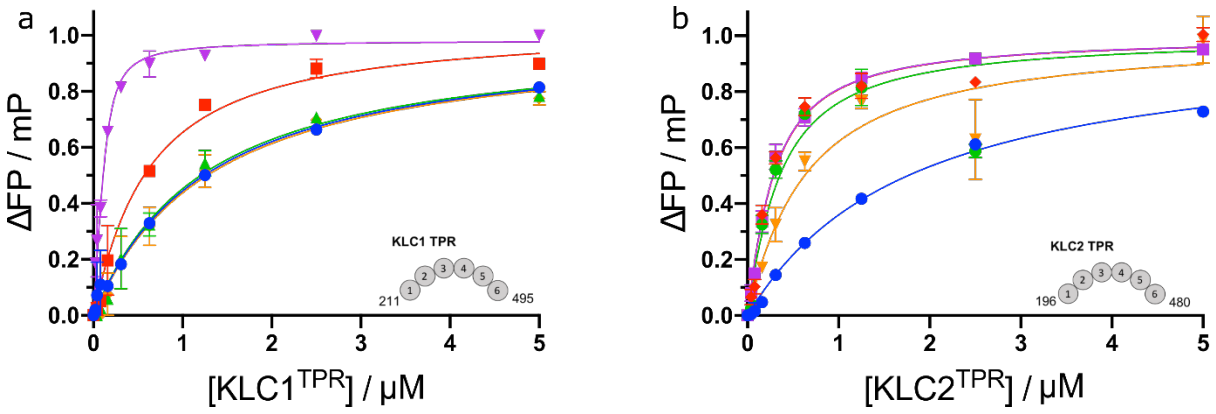

Fig. 3.5 | Synthetic peptides bind KLC^{TPR}s *in vitro* with high affinities. Binding affinities of designed peptides were measured in vitro in fluorescence polarization assays with TAMRA-labelled peptides (150 nM) incubated with increasing concentrations of KLC^{TPR} protein: **a**, KLC1^{TPR} and **b**, KLC2^{TPR}. Key: natural SKIP, blue; J-S(Y), red; J-S(L), green; T-J-S(L), orange; and T-J-S(Y), KinTag, purple. Data were fitted to a single-site binding model with polarization values of the peptide and buffer alone subtracted and values normalised to the calculated B_{max}. Error bars indicate 1 SD from a minimum of 3 replicates

.

Table 3.2 | *In vitro* binding affinities of natural and designed cargo adaptor peptides

Peptide name	K_D KLC1 / nM	K_D KLC2 / nM	K_D KLC1^{ext} / nM	K_D KLC2^{ext} / nM
Peptides from natural cargo adaptors				
SKIP (S)	1170 ± 176	1690 ± 132	7530 ± 125	10650 ± 420
JIP1 (J)	1720 ± 130 [24]	-	-	-
Torsin A (T)	950 ± 90 [24]	-	2210 ± 60 [24]	-
De novo cargo adaptor peptides from mash-up design				
J-S(L)	1120 ± 153	280 ± 94	2840 ± 50	2570 ± 212
J-S(Y)	430 ± 87	210 ± 27	960 ± 26	2500 ± 82
T-J-S(L)	1200 ± 188	657 ± 133	1250 ± 110	2840 ± 135
T-J-S(Y) '*KinTag*'	35 ± 7	207 ± 15	170 ± 7	720 ± 29

3.4 Designed peptides are sensitive to KLC^{TPR} autoinhibition

Full-length KLCs have a conserved autoinhibitory leucine-phenylalanine-proline-containing sequence (LFP-acidic) *N* terminal to their TPR domains (Chapter 1 Fig. 1.5). This binds near TPR2 of the KLC^{TPR} to occlude the W-acidic binding site but not the Y-acidic sites.[59] In fluorescence polarization binding experiments, this reduces the affinity of W-acidic peptides for the TPR domains, but not those of Y-acidic peptides. Consequently, this reduction in binding affinity is a proxy for the capacity to displace the inhibitory interaction.[59,68] Since a functional, transport-activating peptide would require this capacity, the binding of the designed

peptides to TPR constructs incorporating the conserved LFP-acidic region, KLC1^{extTPR} and KLC2^{extTPR}, was investigated (Figs. 3.6, Table 3.2). First, the designed peptides all had improved affinities over the natural sequences. KinTag bound to KLC1^{extTPR} with K_D = 170 nM, which is a 13- to 44-fold increase over the parent peptides (Table 3.2). Moreover, and importantly, the affinities of the designed peptides for KLC^{extTPR} were all reduced compared to those for KLC^{TPR}. This demonstrates the sensitivity of these synthetic adaptor peptides to the presence of the LFP autoinhibitory motif, which can be attributed to retaining the core residues of the W-acidic peptides. In turn, it can be reasoned that these *de novo* cargo-adaptor peptides should retain the capacity to engage the LFP-acidic switch necessary for kinesin-1 activation.

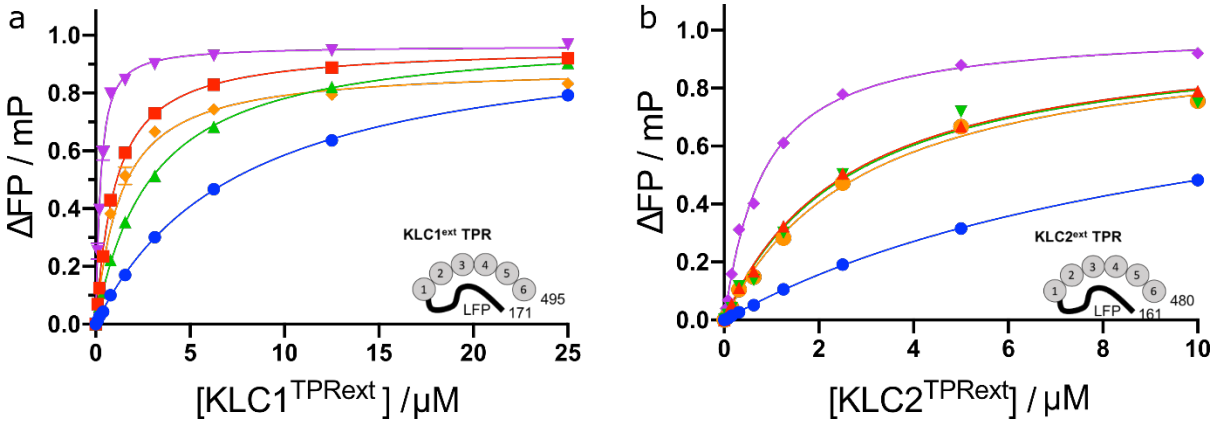

Fig. 3.6 | Designed peptides are sensitive to KLC^{TPR} autoinhibition. Fluorescence polarization assays for TAMRA-labelled peptides (150 nM) incubated with increasing concentrations of protein: **a**, KLC1^{TPRext} and **b**, KLC2^{TPRext}. Key: natural SKIP, blue; J-S(Y), red; J-S(L), green; T-J-S(L), orange; and T-J-S(Y), KinTag, purple. Data were fitted to a single-site binding model with polarization values of the peptide and buffer alone subtracted and values normalised to the calculated B_{max}. Error bars indicate 1 SD from a minimum of 3 replicates.

3.5 The X-ray crystal structure of the KLC1^{TPR}: KinTag complex reveals interactions as designed

To validate the highest-affinity design, the X-ray crystal structure of the KLC1^{TPR}: KinTag complex was solved at the 2.85 Å resolution (Fig. 3.7, Appendix Table 8.1). Following success from previous studies, a chimera with KinTag fused *via* a flexible $(TGS)_4$ linker to the *N* terminus of KLC1^{TPR} was expressed.[67,68] In the crystallographic asymmetric unit, six copies of the KLC1^{TPR}: KinTag complex were found, arranged in three independent head-to-tail dimers (Fig. 3.8). The KinTag core sequence VFTTEDIYEWDDS was well defined in all complexes. However, the *N*-terminal Thr and the *C*-terminal Ala-Ile were more flexible and only partly visible in some of the complexes. As designed, the KinTag peptide binds in an extended

conformation within the concave groove of the TPR domain (Fig. 3.7a) with an interface area of 950 Å^2. This represents an increase of approximately 24% compared to SKIP W-acidic (769 Å^2) and of 7% over the rather extensive Torsin A Y-acidic interface (885 Å^2). A number of H-bonds and salt bridges stabilise the peptide within concave KLC^{TPR} surface together with electrostatic complementarity between the negatively charged peptide and its receptor (Fig. 3.7 b and Fig 3.9). While all amino acids of KinTag contribute to the interface with KLC1^{TPR}, the F, Y, and W residues appear to play a key role being almost totally concealed within their binding pockets with buried surfaces corresponding to 70%, 88%, and 80% of their accessible surfaces, respectively.

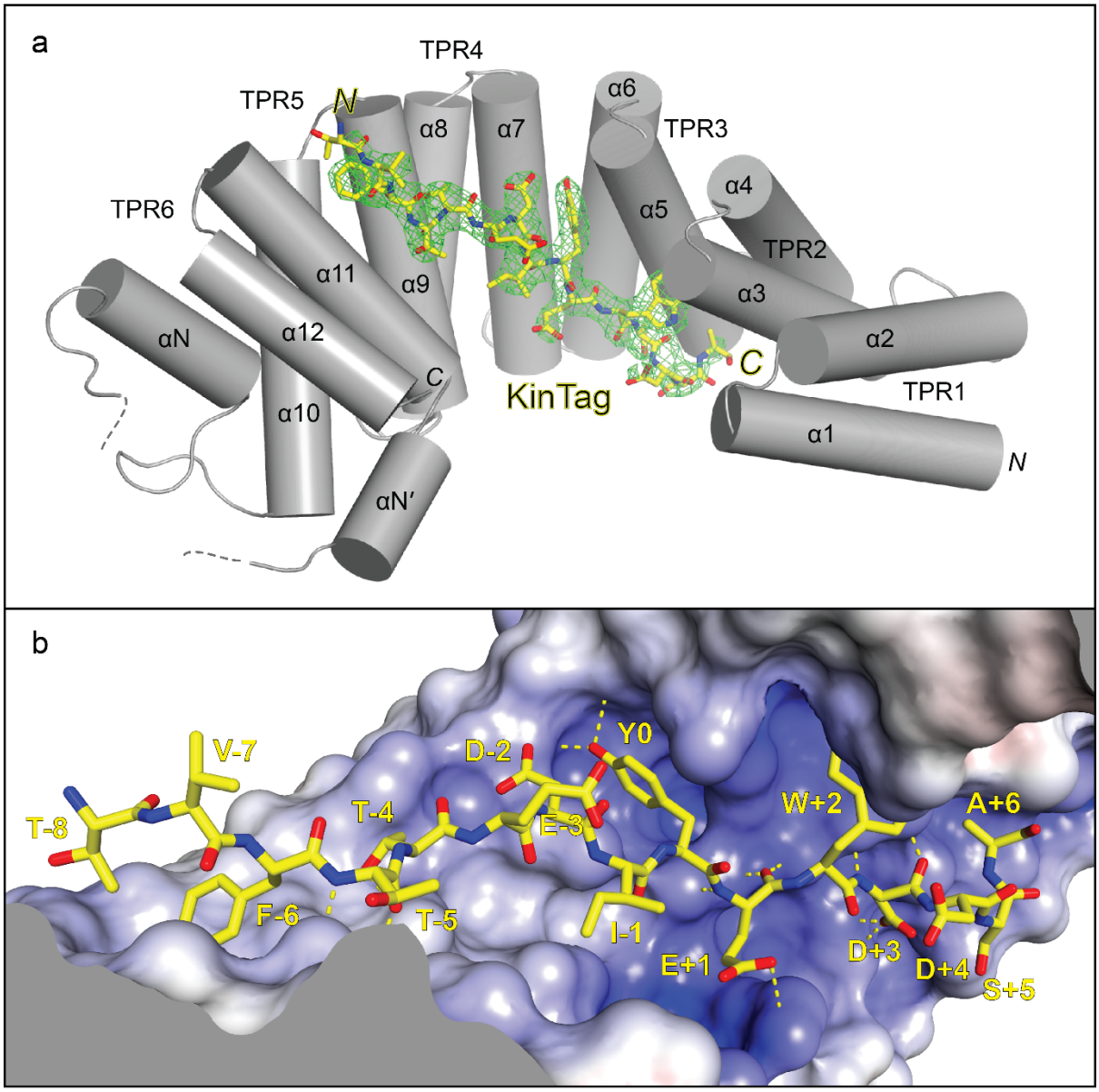

Fig. 3.7 | X-ray crystal structure of KinTag bound to KLC1^{TPR} reveals interactions as designed. **a**, Illustrated representation of the KinTag peptide (displayed as a yellow stick model accompanied by its $2mF_o$-DF_c electron density in green contoured at the 1.0 s level) bound to KLC1^{TPR}. Helices α1 to α12 of the six TPR helix-turn-helix motifs are labelled. In addition to the non-TPR helix (αN) seen in previous structures, another short helix (αN′) is revealed before α11. The flexible region between αN and αN′ is indicated with a broken line, while the engineered disordered linker connecting α12 to the KinTag is not shown for clarity. Color-coded *N* and *C* labels indicate the N and C termini, respectively. Nitrogen and oxygen atoms are coloured dark blue and red, respectively. **b,** Sliced-surface view of KLC1^{TPR} with bound KinTag. The molecular surface is coloured according to its electrostatic potential with positive and negative potential in the $+10k_BT/e$ to $-10k_BT/e$ range shown in blue and red, respectively. KinTag residues are numbered with the central tyrosine residue as reference. Hydrogen bonds and salt bridges are shown as broken yellow lines. Figure by Dr Magda Chegkazi and Prof. Roberto Steiner, Kings College London.

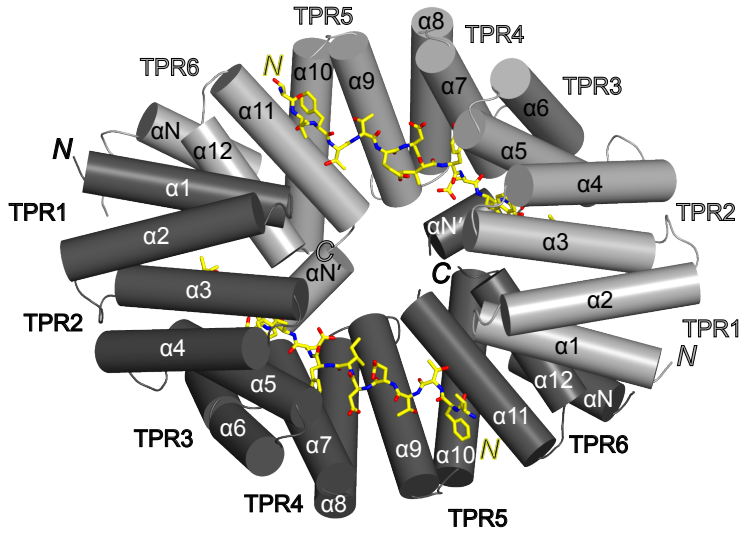

Fig. 3.8 | X-ray crystal structure of KinTag:KLC1^{TPR} dimer. Cartoon representation of the KLC1^{TPR}:KinTag head-to-tail dimer viewed approximately down the two-fold axis. KLC1^{TPR} domains are shown in light and dark grey with helices depicted as cylinders. Each KLC^{TPR} domain is formed of six helix-turn-helix TPR repeats (TPR1 α1 - α2, TPR2 α3 – α4, TPR3 α5 – α6, TPR4 α7 -α8, TPR5 α9 – α10, TPR6 α11 – α12) and two additional non-TPR helices (α N and α N') between TPR5 and TPR6. The KinTag peptides are displayed as yellow sticks with nitrogen and oxygen atoms in blue and red, respectively. Colour-coded *N* and *C* letters indicate *N*- and *C*-termini, respectively. The *C*-terminus of KinTag peptides is behind α3 helices. Figure by Dr Magda Chegkazi and Prof. Roberto Steiner, Kings College London.

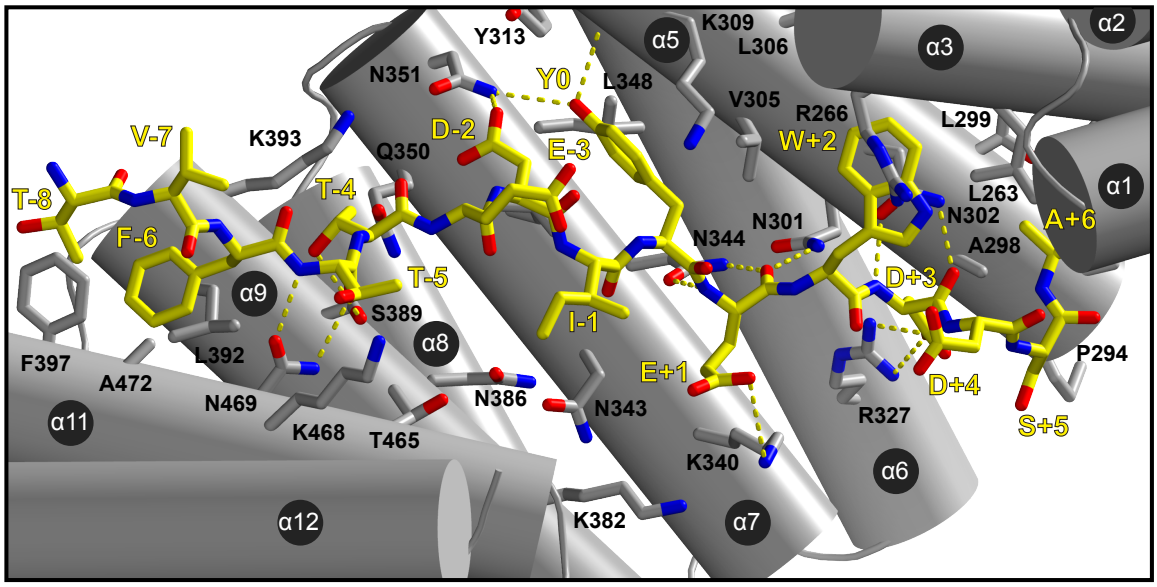

Fig. 3.9| Hydrogen bond network in KinTag:KLC1^{TPR} structure. The KinTag peptide and KLC1^{TPR} residues with which it interacts are shown as sticks in yellow and grey, respectively. Nitrogen and oxygen atoms in blue and red, respectively. Colour-coded labels identify residue numbers. For the KinTag peptide the central tyrosine residue is taken as reference position (Y^0). KLC1^{TPR} helices are also labeled. H-bonds and salt bridges are highlighted by broken lines. Figure by Dr Magda Chegkazi and Prof. Roberto Steiner, Kings College London.

3.6 *In silico* comparison of interactions in X-ray crystal structures fails to predict increase in affinity from Torsin A to KinTag

In silico analysis of the interactions formed by each residue of the TPR domain was used to compare the contacts made in the KLC1^{TPR}: KinTag complex to the KLC^{TPR} : SKIP, JIP1 and TorsinA complexes. For this, two approaches were considered. Firstly, the proportion of each TPR residue buried upon interaction with the adaptor peptide was calculated using the Protein Interfaces, Structures and Assemblies (PISA) algorithm (Fig. 3.10 a, b).[298] Secondly, an alanine scan using the BUDE force field allowed calculation of ΔΔG values for mutation of each TPR residue to alanine (Fig. 3.10c).[297] The two methods of analysis showed largely similar trends: that for the SKIP-KLC2^{TPR} complex the majority of interactions are formed in TPRs 2,3 and 4 and that JIP1 and TorsinA form addition interactions with TPR 5 and 6, respectively. In the KLC1^{TPR}: KinTag complex these interactions are preserved across TPR helices 2-6, as evidenced by the larger binding surface observed in the crystal structure and higher affinity interaction measured *in vitro*. Both algorithms predicted similar interactions for TorsinA and KinTag, in-fact predicting more interactions for the TorsinA complex. This is in contrast to the *in vitro* measured binding affinities. Neither algorithm was able to correctly predict, or explain, the observed increase in affinity of KLC1^{TPR} from micromolar for TorsinA to nanomolar for KinTag.

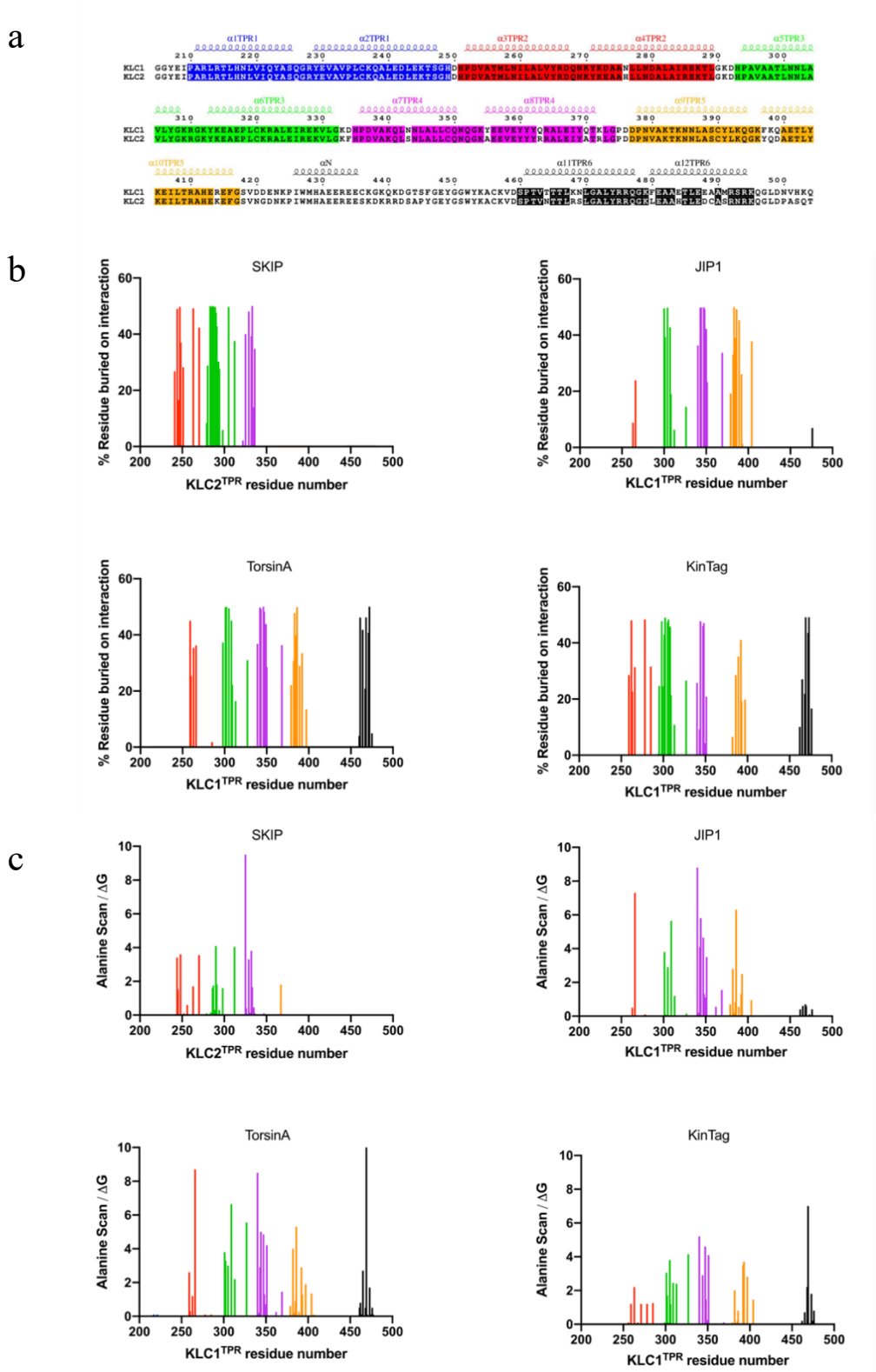

Fig. 3.10| Comparison of KLC^{TPR} interaction maps in natural and designed cargo adaptor peptides. a, Sequence alignment of KLC1^{TPR} and KLC2^{TPR} showing colour coding of each TPR helix as used in b and c. **b**, Interface contact maps for the KLC2^{TPR}-SKIP, KLC1^{TPR}-JIP1/TorsinA/KinTag complexes. Percentage of each residue buried upon interaction with cargo adaptor peptide, analysis performed with the Protein Interfaces, Surfaces and Assemblies (PISA) algorithm. **c**, In silico alanine scanning using BUDE force field (BAlaS) showing ΔΔG binding contribution of each TPR residue.

3.7 Second generation *in silico* structure-guided peptide designs do give any improvements in affinity

The BAlaS algorithm was also be applied to the KLC1^{TPR}: KinTag complex to identify "hot-spot" residues that make important binding contributions in the KinTag sequence (Fig. 3.11). The importance of hydrophobic, and electrostatic, interactions were reinforced by this analysis. Large values of ΔΔG indicate important binding contributions from the Phe, Tyr and Trp residues occupying hydrophobic pockets in the TPR groove, though, again, contributions from Trp are likely underestimated, and Glu residues, making electrostatic interactions with the basic TPR surface.[297] This analysis indicates that other residues confer little contribution to binding and thus, that affinity could be improved by substituting these residues for alternative side chains leading to additional interactions.

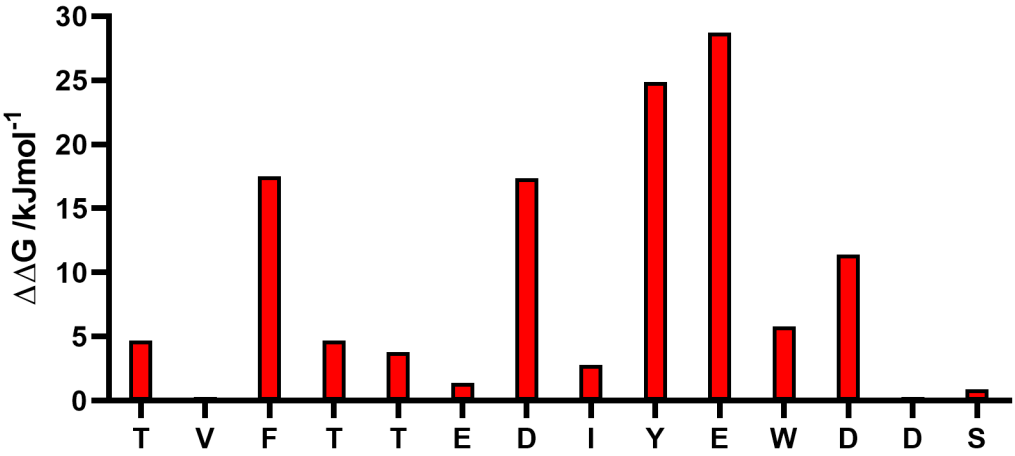

Fig. 3.11 | *In silico* alanine scanning of Kin-Tag:KLC1^{TPR} complex using BUDE force field identifies important residues for binding. ΔΔG values from an *in silico* alanine scan of the Kin-Tag:KLC1^{TPR} complex performed using the Bristol University Docking Engine (BUDE) Alanine Scanning software (BAlaS). Residues were sequentially mutated to alanine and the change in binding free energy calculated using the BUDE force field.[297]

On this basis an *in-silico* saturation mutagenesis scan was completed to predict the change in binding affinity of single-residue mutations (Fig. 3.12). Using the X-ray structure of the KLC1^{TPR}: KinTag complex, each residue in the KinTag sequence was sequentially mutated to a set of 16 other amino acids, the peptide redocked into the TPR binding pocket and the change in binding free energy (ΔΔG) calculated using the BUDE force field. The set of 16 amino acids consists of the 20 natural amino acids but excludes alanine, since this is covered by the BAlaS model, glycine, proline and cysteine due to the unusual side chain properties of these residues

in conferring backbone flexibility, restricted backbone conformation and disulphide bond formation respectively.

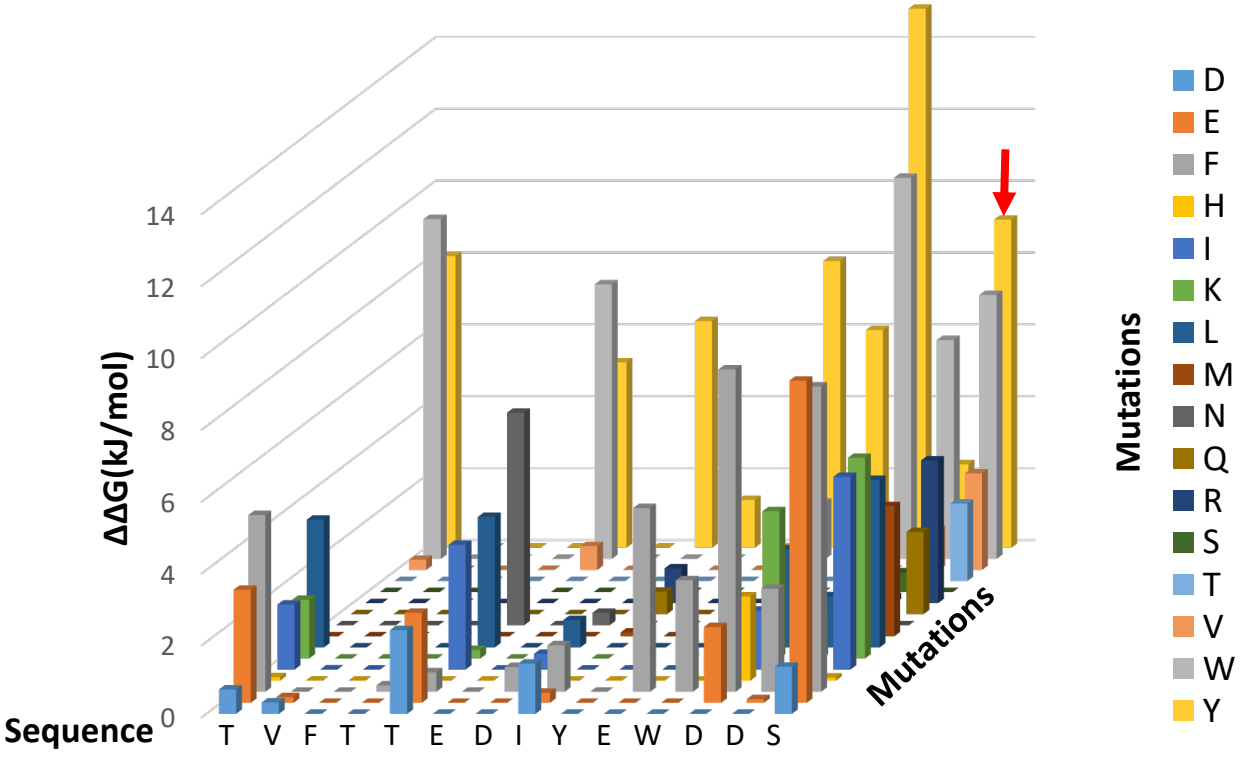

Fig. 3.12 | *In silico* saturation mutagenesis of Kin-Tag:KLC1^{TPR} complex using BUDE force field . ΔΔG values from an *in silico* saturation mutagenesis scan of the Kin-Tag:KLC1^{TPR} complex performed using the Bristol University Docking Engine (BUDE). Residues in the KinTag sequence (x-axis) were sequentially mutated to a set of 16 other amino acids (z-axis) and the change in binding free energy calculated using the BUDE force field (y-axis).[297] For the sake of clarity, negative ΔΔG values are not shown.

The results of this analysis suggest that the introduction of hydrophobic residues, Y and W (yellow and grey bars respectively, figure 3.12), could increase affinity. This is unsurprising since additional hydrophobic residues often increase binding affinity due to the hydrophobic effect: an increase in the buried hydrophobic surface area leads to the entropically favoured displacement of weakly bound water molecules in hydrophobic pockets. The results also suggest that several of the polar threonine and serine residues contribute little binding affinity so have potential to be improved through mutation. We sought to use this analysis to guide mutations to design a second generation of *de novo* cargo adaptor peptides with increased affinity for KLC^{TPR}s. A small library (30) of KinTag peptide analogues with single or multiple mutations were synthesised and binding affinities for KLC1^{extTPR} measured *in vitro* in

fluorescence polarization (FP) assays as described above (Appendix Table 8.3). This construct was chosen as the protein was most stable and easily purified and the observed trend is likely to be the same for all four constructs, as shown previously in table 3.2. In general, this approach was not successful with mutations decreasing binding affinity. The best of these designs involved a single point mutation S15Y, indicated by a red arrow on figure 3.12. The BAlaS algorithm likely predicts this improvement due to additional hydrophobic interactions at the interface, in place of a serine residue which is shown to make little contribution to binding in the structure of the KLC1^{TPR}: KinTag complex. Whilst this peptide, KinTag S15Y, retained high affinity there was no improvement from KinTag so the original design was retained for further experiments (Fig 3.13, Table 3.3).

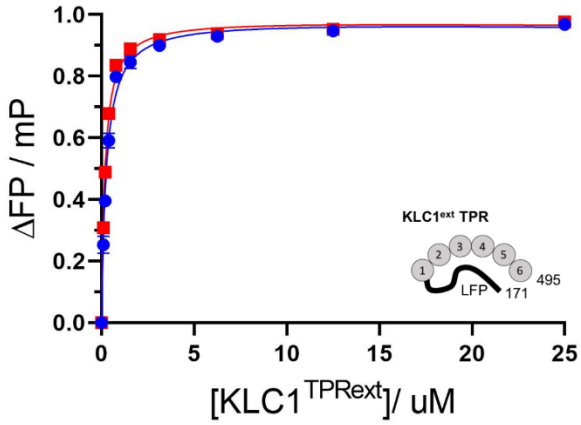

Fig. 3.13 | Example of in *vitro* binding affinities of BUDE guided second generation KinTag peptides for TPR domains. Fluorescence polarization assays for TAMRA-labelled peptides (150 nM) incubated with increasing concentrations of protein KLC1^{extTPR} Key: red; KinTag, blue; KinTag S15Y red. Data were fitted to a single-site binding model with polarization values of the peptide and buffer alone subtracted and values normalised to the calculated B_{max}. Error bars indicate 1 SD from a minimum of 3 replicates

Table 1 | Example of *in vitro* binding affinities of BUDE guided KinTag mutations

Peptide name	Sequence	K_D KLC1^{ext} / nM
KinTag	GTVFTTEDILEWDDSAI	170 ± 7
KinTag S15Y	GTVFTTEDILEWDD**Y**AI	187 ± 9

3.8 KinTag binds to kinesn-1 tetramers in cell lysate

Next, we tested if our best peptide design, KinTag, could bind to kinesin-1 tetramers expressed in a cellular context. A synthetic KinTag peptide was synthesised with a biotin tag and incubated with neutravidin–agarose beads. The high affinity biotin – neutravidin interaction

leads to agarose beads with KinTag displayed on their surface. HeLa cells were transfected with *citrine*-Kif5C*,* a mainly neuronal KHC isoform, and HA-KLC1 or HA-KLC2 and cell lysate incubated with peptide bound beads. Samples of the supernatant and bound fractions from control and KinTag incubated beads were subjected to SDS-PAGE and analysed by western blot using antibodies against HA and GFP (Fig 3.14). Unlike control beads, the KinTag-bound beads interacted with both KLC isoforms. This resulted in bands for HA-KLC in the KinTag bound lanes of the gel. Protein in the supernatant indicated that not all of the KLC bound to KinTag. This may be due to saturation of the beads, but, more likely, it is indicating that the peptide has lower affinity for the kinesin-1 tetramers than the TPR domain construct used in the *in vitro* FP assays. In addition, Kif5C was detected in the KinTag bound fraction suggesting that the peptide successfully acts as a kinesin-1 ligand in the context of fully assembled tetramers. These results indicate a potential application of KinTag-based peptides for purifying tetrameric kinesin-1, for example for structural studies by electron microscopy.

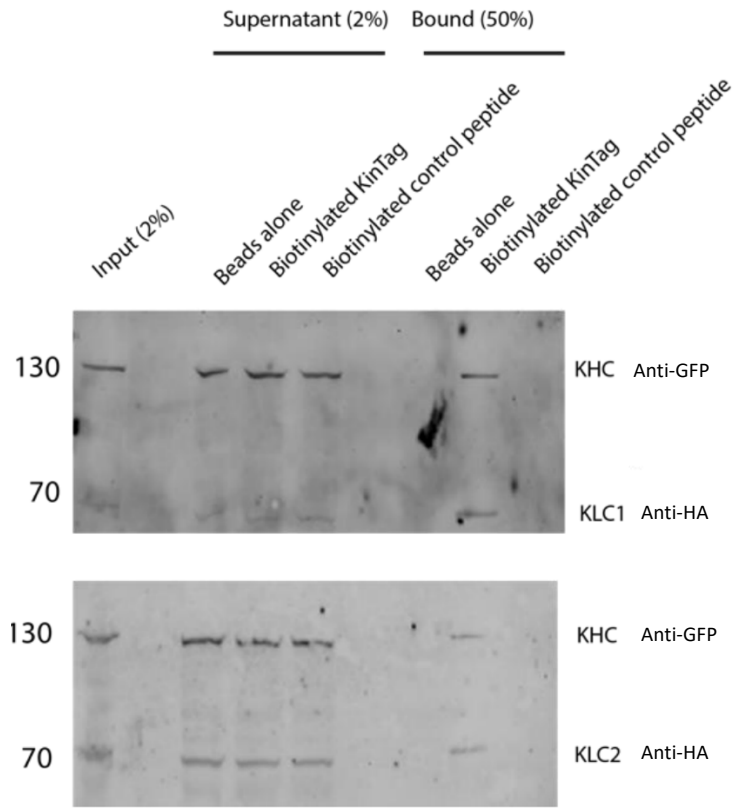

Fig. 3.14 | KinTag binds to kinesn-1 tetramers in cell lysate. Western blot of cell lysate from HeLa cells transfected with *citrine*-Kif5C and HA-KLC1 or HA-KLC2 incubated with control or KinTag-bound beads show KinTag interacts with KLC1/2 and KHC expressed in cells. Cell lysate was added to agarose resin which had been incubated with biotinylated peptide or PBS overnight. Western blots with primary antibodies against HA and GFP and fluorescently labelled secondary antibodies were visualised using dual colour imaging on an Odyssey CLx (LI-COR) infrared imaging system and are displayed with the two channels overlayed.

3.9 Conclusions

Kinesin-1 transport has been shown to be due, in part, to transient protein-protein interactions made between acidic adaptor peptides presented on the surface of cargo and TPR domains of the kinesin-1 light chains ($KLC^{TPR}s$).[67,68,85,88,105,106,108,109,309,310] Unitarily, these natural interactions have μM affinities when measured *in vitro*. This chapter has described a *mash-up* design approach that links low-affinity binding features from multiple natural sequences in a single designed high-affinity peptide, KinTag. This binds to $KLC^{TPR}s$ with nM affinities. An X-ray crystal structure of the $KLC1^{TPR}$:KinTag complex confirms that the key binding interactions are made as designed. This validates the understanding of the key interactions required for motor-cargo binding and the resulting conformational changes required for motor activation.

The structure also reveals that KinTag induces TPR curvature similar to that observed for natural adaptor peptides. The curvature of the KLC^{TPR}:KinTag complex is between that for KLC2^{TPR}:SKIP and KLC1^{TPR}:JIP1.[67,68] This demonstrates a degree of flexibility in ligand binding by these domains, which have also been shown previously to support variable peptide binding modes.[60,62,66] It is feasible that this induced TPR curvature could result in the same downstream activation of the tetrameric motor seen for natural W-acidic adaptor peptides, allowing the peptide to function as a cargo adaptor in the cell. This idea is supported by *in vitro* binding studies. These show that KinTag has W-acidic-like sensitivity to the KLC^{TPR} autoinhibitory LFP interaction, which suggests that KinTag displaces this motif to relieve autoinhibition. This is further validated by evidence that KinTag immobilized on beads can bind to kinesin-1 tetramers expressed in cell lysate.

Therefore, it is likely that KinTag, a *de novo* high affinity kinesin-1 cargo adaptor peptide, could be used *in vivo*, as a tag for transport inside the cell. This could allow the development of a toolkit of peptide ligands across a range of affinities for the orchestrated transport of organelles, and other protein cargo, to investigate the functional role of their positioning within the cell. In turn, this would offer a novel research tool to test the hypothesis that motor-cargo affinity is a limiting factor in transport. These ideas are explored in chapter 4.

More generally*, mash-up* design provides a strategy for developing high-affinity peptide ligands for protein surfaces. The structure of the KLC1^{TPR}:KinTag complex confirms that both general design features (*i.e.*, shape and charge complementarity between the peptide and the protein), and sequence-specific design features (*i.e.*, large side chains of the peptide bind into designated pockets of the protein) are realized. These features appear robust to changes in the overall context of the peptide. The design approach yields an order of magnitude or more increase in binding affinity without dramatically increasing the interface area, highlighting the utility of fragment linking in peptide design, akin to that used with small-molecule pharmacophores.[208,216] Where *a priori* structural information is available from natural ligands, this approach may prove useful in designing high affinity peptides to target other PPIs in the cell. In particular, it may be applicable in the many intracellular membrane trafficking pathways that utilize the recognition of diverse short linear motifs in unstructured regions of client proteins to ensure selectivity and specificity.[311]

Interesting, the key design insights in this process came from manual inspection of structures

of natural TPR-peptide complexes. The *in silico* approaches employed were generally unsuccessful. Alanine scanning using the BUDE force field did not successfully highlight the importance of W hydrophobic binding, although this analysis did correctly predict the higher affinity conferred by Y in place of L in the L/Y pocket. Saturation mutagenesis led to no improvements in affinity in a second-generation peptide designs, with most mutations reducing binding. Comparison of the interactions in the KinTag:TPR versus TosinA:TPR complexes with both the PISA and BAlaS algorithms failed to explain the observed increase in affinity. It is possible that short-comings in these predictions are linked to the induced-fit mode of binding of the peptide-TPR interactions. The *in silico* approaches applied here may be unable to factor in the energetic contributions of these induced-fit structural changes. Further analysis was beyond the scope of this chapter, but it will be interesting to see how developments in this field lead to new and improved methods for modelling and exploiting peptide-protein interfaces.

4 Manipulating intracellular transport using a *de novo* kinesin-1 cargo adaptor peptides

Results described in this chapter have been included in the publications

Fragment-linking peptide design yields a high-affinity ligand for microtubule-based transport
Jessica A. Cross, Magda S. Chegkazi, Roberto A. Steiner, Derek N. Woolfson, Mark P. Dodding *Cell Chemical Biology* **2021, 28,** 1-8 DOI:10.1016/j.chembiol.2021.03.010

De novo designed peptides for cellular delivery and subcellular localisation
Guto G. Rhys†, Jessica A. Cross†, William M. Dawson†, Harry F. Thompson, Sooruban Shanmugaratnam, Nigel J. Savery, Mark P. Dodding, Birte Höcker and Derek N. Woolfson
under review at Nature Chemical Biology

Some of the text in this chapter resembles the manuscripts, for which I am first author and joint first author. Under guidance from my supervisors, the work described here work is my own, with the exception of the d*esign of the de novo antiparallel heterodimer apCC-Di-AB by Dr William Dawson and Dr Guto Rhys.*

4.1 Background

For healthy cell function, and to avoid disease pathologies, organelles and other vesicular cargo must be trafficked to the right place at the right time in a tightly regulated intracellular transport system.[312] As outlined in Chapter 3, the interaction of cargo-adaptor peptides with KLC^{TPR}s is important for the recognition and anterograde transport of organelles by the microtubule motor kinesin-1. Acidic adaptor peptides are expressed in multiple copies on the surface of organelles, and recruit kinesin-1 motors to facilitate their anterograde transport along microtubules. Motor-cargo adaptor interactions also act as regulators, relieving autoinhibition and activating motor function.[25,28,59] Thus, understanding the mechanisms by which kinesin-1 interacts with its cargo in the cell is important to gain insights into the normal and pathological roles it plays in intracellular transport. In addition, developing reagents to hijack this endogenous motor protein could provide new tools to understand the molecular basis of these interactions, to target them in disease states, and to develop routes to new classes of spatially targeted therapeutics.

An example of kinesin-1 cargo recognition is in the transport of lysosomes from the perinuclear region to the cell periphery. In part, this is controlled through interactions of a W-acidic sequence in the lysosome adaptor SKIP with KLC^{TPR}s.[87,112,313,314] Lysosomes are membrane-bound organelles essential for the degradation of macromolecules in the cell,[315,316] forming the terminal degradative compartment of the endocytic and autophagic pathways.[317] Lysosomes are found throughout the cytoplasm of a cell and can move bidirectionally along microtubules,

transported by kinesin and dynein motor proteins.[286,318-321] In non-polarised cells the majority of lysosomes are clustered in the perinuclear region, surrounding the microtubule-organising centre (MTOC), with fewer reaching the plasma membrane.[322] The spatiotemporal regulation of lysosomes is essential for controlling their function; for instance, peripheral lysosomes have been shown to be important for plasma membrane repair while perinuclear lysosomes fuse with autophagosomes to form autolysosomes.[314,323-325] In addition to degradation, it has become clear that lysosomes play important roles in many cellular processes and that healthy regulation of their motility and positioning is essential to avoid cell pathologies.[326] Lysosome positioning has also been shown to be sensitive to nutrient availability and to play a role in coordinating mTOR complex 1 signalling and autophagic flux.[325] The mechanisms by which lysosome positioning coordinates cellular nutrient responses and is dysregulated in diseases such as cancer and neurodegeneration remain active areas of research.

In Chapter 3, fragment-based peptide design was employed to yield a *de novo* kinesin-1 cargo adaptor peptide, KinTag, to bind KLC^{TPR}s with higher affinity than natural sequences *in vitro*. This chapter describes experiments to investigate the design in a cellular context. Fusion proteins to express lysosome associated cargo adaptor sequences are used to compare KinTag to the natural lysosome adaptor sequence from SKIP and to test the hypothesis that adaptor-motor binding affinity is a limiting factor in transport. Using this strategy KinTag is tested for its capacity to effect lysosome transport, both to the periphery of non-polarised cells and into the axons of neuronal cells. In addition, the transport of peroxisomes and mitochondria are investigated to ascertain if KinTag can be used more broadly as a tag for transport. Finally, strategies using cell-penetrating peptides are employed to explore the potential of introducing KinTag as an exogenous reagent.

4.2 LAMP1-GFP fusion proteins enable expression of lysosome associated cargo adaptor sequences

To validate the cellular functionality of the KinTag design, its capacity to hijack endogenous kinesin-1 to drive organelle transport in cells was tested. For this, the KinTag sequence was incorporated into a fusion protein to enable expression of organelle associated cargo adaptor sequences for comparison of the *de novo* high-affinity design with natural sequences. Using the approach described by Pu *et al.*, [112] cargo-adaptor sequences were cloned into a fusion protein between the lysosome-associated membrane protein (LAMP1) and the green

fluorescent protein (mGFP). This should result in lysosomes displaying multiple copies of the sequence on their surface, similar to the natural SKIP protein. The control LAMP1-mGFP protein was incorporated into lysosomes, visible as green puncta, mostly clustered in the perinuclear region of the cell with some dispersed through the cytoplasm (Fig. 4.2a).[279] Inclusion of a natural W-acidic cargo adaptor sequence from SKIP in this construct has been shown previously to recruit kinesin-1 and increase transport of lysosomes to the cell periphery, visible by dispersal of green fluorescence.[112]

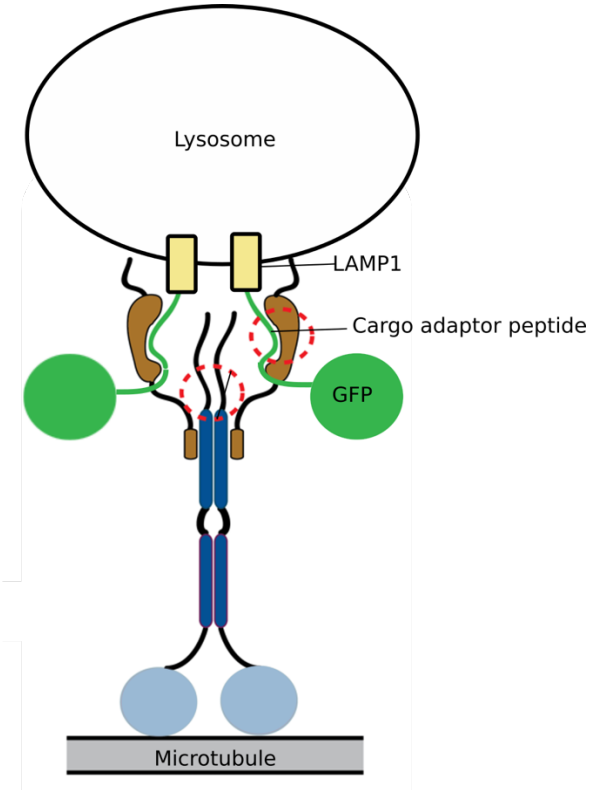

Fig. 4.1 | LAMP1-GFP fusion proteins enable expression of lysosome associated cargo adaptor sequences. Using the approach described by Pu *et al.*, cargo adaptor sequences were cloned into a fusion protein between the lysosome-associated membrane protein (LAMP1) and green fluorescent protein (mGFP) to allow expression of lysosome associated cargo adaptor sequences for recruitment of kinesin-1.

4.3 KinTag outcompetes the natural SKIP W-acidic sequence and disperses lysosomes to the cell periphery

To test if *in vitro* measured binding affinity of the motor-cargo adaptor interaction is correlated with the extent of organelle transport in the cell, HeLa cells were transfected with LAMP1-mGFP, LAMP1-SKIP-mGFP and LAMP1-KinTag-mGFP and imaged for lysosome distribution (Fig 4.2a). In agreement with previous studies,[112] lysosomes expressing the natural

W-acidic sequence from SKIP showed some dispersal of lysosomes to the cell periphery compared to control cells expressing LAMP1-mGFP. Furthermore, incorporation of the high affinity cargo adaptor peptide, KinTag, resulted in dramatic dispersal of lysosomes, with prominent accumulations of fluorescence at the cell periphery (Fig. 4.2). To quantify lysosome positioning, as described by Starling et al., the cell perimeter was defined, the cell area scaled at 10% decrements within this, and the GFP fluorescence intensity measured in each area (Figs. 4.2b, c).[87,286] Notably, the extent of anterograde transport of lysosomes, observed by confocal microscopy, correlated with the binding affinities, measured *in vitro* in fluorescence polarization assays (Chapter 3, Table 3.2). Inclusion of the high-affinity KinTag sequence effected greater dispersion to the periphery than the lower affinity, natural sequence from SKIP. This result adds to previously described examples of *in vitro* properties of *de novo* designed peptides translating to *in cell* functions.[276,327] This illustrates that the *mash-up* design approach has delivered a peptide that can not only bind to the target with high affinity *in vitro*, but can also operate in cells to out-perform natural adaptor sequences and increase kinesin-1-dependent transport of a chosen cargo.

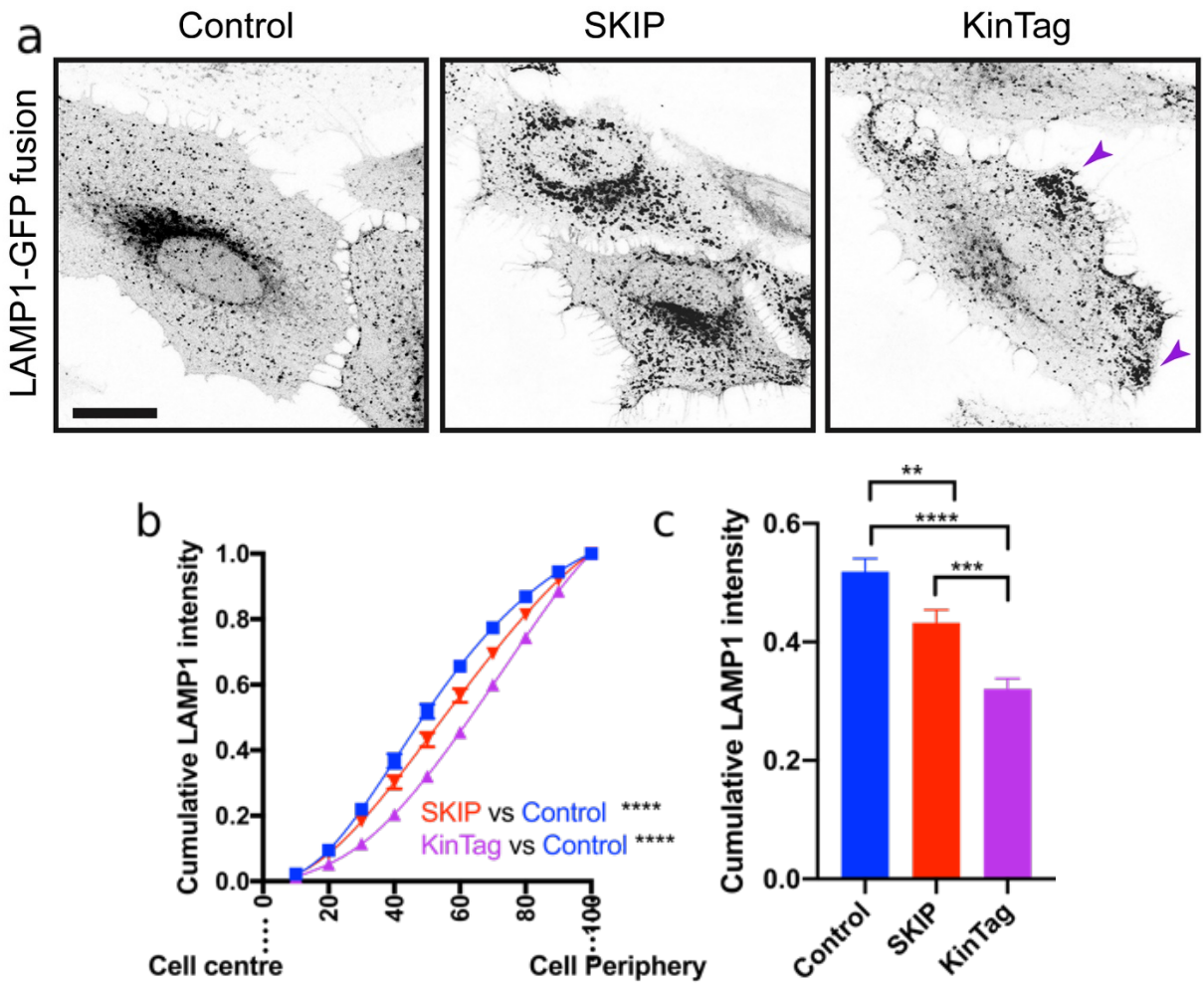

Fig. 4.2| KinTag results in dispersal of lysosomes to the cell periphery. a, Representative inverted confocal images of lysosome dispersal in LAMP1-mGFP (control), LAMP1-SKIP-mGFP (SKIP) and LAMP1-KinTag-mGFP (KinTag) transfected HeLa cells. HeLa cells transfected with LAMP1-mGFP show lysosomes as perinuclear puncta, purple arrows indicate peripheral accumulation of LAMP1-KinTag-mGFP positive lysosomes. **b**, Quantification of lysosome distribution measured by the cumulative LAMP1 fluorescence in concentric rings of equal area in a minimum of 25 cells over 3 independent experiments. SKIP and KinTag fusions result in increased dispersal of lysosomes to the cell periphery. **c**, Unpaired T-test statistical comparison at the 50th percentile from **b.** ** P< 0.01, *** P<0.001, **** P < 0.0001. Error bars show 1 SEM. Scale bars represent 20 μm.

4.4 KinTag delivers lysosomes into neuronal axons

Kinesin-1 transport is particularly important in polarized cells such as neurons. In such cells, molecular motors are critical for the organization of organelles into different regions of the cell, such as the axon, dendrites and soma.[313] Aberrant transport of organelles, resulting in their aggregation or depletion, can contribute to neuron pathogenesis and is associated with neurodegeneration, including Alzheimer's and Parkinson's disease.[130] Next, KinTag was tested for its capacity to direct the transport of organelles between different regions of polarised cells.

For this, the transport of lysosomes from the soma to the axon of neuronal cells was investigated, since this has been shown previously to be kinesin-1 dependent.[313] Rat hippocampal primary neurons were transfected with DNA for the LAMP1-mGFP, LAMP1-SKIP-mGFP and LAMP1-KinTag-mGFP fusion proteins and imaged for lysosome distribution (Fig. 4.3). Inclusion of either kinesin-1-binding peptide (KinTag or SKIP) gave increased transport of lysosomes into axonal initial segments (AIS), which were identified by staining for ankyrin G (Fig. 4.3).[313] To quantify lysosome positioning, the cell area was divided into soma and AIS, and the ratios of mean GFP fluorescence intensity calculated. KinTag drove increased delivery of lysosomes into the axon compared to the natural adaptor SKIP peptide (Fig. 4.3a). This demonstrates, for the first time, that the extent of kinesin-1-dependent axonal transport is positively correlated with the *in vitro* measured binding affinity of the interaction between a cargo-adaptor peptide and the motor complex.

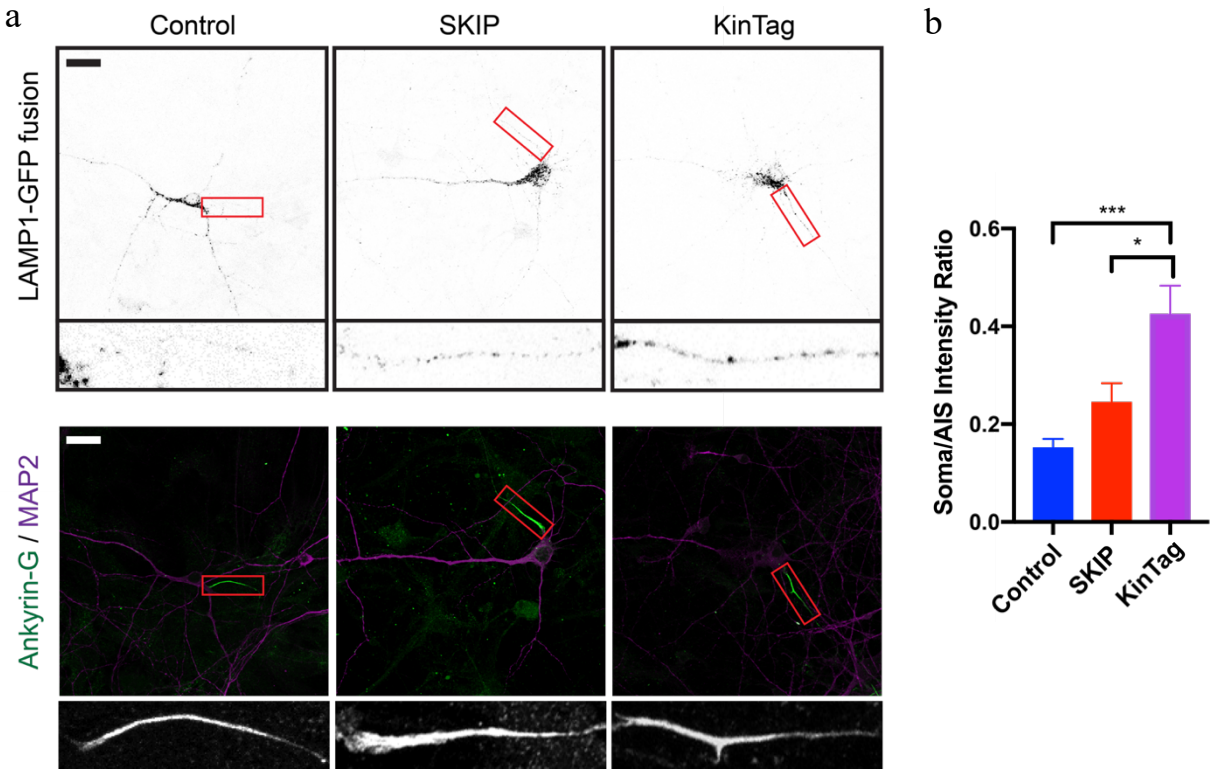

Fig. 4.3 | KinTag delivers lysosomes into neuronal axons. a, Representative confocal images of lysosome dispersal in LAMP1-mGFP (control), LAMP1-SKIP-mGFP (SKIP) and LAMP1-KinTag-mGFP (KinTag) transfected primary neuronal cells (inverted greyscale). LAMP1-mGFP transfected rat hippocampal primary neurons show little LAMP1 in the AIS (defined by ankyrin-G staining), whereas LAMP1-SKIP-mGFP and LAMP1-KinTag-mGFP transfected neurons show increased LAMP1 in this region. **b**, Quantification of ratio of fluorescence intensity in the soma and AIS in transfected neurons in a minimum of 12 cells over 3 independent experiments. ** P< 0.01, *** P<0.001. Error bars show 1 SEM. Scale bars represent 20 μm**.**

4.5 KinTag fused to a peroxisome targeting sequence does not disperse peroxisomes

Having demonstrated the function of KinTag as a lysosomal adaptor peptide for kinesin-1 transport in both non-polarised and polarised cells, the next experiments sought to investigate the capacity of the peptide to effect transport of other cargo. Whilst kinesin–1 is known to transport a range of organelles including peroxisomes and mitochondria, less in understood about the molecular basis of motor recruitment.

Following from the success with lysosomes, KinTag was incorporated into a fusion protein, with a peroxisomal targeting sequence and a fluorescent protein. This construct appended KinTag to the *C* terminus of a fusion comprising the peroxisome targeting sequence PTS1 and mCherry. When transiently expressed in HeLa cells, peroxisomes appeared as red puncta distributed throughout the cell with both control, and KinTag containing, fusions (Fig. 4.4). Quantification of peroxisome positioning showed no significant difference between the two constructs. These initial results indicate that optimisation of construct design is required. The position of the cargo adaptor peptide, in addition to the type of protein it is fused to (e.g. transmembrane) may be important for function. In addition, other organelle-motor interactions may be necessary to effect transport.[69] In this case, the PTS1 targeting sequence is likely to act as an import sequence, preventing KinTag from being located on the cytosolic face of the organelle as required for transport.

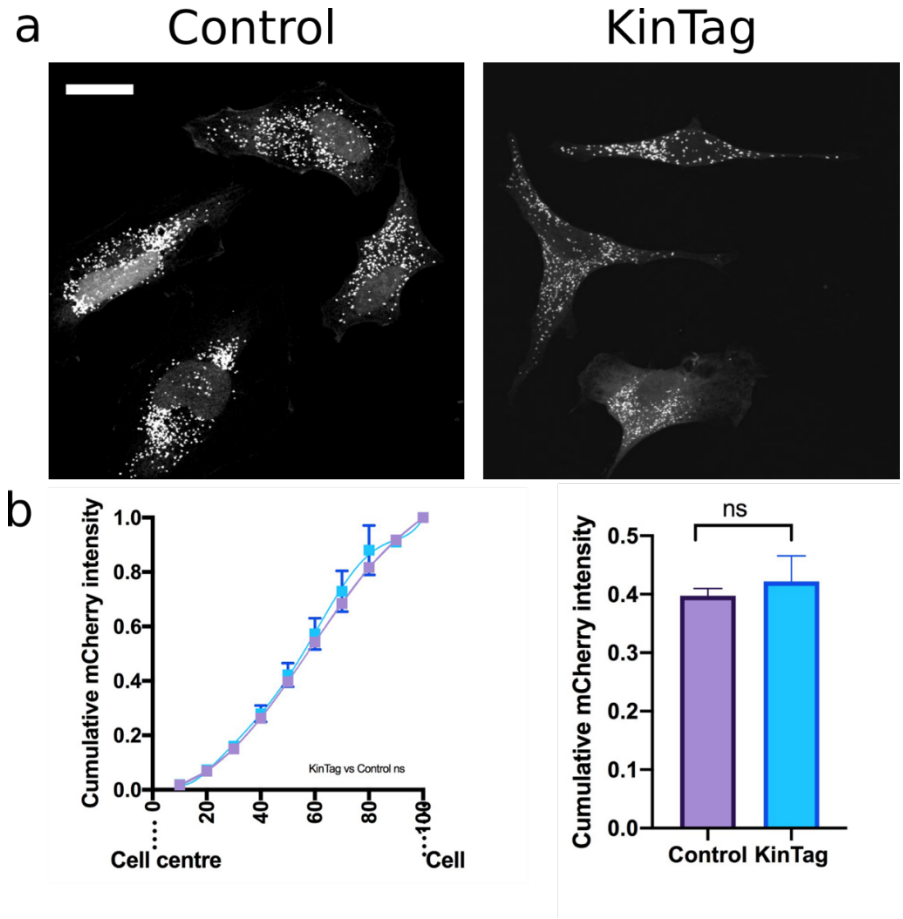

Fig. 4.4 | Fusion of KinTag to peroxisome targeting sequence does not trigger peroxisome dispersal. a, Representative confocal images of peroxisomes in PTS1-mCherry (control) and PTS1-mCherry-KinTag (KinTag) transfected HeLa cells. Peroxisomes appear as puncta throughout the cell. Scale bar 20 μM. **b**, Left, quantification of peroxisome distribution measured by the cumulative mCherry fluorescence in concentric rings of equal area in a minimum of 65 cells over 3 independent expreiments. Right, unpaired T-test statistical comparison at the 50th percentile from **b.** Error bars show 1 SEM.

4.6 KinTag recruited to mitochondria results in dispersal to the cell periphery

Next, to investigate the transport of mitochondria, the KinTag sequence was introduced into a fusion between the outer mitochondrial membrane protein TOMM20 and mCherry. In cells transfected with the control construct a typical mitochondrial staining pattern was observed (Fig 4.5). In contrast, inclusion of the KinTag sequence resulted in punctate fluorescence observed throughout the cell (Fig 4.5). This may be indicative of mitochondrial fragmentation and is likely due to disruption of TOMM20 function in the context of the fusion protein.

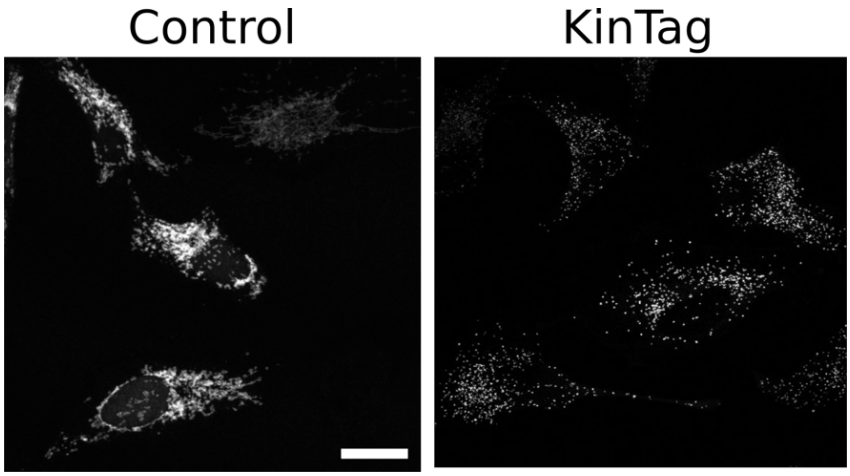

Fig. 4.5 | Fusion of KinTag to TOMM20 results in mitochondrial fragmentation. a, Representative confocal images of mitochondria in TOMM20-mCherry (control) and TOMM20-KinTag-mCherry (KinTag) transfected HeLa cells. Incorporation of the KinTag sequence results in red punctate fluorescence throughout the cell. Scale bar 20 μM

These examples highlight the challenge in designing fusion proteins to incorporate a *de novo* cargo adaptor peptide on the surface of organelles without disrupting their structures and function. An alternative approach is to express KinTag as a soluble protein and recruit it to an organelle of choice through a secondary protein-protein interaction. For this, cells were transfected with KinTag fused to GFP (GFP-KinTag), or GFP alone, and Mito-GBP-en, a mitochondrially targeted GFP nanobody. This aimed to deliver KinTag to the surface of mitochondria without the requirement to design a functional fusion protein. Control cells expressing GFP and Mito-GBP-en displayed green fluorescent mitochondria (Fig 4.6). Incorporation of the KinTag sequence into a GBP-KinTag fusion protein resulted in striking accumulation of peripheral mitochondrial fluorescence (Fig 4.6). In addition, cell shape was altered with elongated cells showing GFP positive projections. To quantify this phenotype, the proportion of dispersed mitochondria was calculated by comparison of fluorescence intensity of the perinuclear cluster with total GFP, as described by Antón et al. (Fig 4.6).[69] This analysis showed that recruitment of KinTag to mitochondria results in significant dispersal to the cell periphery, consistent with increased recruitment of kinesin-1.

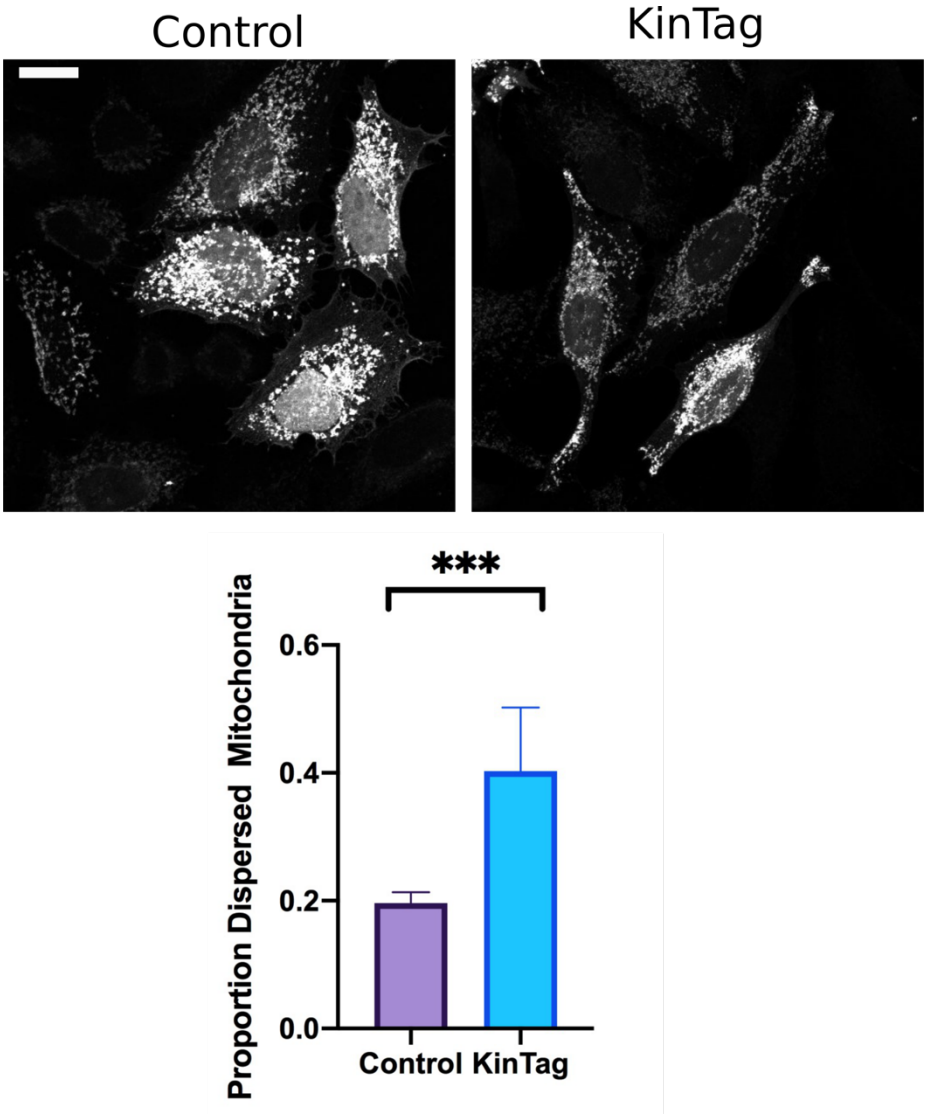

Fig. 4.6| KinTag recruited to mitochondria triggers dispersal to the cell periphery. a, Representative confocal images HeLa cells transfected with GFP (control) or GFP-KinTag and mito-GBPen (a mitochondrially targeted GFP nanobody). Inclusion of the KinTag sequence results in dispersal of fluorescence into peripheral accumulations, elongated cell shape and projections. Scale bar 20 μM **b**, Quantification of mitochondria dispersal in **a**, measured by comparison of GFP fluorescence in the perinuclear cluster compared to the whole cell in a minimum of 25 cells over 3 independent experiments. Error bars show 1 SEM.

This result indicates that the function of KinTag is not limited to the transport of lysosomes and that the sequence could be used to orchestrate the transport of many organelles within the cell, and thus open channels for future studies into organelle positioning or the delivery of therapeutic cargo. Further work will be necessary to ascertain if KinTag can be used universally as a tag for transport. It is clear that the context in which the sequence is expressed will be important for these future studies. It is likely that a nanobody-based approach could be applied to other cargo. Alternatively, other strategies to recruit motor proteins to organelles have recently been described in the literature. One example is optogenetic control of mitochondria

and peroxisome transport, achieved by recruiting motor proteins to the organelles through light induced dimerization of a LOV and PDZ domain.[328] On illumination with blue light the LOV domain exposes a peptide that binds to PDZ. Expression of LOV fusion proteins incorporating a peroxisome targeting sequence or TOM20 in addition to a kinesin-PDZ fusion resulted in light induced transport. In the future, it may be possible to incorporate a KinTag-PDZ fusion into this system to allow light induced recruitment of endogenous kinesin-1 to an organelle of choice. Another approach involves expression of an organelle associated fusion protein incorporating a streptavidin binding protein (SBP) in combination with a streptavidin tagged motor.[329] This triggers recruitment of the motor to the organelle and increased transport. The activity is reversed by addition of biotin to the cell to out compete the interaction. Again, future work could investigate the capacity of a KinTag-streptavidin fusion to facilitate reversible recruitment of endogenous kinesin-1.

4.7 Chariot reagent does not deliver a KinTag peptide into the cell

To explore the function of a soluble KinTag peptide to promote or inhibit kinesin-1 cargo transport in the cell, approaches to confer cell-penetrating properties to the peptide were explored. The aim was to develop a KinTag peptide analogue that could be added directly to cells and delivered into the cytosol. There are a wide range of approaches to conferring cell penetrating properties, including covalent and non-covalent conjugation of cationic and amphipathic cell-penetrating peptides (CPPs).[330-332] Initial experiments tested non-covalent conjugation of KinTag to the commercially available amphipathic peptide Pep-1 (Chariot Reagent, Table 4.1). HeLa cells were treated with Chariot-peptide complexes at a range of concentrations for 2 h as per the manufacturer's instructions (Fig. 4.7). Fluorescence of the TAMRA labelled KinTag peptide was observed in punctate, likely endosomal, structures, and aggregates and did not enter the cytosol. No effect on lysosomal distribution or microtubule organisation was observed. This may be due to the acidic KinTag peptide associating with the basic polylysine regions of the Chariot reagent, causing aggregation and inhibiting direct penetration and dissociation of the complex.

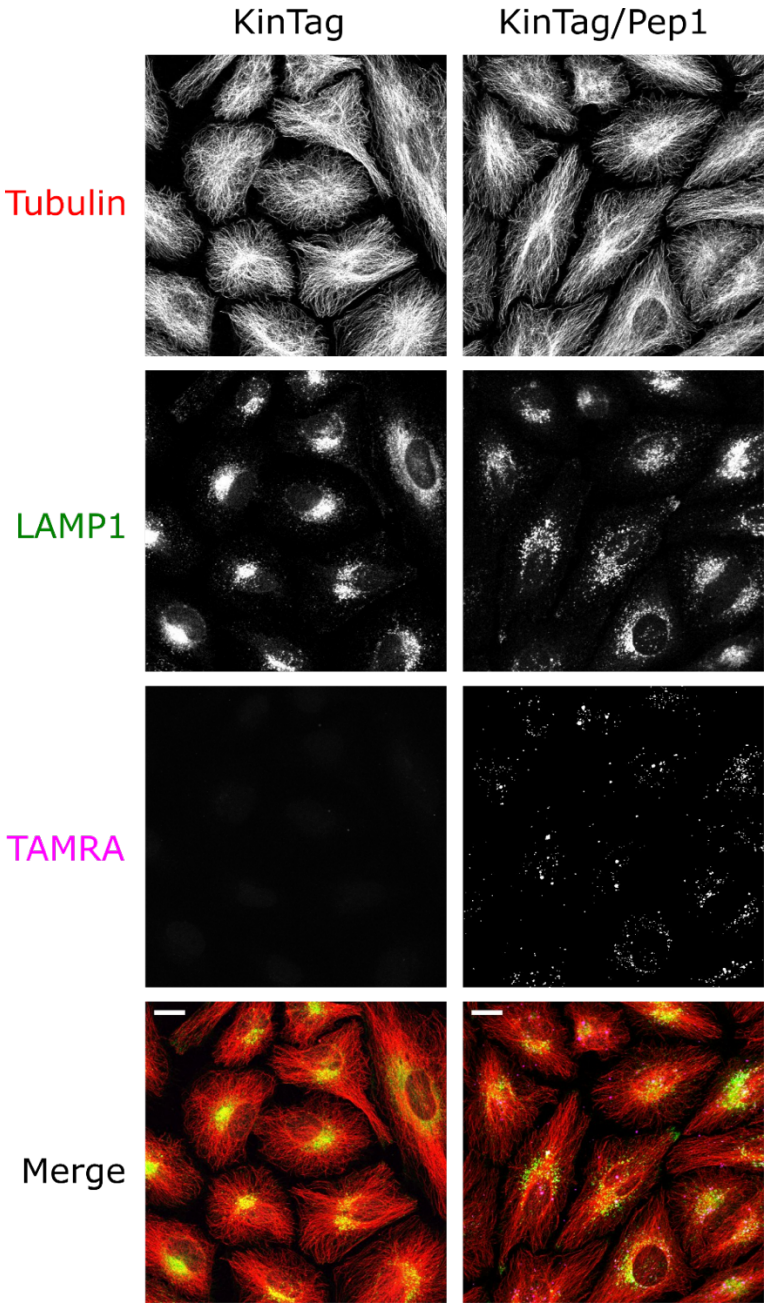

Fig. 4.7 | HeLa cells treated with KinTag or KinTag/Pep-1 complexes do not show direct cell penetration. Representative confocal images of HeLa cells treated with KinTag peptide alone or KinTag in complex with Pep-1 (Charriot reagent) for 2 h as per the manufacturer's instructions. Cells were fixed with 4 % PFA and incubated with antibodies against tubulin and LAMP1. Images are presented as maximal intensity projections. Scale bars represent 20 µm. When incubated with Pep-1, fluorescence of the TAMRA labelled KinTag peptide was observed in punctate structures and aggregates and did not enter the cytosol. No effect on lysosomal distribution or microtubule organisation was observed.

4.8 Polyarginine tags confer cell penetrating properties to a KinTag peptide

An alternative approach is to synthesise a peptide with the KinTag sequence covalently coupled to a cell penetrating tag. Polyarginine stretches have been shown to confer cell-penetrating

properties allowing direct entry to the cytoplasm.[330-332] To investigate this, a series of TAMRA-labelled peptides were synthesised with varying length of polyarginine tags *C* or *N* terminal to the KinTag peptide (Table 4.1). Peptides dissolved in a minimal volume of dimethyl sulfoxide (DMSO) in Dulbecco's Modified Eagle Medium (DMEM) were added to HeLa cells and imaged by confocal microscopy to investigate their cell penetrating properties (Fig. 4.8). At a concentration of 10 μM peptides there were no signs of cytotoxicity after 4 h. KinTag peptides with 6 or 8 arginine residues at the *C* or *N* termini showed diffuse cytosolic fluorescence indicative of direct penetration into the cytoplasm. In addition, fluorescence was observed in the nucleus of these cells. In contrast, KinTag peptides with 0, 2 or 4 arginine residues gave no fluorescence in the cytoplasm. Live cell imaging indicated that internalisation occurred within 1 h at a concentration of 10 μM peptide. This led to the conclusion that 6 arginine residues are necessary and sufficient to confer cell penetrating properties to the KinTag peptide. The position of the polyarginine tag, *C* or *N* terminal to the cargo-adaptor peptide sequence, did not appear to be significant.

Table 4.1 | Sequences of polyarginine tagged KinTag peptides tested for cell penetrating properties

Peptide name	Sequence
KinTag	GTVFTTEDIYEWDDSAI
KinTag-R2	GTVFTTEDIYEWDDSAIRR
KinTag-R4	GTVFTTEDIYEWDDSAIRRRR
KinTag-R6	GTVFTTEDIYEWDDSAIRRRRRR
KinTag-R8	GTVFTTEDIYEWDDSAIRRRRRRRR
R2-KinTag	RRGTVFTTEDIYEWDDSAI
R4-KinTag	RRRRGTVFTTEDIYEWDDSAI
R6-KinTag	RRRRRRGTVFTTEDIYEWDDSAI
R8-KinTag	RRRRRRRRGTVFTTEDIYEWDDSAI
Pep-1 / Chariot	KETWWETWWTEWSQPKKKRKV

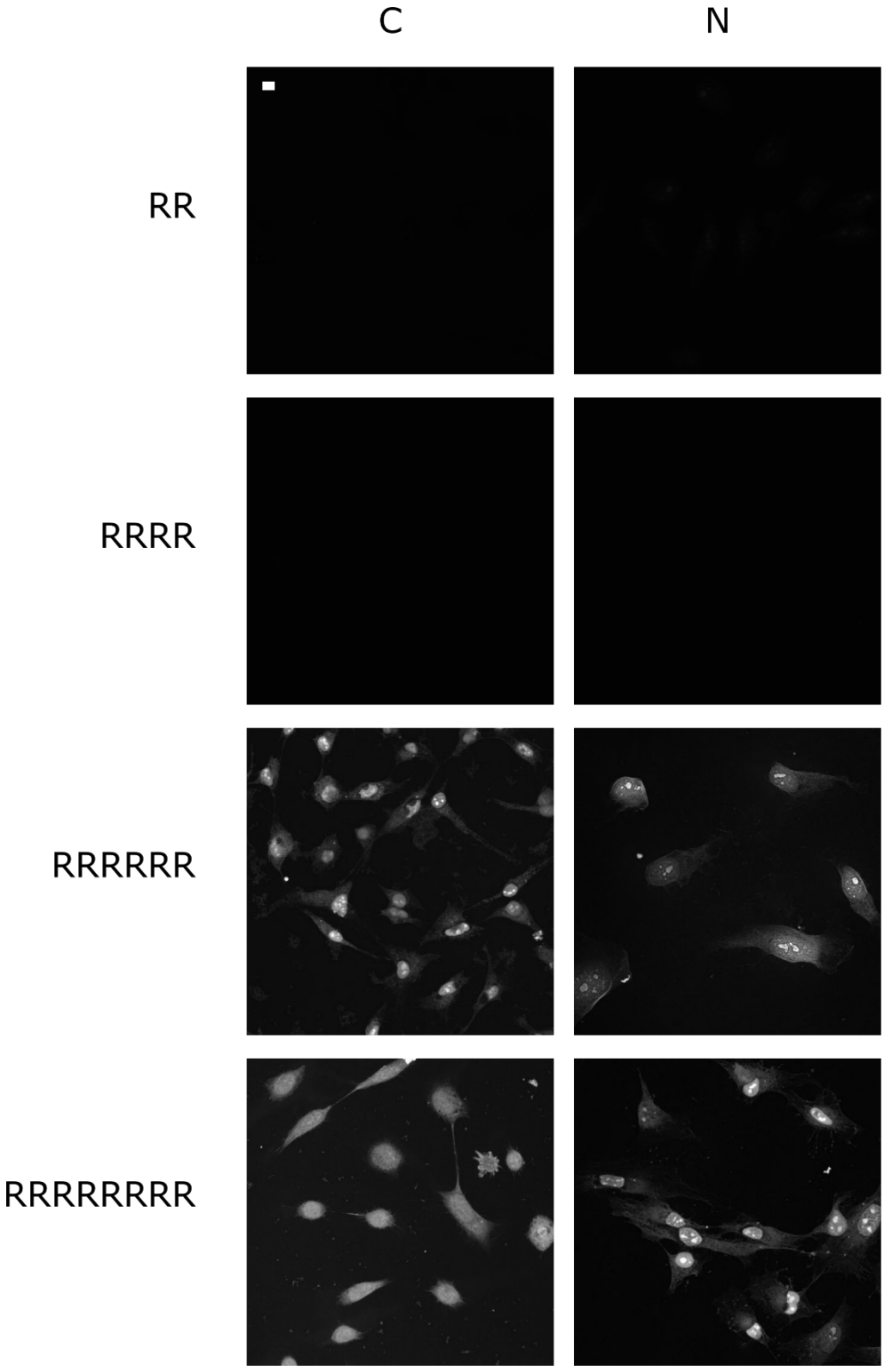

Fig. 4.8 | HeLa cells treated with polyarginine tagged KinTag peptides. Representative confocoal images of TAMRA fluorescence in HeLa cells treated with 10 μM TAMRA labelled KinTag peptides covalently attached to 2, 4, 6 or 8 arginine residues at the *N* or *C* termini at 37 ºC for 1 h, fixed with 4 % PFA and visualised by confocal microscopy. Peptides with 6 or 8 arginine residues at the *C* or *N* termini showed diffuse cytosolic fluorescence and nuclear fluorescence indicative or direct penetration into the cytoplasm and nucleus. Peptides with 0, 2 or 4 arginine residues showed no fluorescence in the cytoplasm. Live cell imaging indicated that internalisation occurred within 1 h at a concentration of 10 μM. Scale bar represents 20 μm.

4.9 Polyarginine tags decrease binding of KinTag peptides to KLC^{TPR}s

Next, the affinities of the cell penetrating KinTag analogues for KLC1^{extTPR} were measured in vitro in fluorescence polarisation assays, as described in Chapter 3. Binding was only observed for KinTag peptides with tags comprising 0, 2 or 4 arginine residues (Table 4.2, Fig 4.9a). Increasing the number of arginine residues decreased affinity for KLC1^{extTPR}. This is likely due to aggregation of the peptide through electrostatic interactions between the acidic KinTag sequence and the basic polyarginine tag. The polyarginine stretch may also inhibit binding through electrostatic repulsion with the basic surface of the TPR domain (Fig 4.9b).

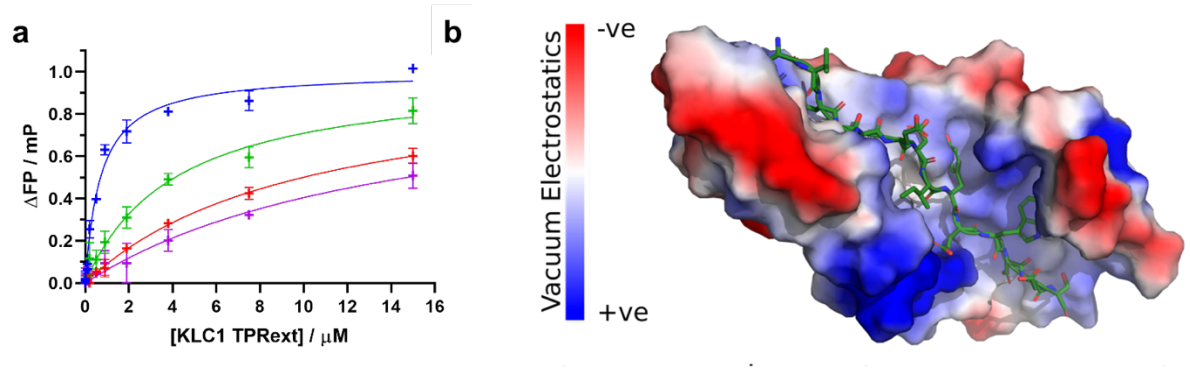

Fig. 4.9 | Polyarginine tagged KinTag peptides show reduced binding affinities for KLC1^{extTPR} *in vitro*. a, Fluorescence polarization assays for TAMRA-labelled arginine tagged KinTag peptides (150 nM) incubated with increasing concentrations of protein KLC1^{TPRext} Key: KinTag, blue; KinTag-R2, red; R2-KinTag, green; R4-KinTag, purple. Data were fitted to a single-site binding model with polarization values of the peptide and buffer alone subtracted and values normalised to the calculated B_{max}. Error bars indicate 1 SD from a minimum of 3 replicates. **b**, Vacuum electrostatics surface showing the positively charged (blue) TPR groove interacting with the overall acidic KinTag peptide, colour coding per residue as shown.

Table 4.2 | Binding affinities of polyarginine tagged KinTag peptides for KLC1^{extTPR}

Peptide name	Sequence	K_D KLC1^{extTPR} / μM
KinTag	GTVFTTEDIYEWDDSAI	0.17 ± 0.007
KinTag-R2	GTVFTTEDIYEWDDSAIRR	9.96 ± 2.0
R2-KinTag	RRGTVFTTEDIYEWDDSAI	4.11 ± 0.70
R4-KinTag	RRRRGTVFTTEDIYEWDDSAI	14.7 ± 6.1

4.10 Cell-penetrating tags can be designed to mask arginine residues after cell entry

Since covalent conjugation of a polyarginine tag conveyed cell-penetrating properties but inhibited the interaction of KinTag with KLC^{TPR}s, an alternative cell penetrating sequence was

designed. This aimed to retain the interaction of guanidinium groups from arginine residues with the phospholipid bilayer but to mask these positive charges after cell entry, and so prevent peptide aggregation and TPR repulsion. The hypothesis was that this could be achieved by designing an arginine rich tag to yield a CPP with a net cationic charge, and an acidic partner sequence to interact with the basic cell-penetrating sequence once inside the cell, burying charged residues in salt-bridge interactions

Charged, unstructured, peptides have been shown to interact in heterodimeric coiled coils with buried salt bridges.[273] In the Woolfson group, Dr William Dawson and Dr Guto Rhys recently described the design of a *de novo* antiparallel heterodimer, apCC-Di-AB These peptides were designed to comprise an acidic (apCC-Di-A) and basic (apCC-Di-B) sequence that are individually unfolded in solution, but interact as a stable heterodimer when mixed (Fig. 4.10, Table 4.3). The apCC-Di-B peptide is arginine rich and follows a similar hydrophobic patterning shown to be important for cell penetration of the mini-protein Zf5:3.[333] The apCC-Di-AB complex has a low net charge of +2, with electrostatic interactions masking charged residues. Therefore, apCC-Di-B was identified as a potential cell-penetrating tag for KinTag (Fig 4.10, Table 4.3).

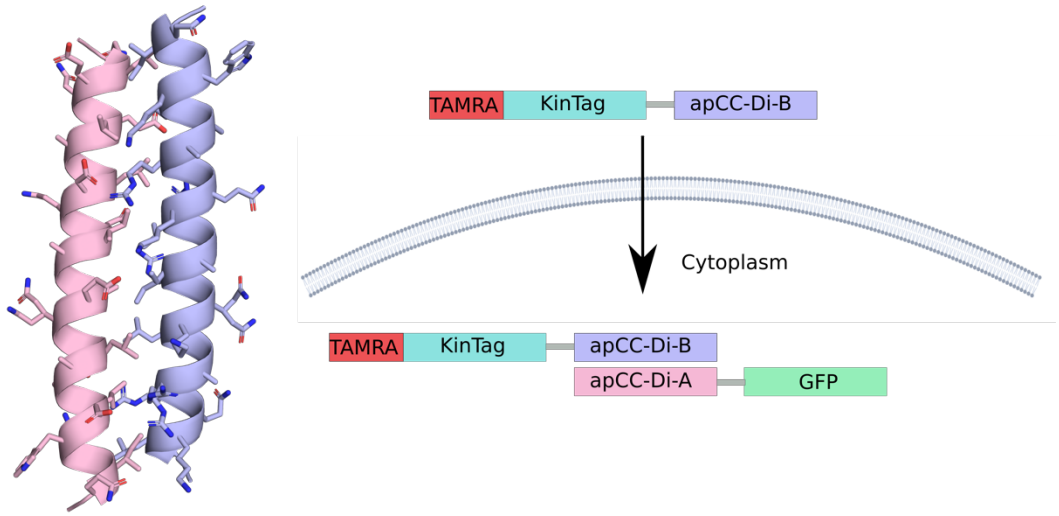

Fig. 4.10 | Design of a *de novo* cell penetrating, coiled-coil peptide to deliver KinTag into cells. X-ray crystal structure of the designed heterodimer apCC-Di-AB and cartoon illustrating apCC-Di-B as a cell penetrating tag to deliver KinTag into cells. After cell entry dimerization of apCC-Di-A and apCC-Di-B results in burial of charged residues to protect KinTag functionality.

Table 4.3 | Peptide sequences for design of a *de novo* cell penetrating kinesin-1 cargo adaptor peptide						
Peptide name	**Sequence**	*cdefgab*	*cdefgab*	*cdefgab*	*cdefgab*	
apCC-Di-A		G QLEQELA	ALDQEIA	AAEQELA	ALDWQIQ	G
apCC-Di-B		G QLKQRRA	ALKQRIA	ALKQRRA	ALKWQIQ	G
KinTag-apCC-Di-B	GTVFTTEDIYEWDDSAITGSTGSG	QLKQRRA	ALKQRIA	ALKQRRA	ALKWQIQ	G

4.11 A *de novo* coiled-coil forming peptide is cell penetrating

To test the cell penetrating properties of apCC-Di-B, the peptide was synthesised with an *N*-terminal fluorophore, TAMRA, appended. HeLa cells were treated with a range of concentrations of this peptide (0.4 – 10 μM) for 1 h. Consistent with cell entry, red fluorescence was observed in the cytosol and nucleus. The corresponding acidic peptide apCC-Di-A showed no evidence of cell penetration under the same conditions. (Fig. 4.11).

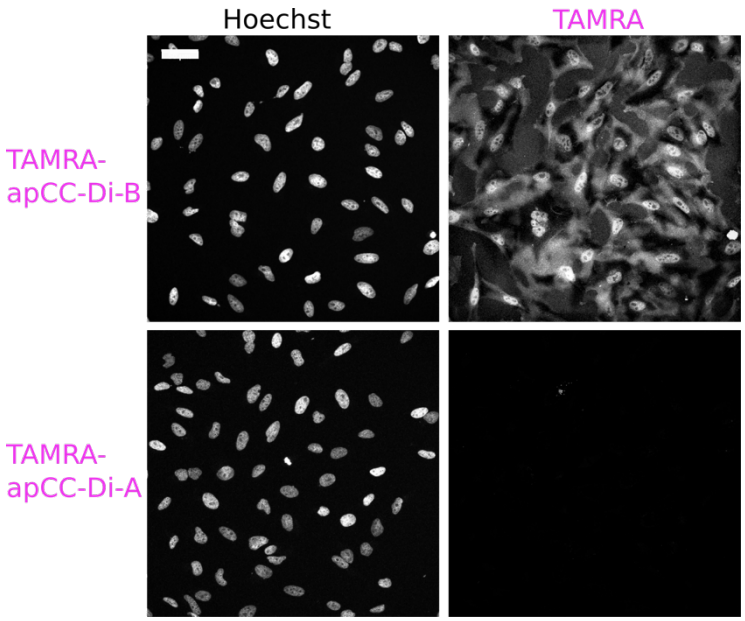

Fig. 4.11 | *De novo* designed peptide apCC-Di-B is cell penetrating. Representative confocal images of HeLa cells treated for 1h with 2 μM TAMRA labelled apCC-Di-B (top) or apCC-Di-A peptides (bottom), designed to interact as an antiparallel heterodimeric coiled coil. apCC-Di-B is cell penetrating shown by TAMRA fluorescence in the cytoplasm and nucleus, apCC-Di-A does not enter the cell. Scale bar 50 μm

Cell entry of apCC-Di-B does not appear to require endocytosis because accumulation of fluorescence signal in the cytosol and nucleus still occurred when the experiment was

performed at 4 °C (Fig. 4.12), and so is more likely due to interaction of guanidinium groups from arginine residues with the phospholipid bilayer of the cell to facilitate direct entry.[334]

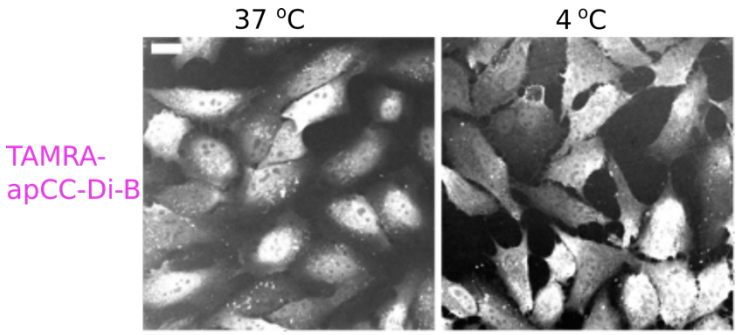

Fig. 4.12 | Cell penetration of apCC-Di-B occurs at 4 °C. Representative confocal images of HeLa cells treated for 1h with 2 μM TAMRA labelled apCC-Di-B at 37 °C (left) or 4 °C (right). TAMRA fluorescence in the cytoplasm and nucleus shows apCC-Di-B enters the cell in a temperature-independent manner suggesting that the mechanism does not require endocytosis. Scale bar 20 μm.

4.12 A *de novo* cell-penetrating peptide can bind its bait sequence in the cell

To investigate whether apCC-Di-B could bind to apCC-Di-A to form a heterodimer in the cell, apCC-Di-A was expressed as a GFP-fusion protein. Cells were transiently transfected and treated with 2 μM TAMRA-apCC-Di-B. Control cells were transfected with GFP alone and/or treated with a vehicle control. Cells were lysed and GFP proteins isolated by GFP-immunoprecipitation. Associated TAMRA fluorescence signal from eluant of boiled beads was measured at 557 nm. Only beads incubated with lysate from cells expressing GFP-apCC-Di-A treated with TAMRA-apCC-Di-B retained significant TAMRA fluorescence, demonstrating the peptides can heterodimerize after cell entry of apCC-Di-B (Fig. 4.13).

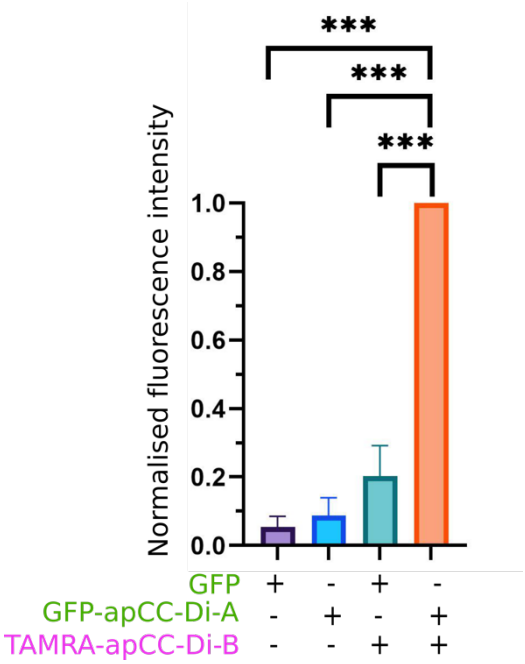

Fig. 4.13 | Cell penetrating peptide apCC-Di-B can interact with apCC-Di-Aexpressed in cells. Cells transfected with GFP or GFP-apCC-Di-A and treated with 2 μM TAMRA-apCC-Di-B or vehicle control were subject to GFP-immunoprecipitation and quantification of TAMRA immobilised on beads measured by fluorescence at 557 nm. TAMRA-apCC-Di-B binds to GFP-apCC-Di-A in cell lysate and is immobilised on beads.

4.13 A *de novo* cell-penetrating peptide can be localised to a subcellular compartment by interaction with its bait

To visualise dimerization directly inside cells, apCC-Di-B was targeted to a subcellular compartment using apCC-Di-A as bait. Two orthogonal approaches were used. First, similarly to that described in section 4.2, apCC-Di-A was targeted to lysosomes by *C*-terminal fusion to LAMP1-mGFP, to expose the bait (apCC-Di-A peptide) on the surface of late endosomal and lysosomal vesicles (Fig. 4.14). This resulted in striking recruitment of TAMRA-apCC-Di-B to the LAMP1 compartment.

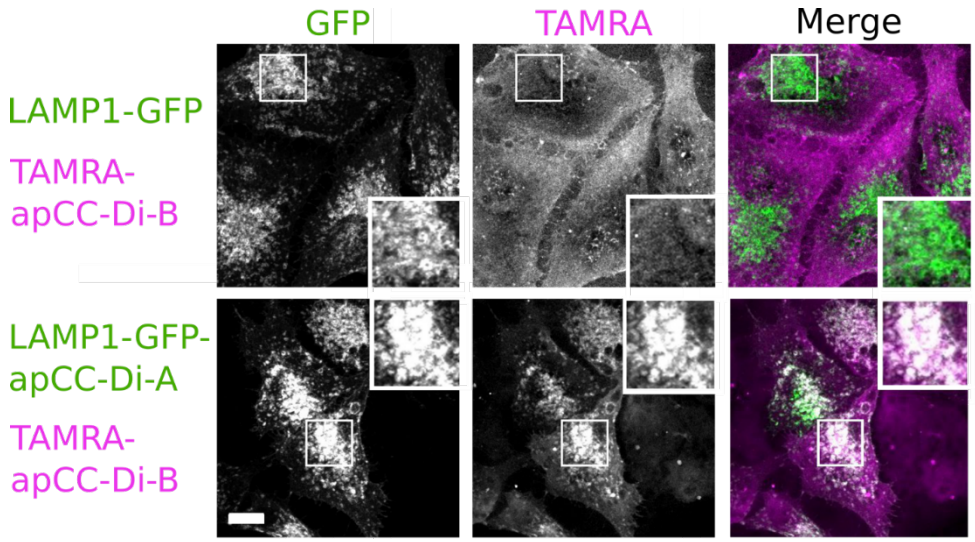

Fig. 4.14 | Cell penetrating peptide apCC-Di-B can localise to lysosomes expressing "bait" apCC-Di-A. Representative confocal images of HeLa cells transfected with GFP-LAMP1 or GFP-LAMP1-apCC-Di-A and treated with 2 µM TAMRA-apCC-Di-B. Colocalization of GFP and TAMRA fluorescence on lysosomes indicates apCC-Di-AB dimerization. Scale bar 20 µm

Second, similarly to that described in section 4.6, a mitochondrially targeted GFP nanobody (pMito-GBPen) was used to trap GFP-apCC-Di-A on mitochondria. Remarkably, this resulted in TAMRA-apCC-Di-B now localising to mitochondria (Fig. 4.15). In conclusion, the *de novo* cell-penetrating peptide, apCC-Di-B, can enter the cell and localise specifically to its target sequence.

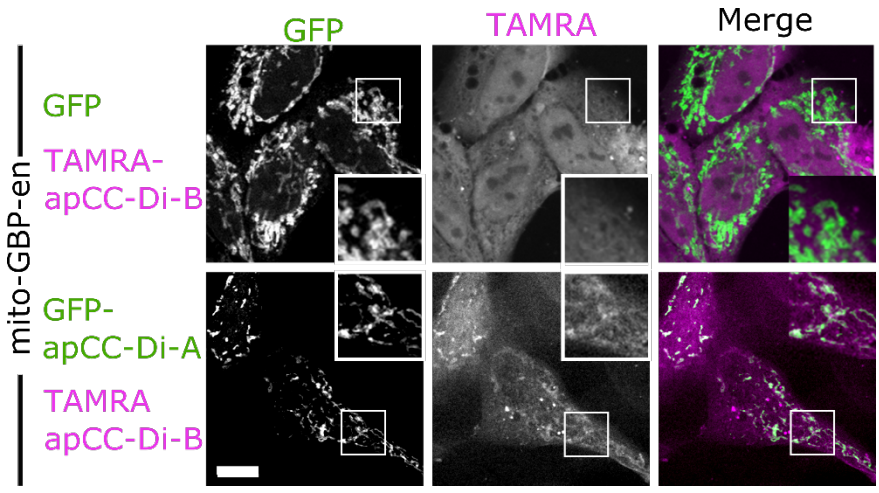

Fig. 4.15 | Cell-penetrating peptide apCC-Di-B can localise to "bait" apCC-Di-A recruited to mitochondria. Representative confocal images of HeLa cells transfected with GFP or GFP-apCC-Di-A and a mitochondrially targeted GFP nanobody (Mito-GBP-en) and treated with 2 µM TAMRA-apCC-Di-B. Colocalization of GFP and TAMRA fluorescence on mitochondria indicates apCC-Di-AB dimerization. Scale bar 20 µm.

4.14 A *de novo* cell-penetrating peptide can deliver KinTag into the cell

Finally, a lysosome transport assay was used to determine whether this system could deliver KinTag into the cell as a functional kinesin-1 cargo adaptor peptide. Based on previous experiments (section 4.3), recruitment of KinTag to lysosomes should promote their transport to the cell periphery. To test this, a peptide comprising the KinTag sequence fused to the apCC-Di-B sequence was synthesised and labelled with an *N*-terminal TAMRA fluorophore (Table 4.3). This arginine- and lysine-rich peptide had a net charge of +4 and was designed, similar to the polyarginine tagged sequences, to deliver KinTag to the cytosol through direct cell penetration. HeLa cells treated with 2 μM peptide for 1 h showed red fluorescence in the cytosol and nucleus, consistent with cell entry.

To test for functionality of the delivered KinTag sequence, cells expressing the LAMP1-mGFP-apCC-Di-A fusion were treated with 2 μM TAMRA-KinTag-apCC-Di-B as an exogenous reagent. Again, colocalization of TAMRA and GFP fluorescence on lysosomal puncta indicated dimerization. Inclusion of KinTag in the apCC-Di-B peptide resulted in dispersal of lysosomes, with peripheral accumulations observed at cell vertices and altered cell-shape with increased GFP and TAMRA positive cell projections (Fig. 4.16). Control cells, without the apCC-Di-A "bait", showed diffuse cytosolic TAMRA fluorescence with a perinuclear clustered LAMP1 phenotype. Together, these data demonstrate that the dimerization of apCC-Di-A and apCC-Di-B can be combined with the cell-penetrating properties of the latter to deliver KinTag as a functional cargo to a specific location in the cell.

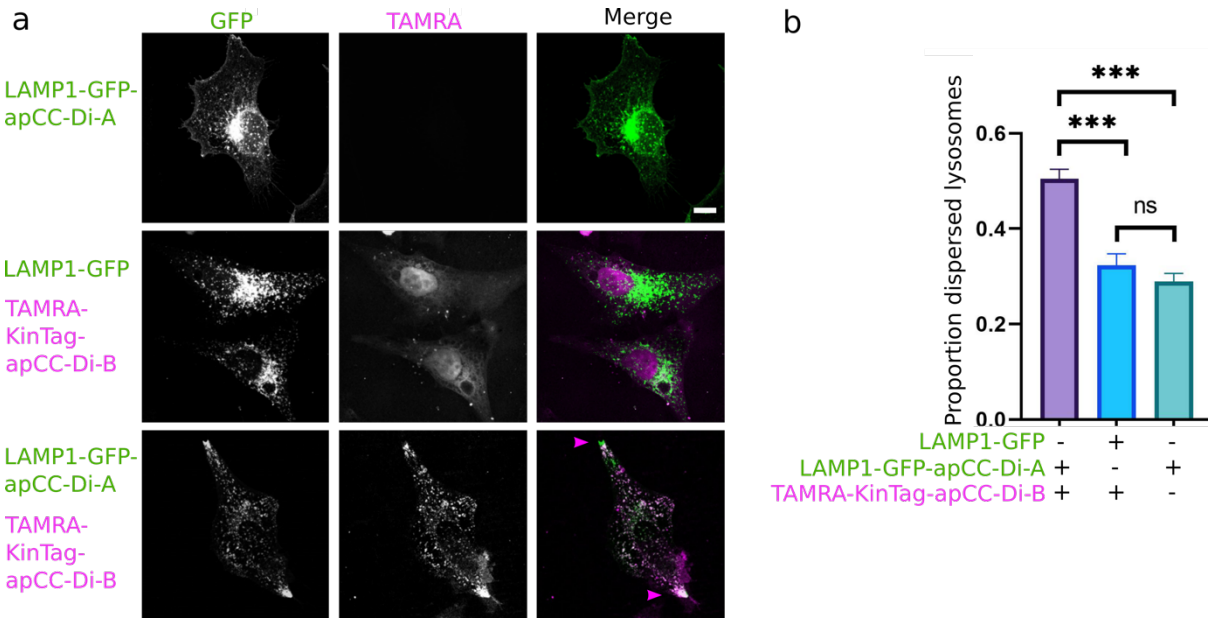

Fig. 4.16 | A cell penetrating peptide, apCC-Di-B, can deliver a functional *de novo* cargo adaptor peptide, KinTag, to lysosomes. a, Representative confocal images of HeLa cells transfected with GFP-LAMP1 or GFP-LAMP1-apCC-Di-A GFP and treated with 2 μM TAMRA-KinTag-apCC-Di-B or vehicle control. KinTag delivered to lysosomes by apCC-Di-AB dimerization promotes transport to the cell periphery. Scale bar 10 μm. **b.** Quantification of lysosome dispersal in in cells expressing LAMP1-GFP or LAMP1-GFP-apCC-Di-A fusion proteins treated with TAMRA labelled apCC-Di-B or KinTag-apCC-Di-B.

4.15 Conclusions

To function as a cargo-adaptor peptide, our *de novo* design must have the capacity to recruit endogenous kinesin-1 motors inside the cell to effect organelle transport. With lysosomes and mitochondria as target cargoes, KinTag has been shown to mediate transport in mammalian cells. Moreover, this has allowed the demonstration that peptide-protein binding affinities measured *in vitro* are positively correlated with the extent of cargo transport in the cell: cargoes fused to KinTag are transported to greater extents than those fused to a natural sequence from the lysosomal cargo-adaptor protein SKIP. This finding should allow a toolkit of peptide ligands with a range of affinities to be developed as transport tags within cells. In turn, this could allow the orchestration of transport of organelles and other cargoes to investigate the functional roles of positioning within the cell. Whilst kinesin-1 motor-microtubule binding and kinetics have been studied extensively, there have been few studies to date considering motor-cargo interactions. These new results suggest that the motor-cargo interface is a key component in transport and may open the door to future investigations into how motor-cargo binding affinities are correlated with transport kinetics.

This transport function has been demonstrated in both HeLa and primary neuronal cells: fusion of KinTag to the lysosomal marker, LAMP1, leads to dispersal of lysosomes to the cell periphery and into the axon, respectively. Kinesin-1 is critical for cargo transport along neuronal axons, which is necessary for neuron function, growth and avoiding pathologies associated with neurodegenerative diseases.[313] Fusion of cargo to KinTag results in upregulated transport into the axon. The transport of lysosomes in this model system has potential utility as lysosomes are important for axonal growth cone development and the turnover of axonal autophagosomes.[313] The delivery of other therapeutic cargoes may have future applications in the treatment of neurodegenerative diseases where axonal transport is impaired.

The cellular functionality of KinTag suggests that peptide binding results in the same downstream activation of the tetrameric motor seen for natural W-acidic adaptor peptides. This re-enforces the *in vitro* data (described in Chapter 3) that binding affinities are sensitive to inclusion of the autoinhibitory LFP motif and structural data that KinTag binding increases TPR curvature. In combination, this biophysical, structural and functional validation of the design highlights that key molecular interactions in this system are becoming understood and that this understanding can be exploited. To date, application of this peptide for the transport of other organelles remains a challenge, since initial attempts to transport peroxisomes were unsuccessful. This highlights that there is still much more to be understood in regard to the activity of kinesin-1 cargo adaptor peptides for organelle transport. Possible explanations include the importance of the context in which the cargo adaptor is expressed; *i.e.*, the position in the fusion protein, or additional protein binding partners or membrane interactions required to make cooperative interactions.[69]

Finally, this chapter has begun to explore the potential applications of KinTag as an exogenous reagent introduced via the cell media rather than directly into cells. Arginine-rich peptide tags proved sufficient to confer cell-penetrating properties. However, these tags disrupted TPR binding, resulting in delivery of a non-functional peptide. To overcome this, a new cell-penetrating tag was designed to form a heterodimeric coiled coil. This comprises a basic peptide that can enter the cell, and an acidic target peptide to which the basic peptide can bind tightly and specifically. The utility of this approach was demonstrated through lysosome transport assays in which delivery of exogenous KinTag to lysosomes, through coiled-coil heterodimerisation, resulted in their dispersal to the cell periphery. This is a unique strategy combining an exogenous cell-penetrating reagent with a genetically encoded “bait” sequence

to deliver a peptide cargo to a sub-cellular location of choice. This work may have future applications in the delivery of other cargo, particularly where cell-penetration with polyarginine tags presents a challenge, for example negatively charged peptides. Having delivered functional, exogenous, KinTag as a transport tag to lysosomes, future work will involve applying this approach to other organelles in addition to investigating a cytosolic construct as an inhibitor, rather than activator, of kinesin-1 transport.

5 Computational and biophysical analysis of the KHC-KLC coiled coil interface

Ideas described in this chapter have been included in the publication

Kinesin-1 captures RNA cargo in its adaptable coils
Jessica A. Cross, Derek N. Woolfson and Mark P. Dodding
Genes Dev. **2021, 35,** 937-939 DOI: 10.1101/gad.348691.121

Some initial experiments in sections 5.4 and 5.5 of this chapter were done with the help of MSci student Catriona Morrison under my supervision and some similar data reported in her MSci thesis.

5.1 Background

Chapters 3 and 4 have described experiments to understand and manipulate the kinesin-1 motor-cargo interface through targeting the TPR domains of the kinesin light chains (KLCs). For motor activity, the KLCs must bind to the heavy chains (KHCs) in the kinesin-1 tetramer.[84,335] In the heterotetramer, the KHCs are thought to dimerise through coiled-coil interactions in an extended α-helical stalk region.[336] The *C*-terminal region of this KHC stalk contains four highly conserved heptad repeats that are proposed to be responsible for the interaction with the *C*-terminal, heptad-repeat region of the KLCs.[337] Motor activity and regulation rely on the assembly of the heterotetramer. Therefore, understanding the nature of these interactions is key to understanding the structure and function of kinesin-1.

Diefenbach *et al.* and Verhey *et al.* have investigated interactions of truncated proteins to map the minimal interacting regions between KLC and KHC, and hypothesised that the protein complex is held together through a heterotetrameric coiled-coil interaction. [83,46] To date this structure has not been resolved and the architecture of this interface remains unknown, *i.e.* whether it is parallel or antiparallel. Elsewhere, coiled-coil domains have been extensively studied and their geometries are well described by a small number of structural parameters.[238] In addition, established sequence-to-structure relationships make coiled coils attractive and viable targets for modelling and peptide design.[151,234,238]

The work described in this chapter sought to understand and structurally characterise the protein sequences involved in the KHC-KLC interface. Coiled-coil design knowledge was applied to make structural predictions, build models of the interface, and to characterise

synthetic peptides and recombinant proteins from this region experimentally. The coiled-coil domains of kinesin-1 have sometimes been associated with rigid spacer-like properties with functions limited to oligomerisation. The experiments described here begin to offer new insights into the KHC stalk as a dynamic and flexible platform for protein-protein interactions, which may play a role in the pH responsive behaviour of the motor in addition to conformational changes associated with release of autoinhibition.

5.2 The KLC binding site of KHCs is predicted to form a conserved coiled coil

Initial studies focussed on the coiled-coil stalk region of the KHCs. Previously, the light chain binding site has been mapped by Verhey *et al.* to residues 682-810 of human KHC isoform Kif5C[83] and by Diefenbach *et al.* to restudies 771-813 of Kif5B.[46] These studies involved mapping interactions of truncated proteins to identify minimal interacting regions. To understand better and to characterise this interface, bioinformatic methods were used to predict structures for the regions of the proteins involved in the interaction.

Canonical coiled coils have 7-residue (heptad) repeat sequences, often labelled ***abcdefg***. These form amphipathic α helices due to predominantly hydrophobic residues at the "core" ***a*** and ***d*** sites. Two or more such helices wrap around one another to bury their hydrophobic faces (Fig 5.1).[233,236] The well-established sequence-to-structure relationships that determine coiled-coil assembly and the parameterisation of these structures have allowed the development of bioinformatic tools for the prediction of coiled-coil domains in natural proteins.[243] One example is Marcoil, which can be used to identify likely coiled-coil regions of protein sequences.[248]

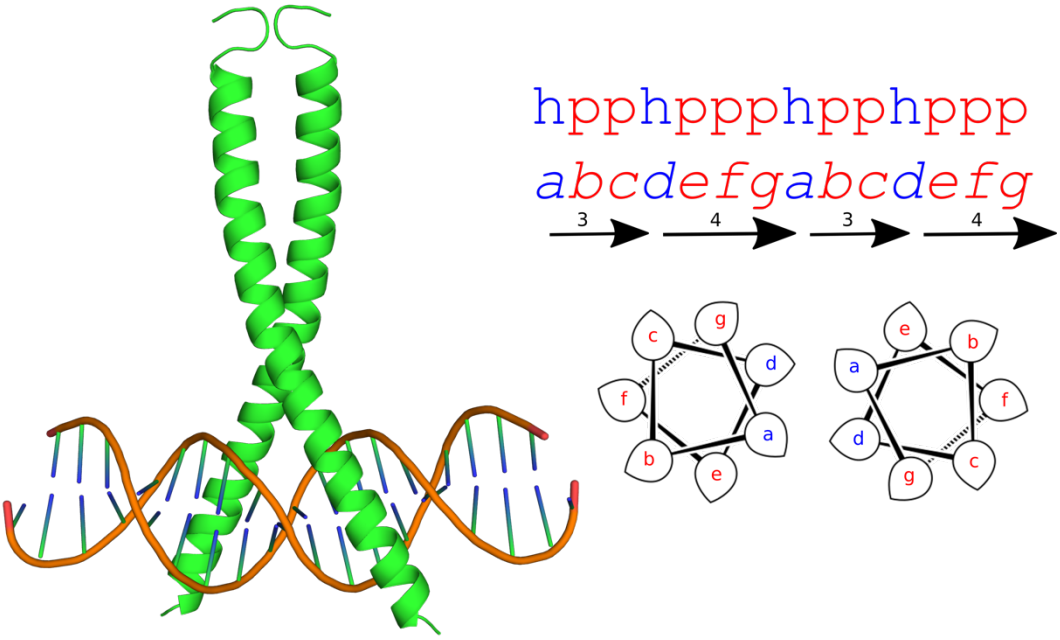

Fig. 5.1 | Coiled coils have 7-residue, heptad, repeat sequences. Left, X-ray structure of the well-studied dimeric coiled-coil transcription activator protein GCN4 bound to DNA, PDB 1DGC. Two or more amphipathic α helices wrap around one another to bury hydrophobic positions in the core of the coiled coil. Sequences follow heptad repeats (labelled ***abcdefg***) with hydrophobic residues repeating every 3 and 4 residues as shown on the helical wheels (bottom right).

Since KHC isoforms have been shown to form tetramers with different KLCs,[45,338] the regions involved in the interaction are likely to be conserved across isoforms. Conserved sequences predicted to form coiled coils within these regions were identified through *in silico* structural phylogenetic analysis (Fig. 5.2, Table 5.1). This analysis indicated four highly conserved contiguous heptad repeats, residues 777-804 in isoform KIF5C (Fig 5.2), as an island within more-divergent sequence. In agreement with previous analysis, this suggests that the KLC binding site is likely comprising residues Kif5C$^{777\text{-}804}$.[46]

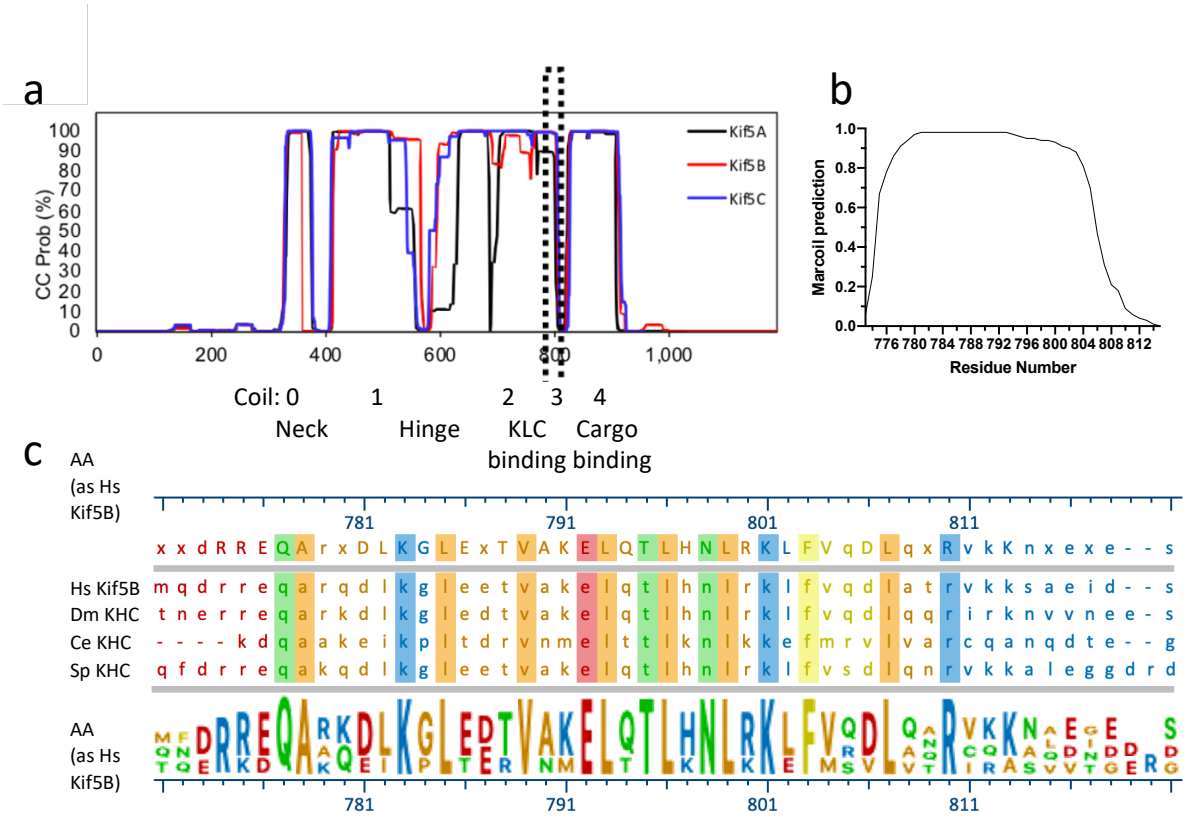

Fig. 5.2 | A conserved four-heptad-repeat region of KHCs is predicted to interact with KLCs in a coiled coil. a, Predictions of coiled-coil regions in human KHC isoforms Kif5A, Kif5B, and Kif5C using Marcoil.[248] This reveals the KLC binding site at the *C*-terminus of the coiled-coil region termed coil 3 in all three isoforms, annotated as described by Hackney.[47] **b**, Marcoil[248] prediction shows a short sequence of KIF5C comprising four conserved heptad repeats, residues 777-804, is predicted to form a coiled coil. **c**, Sequence alignment from *H. sapiens* (Hs), *D. melanogaster* (Dm, fly), *C. elegans* (Ce, worm) and *S. purpuratus* (Sp, sea urchin) of the KLC binding region on KHC with Weblogo.[339] These show an evolutionarily conserved 4-heptad repeat sequence an island within more-divergent sequences.

Table 5.1 | Sequence alignment of the KLC binding region of KHC

	abcdefg	*abcdefg*	*abcdefg*	*abcdefg*
Kif5A[773-800]	HEQSKQD	LKGLEET	VARELQT	LHNLRKL
Kif5B[775-802]	REQARQD	LKGLEET	VAKELQT	LHNLRKL
Kif5C[777-804]	REQARED	LKGLEET	VSRELQT	LHNLRKL
D. Melanogaster	REQARKD	LKGLEDT	VAKELQT	LHNLRKL
C. elegans	KDQAAKE	IKPLTDR	VMNELTT	LKNLKKE
S. Purpuratus	REQAKQD	LKGLEET	VAKELQT	LHNLRKL

Coiled coils most commonly form dimers, trimers and tetramers in nature, with control over oligomeric state and orientation largely directed by patterns of isoleucine (Ile, I) and leucine (Leu, L) in the core and salt bridges formed by adjacent residues.[340] Logicoil is a multi-state coiled-coil oligomeric-state predictor that enables the classification of antiparallel dimers, parallel dimers, trimers and tetramers.[341] Analysis with Logicoil predicted the most probable oligomeric state of Kif5C$^{777-804}$ to be trimer, with the second most probable state an antiparallel dimer (Table 5.2). It is well established that in the cell the KHCs assemble into a parallel homodimer, or in the presence of KLCs, a heterotetramer.[336] The Logicoil analysis therefore failed to predict the oligomeric state for this sequence in the full-length protein. This may suggest a flexibility within this region to accommodate multiple oligomeric states. Such structural promiscuity might be introduced by the leucine-rich core with relatively few beta-branched amino acids. This flexibility is likely important for motor assembly since this hypothesised model requires a shift in oligomeric state from a KHC homodimer to a heteroteramer upon interaction with the KLCs.

Table 5.2 | LOGICOIL oligomeric state prediction of Kif5C$^{777-804}$

Oligomer	Prediction score
Parallel dimer	0.86
Antiparallel dimer	1.01
Trimer	1.38
Tetramer	0.91

Intriguingly, inspection of the KHC coiled-coil sequences revealed a universally conserved polar glutamic acid (Glu, E) residue at the normally hydrophobic *d* position of the third heptad (Fig 5.3). Charged residues in this position are usually unfavoured due to repulsion in the hydrophobic core of the assembly. This residue is conserved across species suggesting the unusual placement may be important for protein function. The Glu residue identified in the core *d* position may also contribute to the structural flexibility by destabilising an ideal KHC dimeric interface to facilitate interaction with the KLCs in a heterotetrameric interface.

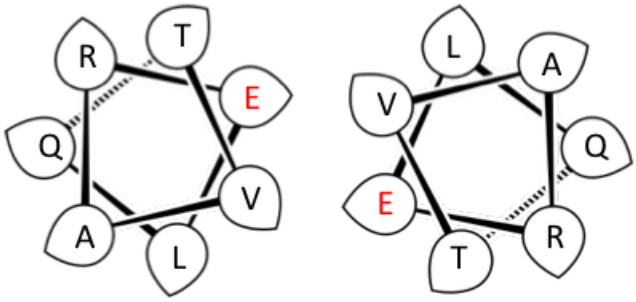

Fig. 5.3 | Register assignment reveals a conserved glutamic acid residue in the core of the KHC coiled coil. Helical wheel showing a conserved glutamic acid in the usually hydrophobic *d* position of the KHC heptad repeat.

5.3 A KHC peptide from the KLC binding site is unfolded at neutral pH

To probe the structure of the predicted coiled-coil region experimentally, the peptide Kif5C$^{777-804}$ was synthesised (Table 5.3). The synthesis, purification and characterisation proved challenging due to peptide aggregation. To improve solubility and reduce the formation of aggregates and larger assemblies, the sequence was flanked by glycine residues and *N*-terminally acetylated. To allow accurate measurement of concentration, a tyrosine residue was included in the sequence. Circular dichroism (CD) spectroscopy was used to determine the secondary structure of the peptide. In contrast to the modelling predictions, the peptide was unfolded at 100 μM in PBS, pH 7.4 (Fig 5.4). This peptide likely does not mimic the structure of this region of the natural protein since it encompasses only a short sequence of 28 residues: in the full-length Kif5C protein, this sequence is found within a long region of predicted coiled coil, termed coils 2 and 3, between residues 616-804 (Fig 5.2a). In the context of the whole protein, it may be that the helical structure is stabilised by the increased number of hydrophobic and electrostatic interactions in a longer coiled-coil region.

Table 5.3 | Sequences of KHC and KLC peptides characterised *in vitro*

	abcdefg abcdefg abcdefg abcdefg abcdefg abcde
Kif5C$^{777-804}$	G REQARED LKGLEET VSRELQT LHNLRKL YG
Kif5C$^{777-804\ E794L}$	G REQARED LKGLEET VSRLLQT LHNLRKL YG
KIF5B$^{767-805\ Q780Y}$	E LTVMQDR REQARYD LKGLEET VAKELQT LHNLRKL FVQ
KLC1$^{104-141\ C114A}$	G QKLRAQ VRRLAQE NQWLRDE LANTQQK LQKSEQS VAQLE G

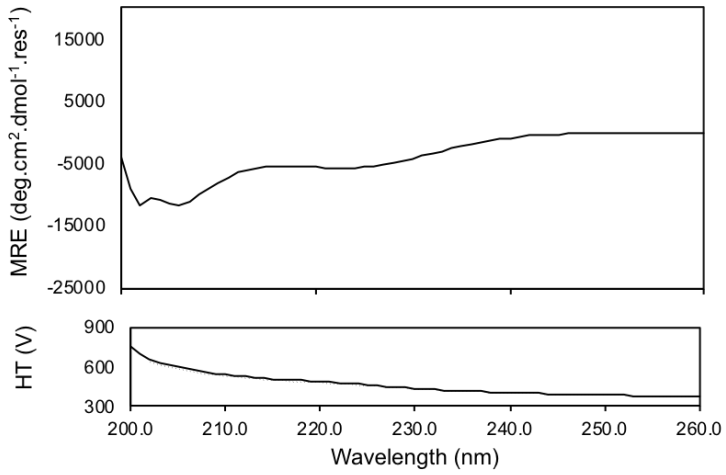

Fig. 5.4 | CD spectroscopy shows peptide Kif5C$^{777-804}$ is unfolded in solution. CD spectrum at 5 °C of 100 μM Kif5C$^{777-804}$ peptide in PBS, pH 7 recorded in a 1 mm cuvette shows the peptide is unfolded under these conditions.

5.4 A *de novo* coiled coil templates the KHC peptide into a dimer

To mimic the dimeric structure of coil-3 in a short peptide, a *de novo* designed homomeric dimer (CC-Di) was incorporated into the sequence. This sequence has been shown to assemble into a hyperstable, parallel, homodimer.[265] Peptides were designed with one, two or three heptads of the CC-Di sequence appended to the *N* terminus of KIF5C$^{777-804}$: CCDi^{1}-KIF5C$^{777-804}$, CCDi^{2}-KIF5C-$^{777-804}$ and CCDi^{3}-KIF5C$^{777-804}$ (Table 5.4). The aim was to template the coiled coil and, so, mimic the stabilising contribution of long-range interactions in the extended α-helical region of full-length KHC. Again, to improve solubility, the sequences were flanked by glycine residues and *N*-terminally acetylated, and in this case a tryptophan residue was included for concentration measurement. These peptides showed α-helical structures by CD spectroscopy with increasing length of the CC-Di component increasing the α helicity (Fig. 5.5). Whilst CCDi^{1}-KIF5C$^{777-804}$ was only 16% α helical, two heptads increased helicity to 56%, and incorporating a third heptad gave 70% helicity (Table 5.5). The increase in helicity of the peptide is greater than the increase in the proportion of the sequence comprising CC-Di residues, demonstrating that increased lengths of CC-Di increase helical folding of the natural sequence (Table 5.5). The oligomeric state of the most helical peptide, CCDi^{3}-KIF5C$^{777-804}$, was measured by sedimentation-equilibrium analytical ultracentrifugation (SE AUC) (Fig 5.5). As envisaged, given the template, this sequence formed a dimer.

Table 5.4 | Sequences of KIF5C$^{777-804}$ peptides templated with increasing lengths of a designed dimer CC-Di	
	abcdefg abcdefg abcdefg abcdefg abcdefg abcdefg abcdefg
CC-Di^{1}-KIF5C$^{777-804}$	GE IAALKQE REQARED LKGLEET VSRELQT LHNLRKL WG
CC-Di^{2}-KIF5C$^{777-804}$	GE NAALKQE IAALKQE REQARED LKGLEET VSRELQT LHNLRKL WG
CC-Di^{3}-KIF5C$^{777-804}$	GE IAALKQE NAALKQE IAALKQE REQARED LKGLEET VSRELQT LHNLRKL WG

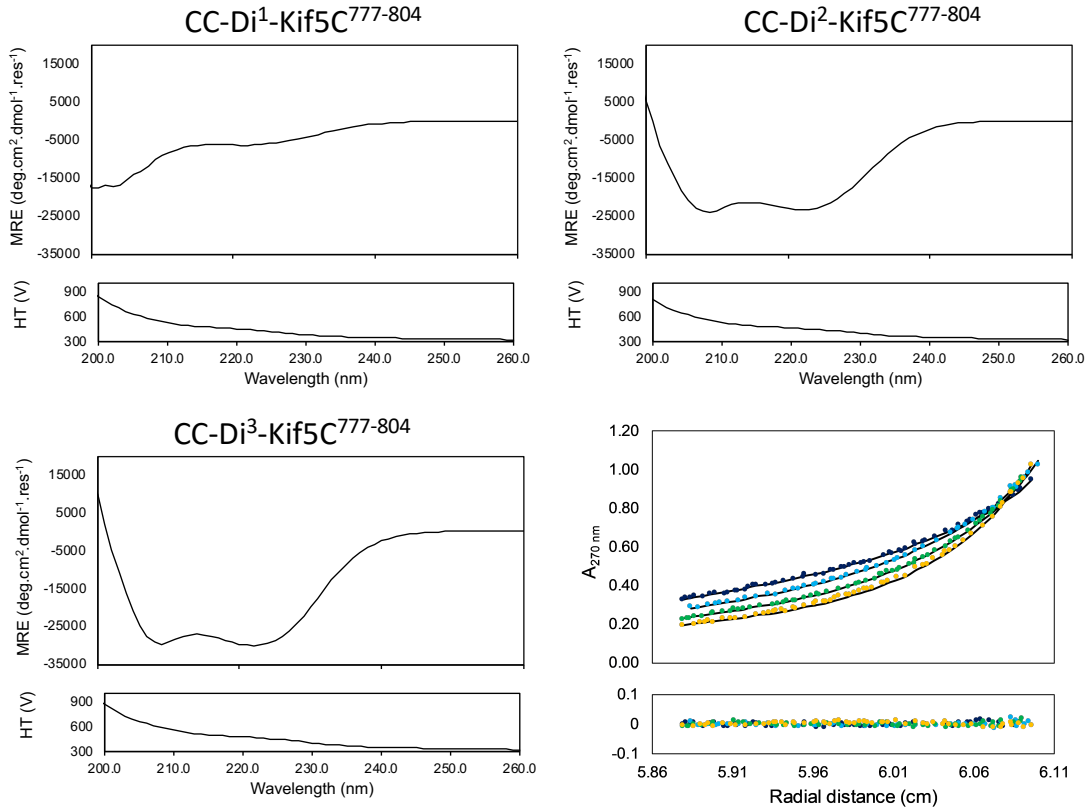

Fig. 5.5 | CD spectroscopy show that the α helicity of Kif5C$^{777-804}$ increases when templated with a *de novo* dimeric coiled coil. CD spectra at 20 ℃ of 100 μM CCDi^{1}-KIF5C$^{777-804}$ (top left), CCDi^{2}-KIF5C$^{777-804}$ (top right) and CCDi^{3}-KIF5C$^{777-804}$ (bottom left) peptide in PBS, pH 7 recorded in a 1 mm cuvette. Increasing length of designed dimer, CC-Di, increases α helicity of KIF5C$^{777-804}$. Sedimentation equilibria data (bottom right) of CCDi^{3}-KIF5C$^{777-804}$ (top, dots) and fitted single-ideal species model curve at 28k (dark blue), 32k (light blue), 36k (green) and 40k (orange) rpm. The fit returned a mass of 10,772 Da (1.8 × monomer mass, 95% confidence limits, 10,584 – 10,967). Bottom: residuals for the above fits using same colour scheme as above. Conditions: 100 μM peptide concentration, PBS (pH 7) at 20℃.

Table 5.5 | Helicity of KIF5C$^{777-804}$ peptides templated with *de novo* peptide CC-Di		
	Overall Percentage Helicity	Percentage of sequence from CC-Di
CC-Di^{1}-KIF5C$^{777-804}$	16.64	20.51
CC-Di^{2}-KIF5C$^{777-804}$	59.58	32.61
CC-Di^{3}-KIF5C$^{777-804}$	75.59	41.51

These experiments demonstrate that a short KHC peptide, encompassing the KLC-binding site, can been templated to fold into a dimeric coiled coil by appending increasing lengths of a designed coiled coil to the *N* terminus of the sequence, akin to that observed in the full length KHC protein. However, this peptide may not be useful in understanding the KHC-KLC interface. Helical read-through from CC-Di to the Kif5C sequence means that the peptide may be forced to form a structure with parameters matching those of the *de novo* CC-Di structure. This idealised dimeric interface is hyper-stable and is likely to lack the conformational flexibility accommodated in the natural sequence and required for a KHC homodimer to KHC-KLC heterotetramer transition.

5.5 Mutation of a core glutamate residue to leucine yields a tetrameric coiled coil

As an alternative strategy to a *de novo* template, mutations of natural sequences were used to stabilise secondary structure. In this sequence, the Glu residue in the core is likely to destabilise a coiled-coil structure.[342-344] Mutation of Glu to Leu, the canonical hydrophobic residue occupying the other *d* sites of the sequence, should stabilise the coiled coil by increased hydrophobic effect and decreased electrostatic repulsion in the core. A peptide was synthesised to incorporate this single-point mutation, KIF5C$^{777\text{-}804\ E794L}$ (Table 5.3). CD spectroscopy revealed a stable α-helical structure (Fig. 5.6). Oligomeric state determination by SE AUC gave a mass of 3.6 times monomer mass, suggesting a tetrameric structure (Fig 5.6).

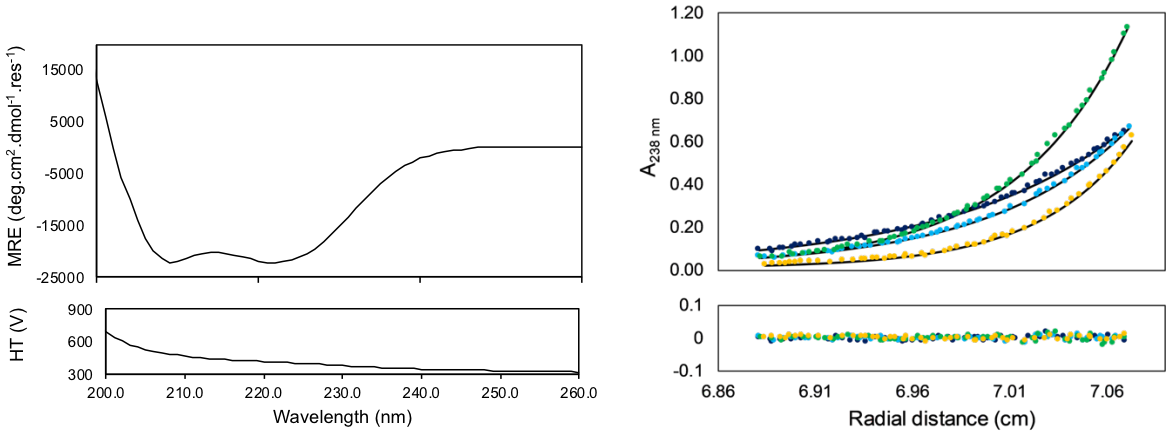

Fig. 5.6 | CD and SE AUC spectroscopy show KIF5C$^{777\text{-}804\ E794L}$ forms a tetrameric coiled coil in solution. a, CD spectrum at 5 ºC of 100 μM Kif5C$^{777\text{-}804\ E794L}$ peptide in PBS, pH 7, recorded in a 1 mm cuvette showed the peptide to be α helical under these conditions. **b,** sedimentation equilibrium data (top, dots) and fitted single-ideal species model curve at 32k (dark blue), 36k (light blue), 40k (green) and 44k (orange) rpm. The fit returned a mass of 13,113 Da (3.6 × monomer mass, 95% confidence limits, 12,995 – 13,230). Bottom: residuals for the above fits using same colour scheme as above. Conditions 100 mM peptide concentrations, PBS (pH 7) at 20℃.

This analysis demonstrates potential for this sequence to be accommodated in a tetrameric coiled-coil interface. As discussed above, in the full protein the longer sequence of coil-3, and the helical stalk in general, may direct a dimeric oligomeric state. In addition, dimerization of the KHCs is mediated through the neck-linker attached to the motor domains, shown also to interact with the tail inhibitory region. Thus, there are likely steric and other structural effects driving a dimeric assembly.

The mutation of this single Glu residue results in a complete change in structure of the short peptide KIF5C-E19L$^{777\text{-}804}$. This residue may play an important role in the protein. Whilst this is not anticipated to involve a transition from unfolded to homo-tetrameric coiled coil as observed here, the properties of this core Glu may be important for motor assembly and regulation. Experiments to test this hypothesis in cells are described in chapter 6.

5.6 The WT peptide folds into a coiled coil at reduced pH

In other systems, Glu residues in the core of coiled coils have been shown to induce pH dependent confirmational switches.[343,344] Since substitution of Glu for Leu stabilised coiled-coil formation, protonation of the Glu side chain could drive a similar transition through reduction of charge repulsion in the core. To test this, CD measurements of the KIF5C$^{777\text{-}804}$ peptide were repeated at pH 5.8 and 7.4 in a 50 mM sodium phosphate, 50 mM NaCl buffer (Fig 5.7). Again, the peptide was unfolded at pH 7.4. However, when the pH was reduced to 5.8 the peptide folded to give an α-helical CD spectrum (Fig. 5.7). This suggests that the Glu residue has a side chain pK_a shifted by 2 - 3 units from the free amino acid (pK_a 4.3). This new result shows that Glu at this ***d*** position is sufficient to drive the pH-dependent helical folding of a KHC peptide in the region that interacts directly with the KLC. The pH-dependent behaviour endowed by this residue may have larger-scale structural significance for the motor. Experiments to test this hypothesis in cells are described in chapter 6. It is notable that this sequence also contains a histidine residue. The imidazole side chain of histidine is unique in that that it can be protonated and deprotonated within physiologically relevant pH ranges. This allows it to act as both an acid and a base, a hydrogen bond donor or acceptor.[345] These versatile properties mean that histidine residues play important roles in pH-responsive functions and stability of many proteins.[346] However, in this case the histidine residue occupies a *b* position in the heptad register and is therefore is unlikely to be involved in the interface.

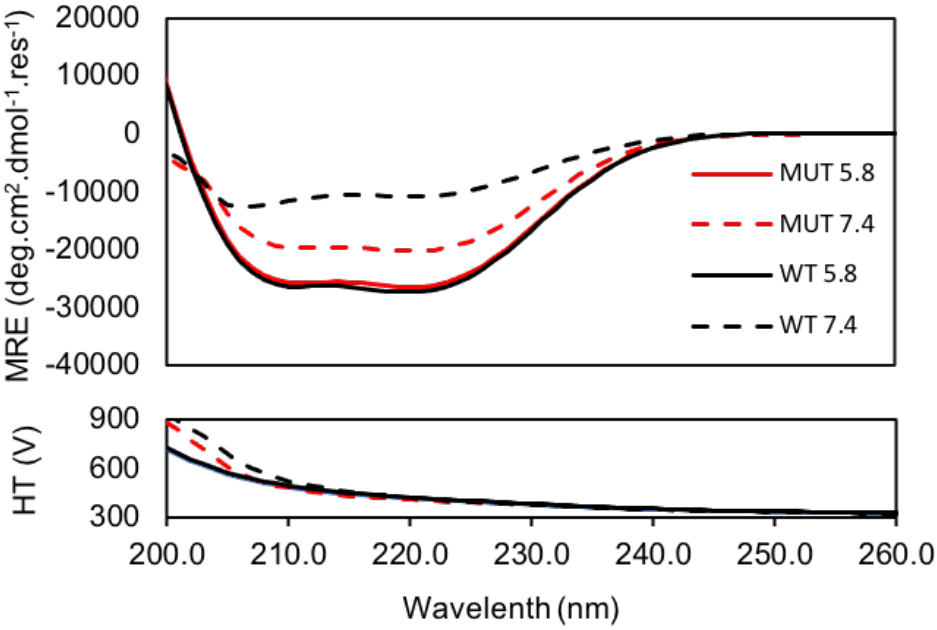

Fig. 5.7 | CD spectroscopy shows KIF5C$^{777\text{-}804}$ folds into an α helix at reduced pH. Left, CD spectra at 5 °C of 100 µM Kif5C$^{777\text{-}804}$ (WT) or Kif5C$^{777\text{-}804\ E794L}$ (MUT) peptide in sodium phosphate buffer (50 mM), NaCl (50 mM), pH 7.4 or 5.8, recorded in a 1 mm cuvette show the WT peptide is unfolded at pH 7.4 but folds into an α helix at pH 5.8. The MUT peptide is partially folded at pH 7.4 and the helicity is increased at pH 5.8.

5.7 X-ray crystallography reveals an antiparallel tetrameric structure

To probe the structure of the KHC region responsible for binding KLCs and to rationalise the pH dependence of the core Glu residue, attempts were made to solve the structure of this region. For this, a series of peptides from isoforms Kif5B and Kif5C were synthesised, encompassing the four conserved heptad repeats, of varying lengths and with different capping residues and chromophores. For peptide Kif5B$^{767\text{-}805\ Q780Y}$ (Table 5.3) crystals were obtained from initial sparce-matrix screening of crystallography conditions. This sequence extends the original 4 heptads with another 11 residues. The peptide was acetylated but not flanked with glycine residues, and it incorporated a tyrosine residue for concentration determination in place of alanine at an *f* position, which is not predicted to be involved in the coiled-coil interface. Crystals were obtained at pH 6.5 but not under any conditions at higher pH, which may support the hypothesis that a reduction in pH to protonate the Glu side chain is required to stabilise assembly.

A structure was solved by molecular replacement using a polyalanine α helix as a search model. Surprisingly and interestingly, this revealed an antiparallel tetrameric coiled coil (Fig. 5.8, Appendix Table 8.2). The tetramer is slipped and density of the terminal EL and ELTV residues are lost from two of the chains. The Glu side chains are in close proximity in the core and likely involved in hydrogen bonding interactions with a water molecule (Fig 5.9). Whilst there is no evidence that the KHCs form antiparallel tetramer in nature, this new structure of a fragment highlights the structural plasticity of the sequence. It is possible that KLC:KHC complexes could interact in a similar manner to form an antiparallel heterotetramer.

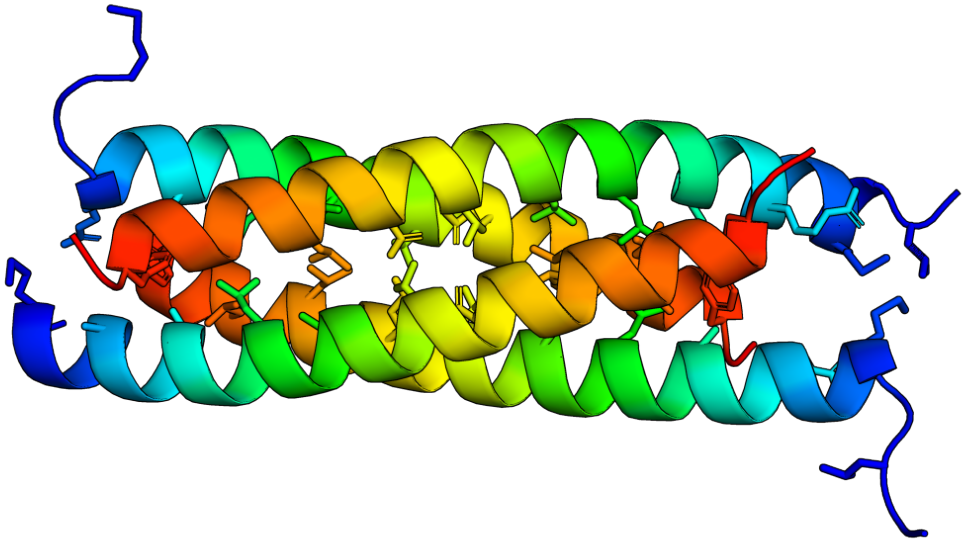

Fig. 5.8 | An X-ray crystal structure of Kif5B$^{767\text{-}805\ Q780Y}$reveals an antiparallel tetramer. Crystals were obtained under conditions of 0.2 M sodium iodide 0.1 M Bis Tris propane and 20 % w/v PEG 3350 at pH 6.5. The structure was solved by molecular replacement with a polyalanine α-helical search model. This reveals an antiparallel tetrameric coiled coil.

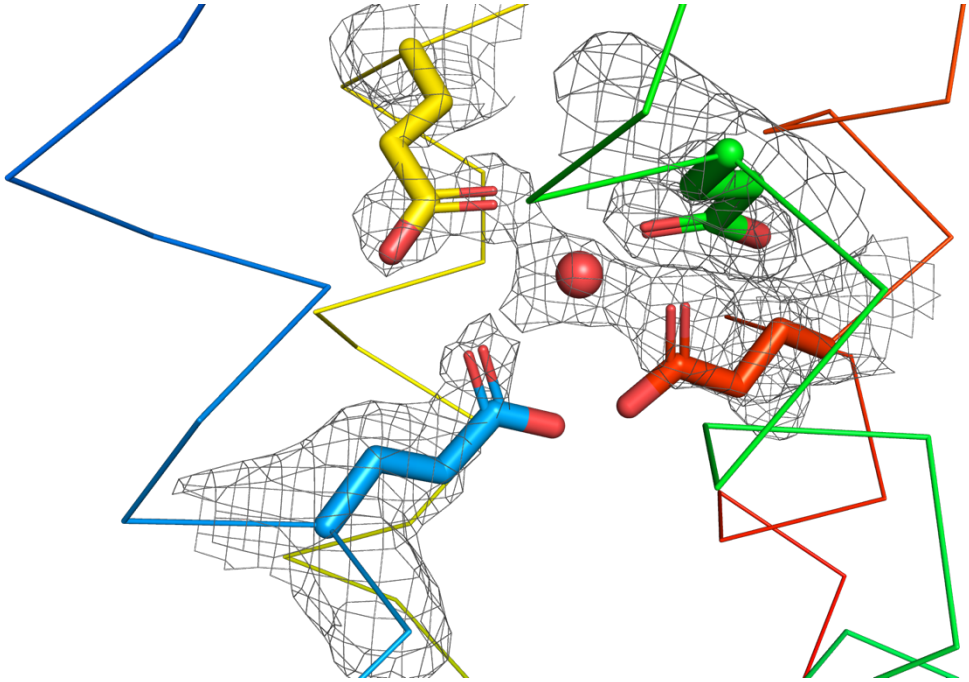

Fig. 5.9 | Electron density map of core Glu residues in Kif5B$^{767\text{-}805\ Q780Y}$. Four Glu residues in the core of the tetramer are in close proximity and likely forming hydrogen bonding interactions with a water molecule in the core.

For comparison, a parallel homodimeric model of this sequence was built and optimised using CCBuilder2.0.[239] This is likely to be a better model for this region of the KHCs in the absence of KLCs, since the motor domains are known to dimerise and bring together the coiled-coil regions in a parallel orientation (Fig. 5.10).[336]

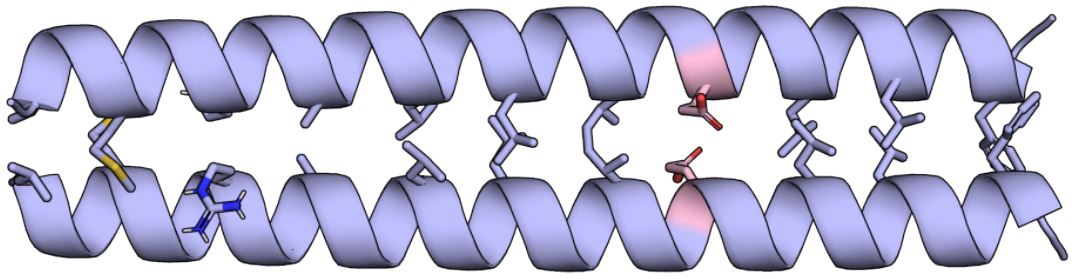

Fig. 5.10 | Model of the KHC homodimeric coiled coil. Parametric model of Kif5B$^{767\text{-}805\ Q780Y}$ built and optimised using CCBuilder2.0[239], a front-end GUI for ISAMBARD.[263] The core Glu residue is highlighted in pink.

The per-chain energy of this model was calculated in ISAMBARD[263] using the BUDE force field and compared to that of the antiparallel tetrameric structure obtained by crystallography (Fig 5.11). This reveals that a parallel dimeric assembly is predicted to be lower energy and therefore more favourable than the antiparallel tetramer. In the future it will be interesting to screen more constructs and conditions to investigate whether this predicted and anticipated homodimeric structure can be determined.

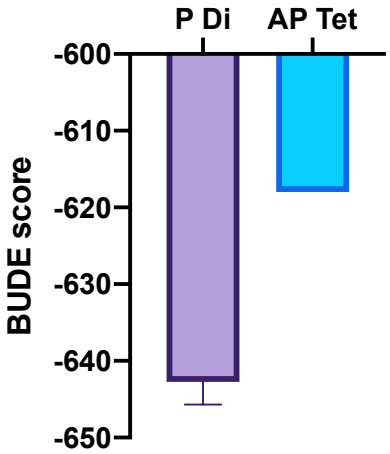

Fig. 5.11 | BUDE scoring of optimized models suggests a KHC parallel dimer is more favorable than an antiparallel tetramer. Per-chain BUDE scoring in ISAMBARD suggest a parametric model of a parallel Kif5B$^{767\text{-}805\ Q780Y}$ dimer is more favourable than the antiparallel tetrameric assembly observed in the crystal structure.

5.8 The KHC binding site of KLCs is predicted to form a conserved coiled coil

In comparison to the KHCs, less is known about the structure of the C-terminal, heptad repeat containing, region of the KLCs. The minimal region of KLC1 required for KHC binding has been described by Verhey *et al.* and Diefenbach *et al.* to involve residues 1-176 and 105-152 respectively. Again, *in silico* structural phylogenetic analysis was employed for human KLC isoforms 1-4 and identified a highly conserved, 9 heptad repeat, comprising residues 88-151 of KLC1 (Table 5.6). Analysis with MARCOIL and LOGICOIL software predicted this sequence to form a parallel dimeric coiled coil. (Fig. 5.12, Table 5.7).

Table 5.6 | Sequence alignment of the KHC binding region of KLC						
	abcdefg	*abcdefg*	*abcdefg*	*abcdefg*	*abcdefg*	*abcdefg*
KLC1[103-144]	KQKLRAQ	VRRLCQE	NQWLRDE	LANTQQK	LQKSEQS	VAQLEEE
KLC2[92-133]	KQKLRAQ	VRRLVQE	NQWLREE	LAGTQQK	LQRSEQA	VAQLEEE
KLC3[102-143]	KQRLRAQ	ARRLAQE	NTWLREE	LEETQRR	LRASEEA	VAQLEEE
KLC4[102-143]	KQRLRAQ	VRRLCQE	NQWLRDE	LAGTQQR	LQRSEQA	VAQLEEE

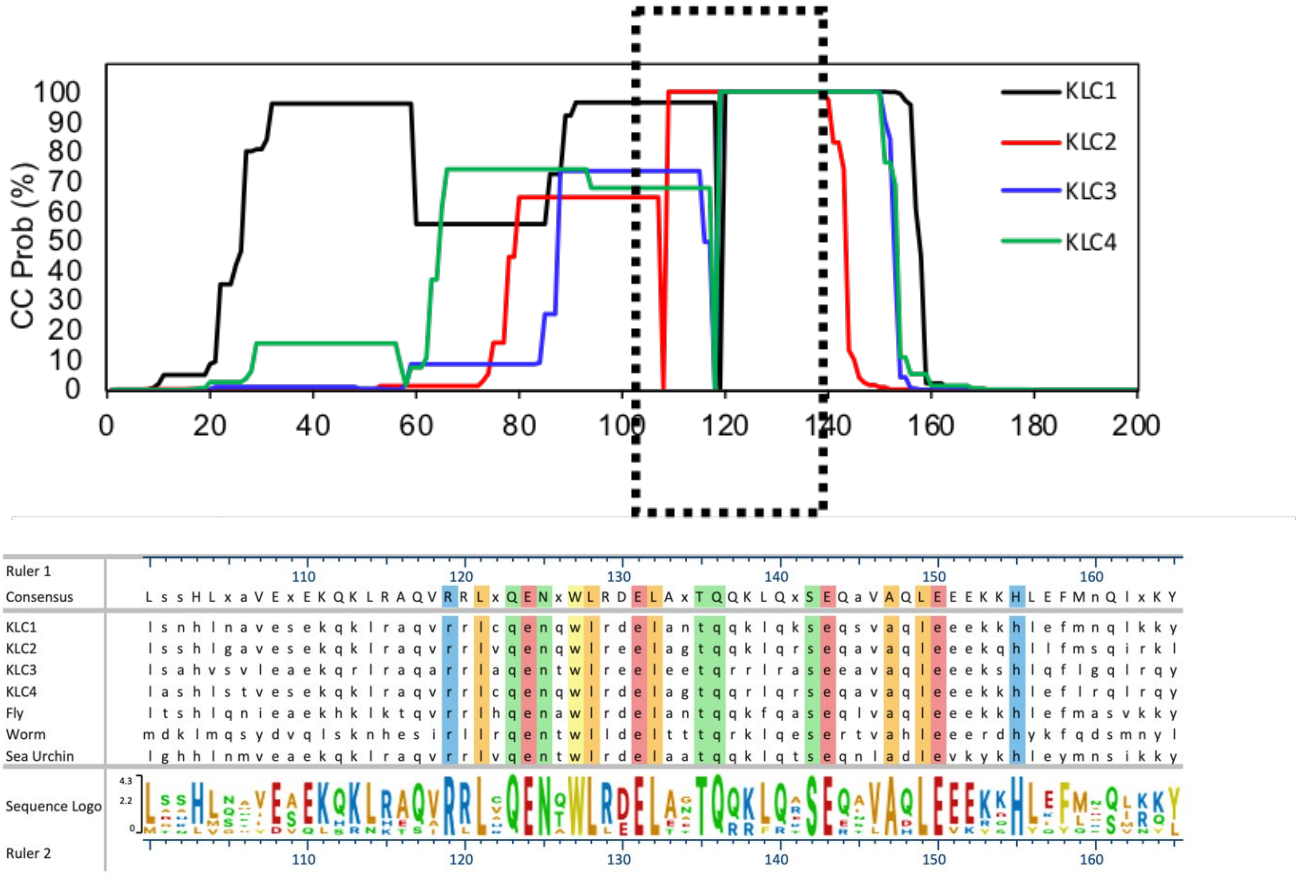

Fig. 5.12 | A conserved six-heptad-repeat region of KLCs is predicted to interact with KHCs in a coiled coil. top, Predictions of coiled-coil regions in human KLC isoforms KLC1-4 using Marcoil[248] show that the KLC binding site is within the C-terminal heptad repeating containing region. bottom, Sequence alignment from H. sapiens (KLC14), *D. melanogaster* (Dm, fly), *C. elegans* (Ce, worm) and *S. purpuratus* (Sp, sea urchin) of the KHC binding region on KLC using MegAlign[347] show an evolutionarily conserved six-heptad-repeat sequence an island within more-divergent sequence.

Table 5.7 | LOGICOIL oligomeric state prediction of KLC1$^{103-144}$	
Oligomer	Prediction score
Parallel dimer	1.66
Antiparallel dimer	0.80
Trimer	0.83
Tetramer	0.71

5.9 A KLC peptide from the KHC binding site forms a dimeric coiled coil in solution

A synthetic peptide comprising residues 104-141 of KLC1 was synthesised and characterised *in vitro* (Table 5.3). To improve solubility the sequence was flanked with glycine residues and the cysteine in position 114 mutated to alanine to prevent disulphide bond formation. Peptide KLC1$^{104-141\ C114A}$ was α helical by CD spectroscopy at 100 μM in PBS, pH 7 (Fig 5.12). Oligomeric state determination by SE AUC showed the peptide to be dimeric in solution (Fig 5.13). This is in agreement with the *in silico* predictions (Table 5.7).

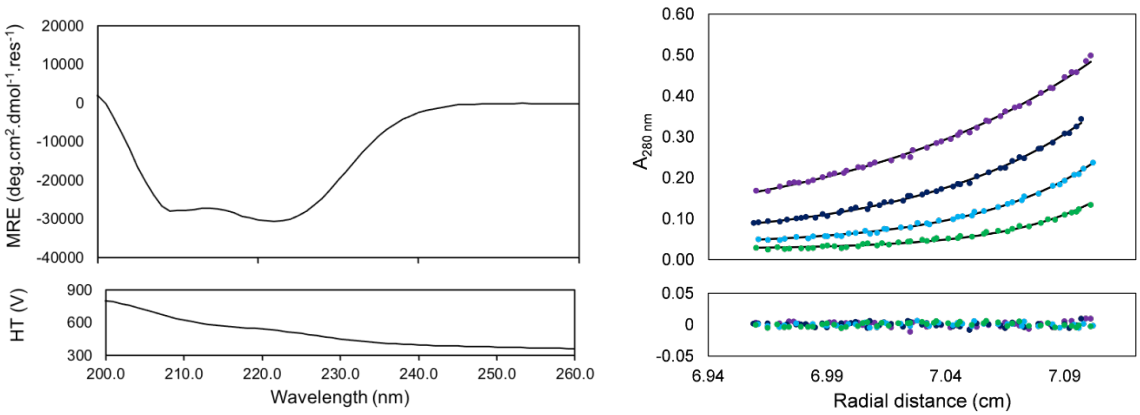

Fig. 5.13 | CD and SE AUC spectroscopy show KLC1$^{104-141\ C114A}$ forms a dimeric coiled coil in solution. Left, CD spectrum at 5 ºC of 100 μM KLC1$^{104-141\ C114A}$ peptide in PBS, pH 7, recorded in a 1mm cuvette shows the peptide is α-helical under these conditions. Right, sedimentation equilibria data (top, dots) and fitted single-ideal species model curve at 32k (green), 36k (light blue), 40k (dark blue) and 44k (purple) rpm. The fit returns a mass of 8368 Da (1.74 x monomer mass). Bottom: residuals for the above fits using same colour scheme as above. Conditions 100 mM peptide concentrations, PBS (pH 7) at 20 ℃.

5.10 Models show the KHC-KLC heterotetrameric complex could accommodate a parallel or antiparallel orientation

Having considered the KHC and KLC peptides from the interacting regions individually, the next investigations sought to investigate their assembly in the tetrameric complex. For this, models of the heterotetramer were built and optimised in ISAMBARD. These models explored

both a parallel and antiparallel orientation of helices. In addition, since the region of KLC1 identified was longer than that of Kif5B, the models explored different heptad interactions within these regions. (Table 5.8, Fig 5.14).

Table 5.8| Sequences of KHC and KLC used in modelling the heterotetrameric assembly

	abcdefg abcdefg abcdefg abcdefg abcdefg abcdefg
Kif5B$^{768\text{-}809}$	LTVMQDR REQARQD LKGLEET VAKELQT LHNLRKL FVQDLAT
1: KLC1$^{89\text{-}131}$	MMALSNH LNAVESE KQKLRAQ VRRLCQE NQWLRDE LANTQQK
2: KLC1$^{96\text{-}138}$	LNAVESE KQKLRAQ VRRLCQE NQWLRDE LANTQQK LQKSEQS
3: KLC1$^{103\text{-}145}$	KQKLRAQ VRRLCQE NQWLRDE LANTQQK LQKSEQS VAQLEEE
4: KLC1$^{110\text{-}152}$	VRRLCQE NQWLRDE LANTQQK LQKSEQS VAQLEEE KKHLEFM

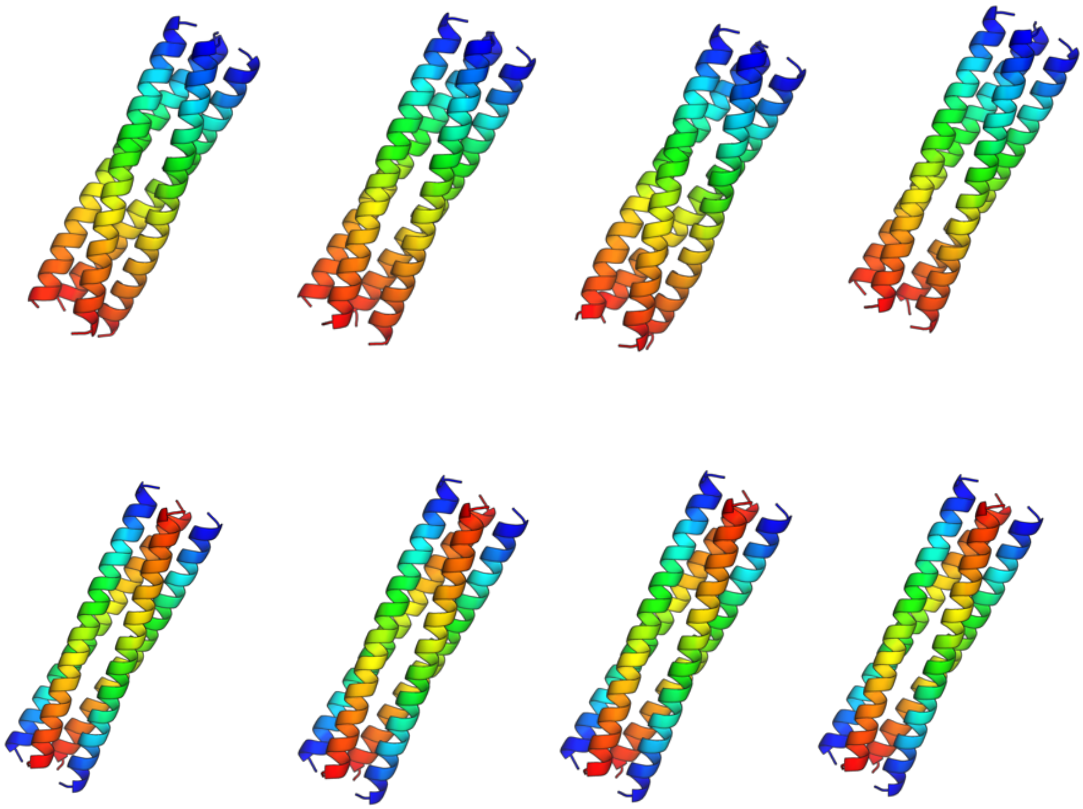

Fig. 5.14 | Models of the KHC-KLC heterotetrameric coiled coil. Parametric models of Kif5B$^{768\text{-}809}$ and six heptads from KLC1$^{89\text{-}152}$ (1-4 in table 5.8, left to right) in a parallel (top) or antiparallel (bottom) orientation, built and optimised in ISAMBARD.[263] The structures were optimised using a genetic algorithm and ranked according to their fitness score.

The per-chain energy of these models was calculated in ISAMBARD using the BUDE force field (Fig 5.15). These results suggest that an antiparallel conformation between the KHCs and KLCs may be favoured. The scores also suggest that these heteromeric KHC-KLC assemblies

are lower in energy than the KHC homodimeric and homotetrameric structures, which may be the driving force for assembly of the tetrameric motor.

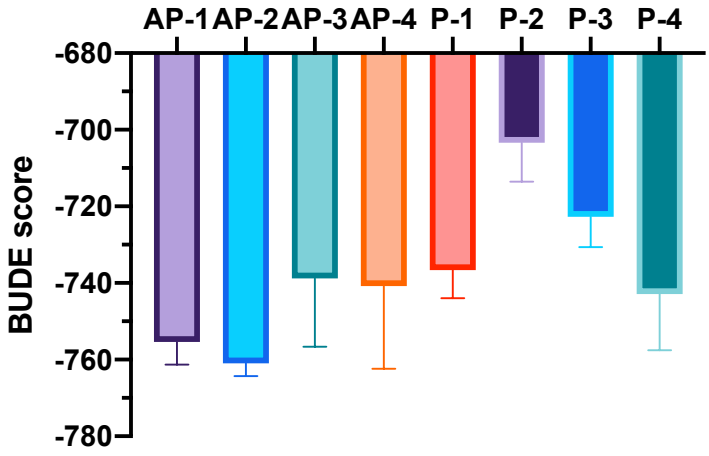

Fig. 5.15 | BUDE scoring of optimized models suggests an antiparallel (AP) KHC-KLC tetramer is favored over a parallel (P) orientation. Per-chain BUDE scoring in ISAMBARD suggest an antiparallel heterotetramer is more favourable than a parallel orientation.

5.11 Short synthetic KHC and KLC peptides do not interact in vitro

Next, synthetic peptides from these regions were mixed *in vitro* and monitored for changes in biophysical properties. For these experiments, peptides Kif5B$^{767\text{-}805\ Q780Y}$ and KLC1$^{104\text{-}141\ C114A}$ were mixed at a concentration of 50 μM of each peptide in PBS, pH 7 and characterised by CD spectroscopy. The spectrum observed for the mixture closely matched the average of the spectra of the two individual peptides, suggesting no interaction between the peptides (Fig 5.16). The addition of α-helical KLC1$^{104\text{-}141\ C114A}$ did not result in folding of the unfolded Kif5B$^{767\text{-}805\ Q780Y}$ peptide as would be expected if the sequences had assembled into a heterotetrameric coiled coil. This analysis was repeated at pH 5.8 to explore whether an interaction would be observed with the folded Kif5B$^{767\text{-}805\ Q780Y}$ peptide at reduced pH. Again, the spectrum observed for the mixture closely matched the average of the spectra of the two individual peptides, suggesting no interaction.

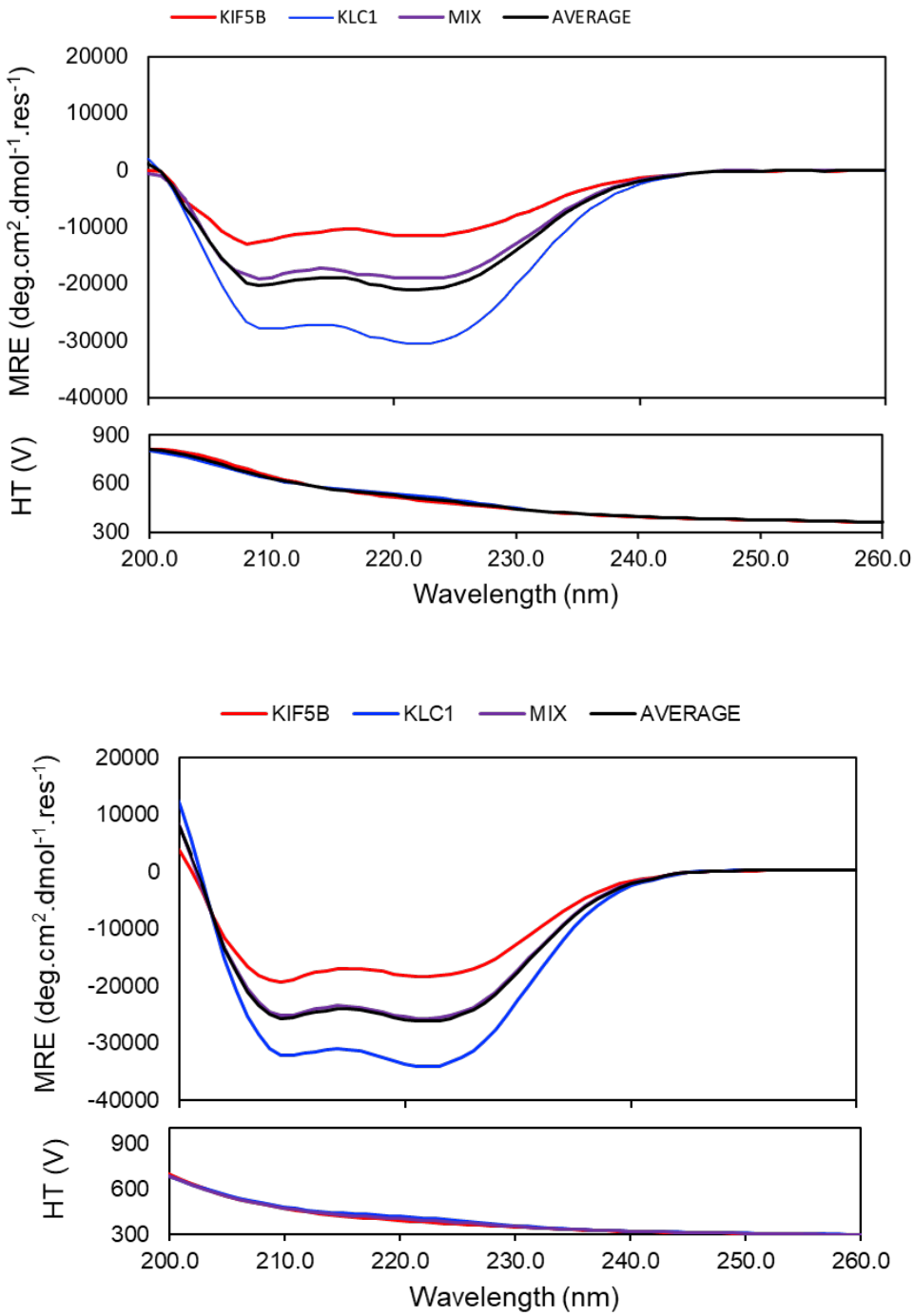

Fig. 5.16 | CD spectroscopy shows peptides Kif5B$^{767\text{-}805\ Q780Y}$ and KLC1$^{104\text{-}141\ C114A}$ do not interact *in vitro*. CD spectra at 5 °C of 100 µM Kif5B$^{767\text{-}805\ Q780Y}$ (red), KLC1$^{104\text{-}141\ C114A}$ (blue), 50 µM of each peptide (purple) and the average of the two individual spectra (black) in sodium phosphate buffer (50 mM), NaCl (50 mM), pH 7.4 (top) or 5.8 (bottom) recorded in a 1 mm cuvette. The spectrum from the mixture closely resembles the average suggesting there is no interaction between the two peptides.

To investigate whether the peptides could anneal to form a tetramer, the mixture was heated from 5 to 95 °C and cooled back to 5 °C. α Helicity was monitored by the CD signal at 222 nm

(Fig 5.17). The mixture showed thermal unfolding but no changes as a result of annealing were observed. These results suggest that the selected peptides are too short to interact *in vitro* and that new constructs will be required for tetramer assembly.

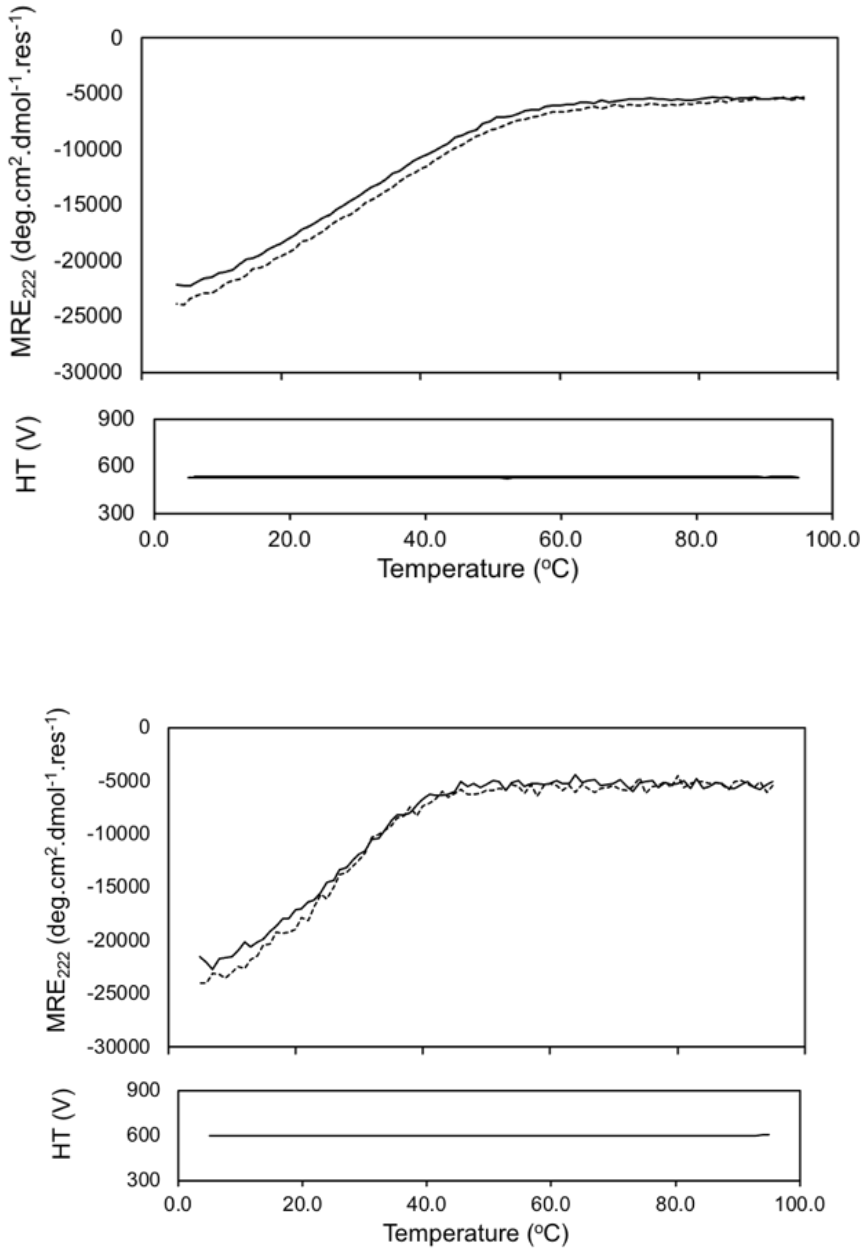

Fig. 5.17 | Variable temperature CD spectroscopy shows peptides Kif5B$^{767\text{-}805\ Q780Y}$ and KLC1$^{104\text{-}141\ C114A}$ do not interact *in vitro*. CD spectra showing signal at 222 nm of a mixture of 50 μM Kif5B$^{767\text{-}805\ Q780Y}$ and 50 μM KLC1$^{104\text{-}141\ C114A}$ whilst heating (solid line) and cooling (dashed line) between 5 and 95°C in sodium phosphate buffer (50 mM), NaCl (50 mM), at pH 7.4 (top) and pH 5.8 (bottom) recorded in a 1 mm cuvette. The heating profile closely resembles the cooling, suggesting that the two peptides do not anneal.

Since short, synthetic peptides from these regions did not interact *in vitro*, it was hypothesised that longer sequences incorporating more of the natural interactions from the full-length proteins would be required to yield a tetramer. Attempts to synthesise and purify longer peptides from Kif5B and KLC1 proved unsuccessful by solid phase peptide synthesis and high-performance liquid chromatography. In the future, further attempts may involve synthesis of these sequences in two fragments followed by native chemical ligation. An alternative strategy involved cloning constructs to allow recombinant protein expression of longer sections of Kif5B and KLC1 in *E. coli*. To date, it has proved challenging to express soluble and stable proteins. In the future these constructs and expression conditions will be optimised. This may involve co-expression of the proteins using a Duet vector system (Novagen).[348]

Interesting, recently released models of KLC1 from the AlphaFold Protein Structure Database predict an extended helix between residues 60-159.[300] In addition, this is shown to interact with a second, shorter, helix between residues 21-55. This can be modelled as a homodimer, showing interactions throughout these regions (Fig 5.18). In the future, it may be worthwhile to attempt expression of a KLC1 protein comprising residues 21-159 since, if this model is accurate, these additional interactions may stabilise the structure.

Fig. 5.18 | Alphafold predicts interacting helices between KLC1 residues 21-159. Models a of $KLC1^{21\text{-}159}$ homodimer built using Alphafold show an extended helical region which may guide design of a longer, more stable, construct in the future.

5.12 KHC and KLC proteins fused to a *de novo* dimeric coiled coil are partially helical and do not interact *in vitro*

Since the Kif5B$^{767\text{-}805\ Q780Y}$ peptide was unfolded, the energetic cost of tetramerization is increased as the peptide must fold into an α helix before oligomerisation. Presumably, in the KHC protein, this sequence is part of a longer helical structure and this energetic requirement is lowered. To investigate this, similarly to the approach described in 5.4, a construct was designed to allow recombinant expression of a *de novo* designed coiled-coil dimer (CC-Di) fused to Kif5B$^{767\text{-}805}$. In this case four heptads of the CC-Di sequence were incorporated to allow assembly of a stable dimeric coiled coil. This aimed to template the KHC sequence into a dimer, mimicking the structure of this region in the full-length protein. To avoid the sequence being forced into a structure with parameters defined by the CC-Di design, and thus lacking the flexibility required for KHC-KLC tetramerization, a flexible linker of 5 glycine residues was introduced between the two sequences. The same approach was taken for KLC1, incorporating residues 88-151. Since the sequence is less well-characterised, this longer region of KLC1 was chosen to maximise the likelihood of including the binding site.

CC-Di-G_5-Kif5B$^{767\text{-}805}$ and CC-Di-G_5-KLC1$^{88\text{-}151}$ were expressed in *E. coli* as *N*-terminally His_6-tagged proteins and purified by Ni^{2+}-affinity chromatography followed by size exclusion chromatography (SEC). Challenges were encountered in expression, purification and solubility of these proteins. Following optimisation, the structure of these proteins was investigated by CD spectroscopy at 5 μM in a buffer of 50 mM sodium phosphate, 50 mM NaCl, pH 7.4 (Fig 5.18). Both proteins gave spectra consistent with a partially folded α-helical structure. Consistent with the peptides, CC-Di-G_5-KLC1$^{88\text{-}151}$was more folded than CC-Di-G_5-Kif5B$^{767\text{-}805}$. Whilst every effort was made to accurately determine the concentrations of these proteins, the instability and rapid precipitation of the samples likely rendered these imprecise. Calculation of percentage helicity of the constructs without accurate concentration measurements was not worthwhile. When mixed together these proteins gave a CD spectrum that deviated from the average of the spectra of the two individual proteins (Fig 5.19). This suggests that the two proteins may be interacting and thus increasing helicity of the complex.

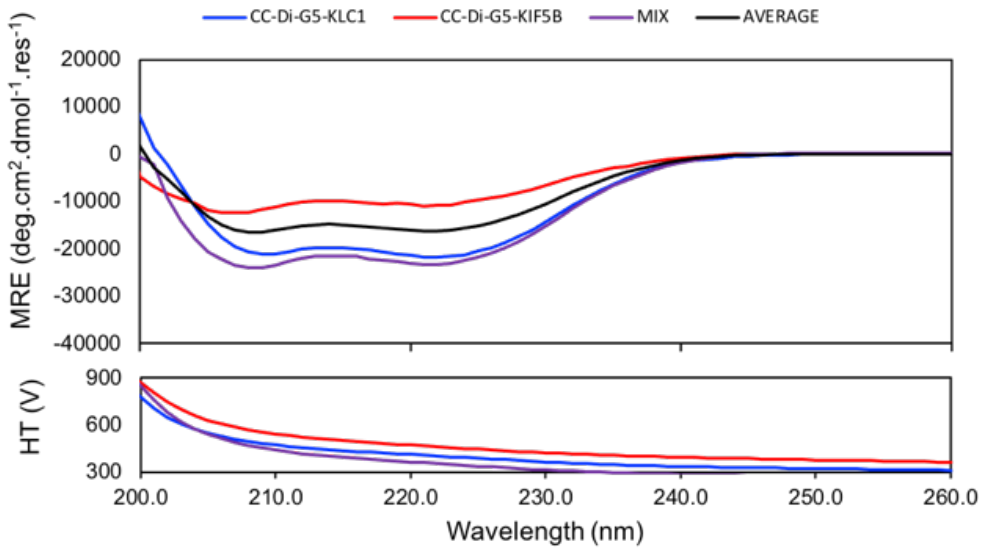

Fig. 5.19 | CD spectroscopy shows proteins CC-Di-G$_5$-Kif5B$^{767-805}$ and CC-Di-G$_5$-KLC1$^{88-151}$ do not interact *in vitro*. CD spectra at 5 °C of 5 μM CC-Di-G$_5$-Kif5B$^{767-805}$ (red), 5 μM CC-Di-G$_5$-KLC1$^{88-151}$ (blue), 2.5 μM of each peptide (purple) and the average of the two individual spectra (black) in sodium phosphate buffer (50 mM), NaCl (50 mM), pH 7.4 recorded in a 5 mm cuvette. The spectrum from the mixture deviates from the average suggesting there may be an interaction between the two proteins.

The proteins were annealed by heating to 95 °C followed by cooling to 5 °C. The α helicity showed a thermal unfolding and refolding profile that deviated from that of the average of the two individual proteins (Fig 5.20). This may suggest an interaction, with the proteins assembling into a different structure after heating. The challenges around protein stability and aggregation make it difficult to draw conclusions from these results.

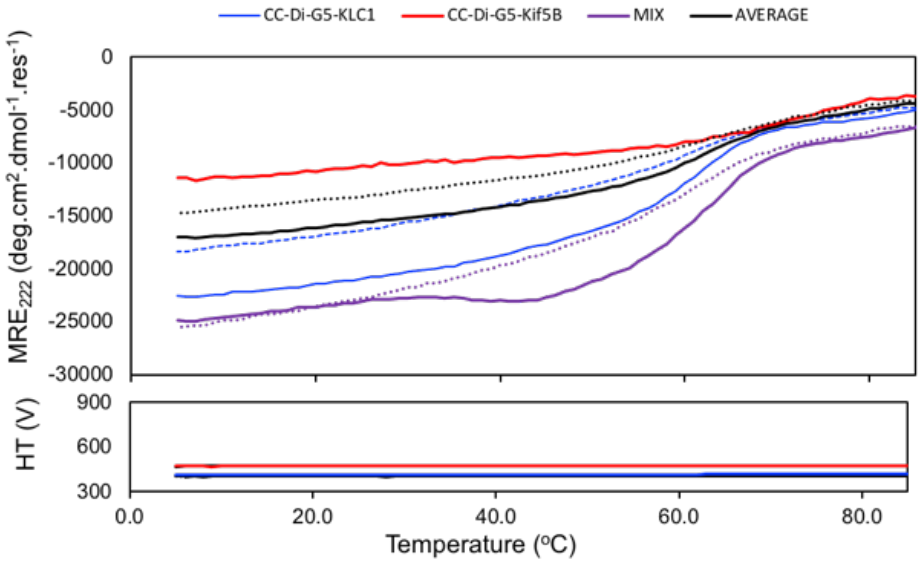

Fig. 5.20 | Variable temperature CD spectroscopy of proteins CC-Di-G_5-Kif5B$^{767-805}$ and CC-Di-G_5-KLC1$^{88-151}$. CD spectra showing signal at 222 nm of 5 μM CC-Di-G_5-Kif5B$^{767-805}$ (red), 5 μM CC-Di-G_5-KLC1$^{88-151}$ (blue), 2.5 μM of each peptide (purple) 2 and the average of the two individual spectra (black) whilst heating (solid line) and cooling (dashed line) between 5 and 95°C in sodium phosphate buffer (50 mM), NaCl (50 mM), pH 7.4 recorded in a 1 mm cuvette. The profile of the mixture deviates from the average suggesting there may be some interaction between the proteins.

5.13 Conclusions

KLCs play an important role in cargo recognition by kinesin-1 through both protein-protein and protein-lipid interactions.[67,69] Tetramerization of the KLCs and KHCs couple these cargo binding domains to the motor activity of the KHCs.[46] It has become clear during this investigation that structurally characterising the KHC and KLC sequences involved in the tetrameric interface is both a challenging and worthwhile goal. Whilst structural data are available for other regions of the proteins, to date there are none for these regions, leaving the nature of the interaction an unsolved puzzle. This work has continued to map the regions of the proteins involved in the interface and begun to characterise these *in silico* and *in vitro*. Work in the Dodding and Woolfson labs will continue to tackle this challenge.

The initial results suggest that the KLC binding site on KHC comprises leucine rich heptad repeats which demonstrate structural plasticity, able to accommodate multiple oligomeric states. This is presumably important to facilitate the transition between a KHC homodimer and the heterotetrametric KHC-KLC assembly. Modelling predictions suggest that an antiparallel

KHC-KLC orientation may be energetically favoured, in contrast to the usually depicted parallel cartoon representation of the tetrameric motor. Going forward, to solve structures of this interface and test this hypothesis, it will be important to identify a KHC sequence that assembles into a homodimer in solution, to display the same KLC binding site observed within coil 3 of the full-length protein. This may require longer constructs, likely through recombinant protein expression. To do this, an immunoprecipitation approach could be employed to finely map the interaction interface and determine the minimal regions required for the characterisation of stable protein constructs. A Duet expression system would allow co-expression of the KHC and KLC proteins, which may facilitate tetramer assembly.[348]

Within the KHC coiled coil responsible for binding KLCs there is a conserved Glu residue in the core of the assembly. This residue has been shown to confer pH-responsive behaviour to the sequence, with a 4-heptad peptide from this region unfolded at pH 7.4 and α helical at pH 5.8. Substitution of Glu for the canonical hydrophobic residue at the other ***d*** sites, Leu, results in a stable α-helical structure at both pH values. These new data show that Glu at this ***d*** position is sufficient to drive the pH-dependent helical folding of the region in KHC that interacts directly with the KLCs. In the future it will be interesting to examine further the pH-dependent metastability of these interacting coiled-coil peptides by mutation of charged residues at the interface and analysis of structural changes. pH titrations will be used to determine the pK_a of the acidic Glu residue in the ***d*** position of the KHC coiled coil. In addition, this residue will be mutated to other ionisable side chains—*e.g.*, D, Q, H, R, K—and changes in pH sensitivity, folding, stability and oligomeric state monitored. For example, aspartate (Asp, D), with a lower pK_a, may require larger pH reduction for helical folding. Finally, studies will seek to identify complementary, basic residues in the KLC sequence, which could form stabilising salt bridges with KHC acidic residues at the interface. It will be important to translate this understanding obtained *in vitro* to make mutations in full-length proteins in cells, this is discussed further in chapter 6.

This work begins to present the KHC coiled coils as a dynamic platform for protein-protein interactions, showing structural plasticity and pH-responsive behaviour. In addition to mediating cargo-binding through assembly with the KLCs, KHCs have also been shown to interact directly with cargo. A recent study from Dimitrova-Paternoga *et al.* reveals that an mRNA cargo adaptor, atypical tropomyosin (aTm1), interacts with KHC at a site immediately downstream of the KLC binding site (Fig. 5.21).[91] aTm1 is important for oskar mRNA

localization to the posterior pole of the *Drosophila* oocyte. This interaction is through an antiparallel trimeric coiled coil, in which one helix of aTm1 binds in an antiparallel orientation to a parallel KHC homodimer (Fig. 5.21c). When not bound to KHCs, aTm1 forms an antiparallel homodimer. Upon interaction of KHC-aTm1, a positively charged expanded binding surface is revealed and interacts with RNA. This region of KHCs is also important for other cargo binding, including SKIP and Sunday driver and the ATP independent microtubule binding site for microtubule-microtubule sliding.[28,87,116] This study presents the first structural characterization of a direct cargo adaptor–KHC interface. To accommodate the aTm1 helix in the trimeric coiled coil, the KHC homodimer must open, suggesting conformational flexibility at the interface (Fig. 5.21b)..[349] Interestingly, recent Alphafold predictions of this region of KHC show a mixture of folded and unfolded structures and a structure of the KHC homodimer without aTm1 was not obtained.[300] This could suggest that the aTm1 helix is required to template folding of the coiled coil.

The structure of the KHC-aTm1 assembly shows promise for future work in determining the structure of the adjacent KHC region in complex with KLCs. In this case, stable protein structures were obtained by recombinant protein expression for crystallography. Future work will seek to understand how these shifts in oligomeric state, in both trimer and tetramer, are linked to larger scale conformational changes in the motor, in a transition from an autoinhibited to active form. In addition, it will be interesting to investigate whether KHC can simultaneously bind aTm1 in a heterotrimer and KLC1 in a heterotetramer. Finally, work will seek to explore whether similar modes of binding extend to other adaptors/microtubule interactions.

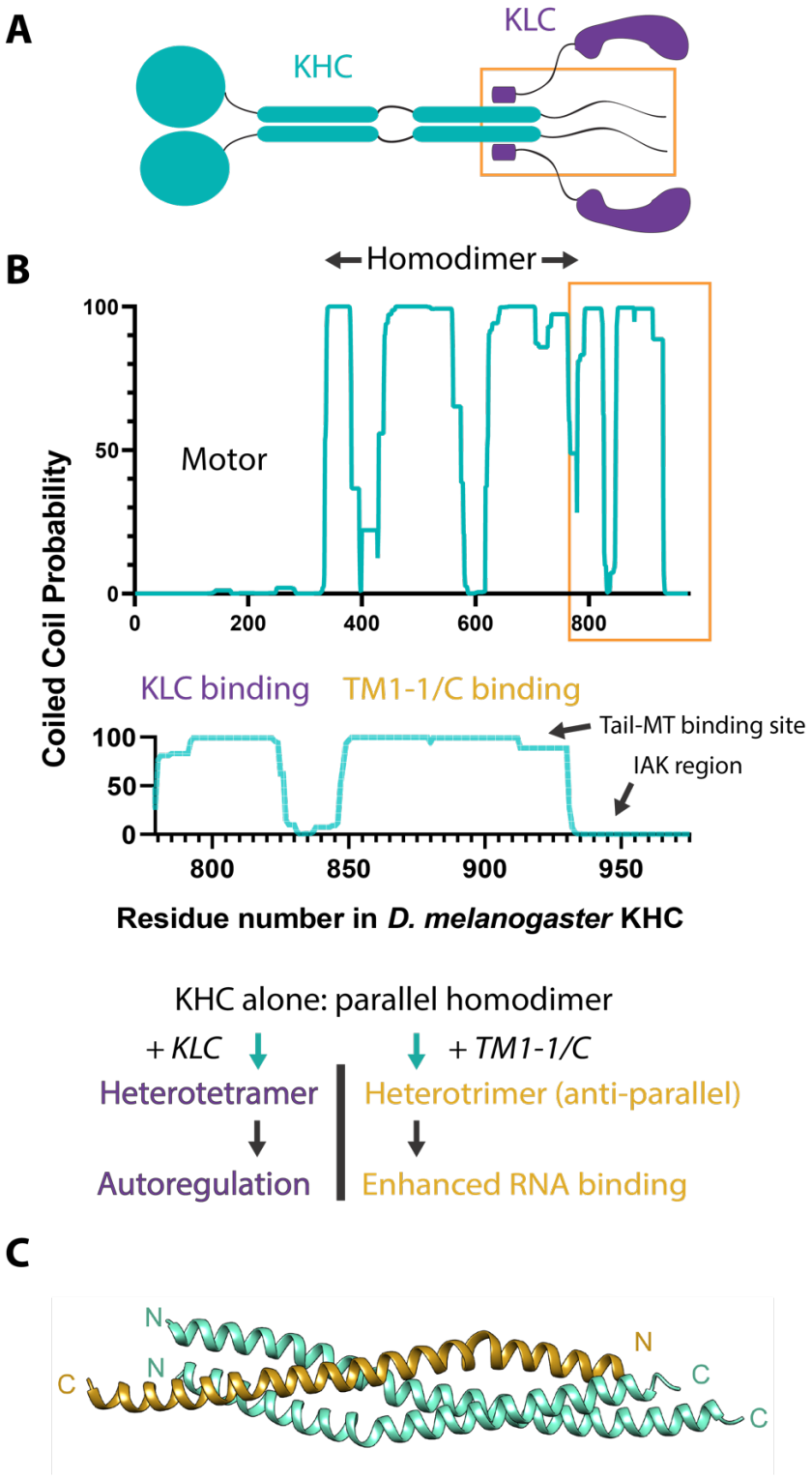

Fig. 5.21 | Structural and functional plasticity of the KHC coiled coils.[349] **a,** Schematic of the kinesin-1 heterotetramer. KHC is in cyan, KLC in purple. Orange boxed region highlights the KHC tail. **b**, Marcoil coiled-coil prediction for KHC, tail region is boxed orange (top). Detailed coiled coil prediction for the KHC tail that contains the binding sites for KLC and Tm1-I/C (middle). Potential structural plasticity and associated function in the KHC coils (bottom). **c,** Crystal structure of the KHC-KHC-Tm1-I/C complex (PDB:7BJS) from Dimitrova-paternoga et al. KHCs are cyan, Tm1-I/C is brown.

6 Exploring a role for pH-sensitivity in kinesin-1 autoinhibition

6.1 Background

Kinesin-1 is regulated through interactions of autoinhibitory motifs within the complex. These hold the motor in an inactive conformation, which prevents unnecessary cycles of ATP hydrolysis when the molecule is not involved in transport.[57,59,79-81] Regulation of the kinesin heavy chains (KHCs) has been mapped to a highly conserved Isoleucine-Alanine-Lysine (IAK) motif of a single KHC tail, which binds to the *N*-terminal motor dimer interface (Chapter 1, Fig 1.6). This cross-links the two motor domains, resulting in a 'double lockdown' mechanism where the domains are held together at the interfaces of the neck coiled coil and motor-tail. This results in highly restricted movement, preventing stable association with microtubules and ADP release, which is thought to require conformational flexibility for undocking of the neck linker.[57,79-81] In addition, autoinhibition of the kinesin light chains (KLCs) is associated with a conserved Leucine-Phenylalanine-Proline motif (LFP), which binds to the TPR domain, occluding the cargo binding site (Chapter 1, Fig 1.3).[59] Whilst it is not clear how the transition from an autoinhibited to active state is regulated, this has been linked to changes in pH, with acidification shown to modulate kinesin-1 autoinhibition *in vitro*.[83,84] Verhey *et al.* show that in the presence of KLCs, KHCs bind to microtubules at acidified pH (<6.8) but not at physiological pH (>7.4). In the absence of KLCs, KHCs bind to microtubules at all pH values. This suggests that kinesin-1 microtubule association is pH sensitive and regulated by the KLC-KHC interaction in some way, requiring the *N*-terminal coiled-coil region of KLCs for autoinhibition.[83] Similarly, Wong and Rice show that binding of the KHC-tail to microtubules is enhanced at reduced pH (6.6) in a KLC-dependent manner.[84]

Interestingly, the position of lysosomes, a kinesin-1 cargo, has also been shown to be sensitive to changes in pH. Cytoplasmic acidification has been shown to increase dispersal of lysosomes to the cell periphery, while moving to alkaline pH returns them to the perinuclear region.[285,350,351] These changes have been shown to be microtubule and kinesin-1 dependent.[110,352] Lysosome positioning has also been correlated with internal (lumenal) lysosomal pH, with more peripheral lysosomes being less acidic.[353] Increased kinesin-1 dependent lysosomal transport, achieved by transfection of Arl8 (a GTPase on the lysosomal surface that binds to kinesin-1 through its effector SKIP[110,354]), increases the proportion of lysosomes at the cell periphery and is associated with an increase in lysosomal pH and

increased rates of proton leakage from lysosomes.[355] The correlative and causative facets of the latter proposition are not clear.

This connection between lysosome transport, kinesin-1 activation and pH has been clear for many years.[110] However, this has been approached largely independently by the motor-protein and membrane-trafficking fields, and is yet to be integrated into a coherent mechanistic model. This chapter investigates the roles of pH acidification and cargo binding, in the release of kinesin-1 autoinhibition and thus activation of kinesin-1 activity. This is investigated alongside a new observation of the pH dependence of microtubule-microtubule sliding, which is a second function of kinesin-1 in regulating the organisation of the microtubule network. A new model of kinesin-1 regulation is developed, in which release of key autoinhibitory motifs acts in parallel with changes in local or global pH for activation of motor function. Our initial results highlight key residues conferring pH dependence to the complex, offer mechanistic insight into this mode of activation, and lead to the proposition that kinesin-1 is both a pH sensor and pH responsive transport effector.

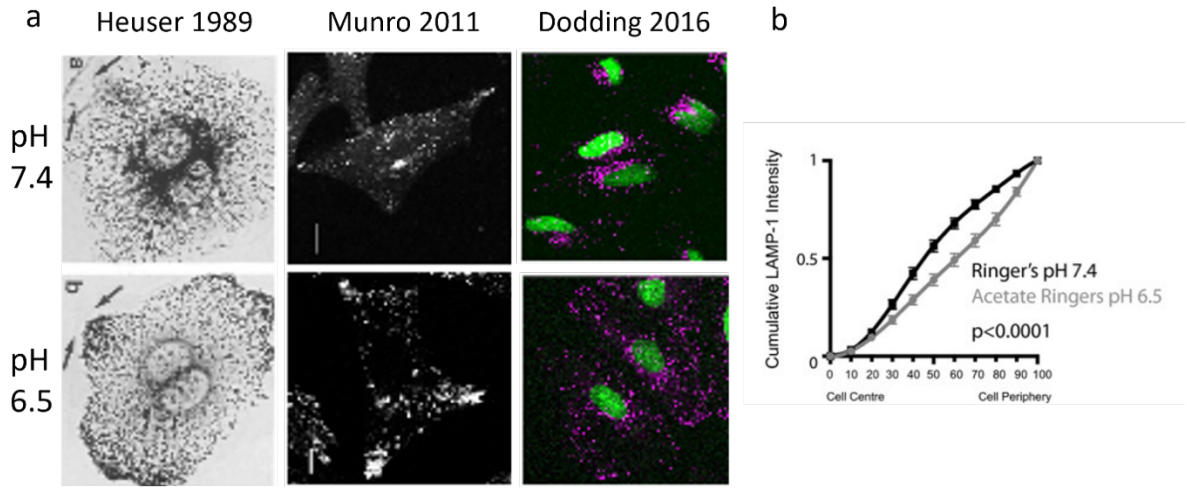

Fig. 6.1 | Lysosome positioning is sensitive to changes in pH. a, Examples of evidence that lysosome positioning is sensitive to changes in pH.[110,285,286] Reduction of cell media pH from 7.4 to 6.5 and concomitant change in intracellular pH causes rapid (30 minutes – 1 h) dispersal of LAMP1 to the cell periphery in HeLa cells stained for LAMP1. Cells were treated for 1 h at 37 °C in Ringers or Ringers acetate buffers at pH 7.4 or 6.5 respectively. **b**, Graph taken from Dodding et al. (2016)[286] showing quantification of lysosome distribution measured by the cumulative LAMP1 fluorescence in concentric rings of equal area

6.2 Kinesin-1 cargo transport and microtubule sliding activities are linked by pH dependence

In addition to organelle transport, kinesin-1 plays a role in microtubule-microtubule sliding. Using microtubule binding sites in both the *N*-terminal motor domain and the *C*-terminal tail of the KHCs, kinesin-1 can bridge two microtubules, allowing them to act as the cargo and track, respectively. As the kinesin moves along the microtubule track it moves the "cargo" microtubule, bound to the *C* terminus of the heavy chain, relative to the track microtubule.[116] This activity has been shown to be important in microtubule remodelling and neuron regeneration.[122]

It has been reported that this function can be activated by a cargo-mimetic small molecule, named kinesore (Fig 6.2).[143]Kinesore competes with cargo-adaptor peptides for KLC^{TPR} binding, resulting in activation of kinesin-1 in the absence of bound cargo, promoting microtubule sliding, The working model is shown below, but it is worth noting that in this system, this has not yet been shown to require the carboxy-terminal KHC microtubule binding site.In the original experiments, kinesore treatments were carried out in Ringers buffer at pH 7.4 for 1 h in a CO_2 incubator.[143] Subsequently, it has become clear that CO_2 from the incubator dissolved in the buffer, which lacks a bicarbonate buffering component, and resulted in a decrease in pH during the treatment. This was the starting point for the experiments described below.

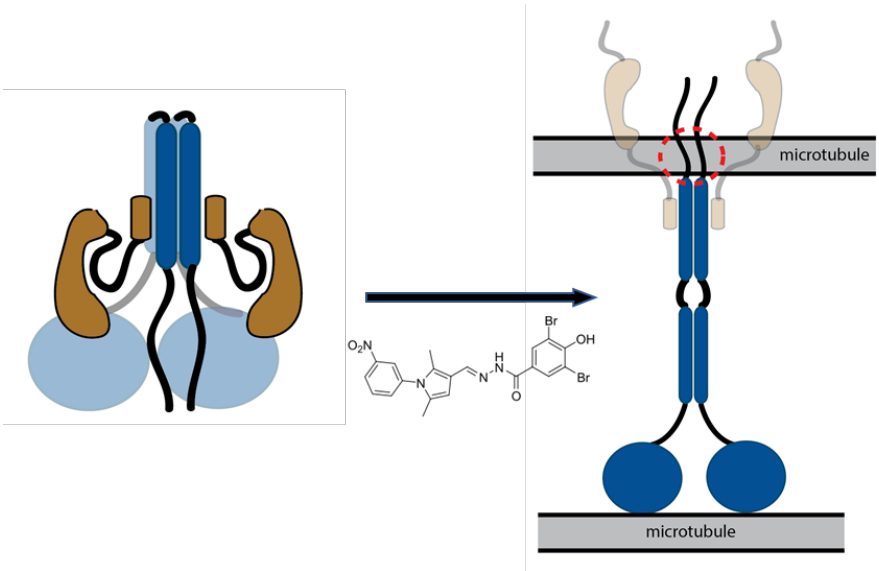

Fig. 6.2 | Cartoon representation of kinesore-induced activation of kinesin-1 microtubule sliding activity. Kinesin-1 can slide pairs of microtubules relative to one another by binding a second microtubule in the *C*-terminal region of the KHCs. A small molecule, kinesore, induces kinesin-1 dependent remodeling of the microtubule network.

To investigate the effect of this pH shift under controlled conditions, treatments were carried out in an incubator without CO_2 using Ringers buffer at pH 7.4 and 6.8. HeLa cells were treated with 50 µM kinesore or 0.1% DMSO (vehicle control) and incubated for 1 h at 37 ºC without CO_2. Cells were fixed with MeOH and probed with antibodies against tubulin and LAMP1 (Fig. 6.3). To quantify these data, the proportion of cells with remodelled microtubules was scored at pH 7.4 and 6.8. These results show that kinesore-induced microtubule remodelling takes place at reduced pH (6.8), with minimal effect observed at pH 7.4 (Fig. 6.3).

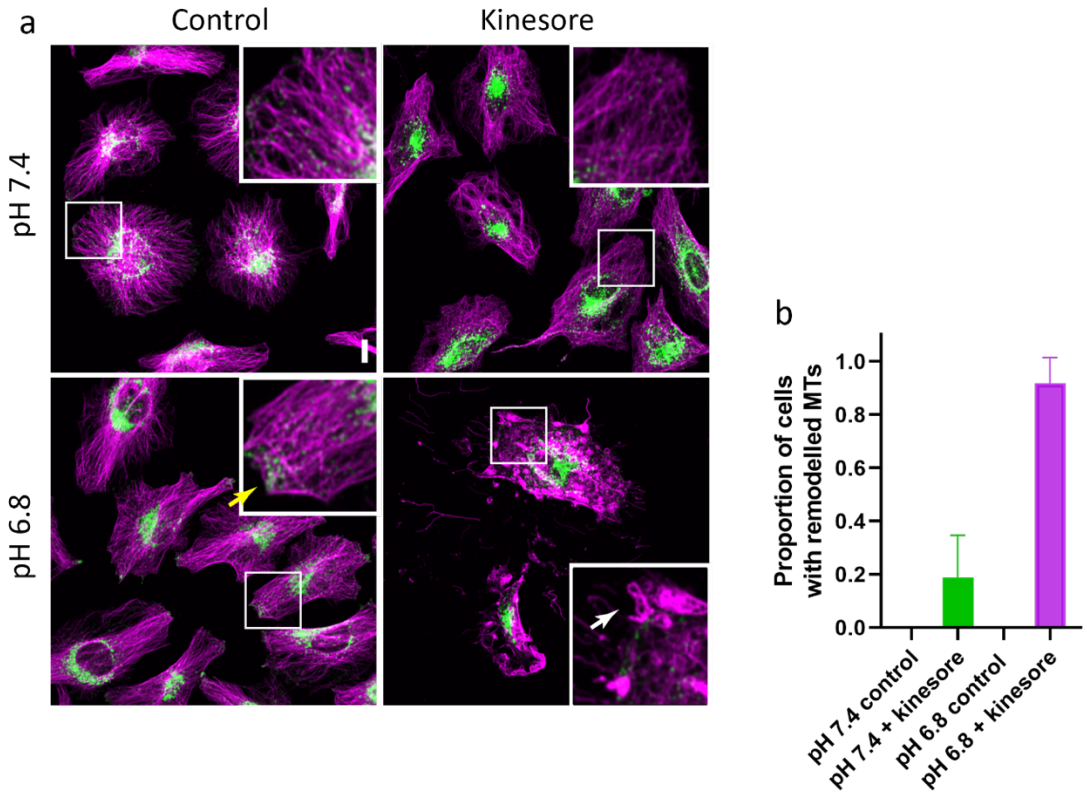

Fig. 6.3 | Microtubule remodeling by kinesin-1 small molecule inhibitor kinesore is sensitive to changes in pH. a, Representative confocal images of HeLa cells incubated at 37 ºC without CO_2 in Ringers buffer with 50 µM kinesore or 0.1% DMSO (control) at pH 7.4 or 6.8 for 1 h, fixed with MeOH and incubated with antibodies against beta tubulin (magenta) and LAMP1 (green). **b**, Quantification of effect of pH on kinesore dependent microtubule remodelling, cells were visually scored as remodelled or control microtubule phenotype. Cells were scored as remodelled if it clearly lacked a well-defined radial microtubule array.

6.3 Acidification may play a role in activation of kinesin-1

Together with previous studies, the above new data suggest a direct pH-dependence of both the organelle transport and microtubule remodelling functions of kinesin-1 in cells. This suggests that these two activities are linked in a shared activation mechanism. A possible model involves a shared 'primed' state. In this model, cargo binding to the KLCs (e.g. SKIP W-acidic TPR binding, see Chapter 3) or binding of a cargo-mimetic small molecule (kinesore) results in release of an element of the autoinhibitory mechanism, but is not in itself sufficient to promote activation. This 'primed' state is then sensitive to local or global acidification, triggering kinesin-1 activation for organelle transport or organisation of the microtubule network (Fig 6.4). It is becoming clear that pH-responsiveness is a key regulator of intracellular transport and cytoskeletal organisation. It is not clear how these pH changes may be achieved in a physiological setting, however it is possible that this could be, in part, due to proton leakage from acidic organelles altering local pH and activating transport.

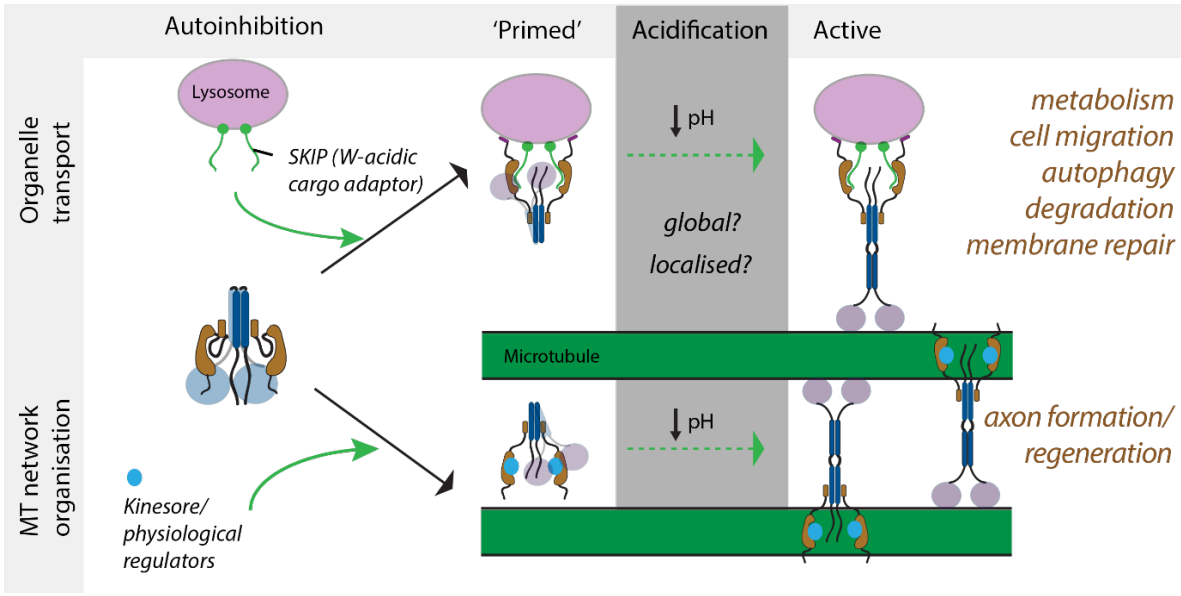

Fig. 6.4 | Model of pH responsive activation of kinesin-1. Engagement of cargo adaptor peptides (e.g. SKIP) for organelle transport or a cargo-mimetic small molecule 'primes' kinesin-1 for pH-dependent activation for cargo transport of organisation of the microtubule (MT) network.

6.4 Mutation of autoinhibitory motifs primes kinesin-1 for pH dependent activation of microtubule-microtubule sliding

To test this model, mutations were introduced in the KHCs and KLCs to relieve autoinhibitory interactions in an attempt to mimic the 'primed' state resulting from cargo or small-molecule

binding (Fig 6.5). For this, 9 amino acids (QIAKPIRPG) in the tail of KHC isoform Kif5C were mutated to alanine (AAAAAAAAA), hereafter denoted IAK/AAA. This region has been shown to be necessary and sufficient for KHC autoinhibition.[79] In addition, the three amino acids (LFP) that are necessary for KLC autoinhibition were mutated to alanine in KLC2 (AAA), LFP/AAA.[59] HeLa cells were transfected with constructs to express either wildtype or 'primed' (IAK/AAA and LFP/AAA) hemagglutinin (HA) tagged Kif5C and GFP-KLC2, treated in Ringers buffer for 1 h at 37 ºC without CO_2, fixed with MeOH and imaged for tubulin and kinesin-1 distribution (Fig 6.5a). At pH 7.4, both WT and 'primed' conditions showed a radial microtubule network with diffuse, cytoplasmic staining of both KLCs and KHCs. At pH 6.5, a similar phenotype was observed for the wildtype proteins. In contrast, at pH 6.5, IAK/AAA and LFP/AAA priming mutations resulted in aggregation of KLCs and KHCs. This phenotype has been observed previously following kinesore treatment, or in the case of overexpression of KLCs or KHCs alone.[83,143] In addition, the microtubule network was remodelled, with looping and bundling of microtubules observed. Whilst this phenotype does not resemble the extent of microtubule remodelling observed with the cargo-mimetic small molecule kinesore, the looping of microtubules suggests a similar mechanism of activation. These data are consistent with the model proposed above that IAK/AAA and LFP/AAA mutations uncouple KHC and KLC autoinhibition, leaving kinesin-1 primed for activation. In the absence of bound cargo, the motor can then bind a second microtubule at the *C*-terminal KHC site. Acidification results in activation, driving microtubule sliding and remodelling of the network (Fig 6.5b).

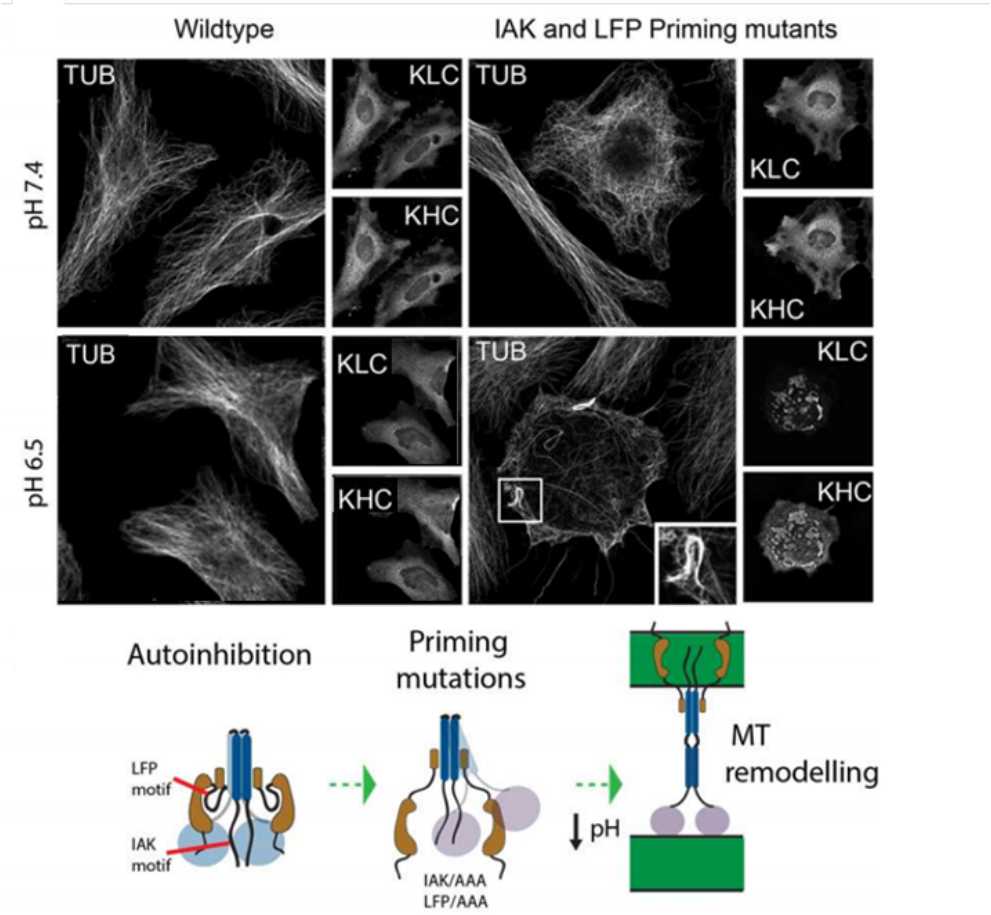

Fig. 6.5 | Mutation of autoinhibitory motifs primes kinesin-1 for pH-dependent activation of microtubule sliding. a, Cells transfected with constructs to express wildtype or IAK/AAA / LFP/AAA mutant HA-Kif5C/GFP-KLC2, treated with Ringer's buffer (pH 7.4) or Acetate Ringer's (pH 6.5) for 1 h, fixed and stained for tubulin and HA. **b,** Model of release of autoinhibition through IAK/AAA and LFP/AAA mutations, leaving kinesin-1 primed for pH-responsive activation of microtubule transport.

6.5 The interaction between the motor domains and an autoinhibitory peptide is pH dependent

One hypothesis that may explain the data presented above is that there is a pH dependence of the protein-protein interactions involved in autoinhibition. To test this, and gain mechanistic insight into kinesin-1 activation, the pH sensitivity of the interaction between the KHC motor domain and autoinhibitory tail (IAK) was investigated. A peptide comprising residues 917-931 of KIF5C, Kif5C^{IAK}, was made by solid-phase peptide synthesis with the 5-carboxytetramethylrhodamine (TAMRA) fluorophore appended *N* terminally, purified by high performance liquid chromatography, and confirmed by MALDI-TOF mass spectrometry (Table 6.1). KHC motor domain from Rat Kif5C (KIF5C$^{2\text{-}401}$) was expressed in *E. coli* as an

N-terminally His_6-tagged protein and purified as a dimer by Ni^{2+}-affinity chromatography followed by size exclusion chromatography (SEC). (The expression and purification of $KIF5C^{2-401}$was done by Dr Johannes Weijman.) The affinity of $KIF5C^{IAK}$ for the motor domain of rat KIF5C ($KIF5C^{2-401}$) was measured in a fluorescence polarisation assay *in vitro*. At pH 7.4, $KIF5C^{IAK}$ binds to the dimeric motor with an affinity (K_D) of 1.01 μM (Table 6.2, Fig. 6.6). In contrast, when the pH was reduced to pH 6.5, the affinity decreased 3-fold to a K_D of 2.85 μM. At pH 5.8 binding was further reduced, but the K_D could not be determined (Table 6.2, Fig. 6.6). A pH of 6.5 is within a range possible within a mammalian cell, suggesting that it is feasible that large changes in apparent affinity for the IAK-region towards the motor may be possible from relatively subtle changes in environmental pH.

Table 6.1 | Sequences of KHC autoinhibitory peptides	
$Kif5C^{IAK}$	A**H**SAQIAKPIRPG**H**Y
$Kif5C^{R\text{-}IAK\text{-}R}$	A**R**SAQIAKPIRPG**R**Y
$Kif5C^{A\text{-}IAK\text{-}A}$	A**A**SAQIAKPIRPG**A**Y

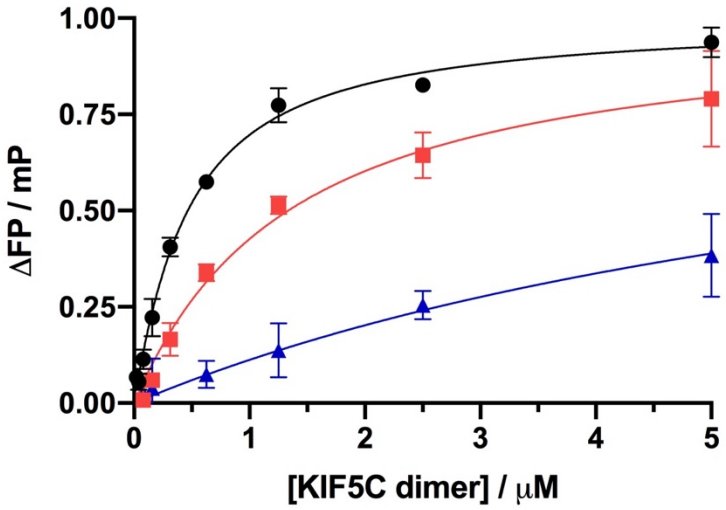

Fig. 6.6 | KHC autoinhibition is pH dependent. Binding affinities of autoinhibitory peptide $Kif5C^{IAK}$ for motor domain $KIF5C^{2-401}$ were measured *in vitro* in fluorescence polarization assays with TAMRA-labelled peptides (150 nM) incubated with increasing concentrations of $KIF5C^{2-401}$ protein in Bis-Tris buffer: Key: black pH 7.2, red; pH 6.4, blue; pH 5.8. Data were fitted to a single-site binding model with polarization values of the peptide and buffer alone subtracted and values normalised to the calculated B_{max}. Error bars indicate 1 SD from a minimum of 3 replicates.

Table 6.2 |Affinities of Kif5C^{IAK} for motor domain KIF5C$^{2-401}$ are pH sensitive			
pH	7.2	6.4	5.8
K_D / µM	1.01 ± 0.04	2.85 ± 0.18	–

6.6 Mutation of histidine residues in an autoinhibitory peptide alters affinity for the motor domains

In mammalian isoforms, the tail IAK motif is flanked both *N* and *C* terminally with histidine (His, H) residues (H918 and H930) (Fig 6.3a). The imidazole side chain of histidine can be protonated and deprotonated within physiologically relevant pH ranges, allowing it to act as both an acid and a base, a hydrogen bond donor or acceptor.[345] Protonation of histidine residues has been shown to be important for structural switches, inducing large-scale conformational changes in protein structures.[342,356] It is plausible that the KHC tail histidine residues flanking the IAK motif play a role in the pH sensitivity of kinesin-1 activity. To test this, peptides were synthesised with both His mutated to either alanine (Ala, A) or arginine (Arg, R), hereafter denoted as A-IAK-A or R-IAK-R, respectively (Table 6.1). Arg was used to mimic a permanently protonated His while Ala was chosen as a non-ionisable substitute. If the protonation of H918 and H930 are important in relieving IAK-binding, then R-IAK-R should decrease binding. Indeed, when measured at pH 7.4 a three-fold reduction in K_D of R-IAK-R with respect to the wildtype IAK peptide was observed (Table 6.3, Fig 6.7). In contrast, the non-ionisable A-IAK-A increased binding by seven-fold compared to WT (Table 6.3, Fig. 6.7).

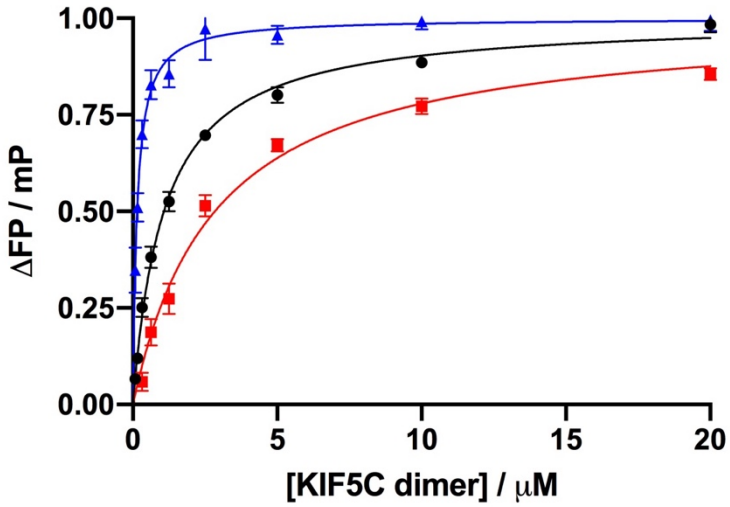

Fig. 6.7 | Mutation of histidine residues flanking the IAK motif alters affinity for motor domains Binding affinities of wildtype and mutant autoinhibitory Kif5C^{IAK} peptides for motor domain KIF5C$^{2-401}$ were measured *in vitro* in fluorescence polarization assays with TAMRA-labelled peptides (150 nM) incubated with increasing concentrations of KIF5C$^{2-401}$ protein in HEPES buffer at pH 7.4: Key: black; wild type Kif5C^{IAK} red; Kif5C$^{R\text{-}IAK\text{-}R\ A}$ blue; Kif5C$^{A\text{-}IAK\text{-}A}$. Data were fitted to a single-site binding model with polarization values of the peptide and buffer alone subtracted and values normalised to the calculated B_{max}. Error bars indicate 1 SD from a minimum of 3 replicates.

Table 6.3| Mutation of His residues in Kif5C^{IAK} alter affinities for motor domain KIF5C$^{2-401}$

	Kif5C^{IAK}	Kif5C$^{R\text{-}IAK\text{-}R}$	Kif5C$^{A\text{-}IAK\text{-}A}$
pH 7.4 K_D / μM	1.01 ± 0.04	2.84 ± 0.30	0.14 ± 0.01

To investigate the role of H918 and H930 in the full-length KHC protein, the same Arg and Ala mutations were introduced into HA-Kif5C. HeLa cells were transiently transfected and imaged for microtubule organisation and kinesin-1 distribution. Unfortunately, challenges were encountered in expression, aggregation and staining and no clear phenotype was observed. This experiment is complicated by the existing pool of endogenous KHCs in the cell. In addition, over-expression of the KHCs has been shown to lead to aggregation, with phenotype dependent on expression levels.[83] Since transient expression resulted in cells expressing different levels of protein this rendered the results difficult to interpret. In the future, it will be important to knock-out the endogenous wildtype protein and express mutants at near-endogenous level. This could be achieved through CRISPR/Cas9 technology to engineer the mutations into endogenous Kif5B (the major non-neuronal KHC paralogue. Alternatively, if single genomic point mutations are not possible, a CRISPR knockout strategy

followed by rescue using wildtype and mutant Kif5B constructs under control of an inducible promoter could be employed.

6.7 Mutations of a glutamate in the KHC-KLC interface drives kinesin-1 activation

An alternative hypothesis involves a pH-dependent conformational shift in another region of the kinesin-1 tetramer after the protein is 'primed' by release of autoinhibition. In chapter 5, analysis of the sequences involved in the KHC-KLC interface revealed a conserved glutamate (Glu, E) in the core of the coiled coil. This was shown to confer pH-responsive structural changes to a short peptide from this region of the KHCs. It was hypothesised that protonation of this Glu on acidification could result in structural changes in the KHC-KLC interface, which could be linked to larger scale conformational changes involved in motor activation.

To investigate a role for this residue in kinesin-1 activation in cells, the E794L mutation, to mimic protonation of Glu and echo the canonical hydrophobic residue at the other ***d*** sites, was introduced into full-length HA-KIF5C (KIF5C^{E794L}). If this hypothesis is valid, by mimicking acidification, this mutation should result in pH independent activation of kinesin-1 (Figure 6.8b). HeLa cells were transfected with constructs to express either wildtype or E794L HA-KIF5C and GFP-KLC2, fixed with paraformaldehyde and imaged for LAMP1 and kinesin-1 distribution. In wildtype cells, KLC and KHC are diffuse and cytoplasmic with lysosomes largely clustered in the perinuclear region. The E794L mutation results in the pH-independent accumulation of kinesin-1 and co-localisation with lysosomes at the cell periphery (Figure 6.8a). This suggests that this part of the coiled-coil interface may be important for the pH sensing and pH-responsive transport activities of kinesin-1.

However, the extent of lysosome dispersal was less than that observed on acidification of the media (Fig 6.1). This is not surprising and suggests that the single mutation is not sufficient to completely uncouple the pH dependence of activation. In the future, it may be possible to identify additional mutations to mimic protonation of other residues in the motor complex. Combining these mutations with autoinhibitory decoupling mutations (IAK/LFP/AAA) will allow us to ask if kinesin-1 shows pH-independent activation of microtubule-microtubule sliding. In addition, as discussed in 6.6, there are issues associated with transient transfection of cells for over expression. In the future, attempts will be made to CRISPR engineer the E794L mutation into endogenous Kif5B.

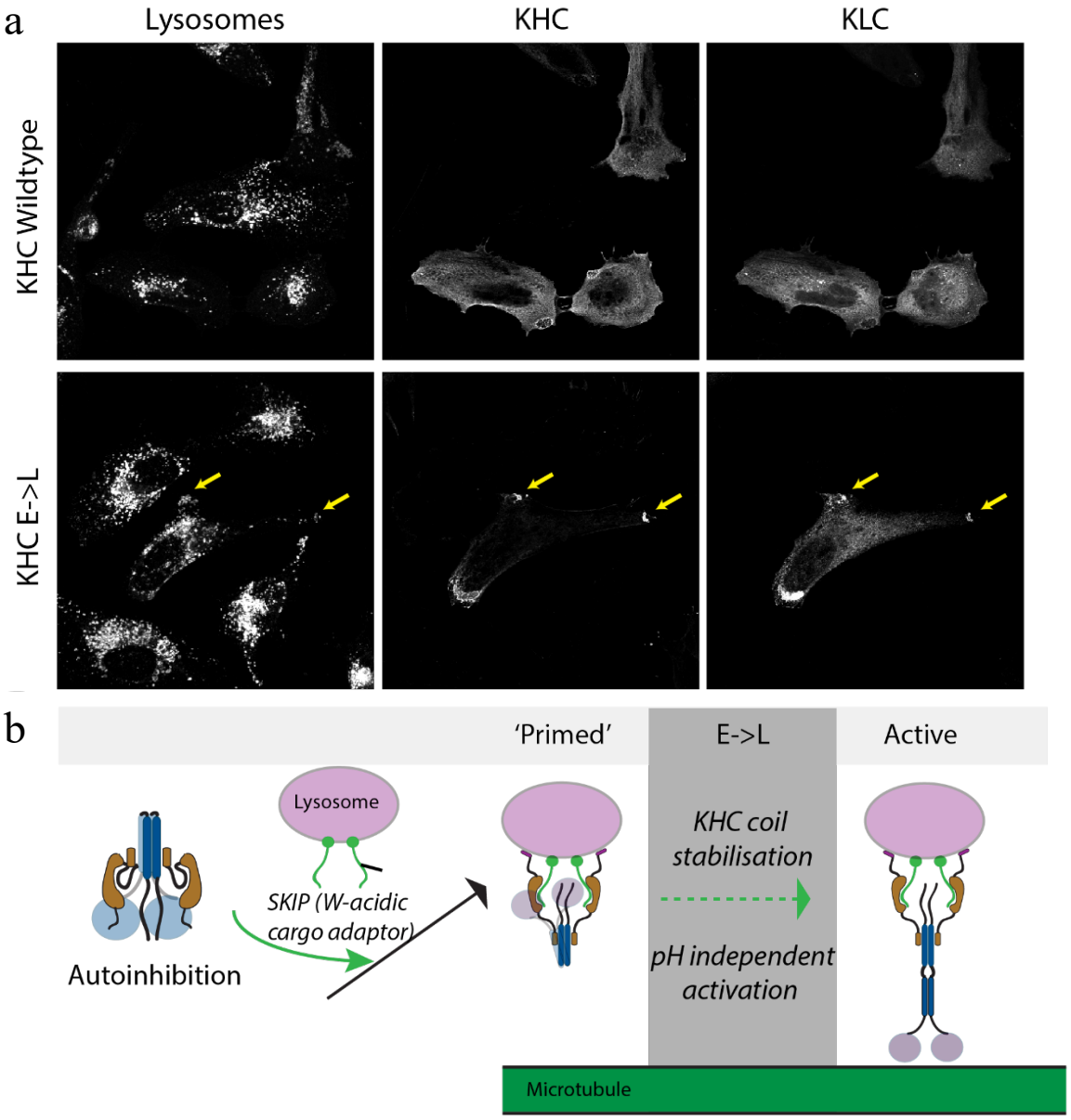

Fig. 6.8 | The E794L mutation at the KHC-KLC interface activates kinesin-1 for pH-independent transport of lysosomes to the cell periphery. a, Representative confocal images of HeLa cells transfected with constructs to express wildtype or E794L HA-Kif5C and GFP-KLC2, fixed with paraformaldehyde and incubated with antibodies against HA and LAMP1. The E794L results in LAMP1 positive peripheral accumulations of kinesin-1. **b**, Model of glutamate to leucine mutation mimicking acidification to allow pH independent activation of cargo transport.

6.8 Conclusions

By virtue of its capacity to engage a wide variety of organelle cargoes and remodel the cytoskeleton, kinesin-1 is a central regulator of subcellular organisation[25,28,116]. Cargo recognition is interwoven with an autoregulatory mechanism that maintains the enzyme in an inactive state in the absence of cargo binding.[25,28] To date, it is unclear how the transition from the inhibited to active state(s) is regulated. It is also not known how kinesin-1 activity is directed between distinct functions of organelle transport and microtubule-microtubule sliding. This chapter has begun to explore the hypothesis that pH is a key regulator in activation of kinesin-1 and may be a shared factor in regulation of both functions.

It is clear from the literature that the pH of the cytosol has profound effects on the distribution of organelles. Slight cytosolic acidification triggers rapid microtubule- and kinesin-1-dependent redistribution of lysosomes and lysosome related organelles from the perinuclear region of the cell to the periphery[110,285,286,350,357] New data described here reveals that small-molecule mediated activation of kinesin-1 by the cargo-mimetic compound kinesore[143] promoting remodelling of the microtubule network also acts in an acidic pH-dependent manner. This suggests pH-responsiveness is a mechanistically unexplained but, nonetheless, important regulator of intracellular transport and cytoskeletal organisation.

Autoinhibition of kinesin-1 has been mapped to key regulatory motifs in the KHCs (IAK) and KLCs (LFP). It was hypothesised that, in addition to the release of these autoinhibitory interactions, pH acidification is required for motor activity. To test this, these autoinhibitory interactions were uncoupled by specific amino-acid mutations. This rendered kinesin-1 sensitive to pH-dependent activation, resulting in microtubule-microtubule sliding. These results suggest a model of activation involving a ‘primed’ state where autoinhibition is relieved (through mutation or binding of cargo or a cargo-mimetic molecule) and the motor is sensitive to activation by subtle changes in pH.

To understand the mechanism of this pH dependent activation, attempts were made to identify the residues involved. Initially, it was hypothesised that two His residues flanking the IAK motif in the KHC tail may play a role in pH responsive autoinhibition. *In vitro*, the affinity of a peptide from this region for the KHC motor domain decreased significantly at reduced pH. Mutation of these residues to Arg, to mimic protonation, also resulted in decreased affinity,

whilst a non-ionisable Ala mutant bound with increased affinity. This suggests that KHC autoinhibition may be sensitive to changes in pH and that acidification may play a role in the release of the KHC tail-motor interaction. In the future, it will be important to validate this hypothesis in full-length proteins in cells.

Following the observation that mutation of Glu to Leu in the KHC-KLC interface results in a pH-responsive structural change in a KHC peptide from this region (Chapter 5), the E794L mutation was introduced into full length KHC in cells. This resulted in the pH-independent accumulation of kinesin-1 and co-localisation with lysosomes at the cell periphery. These preliminary results suggest that this Glu residue in the core of the KHC-KLC coiled coil may play an important role in the pH sensing capacity of kinesin-1.

It is becoming clear that understanding the regulation of kinesin-1 is a complex problem and likely involves interactions in many different regions of the protein. Nonetheless, in the future it will be exciting to continue to explore kinesin-1 as a pH sensor and pH-responsive transport effector and to further investigate the mutations identified here. For this, pH-sensitivity decoupling mutations (H918 and H930, E794L, and others that emerge) will be combined with autoinhibitory decoupling mutations (IAK/LFP/AAA) to ask if kinesin-1 shows pH-independent activation of microtubule-microtubule sliding. In addition, cargo binding mutations from previous studies, e.g. to the TPR domain (KLC2 N287L)[67] and membrane-binding amphipathic-helix (KLC2 L550P)[69], will be incorporated to test the hypothesis that combined uncoupling of organelle-cargo binding and pH-driven activation promote microtubule-microtubule sliding. This will begin to investigate how the mode of kinesin-1 activation promotes functions in organelle transport or microtubule sliding, with pH as a shared regulator. It will also be important to examine the effects of pH-decoupling mutations at endogenous expression level, where the ratio of motor to its regulators is at natural levels. This could be achieved by CRISPR/Cas9 engineering of the mutations directly into endogenous KHC or through a CRISPR knockout strategy followed by rescue under control of an inducible promoter. In addition, *in vitro* studies using recombinantly expressed kinesin-1 tetramers[59,69] would allow microtubule co-sedimentation and microtubule-dependent ATPase assays to examine the effects of mutations. This would deliver insights into how ATP-dependent and independent microtubule binding and ATPase activity are affected by pH.

To investigate these effects in a physiological setting, it will be interesting to understand how proton leakage from acidic organelles may alter their local pH and activate transport. Rather than changes to media pH, a lysosomal permeabilising agent LLOME could be used to raise lysosomal pH and lower cytosolic pH.[358] In addition, use of acidotropic dyes and live-cell imaging could be used to monitor how lysosome pemeabilisation, and a drop in in lysosomal pH, correlate with kinesin-1 dependent transport, and if pH-sensitivity decoupling mutations alter any correlation. It will be interesting to ask whether lysosome permeabilisation synergises with kinesore treatment to promote pH-driven microtubule remodelling. It is also yet to be seen whether the pH-sensitivity of kinesin-1 is lysosome-specific or may extend to other cargo organelles. Furthermore, it will be interesting to ask whether kinesore-mediated microtubule sliding activity can be rendered pH-insensitive by pH decoupling mutations in the KHCs. Whilst the microtubule-sliding phenotype described here is small-molecule induced, there is good evidence for a role of kinesin-1 mediated microtubule-microtubule sliding in many cell types, particularly in the repair of neuronal axons following injury.[359] In the future, it will be interesting to continue these investigations in neuronal systems where the physiological roles and mechanisms of microtubule-microtubule sliding can be explored.

This work may have future applications in developing tools to boost, augment, or supress intracellular transport. Molecules to target kinesin-1 in a pH sensitive manner may be useful as microtubule-targeting agents that are active in specific contexts, for example in the acidic environment associated with solid tumours. Kinesore is the first molecule to target a cytoskeletal motor-cargo recognition and autoregulatory mechanism and drive the function of the motor in promoting microtubule-microtubule sliding. High-affinity analogues of this compound may have applications analogous to that of the classic microtubule-targeting agents such as vinblastine or taxol, which are important chemotherapeutic agents and are thought to have potential in neuronal regeneration.[360,361] To take this forward, a mechanistic understanding of the pH sensitivity of activation will be required.

7 Discussion and future work

7.1 Key conclusions and critical evaluation of this thesis

Kinesin-1 is a central regulator of subcellular organisation with the capacity to engage a wide variety of organelle cargoes and remodel the cytoskeleton.[25,28,116] Careful control of kinesin-1 activity is critical for healthy cell function.[32,362] Cargo recognition is interwoven with an autoregulatory mechanism that maintains the enzyme in an inactive state in the absence of cargo binding.[25,28] To date, it is not known how the transition from the inhibited to active state(s) is regulated. This thesis has employed peptide design to disrupt and augment natural protein-protein interactions to deliver new insights into kinesin-1 cargo binding and activation. This section outlines the key conclusions from the work, alongside their potential applications and limitations, with suggestions for future experiments.

7.1.1 Fragment-linking peptide design yields a high affinity ligand for KLC^{TPR}s

Historically, models of kinesin-mediated transport have focused on motor-microtubule interactions, with less known about motor-cargo attachment and detachment. More recently, studies have delivered insights into the mechanisms of cargo recognition and activation through interactions of cargo adaptor peptides with the kinesin light chain tetratricopeptide repeat domains (KLC^{TPR}s).[25,67,68] This has highlighted the cargo adaptor-TPR protein-protein interaction (PPI) as a possible site for the design of synthetic inhibitors or facilitators to manipulate intracellular transport. Chapter 3 describes the development of a new structure-guided, fragment-linking peptide design approach to deliver a high-affinity peptide ligand, KinTag, that targets the kinesin-1:cargo interface.[283] For this, functional elements of different natural cargo-adaptor sequences are combined into one peptide. A structure of the KLC1^{TPR}:KinTag complex confirms that both general design features (*i.e.*, shape and charge complementarity between the peptide and the protein) and sequence specific design features (*i.e.*, large side chains of the peptide bind into designated pockets of the protein) are realized. The design yields an order of magnitude increase in binding affinity without dramatically increasing the interface area, highlighting the utility of fragment linking in peptide design, akin to that used with small-molecule pharmacophores.[208,216] Importantly, it is possible to retain the capacity to relieve KLC autoinhibition and activate transport,[59,88] demonstrating that complex functionality can be retained from peptide fragments.

This design approach may provide a strategy for developing high-affinity peptide ligands for protein surfaces more broadly, offering an alternative to other techniques, such as affinity maturation. However, this will be limited to PPIs where *a priori* structural information is available from natural ligands. It will also be interesting to determine whether the success of this approach is due specifically to the conformational flexibility and induced-fit binding of the TPR domains or whether this can be extended to other (more rigid) domains. Whilst the initial fragment-linking design attempts were successful, attempts to further improve the design using *in silico* saturation mutagenesis proved unsuccessful. In addition, comparison of the KLC1^{TPR}:KinTag complex with natural bound cargo adaptors fails to explain the increased affinity using both BAlaS and PISA algorithms.[297,298] It is possible that these failures are due to an inability of the models to consider the contributions of induced-fit conformational changes to binding and it will be interesting to see how developments in this field will allow these limitations to be overcome in the future.

7.1.2 The affinity of motor-cargo interactions determines the extent of transport

Natural motor-cargo adaptor interactions have micromolar affinities when measured *in vitro*.[67,68,103,363] It has been proposed that tighter interactions are achieved in the cell through avidity (e.g. multiple adaptors presented on the cargo) but the hypothesis that adaptor-motor binding affinity *per se* is a limiting factor in transport had not previously been formally tested. Measurement of the transport efficiency of a designed high-affinity peptide ligand has allowed this question to be answered in Chapter 4. The *de novo* peptide, KinTag, is effective in hijacking the transport function of endogenous kinesin motors in cells and delivered cargo to the periphery of HeLa cells, and into axons of primary neurons, with a high efficiency that correlates with its enhanced binding affinity.[283] For the first time, this reveals that protein-peptide binding affinities measured *in vitro* correlate with the extent of cargo transport in the cell. This leads to the conclusion that if a motor holds onto its cargo adaptor more tightly, the cargo is transported more efficiently.

Throughout transport and trafficking networks, similar unitarily low-affinity natural interactions are supported through co-operativity, avidity and coincidence detection. It is possible that the design approach introduced by this thesis could be applied to yield high-affinity ligands for other protein targets for further manipulation of intracellular transport. For this, the mechanistic basis of these interactions will need to be understood. For kinesin-1, cargo

recognition is not limited to cargo adaptor peptide-TPR interactions, but also involves PPIs with the kinesin heavy chains (KHCs) and protein-lipid interactions between KLCs and organelle membranes.[69,87,91] Going forward, it will be important to discover how these mechanisms are integrated in cargo recruitment in the cell and to incorporate this understanding into quantitative models of kinesin-1 transport.

Whilst Chapter 4 demonstrates the function of KinTag as a tag for both lysosome and mitochondria transport in the cell, the failed design of fusion proteins incorporating the sequence onto the surface of other organelles underline, perhaps unsurprisingly, that the context in which the cargo adaptor peptide is expressed is important for its activity. In the future, it will be crucial to understand these requirements to allow the widespread application of this tool to other cargos. In addition, further measurements of KinTag activity, such as motor velocities and run lengths, will also be important to shed light on the kinetics of transport. To date, it has not been possible to design a soluble high-affinity kinesin-1 inhibitor. This is an interesting goal for the future, and it will be important to determine whether a peptide inhibitor drives a similar microtubule-looping phenotype observed for the cargo-mimetic small molecule kinesore.

7.1.3 Designed coiled coils can be used as cell-penetrating, localised, peptide tags

If designed peptides are to be used as inhibitors or facilitators of PPIs in natural systems, they must be able to enter the cell. A major challenge in the design of therapeutic agents is to confer the capability to cross biological barriers. In Chapter 4, to enable the cellular delivery of peptide analogues of KinTag, a new cell-penetrating tag is described. This *de novo* basic peptide penetrates cells in culture and forms a dimeric coiled-coil interaction with a genetically encoded acidic partner sequence fused to proteins of interest. This demonstrates that orthogonal, designed PPIs can be introduced inside the cell through the use of an exogenous cell-penetrating peptide (CPP). Moreover, a hybrid KinTag-CPP peptide enters cell and is localized to lysosomes. The capacity of KinTag to recruit kinesin motors results in dispersal of lysosomes to the cell periphery. This is the first example of a synthetic cell-penetrating high-affinity kinesin-1 cargo adaptor peptide for the inducible manipulation of organelle transport in eukaryotic cells.

Down-regulation of axonal organelle transport is associated with neurodegenerative diseases. In the future, it may be possible to develop a KinTag derivative as a tag to boost transport of a specific organelle where this is dysregulated. Currently, the cell-penetrating KinTag transport system relies on the expression of a genetically encoded bait sequence, in addition to an exogenous peptide. Whilst this reagent may prove valuable as a research tool for inducible transport, for future development of therapeutics it will be necessary to develop a cell-penetrating reagent to target kinesin-1 to a specific organelle without genetic manipulation. For this, designs would seek to deliver a stable CPP incorporating both the KinTag and an organelle-targeting sequence. For example, for lysosome transport, based on the success of the expression of LAMP1-KinTag fusion proteins in Chapter 4, a peptide could be designed to bind to LAMP1 with high affinity (LBP). This sequence could then be included in a CPP-KinTag-LBP reagent for the inducible, augmented, transport of lysosomes.

7.1.4 Kinesin heavy chain coiled coils show structural plasticity

Analysis of the interactions between the KHCs and the KLCs in the heterotetrametric kinesin-1 complex may shed light on how conformational changes linked to cargo-binding in the KLCs are coupled to downstream activation of the motor. Two KHCs and two KLCs are thought to interact through coiled coil domains.[46] Nonetheless, the structure and arrangement of this interface remains unknown. In Chapter 5, *in silico* and *in vitro* analysis of these sequences is used to identify and characterise coiled-coil peptides encompassing the minimal interacting regions. Interestingly, an X-ray crystal structure of a peptide from KHC isoform Kif5B reveals an antiparallel tetrameric coiled coil. Since this sequence is known to form a parallel dimer in the full-length protein, this suggests structural plasticity of the sequence, with the capacity to accommodate multiple oligomeric states. This is likely important for the interaction with the KLCs in which the KHC homodimer must show flexibility to accommodate a heterotetrameric arrangement at the interface. This also shows that the sequence has the capacity to be accommodated in an antiparallel assembly. In addition, modelling predictions of the KHC-KLC heterotetramer suggest that an antiparallel organisation of helices may be more energetically favourable. These results begin to question the conventional image of kinesin-1 in which the four chains assemble in a parallel orientation. Further evidence of the KHCs as a dynamic and flexible platform for PPIs comes from the identification of a universally conserved polar Glu residue in the hydrophobic core of the KHC coiled-coil, which is sufficient

to drive the pH-dependent α-helical folding of this sequence. This demonstrates further flexibility, with structural changes resulting from fluctuations in environmental stimuli.

Evaluation of the models of the KHC-KLC heterotetrameric coiled coil will require experimental validation. In the time frame available for this work, it was not possible to obtain a structure or biophysical characterisation of the interface. This was in part due to problems encountered in obtaining and purifying the peptides and proteins in addition to the challenging nature of X-ray crystallography of heteromeric systems. Solving the nature of this interface remains a worthwhile and challenging goal and will be the topic of future research, likely focussing on the expression of longer sequences. At the time of writing, new insights into the nature of the kinesin-1 complex from models built in AlphaFold[300] and structural data from electron microscopy studies by Dr Johannes Weijman suggest that the KHC-KLC interface may be more complex than a discrete heterotetrameric coiled coil. Future models will begin to incorporate the possibility of hinges in both the KHCs and KLCs causing the coiled coils to fold on themselves resulting in a multi-helix bundle at the interface.

7.1.5 Kinesin-1 microtubule sliding activity is pH dependent

In addition to its role in organelle transport, kinesin-1 performs a function in sliding pairs of microtubules relative to one another for regulation of the microtubule network.[120,123,359] Both kinesin-1 autoinhibition and organelle-transport have been shown to be pH dependent, with acidification triggering structural changes in the motor and activation of lysosome transport.[83,84,110,285,286] In Chapter 6, a cargo mimetic small-molecule, kinesore, is used to investigate the pH dependence of kinesin-1 microtubule sliding.[143] These experiments demonstrate that kinesore-induced microtubule sliding occurs at acidified pH but not under neutral conditions. The pH-dependence of both the organelle transport and microtubule remodelling activities suggest that the two are linked in a shared activation mechanism. A possible model for this is proposed. This involves a common ‘primed’ state, resulting from cargo binding to the KLCs (e.g. SKIP W-acidic TPR binding) or binding of a cargo-mimetic small molecule (kinesore) and release of autoinhibition. This ‘primed’ state is hypothesised to be sensitive to local or global acidification, triggering kinesin-1 activation for organelle transport or organisation of the microtubule network. To test this, the KHC^{IAK} and KLC^{LFP} autoinhibitory motifs have been mutated in transiently expressed proteins in cells to mimic the

primed state. Transfected cells are sensitive to pH as predicted, with acidification of media triggering microtubule remodelling.

These results begin to offer a model for the long unexplained mechanism of pH-dependence of lysosome transport. Whilst the microtubule-sliding phenotype described here is small-molecule induced, there is good evidence for a role of kinesin-1 mediated microtubule-microtubule sliding in many cell types, particularly in the repair of neuronal axons following injury.[359] Going forward, it will be interesting to continue these investigations in neuronal systems where the physiological roles and mechanisms of microtubule-microtubule sliding can be explored.

7.1.6 A glutamate in the core of the KHC coiled coil confers pH sensitivity

To investigate the mechanism of acidification-driven kinesin-1 activation, in Chapter 6 single amino-acid mutations are tested for their capacity to uncouple pH-dependence. For this, the KHC core Glu residue, shown to induce pH-dependent conformational changes of a peptide in Chapter 5, is mutated to Leu to mimic protonation and echo the canonical residue found at this position of the coiled-coil sequence repeat. This results in the pH-independent accumulation of kinesin-1 and co-localisation with lysosomes at the cell periphery. These preliminary results suggest that this Glu residue in the core of the KHC-KLC interface may play an important role in the pH sensing capacity of kinesin-1.

The transient transfection approach used in these experiments has limitations due to variable expression levels resulting in different phenotypes and the additional complication of an existing pool of endogenous KHCs in the cell. For future studies, it will be important to examine the effects of pH-decoupling mutations at endogenous expression levels, where the ratio of motor to its regulators is at natural levels. This could be achieved by CRISPR/Cas9 engineering of the mutations directly into endogenous KHC or through a CRISPR knockout strategy followed by rescue under the control of an inducible promoter.[364] Going forward, it will also be important to investigate how these pH changes may be achieved in a physiological setting. It is possible that this could be, in part, due to proton leakage from acidic organelles altering local pH and activating transport. This will be tied into the question of whether the pH-sensitivity of kinesin-1 organelle transport is lysosome-specific or may extend to other cargo.

7.2 Ideas for future work arising from this thesis

Increasingly, evidence is beginning to shed light on both the structure and mechanisms of activation of kinesin-1. Nonetheless, important questions in cell biology remain around this complex machine. There is much scope for future work in this field, which remains an area of active research. Throughout this thesis, future experiments have been described to investigate the kinetics of cargo attachment and detachment further, the design of cell-penetrating kinesin-1 ligands to boost axonal organelle transport, the structure of the KHC-KLC interface, and the mechanism of pH responsive motor activation. In this section, ideas for two new areas of research arising from this thesis are explored.

7.2.1 Design of kinesin heavy chain cargo adaptor peptides

A recent study from Dimitrova-Paternoga *et al.* presents the first structural characterization of a direct cargo adaptor–KHC interface.[91] This reveals that an mRNA cargo adaptor, atypical tropomyosin (aTm1), interacts with KHC at a site immediately downstream of the KLC binding site. The interaction forms an antiparallel trimeric coiled coil in which one helix of aTm1 binds in an antiparallel orientation to a parallel KHC homodimer. This new structural insight highlights the KHC-cargo PPI as a possible target for manipulation through peptide design.

Future work could use coiled-coil design principles to deliver high-affinity KHC ligands as transport tags or inhibitors. For this, the aTm1 sequence involved in the interaction could be modified with mutations to incorporate hydrophobic and salt-bridge interactions known to stabilise canonical coiled coils (Fig.7.1).[147,245,265] By making additional interactions at the interface the designed peptides should bind with increased affinity over the natural sequence, allowing them to compete for binding. In addition to rational design, selection of peptide libraries could be employed to identify high-affinity binders.[365-367] If successful, these would offer *de novo* or engineered high-affinity cargo-adaptor peptides for the KHCs, to be used alongside our KLC adaptor, KinTag. It would also be interesting to investigate whether other kinesin-1 cargoes, known to interact with the KHCs in this region, bind through similar mechanisms.[87,89,301] If overlapping cargo-binding sites are identified, the fragment-linking design approach described in Chapter 3 could also be applied to this interface. This work could shed light on the poorly understood mechanisms of KHC cargo-recognition. Coiled-coil interactions are also important in the recognition of cargo by myosin-V and dynein motors.[26,368]

Therefore, it is plausible that this approach could be applied to other motors to develop high-affinity peptides to target PPIs across the intracellular transport network.

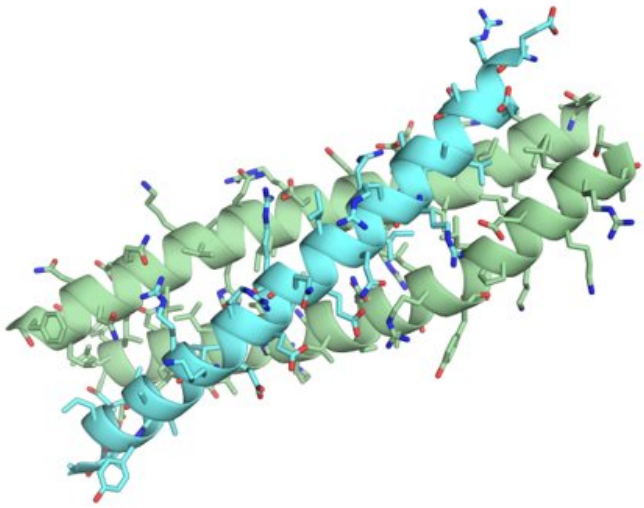

Fig. 7.1| Model of a KHC-cargo adaptor interaction. Model of a *de novo* cargo adaptor peptide interacting with the dimeric KHC *C*-terminal coiled coil in an antiparallel trimeric arrangement based on mutations to the structure of the aTm1-KHC assembly described by Dimitrova-Paternoga *et al.*[91]

7.2.2 Design of a hybrid motor protein

The ultimate test of understanding any natural system is to build a mimic of it from scratch. The growing field of synthetic biology seeks to address this by building synthetic proteins that mimic the functional dynamics of natural proteins and integrating these into biological systems to perform new functions. A goal for the future could be to apply insights from the kinesin-1 motor for the design of self-regulated, cargo-activated, protein machines that can perform transport functions within the complex cellular milieu.

Using insights from Chapters 5 and 6, designs could aim to reduce the complexity of the KHC-KLC coiled-coil interface whilst capturing its salient features. Robust *de novo* coiled coils from the Woolfson lab, which have been characterised by X-ray crystallography (Fig. 7.2 a, b), could be employed in the design of a homodimer that harbours a cryptic pH-dependent hetero-tetramerization region, *i.e.* analogous to the KLC-binding region of KHC (Fig. 7.2 c). In turn, this would recruit a second coiled-coil sequence analogous to KLC. This construct could be engineered into a hybrid motor protein through coupling to the kinesin-1 ATPase motor domains (Fig. 7.2 d). Mechanistic understanding of cargo-binding and autoinhibition from Chapters 3 and 4 could also be employed to incorporate orthogonal cargo recognition and

regulation into the design, e.g., through additional coiled-coil interactions or designed armadillo repeat proteins (dArmRPs) (Fig. 7.2 e). Sophisticated regulatory mechanisms such as phosphorylation[369] could also be introduced and motors of opposite directionality or that utilise other cytoskeletal tracks such as myosins and actin incorporated. The key challenge of this design would be making the components work together in cells, requiring fine tuning of interactions between the natural and designed components. If successful, the design of a self-regulated, cargo-activated motor that functions in mammalian cells would represent a significant milestone in motor-protein design and engineering.

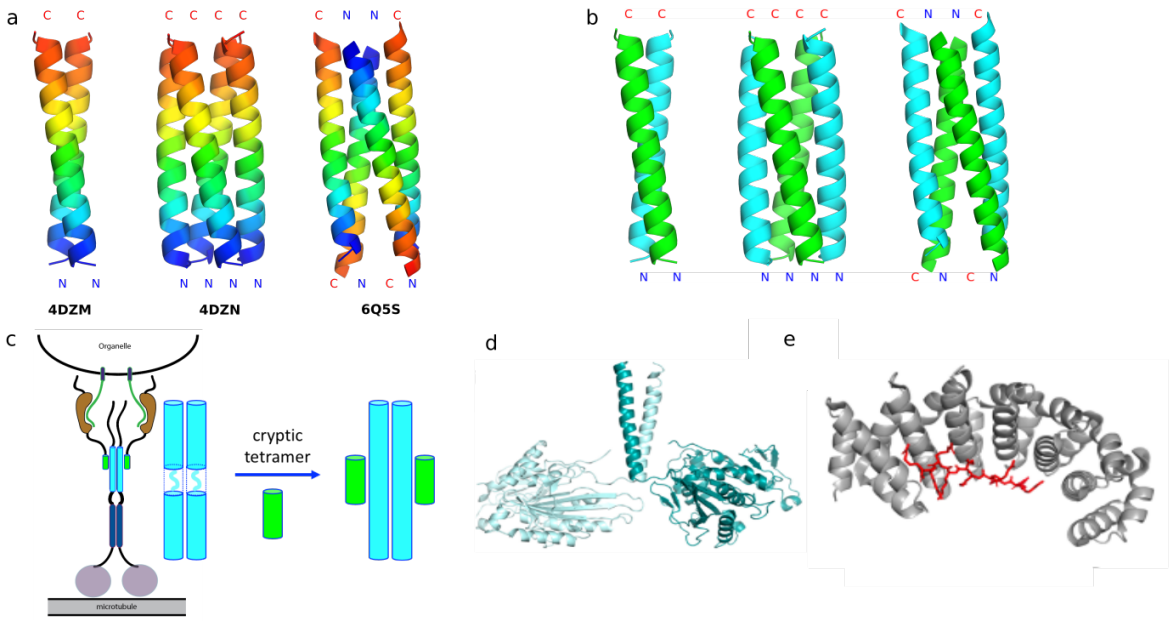

Fig. 7.2| Design of a hybrid motor protein. a, X-ray crystal structures of Woolfson group *de novo* designed homomeric parallel dimeric and tetrameric and antiparallel tetrameric coiled coils.[265] **b,** Illustration of heteromeric coiled coils from the structures in a, designed and characterised in solution. **c,** Design of a dimeric scaffold harbouring a cryptic tetramer **d,** X-ray crystal structures of kinesin-1 dimeric motor domains, PDB:3KIN.[370] **e,** X-ray crystal structures designed armadillo repeat protein for tuneable cargo recognition/inhibition (Plückthun lab).[371,372]

References

1 Duve, C. D., Gianetto, R., Appelmans, F. & Wattiaux, R. Enzymic Content of the Mitochondria Fraction. *Nature* **172**, 1143-1144, doi:10.1038/1721143a0 (1953).

2 Gianetto, R. & De Duve, C. Tissue fractionation studies. 4. Comparative study of the binding of acid phosphatase, beta-glucuronidase and cathepsin by rat-liver particles. *Biochem J* **59**, 433-438, doi:10.1042/bj0590433 (1955).

3 Nijtmans, L. G., Klement, P., Houstěk, J. & van den Bogert, C. Assembly of mitochondrial ATP synthase in cultured human cells: implications for mitochondrial diseases. *Biochim Biophys Acta* **1272**, 190-198, doi:10.1016/0925-4439(95)00087-9 (1995).

4 Bork, P., Sander, C. & Valencia, A. An ATPase domain common to prokaryotic cell cycle proteins, sugar kinases, actin, and hsp70 heat shock proteins. *Proc Natl Acad Sci USA* **89**, 7290 (1992).

5 de Boer, P., Crossley, R. & Rothfield, L. The essential bacterial cell-division protein FtsZ is a GTPase. *Nature* **359**, 254-256, doi:10.1038/359254a0 (1992).

6 Mukherjee, A., Dai, K. & Lutkenhaus, J. Escherichia coli cell division protein FtsZ is a guanine nucleotide binding protein. *Proc Natl Acad Sci USA* **90**, 1053 (1993).

7 RayChaudhuri, D. & Park, J. T. Escherichia coli cell-division gene ftsZ encodes a novel GTP-binding protein. *Nature* **359**, 251-254, doi:10.1038/359251a0 (1992).

8 Erickson, H. P. The discovery of the prokaryotic cytoskeleton: 25th anniversary. *Molecular biology of the cell* **28**, 357-358, doi:10.1091/mbc.E16-03-0183 (2017).

9 Wickstead, B. & Gull, K. The evolution of the cytoskeleton. *The Journal of cell biology* **194**, 513 (2011).

10 Evans, L., Mitchison, T. & Kirschner, M. Influence of the centrosome on the structure of nucleated microtubules. *The Journal of cell biology* **100**, 1185-1191 (1985).

11 Bartolini, F. & Gundersen, G. G. Generation of noncentrosomal microtubule arrays. *J Cell Sci* **119**, 4155-4163, doi:10.1242/jcs.03227 (2006).

12 Howard, J. & Hyman, A. A. Dynamics and mechanics of the microtubule plus end. *Nature* **422**, 753-758, doi:10.1038/nature01600 (2003).

13 de Forges, H., Bouissou, A. & Perez, F. Interplay between microtubule dynamics and intracellular organization. *The international journal of biochemistry & cell biology* **44**, 266-274, doi:10.1016/j.biocel.2011.11.009 (2012).

14 Hirokawa, N. Kinesin and dynein superfamily proteins and the mechanism of organelle transport. *Science* **279**, 519-526 (1998).

15 Berg, J. S., Powell, B. C. & Cheney, R. E. A millennial myosin census. *Molecular biology of the cell* **12**, 780-794, doi:10.1091/mbc.12.4.780 (2001).

16 Peckham, M. & Knight, P. J. When a predicted coiled coil is really a single α-helix, in myosins and other proteins. *Soft Matter* **5**, 2493-2503, doi:10.1039/B822339D (2009).

17 Huxley, H. E. Fifty years of muscle and the sliding filament hypothesis. *European Journal of Biochemistry* **271**, 1403-1415, doi:https://doi.org/10.1111/j.1432-1033.2004.04044.x (2004).

18 Vicente-Manzanares, M., Ma, X., Adelstein, R. S. & Horwitz, A. R. Non-muscle myosin II takes centre stage in cell adhesion and migration. *Nature Reviews Molecular Cell Biology* **10**, 778-790, doi:10.1038/nrm2786 (2009).

19 Hartman, M. A. & Spudich, J. A. The myosin superfamily at a glance. *Journal of cell science* **125**, 1627-1632, doi:10.1242/jcs.094300 (2012).

20 De La Cruz, E. M. & Ostap, E. M. Relating biochemistry and function in the myosin superfamily. *Current Opinion in Cell Biology* **16**, 61-67, doi:https://doi.org/10.1016/j.ceb.2003.11.011 (2004).
21 Gibbons, I. R. & Rowe, A. J. Dynein: A Protein with Adenosine Triphosphatase Activity from Cilia. *Science (New York, N.Y.)* **149**, 424-426, doi:10.1126/science.149.3682.424 (1965).
22 Paschal, B. M., Shpetner, H. S. & Vallee, R. B. MAP 1C is a microtubule-activated ATPase which translocates microtubules in vitro and has dynein-like properties. *J Cell Biol* **105**, 1273-1282, doi:10.1083/jcb.105.3.1273 (1987).
23 Schroer, T. A., Steuer, E. R. & Sheetz, M. P. Cytoplasmic dynein is a minus end-directed motor for membranous organelles. *Cell* **56**, 937-946, doi:10.1016/0092-8674(89)90627-2 (1989).
24 Vallee, R. B., Williams, J. C., Varma, D. & Barnhart, L. E. Dynein: An ancient motor protein involved in multiple modes of transport. *J Neurobiol* **58**, 189-200, doi:10.1002/neu.10314 (2004).
25 Cross, J. A. & Dodding, M. P. Motor-cargo adaptors at the organelle-cytoskeleton interface. *Curr Opin Cell Biol* **59**, 16-23, doi:10.1016/j.ceb.2019.02.010 (2019).
26 Reck-Peterson, S. L., Redwine, W. B., Vale, R. D. & Carter, A. P. The cytoplasmic dynein transport machinery and its many cargoes. *Nature Reviews Molecular Cell Biology* **19**, 382-398, doi:10.1038/s41580-018-0004-3 (2018).
27 Lawrence, C. J. *et al.* A standardized kinesin nomenclature. *The Journal of cell biology* **167**, 19-22, doi:10.1083/jcb.200408113 (2004).
28 Verhey, K. J. & Hammond, J. W. Traffic control: regulation of kinesin motors. *Nature reviews. Molecular cell biology* **10**, 765-777, doi:10.1038/nrm2782 (2009).
29 Hirokawa, N., Noda, Y., Tanaka, Y. & Niwa, S. Kinesin superfamily motor proteins and intracellular transport. *Nature reviews. Molecular cell biology* **10**, 682-696, doi:10.1038/nrm2774 (2009).
30 Goodson, H. V., Kang, S. J. & Endow, S. A. Molecular phylogeny of the kinesin family of microtubule motor proteins. *J Cell Sci* **107 (Pt 7)**, 1875-1884, doi:10.1242/jcs.107.7.1875 (1994).
31 Vale, R. D., Reese, T. S. & Sheetz, M. P. Identification of a novel force-generating protein, kinesin, involved in microtubule-based motility. *Cell* **42**, 39-50 (1985).
32 Dodding, M. P. & Way, M. Coupling viruses to dynein and kinesin-1. *The EMBO journal* **30**, 3527-3539, doi:10.1038/emboj.2011.283 (2011).
33 Boucrot, E., Henry, T., Borg, J. P., Gorvel, J. P. & Meresse, S. The intracellular fate of Salmonella depends on the recruitment of kinesin. *Science* **308**, 1174-1178, doi:10.1126/science.1110225 (2005).
34 Morihara, T. *et al.* Transcriptome analysis of distinct mouse strains reveals kinesin light chain-1 splicing as an amyloid-beta accumulation modifier. *Proc Natl Acad Sci U S A* **111**, 2638-2643, doi:10.1073/pnas.1307345111 (2014).
35 Bagshaw, C. R. & Trentham, D. R. The characterization of myosin-product complexes and of product-release steps during the magnesium ion-dependent adenosine triphosphatase reaction. *Biochem J* **141**, 331-349, doi:10.1042/bj1410331 (1974).
36 Hackney, D. D. Kinesin ATPase: rate-limiting ADP release. *Proceedings of the National Academy of Sciences of the United States of America* **85**, 6314-6318, doi:10.1073/pnas.85.17.6314 (1988).

37 Walker, M. L. *et al.* Two-headed binding of a processive myosin to F-actin. *Nature* **405**, 804-807, doi:10.1038/35015592 (2000).
38 Svoboda, K., Schmidt, C. F., Schnapp, B. J. & Block, S. M. Direct observation of kinesin stepping by optical trapping interferometry. *Nature* **365**, 721-727, doi:10.1038/365721a0 (1993).
39 Jon Kull, F., Sablin, E. P., Lau, R., Fletterick, R. J. & Vale, R. D. Crystal structure of the kinesin motor domain reveals a structural similarity to myosin. *Nature* **380**, 550-555, doi:10.1038/380550a0 (1996).
40 Hirokawa, N. *et al.* Submolecular domains of bovine brain kinesin identified by electron microscopy and monoclonal antibody decoration. *Cell* **56**, 867-878 (1989).
41 Kuznetsov, S. A. *et al.* The quaternary structure of bovine brain kinesin. *The EMBO journal* **7**, 353-356 (1988).
42 Xia, C., Rahman, A., Yang, Z. & Goldstein, L. S. Chromosomal localization reveals three kinesin heavy chain genes in mouse. *Genomics* **52**, 209-213, doi:10.1006/geno.1998.5427 (1998).
43 Stenson, P. D. *et al.* The Human Gene Mutation Database: towards a comprehensive repository of inherited mutation data for medical research, genetic diagnosis and next-generation sequencing studies. *Hum Genet* **136**, 665-677, doi:10.1007/s00439-017-1779-6 (2017).
44 Liu, Y. T. *et al.* Extended phenotypic spectrum of KIF5A mutations: From spastic paraplegia to axonal neuropathy. *Neurology* **83**, 612-619, doi:10.1212/wnl.0000000000000691 (2014).
45 DeBoer, S. R. *et al.* Conventional kinesin holoenzymes are composed of heavy and light chain homodimers. *Biochemistry* **47**, 4535-4543, doi:10.1021/bi702445j (2008).
46 Diefenbach, R. J., Mackay, J. P., Armati, P. J. & Cunningham, A. L. The C-terminal region of the stalk domain of ubiquitous human kinesin heavy chain contains the binding site for kinesin light chain. *Biochemistry* **37**, 16663-16670, doi:10.1021/bi981163r (1998).
47 Hackney, D. D. Jump-starting kinesin. *The Journal of cell biology* **176**, 7 (2007).
48 Yildiz, A., Tomishige, M., Gennerich, A. & Vale, R. D. Intramolecular strain coordinates kinesin stepping behavior along microtubules. *Cell* **134**, 1030-1041, doi:10.1016/j.cell.2008.07.018 (2008).
49 Rice, S. *et al.* A structural change in the kinesin motor protein that drives motility. *Nature* **402**, 778-784, doi:10.1038/45483 (1999).
50 Hackney, D. D. The tethered motor domain of a kinesin-microtubule complex catalyzes reversible synthesis of bound ATP. *Proceedings of the National Academy of Sciences of the United States of America* **102**, 18338-18343, doi:10.1073/pnas.0505288102 (2005).
51 Uemura, S. & Ishiwata, S. Loading direction regulates the affinity of ADP for kinesin. *Nat Struct Biol* **10**, 308-311, doi:10.1038/nsb911 (2003).
52 Asbury, C. L., Fehr, A. N. & Block, S. M. Kinesin moves by an asymmetric hand-over-hand mechanism. *Science (New York, N.Y.)* **302**, 2130-2134, doi:10.1126/science.1092985 (2003).
53 Yildiz, A., Tomishige, M., Vale, R. D. & Selvin, P. R. Kinesin Walks Hand-Over-Hand. *Science (New York, N.Y.)* **303**, 676, doi:10.1126/science.1093753 (2004).
54 Kawaguchi, K. Energetics of kinesin-1 stepping mechanism. *FEBS Letters* **582**, 3719-3722, doi:10.1016/j.febslet.2008.10.019 (2008).

55 Navone, F. *et al.* Cloning and expression of a human kinesin heavy chain gene: interaction of the COOH-terminal domain with cytoplasmic microtubules in transfected CV-1 cells. *The Journal of cell biology* **117**, 1263-1275 (1992).
56 Seeger, M. A. & Rice, S. E. Microtubule-associated protein-like binding of the kinesin-1 tail to microtubules. *The Journal of biological chemistry* **285**, 8155-8162, doi:10.1074/jbc.M109.068247 (2010).
57 Dietrich, K. A. *et al.* The kinesin-1 motor protein is regulated by a direct interaction of its head and tail. *Proc Natl Acad Sci U S A* **105**, 8938-8943, doi:10.1073/pnas.0803575105 (2008).
58 DeLuca, J. G., Newton, C. N., Himes, R. H., Jordan, M. A. & Wilson, L. Purification and characterization of native conventional kinesin, HSET, and CENP-E from mitotic hela cells. *The Journal of biological chemistry* **276**, 28014-28021, doi:10.1074/jbc.M102801200 (2001).
59 Yip, Y. Y. *et al.* The light chains of kinesin-1 are autoinhibited. *Proceedings of the National Academy of Sciences of the United States of America* **113**, 2418-2423, doi:10.1073/pnas.1520817113 (2016).
60 D'Andrea, L. D. & Regan, L. TPR proteins: the versatile helix. *Trends in biochemical sciences* **28**, 655-662, doi:10.1016/j.tibs.2003.10.007 (2003).
61 Lamb, J. R., Tugendreich, S. & Hieter, P. Tetratrico peptide repeat interactions: to TPR or not to TPR? *Trends in biochemical sciences* **20**, 257-259 (1995).
62 Scheufler, C. *et al.* Structure of TPR domain-peptide complexes: critical elements in the assembly of the Hsp70-Hsp90 multichaperone machine. *Cell* **101**, 199-210, doi:10.1016/s0092-8674(00)80830-2 (2000).
63 Gatto, G. J., Jr., Geisbrecht, B. V., Gould, S. J. & Berg, J. M. Peroxisomal targeting signal-1 recognition by the TPR domains of human PEX5. *Nat Struct Biol* **7**, 1091-1095, doi:10.1038/81930 (2000).
64 Cliff, M. J., Harris, R., Barford, D., Ladbury, J. E. & Williams, M. A. Conformational diversity in the TPR domain-mediated interaction of protein phosphatase 5 with Hsp90. *Structure* **14**, 415-426, doi:10.1016/j.str.2005.12.009 (2006).
65 Hammond, J. W., Griffin, K., Jih, G. T., Stuckey, J. & Verhey, K. J. Co-operative versus independent transport of different cargoes by Kinesin-1. *Traffic (Copenhagen, Denmark)* **9**, 725-741, doi:10.1111/j.1600-0854.2008.00722.x (2008).
66 Cortajarena, A. L. & Regan, L. Ligand binding by TPR domains. *Protein science : a publication of the Protein Society* **15**, 1193-1198, doi:10.1110/ps.062092506 (2006).
67 Pernigo, S., Lamprecht, A., Steiner, R. A. & Dodding, M. P. Structural basis for kinesin-1:cargo recognition. *Science* **340**, 356-359, doi:10.1126/science.1234264 (2013).
68 Pernigo, S. *et al.* Structural basis for isoform-specific kinesin-1 recognition of Y-acidic cargo adaptors. *eLife* **7**, doi:10.7554/eLife.38362 (2018).
69 Antón, Z. *et al.* Molecular mechanism for kinesin-1 direct membrane recognition. *Sci Adv* **7**, doi:10.1126/sciadv.abg6636 (2021).
70 Gyoeva, F. K., Bybikova, E. M. & Minin, A. A. An isoform of kinesin light chain specific for the Golgi complex. *Journal of cell science* **113 (Pt 11)**, 2047-2054 (2000).
71 Woźniak, M. J. & Allan, V. J. Cargo selection by specific kinesin light chain 1 isoforms. *The EMBO journal* **25**, 5457-5468, doi:10.1038/sj.emboj.7601427 (2006).
72 Khodjakov, A., Lizunova, E. M., Minin, A. A., Koonce, M. P. & Gyoeva, F. K. A specific light chain of kinesin associates with mitochondria in cultured cells. *Molecular biology of the cell* **9**, 333-343, doi:10.1091/mbc.9.2.333 (1998).

73 Maliga, Z. *et al.* A genomic toolkit to investigate kinesin and myosin motor function in cells. *Nat Cell Biol* **15**, 325-334, doi:10.1038/ncb2689 (2013).
74 Hisanaga, S. *et al.* The molecular structure of adrenal medulla kinesin. *Cell Motil Cytoskeleton* **12**, 264-272, doi:10.1002/cm.970120407 (1989).
75 Hackney, D. D., Levitt, J. D. & Suhan, J. Kinesin undergoes a 9 S to 6 S conformational transition. *The Journal of biological chemistry* **267**, 8696-8701 (1992).
76 Stock, M. F. *et al.* Formation of the compact confomer of kinesin requires a COOH-terminal heavy chain domain and inhibits microtubule-stimulated ATPase activity. *The Journal of biological chemistry* **274**, 14617-14623, doi:10.1074/jbc.274.21.14617 (1999).
77 Cai, D., Hoppe, A. D., Swanson, J. A. & Verhey, K. J. Kinesin-1 structural organization and conformational changes revealed by FRET stoichiometry in live cells. *The Journal of cell biology* **176**, 51-63, doi:10.1083/jcb.200605097 (2007).
78 Coy, D. L., Hancock, W. O., Wagenbach, M. & Howard, J. Kinesin's tail domain is an inhibitory regulator of the motor domain. *Nat Cell Biol* **1**, 288-292, doi:10.1038/13001 (1999).
79 Hackney, D. D., Baek, N. & Snyder, A. C. Half-site inhibition of dimeric kinesin head domains by monomeric tail domains. *Biochemistry* **48**, 3448-3456, doi:10.1021/bi8022575 (2009).
80 Hackney, D. D. & Stock, M. F. Kinesin's IAK tail domain inhibits initial microtubule-stimulated ADP release. *Nature cell biology* **2**, 257-260, doi:10.1038/35010525 (2000).
81 Kaan, H. Y., Hackney, D. D. & Kozielski, F. The structure of the kinesin-1 motor-tail complex reveals the mechanism of autoinhibition. *Science* **333**, 883-885, doi:10.1126/science.1204824 (2011).
82 Friedman, D. S. & Vale, R. D. Single-molecule analysis of kinesin motility reveals regulation by the cargo-binding tail domain. *Nat Cell Biol* **1**, 293-297, doi:10.1038/13008 (1999).
83 Verhey, K. J. *et al.* Light chain-dependent regulation of Kinesin's interaction with microtubules. *The Journal of cell biology* **143**, 1053-1066 (1998).
84 Wong, Y. L. & Rice, S. E. Kinesin's light chains inhibit the head- and microtubule-binding activity of its tail. *Proc Natl Acad Sci USA* **107**, 11781, doi:10.1073/pnas.1005854107 (2010).
85 Fu, M. M. & Holzbaur, E. L. Integrated regulation of motor-driven organelle transport by scaffolding proteins. *Trends in cell biology* **24**, 564-574, doi:10.1016/j.tcb.2014.05.002 (2014).
86 Blasius, T. L., Cai, D., Jih, G. T., Toret, C. P. & Verhey, K. J. Two binding partners cooperate to activate the molecular motor Kinesin-1. *The Journal of cell biology* **176**, 11-17, doi:10.1083/jcb.200605099 (2007).
87 Sanger, A. *et al.* SKIP controls lysosome positioning using a composite kinesin-1 heavy and light chain-binding domain. *Journal of cell science* **130**, 1637-1651, doi:10.1242/jcs.198267 (2017).
88 Kawano, T. *et al.* A small peptide sequence is sufficient for initiating kinesin-1 activation through part of TPR region of KLC1. *Traffic (Copenhagen, Denmark)* **13**, 834-848, doi:10.1111/j.1600-0854.2012.01350.x (2012).
89 Sun, F., Zhu, C., Dixit, R. & Cavalli, V. Sunday Driver/JIP3 binds kinesin heavy chain directly and enhances its motility. *The EMBO journal* **30**, 3416-3429, doi:10.1038/emboj.2011.229 (2011).

90 Gindhart, J. G. *et al.* The kinesin-associated protein UNC-76 is required for axonal transport in the Drosophila nervous system. *Molecular biology of the cell* **14**, 3356-3365, doi:10.1091/mbc.e02-12-0800 (2003).
91 Dimitrova-Paternoga, L. *et al.* Molecular basis of mRNA transport by a kinesin-1-atypical tropomyosin complex. *Genes Dev* **35**, 976-991, doi:10.1101/gad.348443.121 (2021).
92 Barry, J. *et al.* Ankyrin-G directly binds to kinesin-1 to transport voltage-gated Na+ channels into axons. *Developmental cell* **28**, 117-131, doi:10.1016/j.devcel.2013.11.023 (2014).
93 Xu, M., Gu, Y., Barry, J. & Gu, C. Kinesin I transports tetramerized Kv3 channels through the axon initial segment via direct binding. *The Journal of neuroscience : the official journal of the Society for Neuroscience* **30**, 15987-16001, doi:10.1523/jneurosci.3565-10.2010 (2010).
94 Setou, M. *et al.* Glutamate-receptor-interacting protein GRIP1 directly steers kinesin to dendrites. *Nature* **417**, 83-87, doi:10.1038/nature743 (2002).
95 Macioce, P. *et al.* Beta-dystrobrevin interacts directly with kinesin heavy chain in brain. *J Cell Sci* **116**, 4847-4856, doi:10.1242/jcs.00805 (2003).
96 Randall, T. S., Moores, C. & Stephenson, F. A. Delineation of the TRAK binding regions of the kinesin-1 motor proteins. *FEBS letters* **587**, 3763-3769, doi:10.1016/j.febslet.2013.09.049 (2013).
97 Diefenbach, R. J. *et al.* Herpes simplex virus tegument protein US11 interacts with conventional kinesin heavy chain. *J Virol* **76**, 3282-3291, doi:10.1128/jvi.76.7.3282-3291.2002 (2002).
98 Brickley, K., Smith, M. J., Beck, M. & Stephenson, F. A. GRIF-1 and OIP106, Members of a Novel Gene Family of Coiled-Coil Domain Proteins: ASSOCIATION IN VIVO AND IN VITRO WITH KINESIN*. *Journal of Biological Chemistry* **280**, 14723-14732, doi:https://doi.org/10.1074/jbc.M409095200 (2005).
99 Diefenbach, R. J., Diefenbach, E., Douglas, M. W. & Cunningham, A. L. The Heavy Chain of Conventional Kinesin Interacts with the SNARE Proteins SNAP25 and SNAP23. *Biochemistry* **41**, 14906-14915, doi:10.1021/bi026417u (2002).
100 Cai, Y., Singh, B. B., Aslanukov, A., Zhao, H. & Ferreira, P. A. The docking of kinesins, KIF5B and KIF5C, to Ran-binding protein 2 (RanBP2) is mediated via a novel RanBP2 domain. *The Journal of biological chemistry* **276**, 41594-41602, doi:10.1074/jbc.M104514200 (2001).
101 Ong, L. L., Lim, A. P., Er, C. P., Kuznetsov, S. A. & Yu, H. Kinectin-kinesin binding domains and their effects on organelle motility. *The Journal of biological chemistry* **275**, 32854-32860, doi:10.1074/jbc.M005650200 (2000).
102 Huang, J. D. *et al.* Direct interaction of microtubule- and actin-based transport motors. *Nature* **397**, 267-270, doi:10.1038/16722 (1999).
103 Zhu, H. *et al.* Crystal structures of the tetratricopeptide repeat domains of kinesin light chains: insight into cargo recognition mechanisms. *PloS one* **7**, e33943, doi:10.1371/journal.pone.0033943 (2012).
104 Cockburn, J. J. B. *et al.* Insights into Kinesin-1 Activation from the Crystal Structure of KLC2 Bound to JIP3. *Structure* **26**, 1486-1498.e1486, doi:https://doi.org/10.1016/j.str.2018.07.011 (2018).

105 Dodding, M. P., Mitter, R., Humphries, A. C. & Way, M. A kinesin-1 binding motif in vaccinia virus that is widespread throughout the human genome. *The EMBO journal* **30**, 4523-4538, doi:10.1038/emboj.2011.326 (2011).
106 Aoyama, T. *et al.* Cayman ataxia protein caytaxin is transported by kinesin along neurites through binding to kinesin light chains. *J. Cell Sci.* **122**, 4177 (2009).
107 Konecna, A. *et al.* Calsyntenin-1 docks vesicular cargo to kinesin-1. *Molecular biology of the cell* **17**, 3651-3663, doi:10.1091/mbc.e06-02-0112 (2006).
108 Schmidt, M. R. *et al.* Regulation of endosomal membrane traffic by a Gadkin/AP-1/kinesin KIF5 complex. *Proc Natl Acad Sci U S A* **106**, 15344-15349, doi:10.1073/pnas.0904268106 (2009).
109 Araki, Y. *et al.* The novel cargo Alcadein induces vesicle association of kinesin-1 motor components and activates axonal transport. *The EMBO journal* **26**, 1475-1486, doi:10.1038/sj.emboj.7601609 (2007).
110 Rosa-Ferreira, C. & Munro, S. Arl8 and SKIP act together to link lysosomes to kinesin-1. *Developmental cell* **21**, 1171-1178, doi:10.1016/j.devcel.2011.10.007 (2011).
111 McGuire, J. R., Rong, J., Li, S. H. & Li, X. J. Interaction of Huntingtin-associated protein-1 with kinesin light chain: implications in intracellular trafficking in neurons. *The Journal of biological chemistry* **281**, 3552-3559, doi:10.1074/jbc.M509806200 (2006).
112 Pu, J. *et al.* BORC, a multisubunit complex that regulates lysosome positioning. *Developmental cell* **33**, 176-188, doi:10.1016/j.devcel.2015.02.011 (2015).
113 Matsuda, S. *et al.* c-Jun N-terminal kinase (JNK)-interacting protein-1b/islet-brain-1 scaffolds Alzheimer's amyloid precursor protein with JNK. *J Neurosci* **21**, 6597-6607 (2001).
114 Scheinfeld, M. H. *et al.* Jun NH2-terminal kinase (JNK) interacting protein 1 (JIP1) binds the cytoplasmic domain of the Alzheimer's beta-amyloid precursor protein (APP). *The Journal of biological chemistry* **277**, 3767-3775, doi:10.1074/jbc.M108357200 (2002).
115 Kamm, C. *et al.* The early onset dystonia protein torsinA interacts with kinesin light chain 1. *The Journal of biological chemistry* **279**, 19882-19892, doi:10.1074/jbc.M401332200 (2004).
116 Lu, W. & Gelfand, V. I. Moonlighting Motors: Kinesin, Dynein, and Cell Polarity. *Trends in cell biology* **27**, 505-514, doi:10.1016/j.tcb.2017.02.005 (2017).
117 Riechmann, V. & Ephrussi, A. Axis formation during Drosophila oogenesis. *Current Opinion in Genetics & Development* **11**, 374-383, doi:https://doi.org/10.1016/S0959-437X(00)00207-0 (2001).
118 Brendza, R. P., Serbus, L. R., Duffy, J. B. & Saxton, W. M. A function for kinesin I in the posterior transport of oskar mRNA and Staufen protein. *Science (New York, N.Y.)* **289**, 2120-2122, doi:10.1126/science.289.5487.2120 (2000).
119 Palacios, I. M. & St Johnston, D. Kinesin light chain-independent function of the Kinesin heavy chain in cytoplasmic streaming and posterior localisation in the Drosophila oocyte. *Development* **129**, 5473-5485, doi:10.1242/dev.00119 (2002).
120 Lu, W., Winding, M., Lakonishok, M., Wildonger, J. & Gelfand, V. I. Microtubule–microtubule sliding by kinesin-1 is essential for normal cytoplasmic streaming in Drosophila oocytes. *Proc Natl Acad Sci USA* **113**, E4995-E5004, doi:10.1073/pnas.1522424113 (2016).
121 Lu, W., Fox, P., Lakonishok, M., Davidson, M. W. & Gelfand, V. I. Initial neurite outgrowth in Drosophila neurons is driven by kinesin-powered microtubule sliding. *Curr Biol* **23**, 1018-1023, doi:10.1016/j.cub.2013.04.050 (2013).

122 Lu, W., Lakonishok, M. & Gelfand, V. I. Kinesin-1-powered microtubule sliding initiates axonal regeneration in Drosophila cultured neurons. *Molecular biology of the cell* **26**, 1296-1307, doi:10.1091/mbc.E14-10-1423 (2015).
123 Straube, A., Hause, G., Fink, G. & Steinberg, G. Conventional kinesin mediates microtubule-microtubule interactions in vivo. *Molecular biology of the cell* **17**, 907-916, doi:10.1091/mbc.e05-06-0542 (2006).
124 Steinberg, G., Wedlich-Söldner, R., Brill, M. & Schulz, I. Microtubules in the fungal pathogen Ustilago maydis are highly dynamic and determine cell polarity. *J Cell Sci* **114**, 609-622 (2001).
125 Kulić, I. M. *et al.* The role of microtubule movement in bidirectional organelle transport. *Proc Natl Acad Sci USA* **105**, 10011-10016, doi:10.1073/pnas.0800031105 (2008).
126 Jolly, A. L. *et al.* Kinesin-1 heavy chain mediates microtubule sliding to drive changes in cell shape. *Proc Natl Acad Sci USA* **107**, 12151-12156, doi:10.1073/pnas.1004736107 (2010).
127 Bicek, A. D. *et al.* Anterograde microtubule transport drives microtubule bending in LLC-PK1 epithelial cells. *Molecular biology of the cell* **20**, 2943-2953, doi:10.1091/mbc.e08-09-0909 (2009).
128 De Vos, K. J., Grierson, A. J., Ackerley, S. & Miller, C. C. Role of axonal transport in neurodegenerative diseases. *Annual review of neuroscience* **31**, 151-173, doi:10.1146/annurev.neuro.31.061307.090711 (2008).
129 Millecamps, S. & Julien, J. P. Axonal transport deficits and neurodegenerative diseases. *Nature reviews. Neuroscience* **14**, 161-176, doi:10.1038/nrn3380 (2013).
130 Hirokawa, N., Niwa, S. & Tanaka, Y. Molecular motors in neurons: transport mechanisms and roles in brain function, development, and disease. *Neuron* **68**, 610-638, doi:10.1016/j.neuron.2010.09.039 (2010).
131 Hardy, J. A hundred years of Alzheimer's disease research. *Neuron* **52**, 3-13, doi:10.1016/j.neuron.2006.09.016 (2006).
132 Kamal, A., Stokin, G. B., Yang, Z., Xia, C.-H. & Goldstein, L. S. B. Axonal Transport of Amyloid Precursor Protein Is Mediated by Direct Binding to the Kinesin Light Chain Subunit of Kinesin-I. **28**, 449-459 (2000).
133 Lazarov, O. *et al.* Axonal transport, amyloid precursor protein, kinesin-1, and the processing apparatus: revisited. *The Journal of neuroscience : the official journal of the Society for Neuroscience* **25**, 2386-2395, doi:10.1523/jneurosci.3089-04.2005 (2005).
134 Stokin, G. B. *et al.* Axonopathy and transport deficits early in the pathogenesis of Alzheimer's disease. *Science* **307**, 1282-1288, doi:10.1126/science.1105681 (2005).
135 Pigino, G. *et al.* Alzheimer's presenilin 1 mutations impair kinesin-based axonal transport. *The Journal of neuroscience : the official journal of the Society for Neuroscience* **23**, 4499-4508 (2003).
136 Vagnoni, A. *et al.* Calsyntenin-1 mediates axonal transport of the amyloid precursor protein and regulates Aβ production. *Hum Mol Genet* **21**, 2845-2854, doi:10.1093/hmg/dds109 (2012).
137 Dumont, A. *et al.* SKIP, the host target of the Salmonella virulence factor SifA, promotes kinesin-1-dependent vacuolar membrane exchanges. *Traffic (Copenhagen, Denmark)* **11**, 899-911, doi:10.1111/j.1600-0854.2010.01069.x (2010).

138 Loong, H. H. & Yeo, W. Microtubule-targeting agents in oncology and therapeutic potential in hepatocellular carcinoma. *OncoTargets and therapy* **7**, 575-585, doi:10.2147/ott.S46019 (2014).
139 Yang, C. H. & Horwitz, S. B. Taxol(®): The First Microtubule Stabilizing Agent. *International journal of molecular sciences* **18**, doi:10.3390/ijms18081733 (2017).
140 Himes, R. H. Interactions of the catharanthus (Vinca) alkaloids with tubulin and microtubules. *Pharmacology & therapeutics* **51**, 257-267 (1991).
141 Pei, Y. Y., Li, G. C., Ran, J. & Wei, F. X. Kinesin family member 11 contributes to the progression and prognosis of human breast cancer. *Oncology letters* **14**, 6618-6626, doi:10.3892/ol.2017.7053 (2017).
142 Varidaki, A., Hong, Y. & Coffey, E. T. Repositioning Microtubule Stabilizing Drugs for Brain Disorders. *Frontiers in cellular neuroscience* **12**, 226, doi:10.3389/fncel.2018.00226 (2018).
143 Randall, T. S. *et al.* A small-molecule activator of kinesin-1 drives remodeling of the microtubule network. *Proc Natl Acad Sci U S A* **114**, 13738-13743, doi:10.1073/pnas.1715115115 (2017).
144 Ruffner, H., Bauer, A. & Bouwmeester, T. Human protein-protein interaction networks and the value for drug discovery. *Drug Discov Today* **12**, 709-716, doi:10.1016/j.drudis.2007.07.011 (2007).
145 Braun, P. & Gingras, A. C. History of protein-protein interactions: from egg-white to complex networks. *Proteomics* **12**, 1478-1498, doi:10.1002/pmic.201100563 (2012).
146 Berman, H. M. *et al.* The Protein Data Bank. *Nucleic Acids Research* **28**, 235-242, doi:10.1093/nar/28.1.235 (2000).
147 Woolfson, D. N. A Brief History of De Novo Protein Design: Minimal, Rational, and Computational. *Journal of Molecular Biology* **433**, 167160, doi:https://doi.org/10.1016/j.jmb.2021.167160 (2021).
148 Yennamalli, R. M. in *Encyclopedia of Bioinformatics and Computational Biology* (eds Shoba Ranganathan, Michael Gribskov, Kenta Nakai, & Christian Schönbach) 644-651 (Academic Press, 2019).
149 Lupas, A. N. What I cannot create, I do not understand. *Science (New York, N.Y.)* **346**, 1455, doi:10.1126/science.aaa2721 (2014).
150 Rose, P. W. *et al.* The RCSB protein data bank: integrative view of protein, gene and 3D structural information. *Nucleic acids research* **45**, D271-d281, doi:10.1093/nar/gkw1000 (2017).
151 Walshaw, J. & Woolfson, D. N. SOCKET: A program for identifying and analysing coiled-coil motifs within protein structures. *J. Mol. Biol.* **307**, 1427-1450, doi:10.1006/jmbi.2001.4545 (2001).
152 Brannigan, J. A. & Wilkinson, A. J. Protein engineering 20 years on. *Nature Reviews Molecular Cell Biology* **3**, 964-970, doi:10.1038/nrm975 (2002).
153 Shaw, W. V. Protein engineering. The design, synthesis and characterization of factitious proteins. *Biochem J* **246**, 1-17, doi:10.1042/bj2460001 (1987).
154 Main, E. R., Lowe, A. R., Mochrie, S. G., Jackson, S. E. & Regan, L. A recurring theme in protein engineering: the design, stability and folding of repeat proteins. *Current opinion in structural biology* **15**, 464-471, doi:10.1016/j.sbi.2005.07.003 (2005).
155 Brustad, E. M. & Arnold, F. H. Optimizing non-natural protein function with directed evolution. *Curr Opin Chem Biol* **15**, 201-210, doi:10.1016/j.cbpa.2010.11.020 (2011).

156 Chica, R. A., Doucet, N. & Pelletier, J. N. Semi-rational approaches to engineering enzyme activity: combining the benefits of directed evolution and rational design. *Curr Opin Biotechnol* **16**, 378-384, doi:10.1016/j.copbio.2005.06.004 (2005).
157 Arnold, F. H. Engineering enzymes for non-aqueous solvents. *Trends in Biotechnology* **8**, 244-249, doi:https://doi.org/10.1016/0167-7799(90)90186-2 (1990).
158 Wijma, H. & Janssen, D. Computational design gains momentum in enzyme catalysis engineering. *The FEBS journal*, doi:10.1111/febs.12324 (2013).
159 Arnold, F. H. Protein design for non-aqueous solvents. *Protein Engineering, Design and Selection* **2**, 21-25, doi:10.1093/protein/2.1.21 (1988).
160 Jäckel, C., Bloom, J. D., Kast, P., Arnold, F. H. & Hilvert, D. Consensus protein design without phylogenetic bias. *J Mol Biol* **399**, 541-546, doi:10.1016/j.jmb.2010.04.039 (2010).
161 Chen, K. & Arnold, F. H. Tuning the activity of an enzyme for unusual environments: sequential random mutagenesis of subtilisin E for catalysis in dimethylformamide. *Proceedings of the National Academy of Sciences of the United States of America* **90**, 5618-5622, doi:10.1073/pnas.90.12.5618 (1993).
162 Arnold, F. H. Design by Directed Evolution. *Accounts of Chemical Research* **31**, 125-131, doi:10.1021/ar960017f (1998).
163 Barderas, R. & Benito-Peña, E. The 2018 Nobel Prize in Chemistry: phage display of peptides and antibodies. *Anal Bioanal Chem* **411**, 2475-2479, doi:10.1007/s00216-019-01714-4 (2019).
164 Smith, G. P. & Petrenko, V. A. Phage Display. *Chem. Rev.* **97**, 391-410, doi:10.1021/cr960065d (1997).
165 Hoogenboom, H. R. *et al.* Multi-subunit proteins on the surface of filamentous phage: methodologies for displaying antibody (Fab) heavy and light chains. *Nucleic acids research* **19**, 4133-4137, doi:10.1093/nar/19.15.4133 (1991).
166 Porter, J. L., Rusli, R. A. & Ollis, D. L. Directed Evolution of Enzymes for Industrial Biocatalysis. *Chembiochem* **17**, 197-203, doi:10.1002/cbic.201500280 (2016).
167 Kumar, A. & Singh, S. Directed evolution: tailoring biocatalysts for industrial applications. *Crit Rev Biotechnol* **33**, 365-378, doi:10.3109/07388551.2012.716810 (2013).
168 Liu, C. C. & Schultz, P. G. Adding New Chemistries to the Genetic Code. *Annual Review of Biochemistry* **79**, 413-444, doi:10.1146/annurev.biochem.052308.105824 (2010).
169 Wang, L., Xie, J. & Schultz, P. G. Expanding the genetic code. *Annu Rev Biophys Biomol Struct* **35**, 225-249, doi:10.1146/annurev.biophys.35.101105.121507 (2006).
170 Axup, J. Y. *et al.* Synthesis of site-specific antibody-drug conjugates using unnatural amino acids. *Proc Natl Acad Sci USA* **109**, 16101, doi:10.1073/pnas.1211023109 (2012).
171 Hutchins, Benjamin M. *et al.* Selective Formation of Covalent Protein Heterodimers with an Unnatural Amino Acid. *Chemistry & Biology* **18**, 299-303, doi:https://doi.org/10.1016/j.chembiol.2011.01.006 (2011).
172 Mandecki, W. The game of chess and searches in protein sequence space. *Trends in Biotechnology* **16**, 200-202, doi:10.1016/S0167-7799(98)01188-3 (1998).
173 Dryden, D. T., Thomson, A. R. & White, J. H. How much of protein sequence space has been explored by life on Earth? *J R Soc Interface* **5**, 953-956, doi:10.1098/rsif.2008.0085 (2008).

174 Smith, J. M. Natural selection and the concept of a protein space. *Nature* **225**, 563-564, doi:10.1038/225563a0 (1970).
175 Taylor, W. R., Chelliah, V., Hollup, S. M., MacDonald, J. T. & Jonassen, I. Probing the "dark matter" of protein fold space. *Structure* **17**, 1244-1252, doi:10.1016/j.str.2009.07.012 (2009).
176 Woolfson, D. N. *et al.* De novo protein design: how do we expand into the universe of possible protein structures? *Current opinion in structural biology* **33**, 16-26, doi:10.1016/j.sbi.2015.05.009 (2015).
177 Richardson, J. S. & Richardson, D. C. The de novo design of protein structures. *Trends in biochemical sciences* **14**, 304-309, doi:10.1016/0968-0004(89)90070-4 (1989).
178 Yue, K. & Dill, K. A. Inverse protein folding problem: designing polymer sequences. *Proceedings of the National Academy of Sciences of the United States of America* **89**, 4163-4167, doi:10.1073/pnas.89.9.4163 (1992).
179 Pabo, C. Molecular technology: Designing proteins and peptides. *Nature* **301**, 200-200, doi:10.1038/301200a0 (1983).
180 Pawson, T. & Scott, J. D. Signaling through scaffold, anchoring, and adaptor proteins. *Science* **278**, 2075-2080 (1997).
181 Sudol, M. From Src Homology domains to other signaling modules: proposal of the 'protein recognition code'. *Oncogene* **17**, 1469-1474, doi:10.1038/sj.onc.1202182 (1998).
182 Puntervoll, P. *et al.* ELM server: A new resource for investigating short functional sites in modular eukaryotic proteins. *Nucleic acids research* **31**, 3625-3630 (2003).
183 Neduva, V. *et al.* Systematic discovery of new recognition peptides mediating protein interaction networks. *PLoS biology* **3**, e405, doi:10.1371/journal.pbio.0030405 (2005).
184 London, N., Raveh B Fau - Schueler-Furman, O. & Schueler-Furman, O. Druggable protein-protein interactions--from hot spots to hot segments.
185 Prelich, G. & Stillman, B. Coordinated leading and lagging strand synthesis during SV40 DNA replication in vitro requires PCNA. *Cell* **53**, 117-126 (1988).
186 Pawson, T. & Nash, P. Assembly of cell regulatory systems through protein interaction domains. *Science* **300**, 445-452, doi:10.1126/science.1083653 (2003).
187 Paroush, Z. *et al.* Groucho is required for Drosophila neurogenesis, segmentation, and sex determination and interacts directly with hairy-related bHLH proteins. *Cell* **79**, 805-815 (1994).
188 Neduva, V. & Russell, R. B. Linear motifs: evolutionary interaction switches. *FEBS letters* **579**, 3342-3345, doi:10.1016/j.febslet.2005.04.005 (2005).
189 Reichen, C., Hansen, S. & Pluckthun, A. Modular peptide binding: from a comparison of natural binders to designed armadillo repeat proteins. *J Struct Biol* **185**, 147-162, doi:10.1016/j.jsb.2013.07.012 (2014).
190 Grove, T. Z., Cortajarena, A. L. & Regan, L. Ligand binding by repeat proteins: natural and designed. *Current opinion in structural biology* **18**, 507-515, doi:10.1016/j.sbi.2008.05.008 (2008).
191 Teague, S. J. Implications of protein flexibility for drug discovery. *Nature reviews. Drug discovery* **2**, 527-541, doi:10.1038/nrd1129 (2003).
192 Clackson, T. & Wells, J. A. A hot spot of binding energy in a hormone-receptor interface. *Science* **267**, 383-386 (1995).

193 Arkin, M. R., Tang, Y. & Wells, J. A. Small-molecule inhibitors of protein-protein interactions: progressing toward the reality. *Chemistry & biology* **21**, 1102-1114, doi:10.1016/j.chembiol.2014.09.001 (2014).
194 Cunningham, B. C. & Wells, J. A. High-resolution epitope mapping of hGH-receptor interactions by alanine-scanning mutagenesis. *Science* **244**, 1081-1085 (1989).
195 Wells, J. A. & McClendon, C. L. Reaching for high-hanging fruit in drug discovery at protein–protein interfaces. **450**, 1001 (2007).
196 Vassilev, L. T. *et al.* In vivo activation of the p53 pathway by small-molecule antagonists of MDM2. *Science* **303**, 844-848, doi:10.1126/science.1092472 (2004).
197 Petros, A. M. *et al.* Discovery of a potent inhibitor of the antiapoptotic protein Bcl-xL from NMR and parallel synthesis. *Journal of medicinal chemistry* **49**, 656-663, doi:10.1021/jm0507532 (2006).
198 Thanos, C. D., Randal, M. & Wells, J. A. Potent small-molecule binding to a dynamic hot spot on IL-2. *J Am Chem Soc* **125**, 15280-15281, doi:10.1021/ja0382617 (2003).
199 Taylor, I. R. *et al.* High-throughput screen for inhibitors of protein-protein interactions in a reconstituted heat shock protein 70 (Hsp70) complex. *The Journal of biological chemistry* **293**, 4014-4025, doi:10.1074/jbc.RA117.001575 (2018).
200 Hamzeh-Mivehroud, M., Alizadeh Aa Fau - Morris, M. B., Morris Mb Fau - Church, W. B., Church Wb Fau - Dastmalchi, S. & Dastmalchi, S. Phage display as a technology delivering on the promise of peptide drug discovery.
201 Willats, W. G. Phage display: practicalities and prospects. *Plant molecular biology* **50**, 837-854 (2002).
202 Kondo, A. & Ueda, M. Yeast cell-surface display--applications of molecular display. *Applied microbiology and biotechnology* **64**, 28-40, doi:10.1007/s00253-003-1492-3 (2004).
203 van Bloois, E., Winter, R. T., Kolmar, H. & Fraaije, M. W. Decorating microbes: surface display of proteins on Escherichia coli. *Trends in biotechnology* **29**, 79-86, doi:10.1016/j.tibtech.2010.11.003 (2011).
204 Beerli, R. R. *et al.* Isolation of human monoclonal antibodies by mammalian cell display. *Proc Natl Acad Sci U S A* **105**, 14336-14341, doi:10.1073/pnas.0805942105 (2008).
205 London, N., Raveh, B. & Schueler-Furman, O. Peptide docking and structure-based characterization of peptide binding: from knowledge to know-how. *Current opinion in structural biology* **23**, 894-902, doi:10.1016/j.sbi.2013.07.006 (2013).
206 Rajamani, D., Thiel, S., Vajda, S. & Camacho, C. J. Anchor residues in protein-protein interactions. *Proc Natl Acad Sci U S A* **101**, 11287-11292, doi:10.1073/pnas.0401942101 (2004).
207 Massova, I. & Kollman, P. A. Computational Alanine Scanning To Probe Protein−Protein Interactions: A Novel Approach To Evaluate Binding Free Energies. *J. Am. Chem. Soc.* **121**, 8133-8143 (1999).
208 Hall, D. R., Kozakov, D., Whitty, A. & Vajda, S. Lessons from Hot Spot Analysis for Fragment-Based Drug Discovery. *Trends in pharmacological sciences* **36**, 724-736, doi:10.1016/j.tips.2015.08.003 (2015).
209 Jochim, A. L. & Arora, P. S. Systematic analysis of helical protein interfaces reveals targets for synthetic inhibitors. *ACS chemical biology* **5**, 919-923, doi:10.1021/cb1001747 (2010).

210 Guharoy, M. & Chakrabarti, P. Secondary structure based analysis and classification of biological interfaces: identification of binding motifs in protein-protein interactions. *Bioinformatics* **23**, 1909-1918, doi:10.1093/bioinformatics/btm274 (2007).
211 Rezaei Araghi, R. & Keating, A. E. Designing helical peptide inhibitors of protein-protein interactions. *Current opinion in structural biology* **39**, 27-38, doi:10.1016/j.sbi.2016.04.001 (2016).
212 Pelay-Gimeno, M., Glas, A., Koch, O. & Grossmann, T. N. Structure-Based Design of Inhibitors of Protein-Protein Interactions: Mimicking Peptide Binding Epitopes. *Angewandte Chemie (International ed. in English)* **54**, 8896-8927, doi:10.1002/anie.201412070 (2015).
213 Verdine, G. L. & Hilinski, G. J. Stapled peptides for intracellular drug targets. *Methods in enzymology* **503**, 3-33, doi:10.1016/b978-0-12-396962-0.00001-x (2012).
214 Rooklin, D., Wang, C., Katigbak, J., Arora, P. S. & Zhang, Y. AlphaSpace: Fragment-Centric Topographical Mapping To Target Protein-Protein Interaction Interfaces. *Journal of chemical information and modeling* **55**, 1585-1599, doi:10.1021/acs.jcim.5b00103 (2015).
215 Erlanson, D. A. *et al.* Site-directed ligand discovery. *Proc Natl Acad Sci U S A* **97**, 9367-9372 (2000).
216 Erlanson, D. A. Introduction to fragment-based drug discovery. *Topics in current chemistry* **317**, 1-32, doi:10.1007/128_2011_180 (2012).
217 Arkin, M. R. *et al.* Binding of small molecules to an adaptive protein-protein interface. *Proc Natl Acad Sci U S A* **100**, 1603-1608, doi:10.1073/pnas.252756299 (2003).
218 Modell, A. E., Blosser, S. L. & Arora, P. S. Systematic Targeting of Protein-Protein Interactions. *Trends in pharmacological sciences* **37**, 702-713, doi:10.1016/j.tips.2016.05.008 (2016).
219 Rackham, O. J. *et al.* The evolution and structure prediction of coiled coils across all genomes. *J Mol Biol* **403**, 480-493, doi:10.1016/j.jmb.2010.08.032 (2010).
220 Strauss, H. M. & Keller, S. Pharmacological interference with protein-protein interactions mediated by coiled-coil motifs. *Handb Exp Pharmacol*, 461-482, doi:10.1007/978-3-540-72843-6_19 (2008).
221 Lupas, A., Bassler, J. & Dunin-Horkawicz, S. The Structure and Topology of α-Helical Coiled Coils. *Sub-cellular Biochemistry* **82**, 95-129 (2017).
222 Hartmann, M. D. Functional and Structural Roles of Coiled Coils. *Subcell Biochem* **82**, 63-93, doi:10.1007/978-3-319-49674-0_3 (2017).
223 Rose, A. & Meier, I. Scaffolds, levers, rods and springs: diverse cellular functions of long coiled-coil proteins. *Cell Mol Life Sci* **61**, 1996-2009, doi:10.1007/s00018-004-4039-6 (2004).
224 Rose, A., Schraegle, S. J., Stahlberg, E. A. & Meier, I. Coiled-coil protein composition of 22 proteomes--differences and common themes in subcellular infrastructure and traffic control. *BMC Evol Biol* **5**, 66, doi:10.1186/1471-2148-5-66 (2005).
225 Gruber, M. & Lupas, A. N. Historical review: another 50th anniversary--new periodicities in coiled coils. *Trends in biochemical sciences* **28**, 679-685, doi:10.1016/j.tibs.2003.10.008 (2003).
226 Mason, J. M. & Arndt, K. M. Coiled coil domains: stability, specificity, and biological implications. *Chembiochem : a European journal of chemical biology* **5**, 170-176, doi:10.1002/cbic.200300781 (2004).

227 Burkhard, P., Stetefeld, J. & Strelkov, S. V. Coiled coils: a highly versatile protein folding motif. *Trends in cell biology* **11**, 82-88, doi:10.1016/s0962-8924(00)01898-5 (2001).
228 Herrmann, H., Strelkov, S. V., Burkhard, P. & Aebi, U. Intermediate filaments: primary determinants of cell architecture and plasticity. *J Clin Invest* **119**, 1772-1783, doi:10.1172/jci38214 (2009).
229 Peckham, M. Coiled coils and SAH domains in cytoskeletal molecular motors. *Biochem Soc Trans* **39**, 1142-1148, doi:10.1042/bst0391142 (2011).
230 Shea, E. K., Rutkowski, R. & Kim, P. S. Evidence that the leucine zipper is a coiled coil. *Science* **243**, 538, doi:10.1126/science.2911757 (1989).
231 Gao, R. & Lynn, D. G. Integration of Rotation and Piston Motions in Coiled-Coil Signal Transduction. *Journal of Bacteriology* **189**, 6048, doi:10.1128/JB.00459-07 (2007).
232 Langosch, D. & Heringa, J. Interaction of transmembrane helices by a knobs-into-holes packing characteristic of soluble coiled coils. *Proteins: Structure, Function, and Bioinformatics* **31**, 150-159, doi:10.1002/(SICI)1097-0134(19980501)31:2<150::AID-PROT5>3.0.CO;2-Q (1998).
233 Lupas, A. Coiled coils: new structures and new functions. *Trends in biochemical sciences* **21**, 375-382 (1996).
234 Woolfson, D. N. The design of coiled-coil structures and assemblies. *Adv Protein Chem* **70**, 79-112, doi:10.1016/s0065-3233(05)70004-8 (2005).
235 Lupas, A. N. & Gruber, M. in *Advances in Protein Chemistry* Vol. 70 37-38 (Academic Press, 2005).
236 Crick, F. H. C. THE PACKING OF ALPHA-HELICES - SIMPLE COILED-COILS. *Acta Crystallographica* **6**, 689-697, doi:10.1107/s0365110x53001964 (1953).
237 Crick, F. H. C. The packing of α-helices: simple coiled-coils. *Acta Crystallographica* **6**, 689-697, doi:doi:10.1107/S0365110X53001964 (1953).
238 Grigoryan, G. & DeGrado, W. F. Probing Designability via a Generalized Model of Helical Bundle Geometry. *J. Mol. Biol.* **405**, 1079-1100, doi:10.1016/j.jmb.2010.08.058 (2011).
239 Wood, C. W. *et al.* CCBuilder: an interactive web-based tool for building, designing and assessing coiled-coil protein assemblies. *Bioinformatics* **30**, 3029-3035, doi:10.1093/bioinformatics/btu502 (2014).
240 Wood, C. W. & Woolfson, D. N. CCBuilder 2.0: Powerful and accessible coiled-coil modeling. *Protein science : a publication of the Protein Society* **27**, 103-111, doi:10.1002/pro.3279 (2018).
241 Crick, F. H. Is alpha-keratin a coiled coil? *Nature* **170**, 882-883, doi:10.1038/170882b0 (1952).
242 Crick, F. The Fourier transform of a coiled-coil. *Acta Crystallographica* **6**, 685-689, doi:doi:10.1107/S0365110X53001952 (1953).
243 Lupas, A. Predicting coiled-coil regions in proteins. *Current opinion in structural biology* **7**, 388-393, doi:10.1016/s0959-440x(97)80056-5 (1997).
244 Lupas, A., Van Dyke, M. & Stock, J. Predicting coiled coils from protein sequences. *Science* **252**, 1162, doi:10.1126/science.252.5009.1162 (1991).
245 Woolfson, D. N. Coiled-Coil Design: Updated and Upgraded. *Subcell Biochem* **82**, 35-61, doi:10.1007/978-3-319-49674-0_2 (2017).
246 Parry, D. A. Coiled-coils in alpha-helix-containing proteins: analysis of the residue types within the heptad repeat and the use of these data in the prediction of coiled-coils in other proteins. *Biosci Rep* **2**, 1017-1024, doi:10.1007/bf01122170 (1982).

247 Gruber, M., Söding, J. & Lupas, A. N. Comparative analysis of coiled-coil prediction methods. *Journal of Structural Biology* **155**, 140-145, doi:https://doi.org/10.1016/j.jsb.2006.03.009 (2006).
248 Delorenzi, M. & Speed, T. An HMM model for coiled-coil domains and a comparison with PSSM-based predictions. *Bioinformatics* **18**, 617-625, doi:10.1093/bioinformatics/18.4.617 (2002).
249 Ludwiczak, J., Winski, A., Szczepaniak, K., Alva, V. & Dunin-Horkawicz, S. DeepCoil-a fast and accurate prediction of coiled-coil domains in protein sequences. *Bioinformatics* **35**, 2790-2795, doi:10.1093/bioinformatics/bty1062 (2019).
250 Testa, O. D., Moutevelis, E. & Woolfson, D. N. CC+: a relational database of coiled-coil structures. *Nucleic acids research* **37**, D315-D322, doi:10.1093/nar/gkn675 (2008).
251 Moutevelis, E. & Woolfson, D. N. A periodic table of coiled-coil protein structures. *J Mol Biol* **385**, 726-732, doi:10.1016/j.jmb.2008.11.028 (2009).
252 Heal, J. W., Bartlett, G. J., Wood, C. W., Thomson, A. R. & Woolfson, D. N. Applying graph theory to protein structures: an Atlas of coiled coils. *Bioinformatics* **34**, 3316-3323, doi:10.1093/bioinformatics/bty347 (2018).
253 Mahrenholz, C. C., Abfalter, I. G., Bodenhofer, U., Volkmer, R. & Hochreiter, S. Complex networks govern coiled-coil oligomerization–predicting and profiling by means of a machine learning approach. *Molecular & Cellular Proteomics* **10** (2011).
254 Armstrong, C. T., Vincent, T. L., Green, P. J. & Woolfson, D. N. SCORER 2.0: an algorithm for distinguishing parallel dimeric and trimeric coiled-coil sequences. *Bioinformatics* **27**, 1908-1914, doi:10.1093/bioinformatics/btr299 (2011).
255 Li, C., Wang, X. F., Chen, Z., Zhang, Z. & Song, J. Computational characterization of parallel dimeric and trimeric coiled-coils using effective amino acid indices. *Mol Biosyst* **11**, 354-360, doi:10.1039/c4mb00569d (2015).
256 Vincent, T. L., Green, P. J. & Woolfson, D. N. LOGICOIL—multi-state prediction of coiled-coil oligomeric state. *Bioinformatics* **29**, 69-76, doi:10.1093/bioinformatics/bts648 (2012).
257 Harbury, P. B., Kim, P. S. & Alber, T. Crystal structure of an isoleucine-zipper trimer. *Nature* **371**, 80-83, doi:10.1038/371080a0 (1994).
258 Harbury, P. B., Zhang, T., Kim, P. S. & Alber, T. A switch between two-, three-, and four-stranded coiled coils in GCN4 leucine zipper mutants. *Science* **262**, 1401-1407, doi:10.1126/science.8248779 (1993).
259 O'Shea, E. K., Rutkowski, R. & Kim, P. S. Evidence that the leucine zipper is a coiled coil. *Science* **243**, 538-542, doi:10.1126/science.2911757 (1989).
260 Harbury, P. B., Tidor, B. & Kim, P. S. Repacking protein cores with backbone freedom: structure prediction for coiled coils. *Proc Natl Acad Sci U S A* **92**, 8408-8412, doi:10.1073/pnas.92.18.8408 (1995).
261 Watkins, A. M., Wuo, M. G. & Arora, P. S. Protein-Protein Interactions Mediated by Helical Tertiary Structure Motifs. *J Am Chem Soc* **137**, 11622-11630, doi:10.1021/jacs.5b05527 (2015).
262 Wang, Y. *et al.* Coiled-coil networking shapes cell molecular machinery. *Molecular biology of the cell* **23**, 3911-3922, doi:10.1091/mbc.E12-05-0396 (2012).
263 Wood, C. W. *et al.* ISAMBARD: an open-source computational environment for biomolecular analysis, modelling and design. *Bioinformatics (Oxford, England)* **33**, 3043-3050, doi:10.1093/bioinformatics/btx352 (2017).

264 Huang, P. S. *et al.* High thermodynamic stability of parametrically designed helical bundles. *Science* **346**, 481-485, doi:10.1126/science.1257481 (2014).
265 Fletcher, J. M. *et al.* A Basis Set of de Novo Coiled-Coil Peptide Oligomers for Rational Protein Design and Synthetic Biology. *ACS Synth. Biol.* **1**, 240-250, doi:10.1021/sb300028q (2012).
266 Thomson, A. R. *et al.* Computational design of water-soluble α-helical barrels. *Science* **346**, 485, doi:10.1126/science.1257452 (2014).
267 Grigoryan, G. *et al.* Computational design of virus-like protein assemblies on carbon nanotube surfaces. *Science* **332**, 1071-1076, doi:10.1126/science.1198841 (2011).
268 Joh, N. H. *et al.* De novo design of a transmembrane Zn^{2+}-transporting four-helix bundle. *Science* **346**, 1520-1524, doi:10.1126/science.1261172 (2014).
269 Berwick, M. R. *et al.* De Novo Design of Ln(III) Coiled Coils for Imaging Applications. *Journal of the American Chemical Society* **136**, 1166-1169, doi:10.1021/ja408741h (2014).
270 Lee, M. J. *et al.* Engineered synthetic scaffolds for organizing proteins within the bacterial cytoplasm. *Nature Chemical Biology* **14**, 142-147, doi:10.1038/nchembio.2535 (2018).
271 Small, L. S. R. *et al.* Construction of a Chassis for a Tripartite Protein-Based Molecular Motor. *ACS Synth Biol* **6**, 1096-1102, doi:10.1021/acssynbio.7b00037 (2017).
272 Zaccai, N. R. *et al.* A de novo peptide hexamer with a mutable channel. *Nature Chemical Biology* **7**, 935-941, doi:10.1038/nchembio.692 (2011).
273 Thomas, F., Boyle, A. L., Burton, A. J. & Woolfson, D. N. A Set of de Novo Designed Parallel Heterodimeric Coiled Coils with Quantified Dissociation Constants in the Micromolar to Sub-nanomolar Regime. *Journal of the American Chemical Society* **135**, 5161-5166, doi:10.1021/ja312310g (2013).
274 Dixon, A. S. *et al.* Disruption of Bcr-Abl coiled coil oligomerization by design. *The Journal of biological chemistry* **286**, 27751-27760, doi:10.1074/jbc.M111.264903 (2011).
275 Edgell, C. L., Smith, A. J., Beesley, J. L., Savery, N. J. & Woolfson, D. N. De Novo Designed Protein-Interaction Modules for In-Cell Applications. *ACS Synth. Biol.* **9**, 427-436, doi:10.1021/acssynbio.9b00453 (2020).
276 Smith, A. J., Thomas, F., Shoemark, D., Woolfson, D. N. & Savery, N. J. Guiding Biomolecular Interactions in Cells Using de Novo Protein-Protein Interfaces. *ACS Synth Biol* **8**, 1284-1293, doi:10.1021/acssynbio.8b00501 (2019).
277 Lebar, T., Lainšček, D., Merljak, E., Aupič, J. & Jerala, R. A tunable orthogonal coiled-coil interaction toolbox for engineering mammalian cells. *Nature Chemical Biology* **16**, 513-519, doi:10.1038/s41589-019-0443-y (2020).
278 Fletcher, J. M. *et al.* De novo coiled-coil peptides as scaffolds for disrupting protein-protein interactions. *Chem Sci* **9**, 7656-7665, doi:10.1039/c8sc02643b (2018).
279 Falcón-Pérez, J. M., Nazarian, R., Sabatti, C. & Dell'Angelica, E. C. Distribution and dynamics of Lamp1-containing endocytic organelles in fibroblasts deficient in BLOC-3. *J Cell Sci* **118**, 5243-5255, doi:10.1242/jcs.02633 (2005).
280 Xiang, G. *et al.* BNIP3L-dependent mitophagy accounts for mitochondrial clearance during 3 factors-induced somatic cell reprogramming. *Autophagy* **13**, 1543-1555, doi:10.1080/15548627.2017.1338545 (2017).

281 Roberts, B. *et al.* Systematic gene tagging using CRISPR/Cas9 in human stem cells to illuminate cell organization. *Molecular biology of the cell* **28**, 2854-2874, doi:10.1091/mbc.E17-03-0209 (2017).
282 Küey, C., Larocque, G., Clarke, N. I. & Royle, S. J. Unintended perturbation of protein function using GFP nanobodies in human cells. *J Cell Sci* **132**, doi:10.1242/jcs.234955 (2019).
283 Cross, J. A., Chegkazi, M. S., Steiner, R. A., Woolfson, D. N. & Dodding, M. P. Fragment-linking peptide design yields a high-affinity ligand for microtubule-based transport. *Cell Chemical Biology* **28**, 1347-1355.e1345, doi:10.1016/j.chembiol.2021.03.010 (2021).
284 Martin, S. & Henley, J. M. Activity-dependent endocytic sorting of kainate receptors to recycling or degradation pathways. *The EMBO journal* **23**, 4749-4759, doi:10.1038/sj.emboj.7600483 (2004).
285 Heuser, J. Changes in lysosome shape and distribution correlated with changes in cytoplasmic pH. *The Journal of cell biology* **108**, 855-864 (1989).
286 Starling, G. P. *et al.* Folliculin directs the formation of a Rab34-RILP complex to control the nutrient-dependent dynamic distribution of lysosomes. *EMBO reports* **17**, 823-841, doi:10.15252/embr.201541382 (2016).
287 Pollard, T. D. A guide to simple and informative binding assays. *Molecular biology of the cell* **21**, 4061-4067, doi:10.1091/mbc.E10-08-0683 (2010).
288 Cole, J. L., Lary, J. W., Moody, T. P. & Laue, T. M. Analytical ultracentrifugation: Sedimentation velocity and sedimentation equilibrium. *Biophysical Tools for Biologists: Vol 1 in Vitro Techniques* **84**, 143-179, doi:10.1016/s0091-679x(07)84006-4 (2008).
289 Zhao, H., Piszczek, G. & Schuck, P. SEDPHAT--a platform for global ITC analysis and global multi-method analysis of molecular interactions. *Methods* **76**, 137-148, doi:10.1016/j.ymeth.2014.11.012 (2015).
290 Evans, P. R. & Murshudov, G. N. How good are my data and what is the resolution? *Acta Crystallogr D Biol Crystallogr* **69**, 1204-1214, doi:10.1107/s0907444913000061 (2013).
291 Winn, M. D. *et al.* Overview of the CCP4 suite and current developments. *Acta Crystallogr D Biol Crystallogr* **67**, 235-242, doi:10.1107/s0907444910045749 (2011).
292 McCoy, A. J. *et al.* Phaser crystallographic software. *J Appl Crystallogr* **40**, 658-674, doi:10.1107/s0021889807021206 (2007).
293 Emsley, P. & Cowtan, K. Coot: model-building tools for molecular graphics. *Acta Crystallogr D Biol Crystallogr* **60**, 2126-2132, doi:10.1107/s0907444904019158 (2004).
294 Emsley, P., Lohkamp, B., Scott, W. G. & Cowtan, K. Features and development of Coot. *Acta Crystallogr D Biol Crystallogr* **66**, 486-501, doi:10.1107/s0907444910007493 (2010).
295 Murshudov, G. N., Vagin, A. A. & Dodson, E. J. Refinement of macromolecular structures by the maximum-likelihood method. *Acta Crystallogr D Biol Crystallogr* **53**, 240-255, doi:10.1107/s0907444996012255 (1997).
296 Altschul, S. F., Gish, W., Miller, W., Myers, E. W. & Lipman, D. J. Basic local alignment search tool. *J Mol Biol* **215**, 403-410, doi:10.1016/s0022-2836(05)80360-2 (1990).
297 Wood, C. W. *et al.* BAlaS: fast, interactive and accessible computational alanine-scanning using BudeAlaScan. *Bioinformatics* **36**, 2917-2919, doi:10.1093/bioinformatics/btaa026 (2020).

298 Krissinel, E. & Henrick, K. Inference of macromolecular assemblies from crystalline state. *J Mol Biol* **372**, 774-797, doi:10.1016/j.jmb.2007.05.022 (2007).
299 Hetherington, K. *et al.* Towards optimizing peptide-based inhibitors of protein-protein interactions: predictive saturation variation scanning (PreSaVS). *RSC Chem Biol* **2**, 1474-1478, doi:10.1039/d1cb00137j (2021).
300 Jumper, J. *et al.* Highly accurate protein structure prediction with AlphaFold. *Nature* **596**, 583-589, doi:10.1038/s41586-021-03819-2 (2021).
301 Fu, M.-m. & Holzbaur, E. L. F. JIP1 regulates the directionality of APP axonal transport by coordinating kinesin and dynein motors. *Journal of Cell Biology* **202**, 495-508, doi:10.1083/jcb.201302078 (2013).
302 Perez-Riba, A. & Itzhaki, L. S. The tetratricopeptide-repeat motif is a versatile platform that enables diverse modes of molecular recognition. *Curr Opin Struct Biol* **54**, 43-49, doi:10.1016/j.sbi.2018.12.004 (2019).
303 Binz, H. K. *et al.* High-affinity binders selected from designed ankyrin repeat protein libraries. *Nat Biotechnol* **22**, 575-582, doi:10.1038/nbt962 (2004).
304 Verhey, K. J. *et al.* Cargo of Kinesin Identified as Jip Scaffolding Proteins and Associated Signaling Molecules. *Journal of Cell Biology* **152**, 959-970, doi:10.1083/jcb.152.5.959 (2001).
305 Lefèvre, F., Rémy, M.-H. & Masson, J.-M. Alanine-stretch scanning mutagenesis: a simple and efficient method to probe protein structure and function. *Nucleic acids research* **25**, 447-448, doi:10.1093/nar/25.2.447 (1997).
306 Forrer, P., Binz, H. K., Stumpp, M. T. & Plückthun, A. Consensus design of repeat proteins. *Chembiochem : a European journal of chemical biology* **5**, 183-189, doi:10.1002/cbic.200300762 (2004).
307 Kajander, T., Cortajarena, A. L. & Regan, L. Consensus design as a tool for engineering repeat proteins. *Methods Mol Biol* **340**, 151-170, doi:10.1385/1-59745-116-9:151 (2006).
308 Morgan, G. W. *et al.* Vaccinia protein F12 has structural similarity to kinesin light chain and contains a motor binding motif required for virion export. *PLoS pathogens* **6**, e1000785, doi:10.1371/journal.ppat.1000785 (2010).
309 Konecna, A. *et al.* Calsyntenin-1 Docks Vesicular Cargo to Kinesin-1. *Molecular biology of the cell* **17**, 3651-3663, doi:10.1091/mbc.e06-02-0112 (2006).
310 Wilson, M. H. & Holzbaur, E. L. F. Nesprins anchor kinesin-1 motors to the nucleus to drive nuclear distribution in muscle cells. *Development* **142**, 218, doi:10.1242/dev.114769 (2015).
311 Kumar, M. *et al.* ELM—the eukaryotic linear motif resource in 2020. *Nucleic acids research* **48**, D296-D306, doi:10.1093/nar/gkz1030 (2019).
312 Guedes-Dias, P. & Holzbaur, E. L. F. Axonal transport: Driving synaptic function. *Science* **366**, doi:10.1126/science.aaw9997 (2019).
313 Farías, G. G., Guardia, C. M., De Pace, R., Britt, D. J. & Bonifacino, J. S. BORC/kinesin-1 ensemble drives polarized transport of lysosomes into the axon. *Proc Natl Acad Sci USA* **114**, E2955-E2964, doi:10.1073/pnas.1616363114 (2017).
314 Cabukusta, B. & Neefjes, J. Mechanisms of lysosomal positioning and movement. *Traffic (Copenhagen, Denmark)* **19**, 761-769, doi:10.1111/tra.12587 (2018).
315 De Duve, C., Pressman, B. C., Gianetto, R., Wattiaux, R. & Appelmans, F. Tissue fractionation studies. 6. Intracellular distribution patterns of enzymes in rat-liver tissue. *Biochem J* **60**, 604-617, doi:10.1042/bj0600604 (1955).

316 de Duve, C. The lysosome turns fifty. *Nat Cell Biol* **7**, 847-849, doi:10.1038/ncb0905-847 (2005).
317 Ballabio, A. The awesome lysosome. *EMBO Mol Med* **8**, 73-76, doi:10.15252/emmm.201505966 (2016).
318 Jordens, I. *et al.* The Rab7 effector protein RILP controls lysosomal transport by inducing the recruitment of dynein-dynactin motors. *Current biology : CB* **11**, 1680-1685, doi:10.1016/S0960-9822(01)00531-0 (2001).
319 Matteoni, R. & Kreis, T. E. Translocation and clustering of endosomes and lysosomes depends on microtubules. *Journal of Cell Biology* **105**, 1253-1265, doi:10.1083/jcb.105.3.1253 (1987).
320 Harada, A. *et al.* Golgi vesiculation and lysosome dispersion in cells lacking cytoplasmic dynein. *J Cell Biol* **141**, 51-59 (1998).
321 Hollenbeck, P. J. & Swanson, J. A. Radial extension of macrophage tubular lysosomes supported by kinesin. *Nature* **346**, 864-866, doi:10.1038/346864a0 (1990).
322 Jongsma, Marlieke L. M. *et al.* An ER-Associated Pathway Defines Endosomal Architecture for Controlled Cargo Transport. *Cell* **166**, 152-166, doi:https://doi.org/10.1016/j.cell.2016.05.078 (2016).
323 Encarnação, M. *et al.* A Rab3a-dependent complex essential for lysosome positioning and plasma membrane repair. *Journal of Cell Biology* **213**, 631-640, doi:10.1083/jcb.201511093 (2016).
324 Nakamura, S. & Yoshimori, T. New insights into autophagosome-lysosome fusion. *Journal of cell science* **130**, 1209-1216, doi:10.1242/jcs.196352 (2017).
325 Korolchuk, V. I. *et al.* Lysosomal positioning coordinates cellular nutrient responses. *Nature cell biology* **13**, 453-460, doi:10.1038/ncb2204 (2011).
326 Pu, J., Guardia, C. M., Keren-Kaplan, T. & Bonifacino, J. S. Mechanisms and functions of lysosome positioning. *J Cell Sci* **129**, 4329-4339, doi:10.1242/jcs.196287 (2016).
327 Ljubetič, A. *et al.* Design of coiled-coil protein-origami cages that self-assemble in vitro and in vivo. *Nature Biotechnology* **35**, doi:10.1038/nbt.3994 (2017).
328 van Bergeijk, P., Adrian, M., Hoogenraad, C. C. & Kapitein, L. C. Optogenetic control of organelle transport and positioning. *Nature* **518**, 111-114, doi:10.1038/nature14128 (2015).
329 Guardia, C. M. *et al.* Reversible association with motor proteins (RAMP): A streptavidin-based method to manipulate organelle positioning. *PLoS biology* **17**, e3000279, doi:10.1371/journal.pbio.3000279 (2019).
330 Guidotti, G., Brambilla, L. & Rossi, D. Cell-Penetrating Peptides: From Basic Research to Clinics. *Trends in pharmacological sciences* **38**, 406-424, doi:10.1016/j.tips.2017.01.003 (2017).
331 Bohmova, E. *et al.* Cell-penetrating peptides: a useful tool for the delivery of various cargoes into cells. *Physiological research* **67**, S267-s279 (2018).
332 Stewart, K. M., Horton, K. L. & Kelley, S. O. Cell-penetrating peptides as delivery vehicles for biology and medicine. *Organic & biomolecular chemistry* **6**, 2242-2255, doi:10.1039/b719950c (2008).
333 Appelbaum, J. S. *et al.* Arginine topology controls escape of minimally cationic proteins from early endosomes to the cytoplasm. *Chem Biol* **19**, 819-830, doi:10.1016/j.chembiol.2012.05.022 (2012).

334 Ter-Avetisyan, G. *et al.* Cell entry of arginine-rich peptides is independent of endocytosis. *The Journal of biological chemistry* **284**, 3370-3378, doi:10.1074/jbc.M805550200 (2009).
335 Gindhart, J. G., Jr., Desai, C. J., Beushausen, S., Zinn, K. & Goldstein, L. S. Kinesin light chains are essential for axonal transport in Drosophila. *The Journal of cell biology* **141**, 443-454, doi:10.1083/jcb.141.2.443 (1998).
336 Decuevas, M., Tao, T. & Goldstein, L. S. B. EVIDENCE THAT THE STALK OF DROSOPHILA KINESIN HEAVY-CHAIN IS AN ALPHA-HELICAL COILED COIL. *Journal of Cell Biology* **116**, 957-965, doi:10.1083/jcb.116.4.957 (1992).
337 Hirokawa, N. *et al.* SUBMOLECULAR DOMAINS OF BOVINE BRAIN KINESIN IDENTIFIED BY ELECTRON-MICROSCOPY AND MONOCLONAL-ANTIBODY DECORATION. *Cell* **56**, 867-878, doi:10.1016/0092-8674(89)90691-0 (1989).
338 Gyoeva, F. K., Sarkisov, D. V., Khodjakov, A. L. & Minin, A. A. The tetrameric molecule of conventional kinesin contains identical light chains. *Biochemistry* **43**, 13525-13531, doi:10.1021/bi049288l (2004).
339 Crooks, G. E., Hon, G., Chandonia, J. M. & Brenner, S. E. WebLogo: a sequence logo generator. *Genome Res* **14**, 1188-1190, doi:10.1101/gr.849004 (2004).
340 Woolfson, D. N., Bartlett, G. J., Bruning, M. & Thomson, A. R. New currency for old rope: from coiled-coil assemblies to α-helical barrels. *Current opinion in structural biology* **22**, 432-441, doi:10.1016/j.sbi.2012.03.002 (2012).
341 Vincent, T. L., Green, P. J. & Woolfson, D. N. LOGICOIL-multi-state prediction of coiled-coil oligomeric state. *Bioinformatics (Oxford, England)* **29**, 69-76, doi:10.1093/bioinformatics/bts648 (2013).
342 Rotzschke, O., Lau, J. M., Hofstatter, M., Falk, K. & Strominger, J. L. A pH-sensitive histidine residue as control element for ligand release from HLA-DR molecules. *Proc Natl Acad Sci U S A* **99**, 16946-16950, doi:10.1073/pnas.212643999 (2002).
343 Suzuki, K., Yamada, T. & Tanaka, T. Role of the buried glutamate in the alpha-helical coiled coil domain of the macrophage scavenger receptor. *Biochemistry* **38**, 1751-1756, doi:10.1021/bi9821014 (1999).
344 Nagarkar, R. P., Fichman, G. & Schneider, J. P. Engineering and characterization of a pH-sensitive homodimeric antiparallel coiled coil. *Peptide Science* **112**, e24180, doi:https://doi.org/10.1002/pep2.24180 (2020).
345 Li, S. & Hong, M. Protonation, tautomerization, and rotameric structure of histidine: a comprehensive study by magic-angle-spinning solid-state NMR. *Journal of the American Chemical Society* **133**, 1534-1544, doi:10.1021/ja108943n (2011).
346 Liao, S.-M., Du, Q.-S., Meng, J.-Z., Pang, Z.-W. & Huang, R.-B. The multiple roles of histidine in protein interactions. *Chemistry Central Journal* **7**, 44, doi:10.1186/1752-153X-7-44 (2013).
347 Clewley, J. P. & Arnold, C. MEGALIGN. The multiple alignment module of LASERGENE. *Methods Mol Biol* **70**, 119-129 (1997).
348 Rosano, G. L. & Ceccarelli, E. A. Recombinant protein expression in Escherichia coli: advances and challenges. *Front Microbiol* **5**, 172, doi:10.3389/fmicb.2014.00172 (2014).
349 Cross, J. A., Woolfson, D. N. & Dodding, M. P. Kinesin-1 captures RNA cargo in its adaptable coils. *Genes Dev* **35**, 937-939, doi:10.1101/gad.348691.121 (2021).

350 Parton, R. G. *et al.* pH-induced microtubule-dependent redistribution of late endosomes in neuronal and epithelial cells. *Journal of Cell Biology* **113**, 261-274, doi:10.1083/jcb.113.2.261 (1991).
351 Moolenaar, W. H. Effects of Growth Factors on Intracellular pH Regulation. *Annual Review of Physiology* **48**, 363-376, doi:10.1146/annurev.ph.48.030186.002051 (1986).
352 Tanaka, Y. *et al.* Targeted Disruption of Mouse Conventional Kinesin Heavy Chain kif5B, Results in Abnormal Perinuclear Clustering of Mitochondria. *Cell* **93**, 1147-1158, doi:10.1016/S0092-8674(00)81459-2 (1998).
353 Ohkuma, S. & Poole, B. Fluorescence probe measurement of the intralysosomal pH in living cells and the perturbation of pH by various agents. *Proceedings of the National Academy of Sciences of the United States of America* **75**, 3327-3331 (1978).
354 Hofmann, I. & Munro, S. An N-terminally acetylated Arf-like GTPase is localised to lysosomes and affects their motility. *J Cell Sci* **119**, 1494-1503, doi:10.1242/jcs.02958 (2006).
355 Johnson, D. E., Ostrowski, P., Jaumouillé, V. & Grinstein, S. The position of lysosomes within the cell determines their luminal pH. *The Journal of cell biology* **212**, 677-692, doi:10.1083/jcb.201507112 (2016).
356 Nyarko, A. *et al.* Ionization of His 55 at the dimer interface of dynein light-chain LC8 is coupled to dimer dissociation. *Biochemistry* **44**, 14248-14255, doi:10.1021/bi0512694 (2005).
357 Glunde, K. *et al.* Extracellular acidification alters lysosomal trafficking in human breast cancer cells. *Neoplasia* **5**, 533-545, doi:10.1016/s1476-5586(03)80037-4 (2003).
358 Johmura, Y. *et al.* Senolysis by glutaminolysis inhibition ameliorates various age-associated disorders. *Science (New York, N.Y.)* **371**, 265-270, doi:10.1126/science.abb5916 (2021).
359 Lu, W., Lakonishok, M. & Gelfand, V. I. Kinesin-1–powered microtubule sliding initiates axonal regeneration in Drosophila cultured neurons. *Molecular biology of the cell* **26**, 1296-1307, doi:10.1091/mbc.E14-10-1423 (2015).
360 Steinmetz, M. O. & Prota, A. E. Microtubule-Targeting Agents: Strategies To Hijack the Cytoskeleton. *Trends in cell biology* **28**, 776-792, doi:10.1016/j.tcb.2018.05.001 (2018).
361 Hellal, F. *et al.* Microtubule Stabilization Reduces Scarring and Causes Axon Regeneration After Spinal Cord Injury. *Science* **331**, 928-931, doi:doi:10.1126/science.1201148 (2011).
362 Sleigh, J. N., Rossor, A. M., Fellows, A. D., Tosolini, A. P. & Schiavo, G. Axonal transport and neurological disease. *Nat Rev Neurol* **15**, 691-703, doi:10.1038/s41582-019-0257-2 (2019).
363 Nguyen, T. Q. *et al.* Characterization of the binding mode of JNK-interacting protein 1 (JIP1) to kinesin-light chain 1 (KLC1). *The Journal of biological chemistry* **293**, 13946-13960, doi:10.1074/jbc.RA118.003916 (2018).
364 Ran, F. A. *et al.* Genome engineering using the CRISPR-Cas9 system. *Nature Protocols* **8**, 2281-2308, doi:10.1038/nprot.2013.143 (2013).
365 Liu, I. J. *et al.* Disease-specific B Cell epitopes for serum antibodies from patients with severe acute respiratory syndrome (SARS) and serologic detection of SARS antibodies by epitope-based peptide antigens. *J Infect Dis* **190**, 797-809, doi:10.1086/422753 (2004).

366 Khurana, S. *et al.* Antigenic fingerprinting of H5N1 avian influenza using convalescent sera and monoclonal antibodies reveals potential vaccine and diagnostic targets. *PLoS Med* **6**, e1000049, doi:10.1371/journal.pmed.1000049 (2009).
367 Santamaria, H. *et al.* Identification of peptide sequences specific for serum antibodies from human papillomavirus-infected patients using phage display libraries. *Clin Immunol* **101**, 296-302, doi:10.1006/clim.2001.5126 (2001).
368 Wei, Z., Liu, X., Yu, C. & Zhang, M. Structural basis of cargo recognitions for class V myosins. *Proc Natl Acad Sci USA* **110**, 11314-11319, doi:10.1073/pnas.1306768110 (2013).
369 Harrington, L., Fletcher, J. M., Heermann, T., Woolfson, D. N. & Schwille, P. De novo design of a reversible phosphorylation-dependent switch for membrane targeting. *Nature Communications* **12**, 1472, doi:10.1038/s41467-021-21622-5 (2021).
370 Kozielski, F. *et al.* The Crystal Structure of Dimeric Kinesin and Implications for Microtubule-Dependent Motility. *Cell* **91**, 985-994, doi:10.1016/S0092-8674(00)80489-4 (1997).
371 Hansen, S., Kiefer, J. D., Madhurantakam, C., Mittl, P. R. E. & Plückthun, A. Structures of designed armadillo repeat proteins binding to peptides fused to globular domains. *Protein science : a publication of the Protein Society* **26**, 1942-1952, doi:10.1002/pro.3229 (2017).
372 Hansen, S. *et al.* Structure and Energetic Contributions of a Designed Modular Peptide-Binding Protein with Picomolar Affinity. *J. Am. Chem. Soc.* **138**, 3526-3532, doi:10.1021/jacs.6b00099 (2016).

8 Appendix

8.1 Peptide characterisation

TAMRA-J-S(Y) GTEDIYEWDDSAI, Calculated Mass: 1924.96 Observed Mass: 1926.78.
HPLC plotted from 2 mins due to injection peak

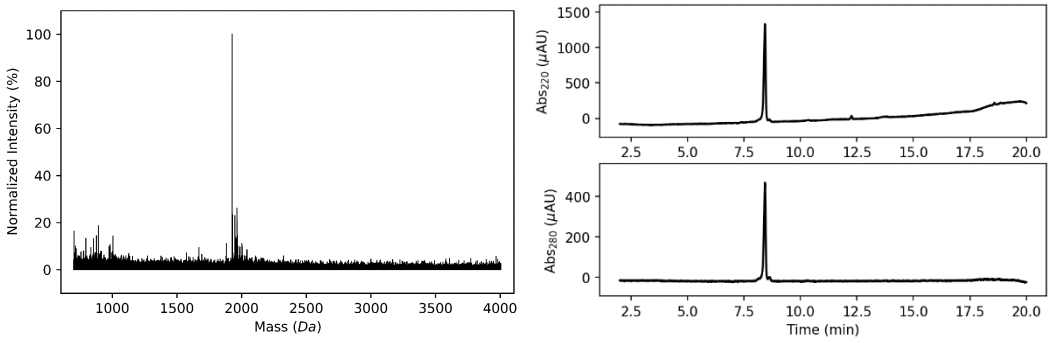

TAMRA-J-S(L) GTEDILEWDDSAI, Calculated Mass: 1874.95 Observed Mass: 1876.81. *HPLC plotted from 2 mins due to injection peak*

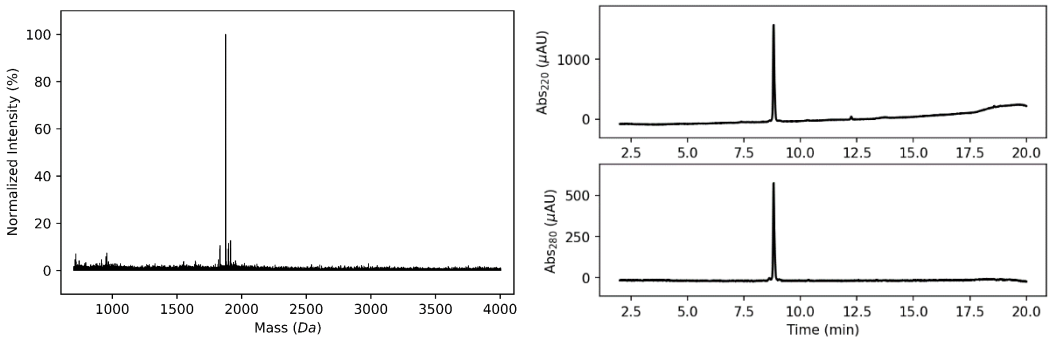

TAMRA-T-J-S(Y) GTVFTTEDIYEWDDSAI, Calculated Mass: 2373.48 Observed Mass: 2374.87. *HPLC plotted from 2 mins due to injection peak*

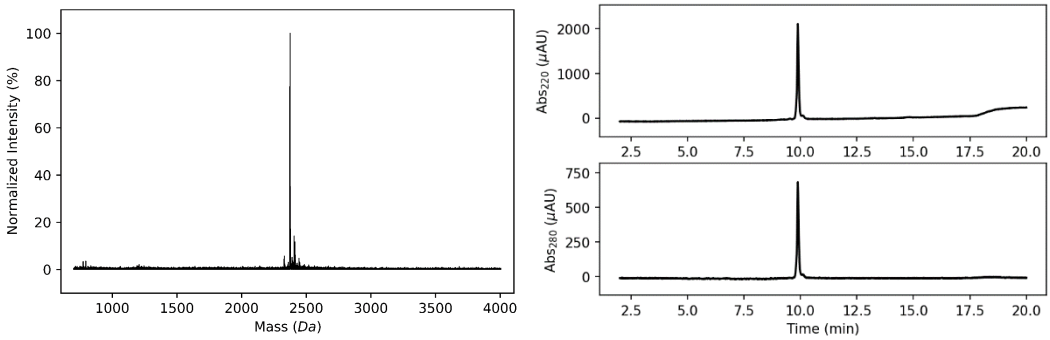

TAMRA-T-J-S(L) GTVFTTEDILEWDDSAI, Calculated Mass: 2323.46 Observed Mass: 2325.06. *HPLC plotted from 2 mins due to injection peak*

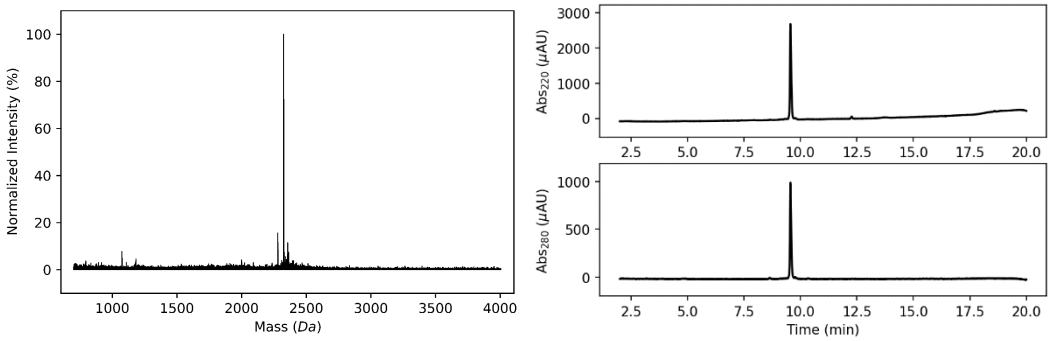

TAMRA-R6-KinTag RRRRRRGTVFTTEDIYEWDDSAI, Calculated Mass: 3310.59 Observed Mass: 3312.53. *HPLC plotted from 2 mins due to injection peak*

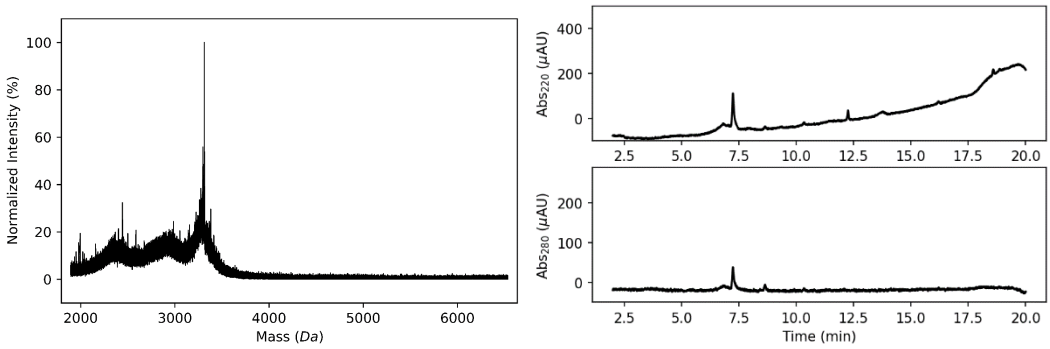

TAMRA-KinTag-R8 GTVFTTEDIYEWDDSAIRRRRRRRRR, Calculated Mass: 3252.57 Observed Mass: 3253.72. *HPLC plotted from 2 mins due to injection peak*

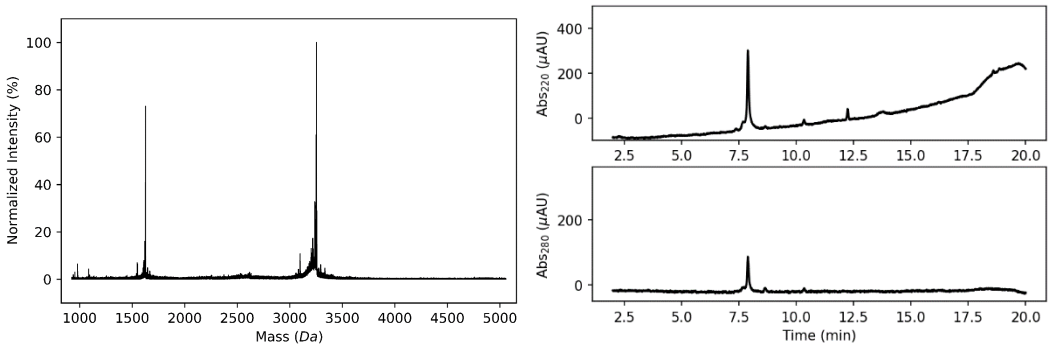

TAMRA-KinTag-R2 GTVFTTEDIYEWDDSAIRR, Calculated Mass: 2685.85 Observed Mass: 2686.22. *HPLC plotted from 2 mins due to injection peak*

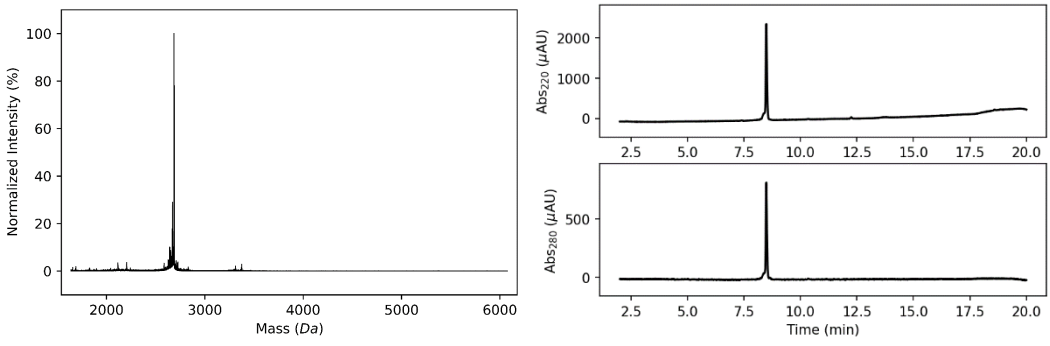

TAMRA-KinTag-R6 GTVFTTEDIYEWDDSAIRRRRRR, Calculated Mass: 3310.59 Observed Mass: 3313.24. *HPLC plotted from 2 mins due to injection peak*

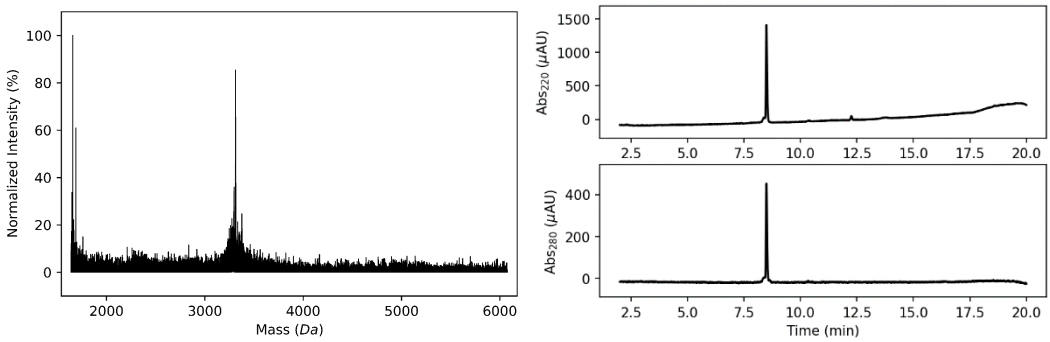

TAMRA-R2-KinTag RRGTVFTTEDIYEWDDSAI, Calculated Mass: 2685.85 Observed Mass: 2686.60. *HPLC plotted from 2 mins due to injection peak*

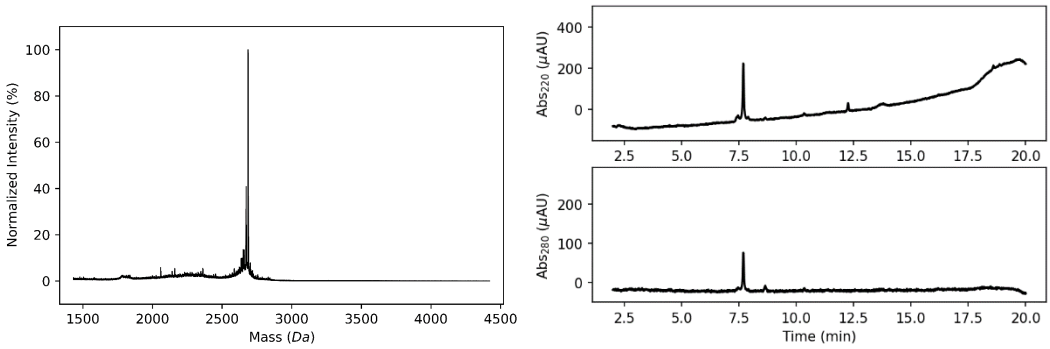

TAMRA-KinTag-R4 GTVFTTEDIYEWDDSAIRRRR, Calculated Mass: 2998.22 Observed Mass: 2998.36. *HPLC plotted from 2 mins due to injection peak*

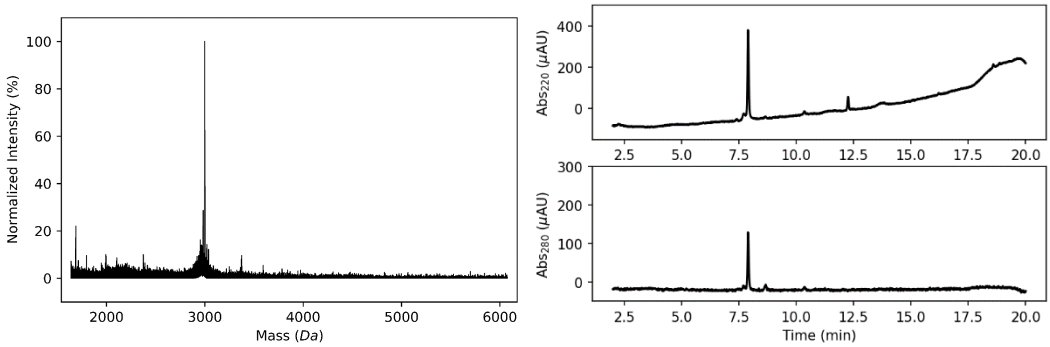

TAMRA-R8-KinTag RRRRRRRRRGTVFTTEDIYEWDDSAI, Calculated Mass: 3622.97 Observed Mass: 3621.11. *HPLC plotted from 2 mins due to injection peak*

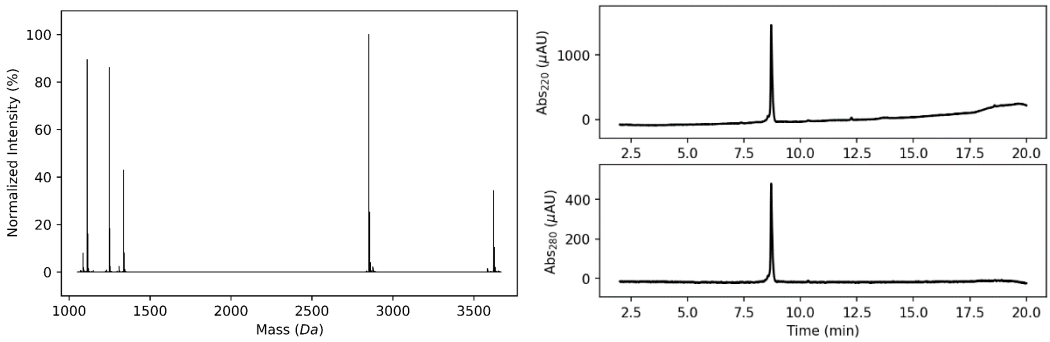

TAMRA-apCC-Di-B GQLKQRRAALKQRIAALKQRRAALKWQIQG, Calculated Mass: 3527.19 Observed Mass: 3526.08.

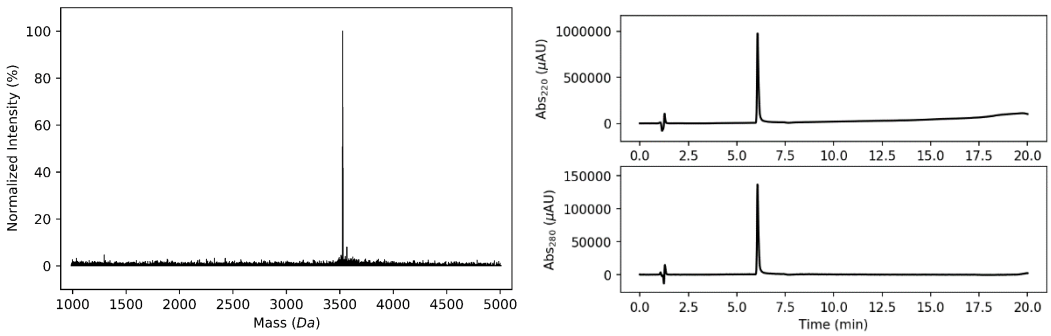

TAMRA-KinTag-apCC-Di-B GTVFTTEDIYEWDDSAITGSTGSGQLKQRRAALKQRIAALKQRRAALKWQIQG , Calculated Mass: 6332.06 Observed Mass: 6331.38

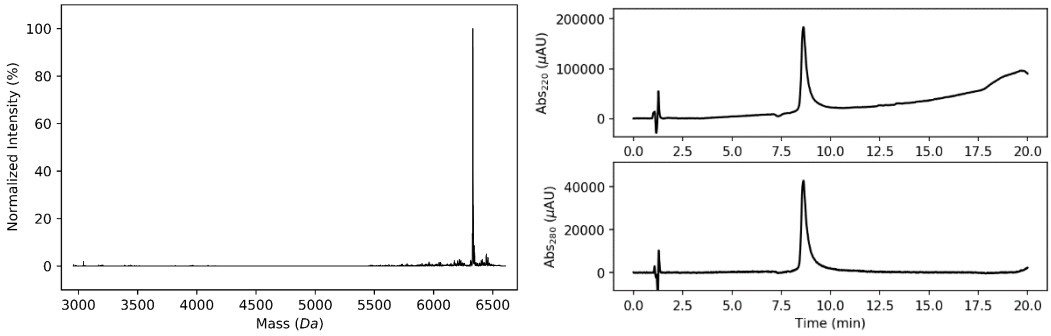

Kif5C$^{777\text{-}804}$ GREQAREDLKGLEETVSRELQTLHNLRKLYG, Calculated Mass: 3681.08 Observed Mass: 3681.14. *HPLC plotted from 2 mins due to injection peak*

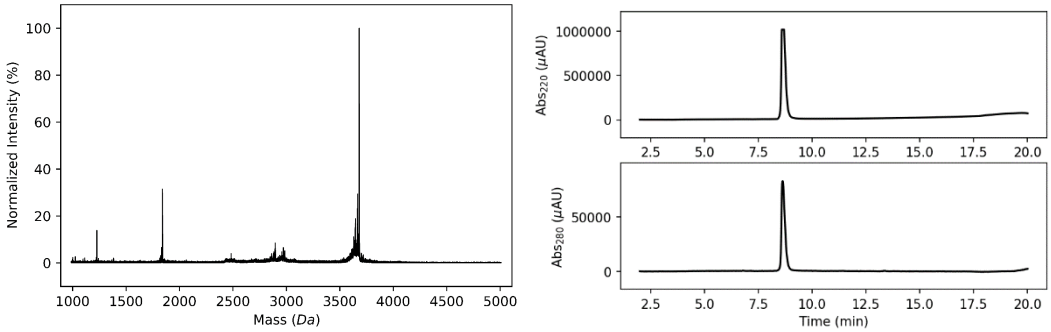

Kif5C$^{777\text{-}804\ E794L}$ GREQAREDLKGLEETVSRLLQTLHNLRKLYG, Calculated Mass: 3665.12 Observed Mass: 3665.10. *HPLC plotted from 2 mins due to injection peak*

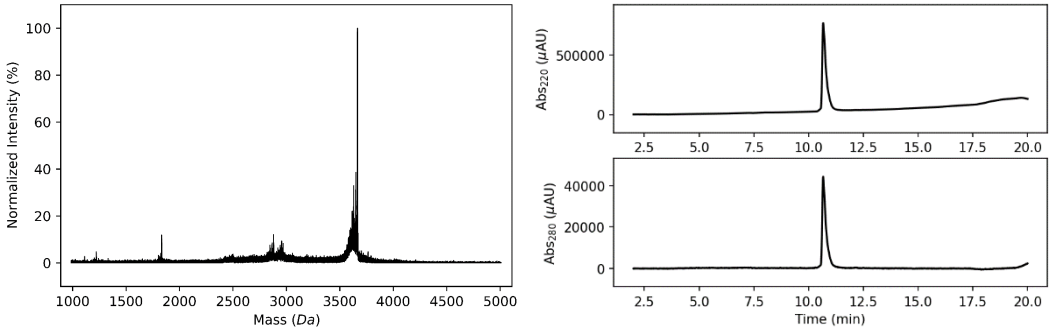

Kif5B$^{767\text{-}805\ Q780Y}$ ELTVMQDRREQARYDLKGLEETVAKELQTLHNLRKLFVQ, Calculated Mass: 4741.39 Observed Mass: 4743.25. *HPLC plotted from 2 mins due to injection peak*

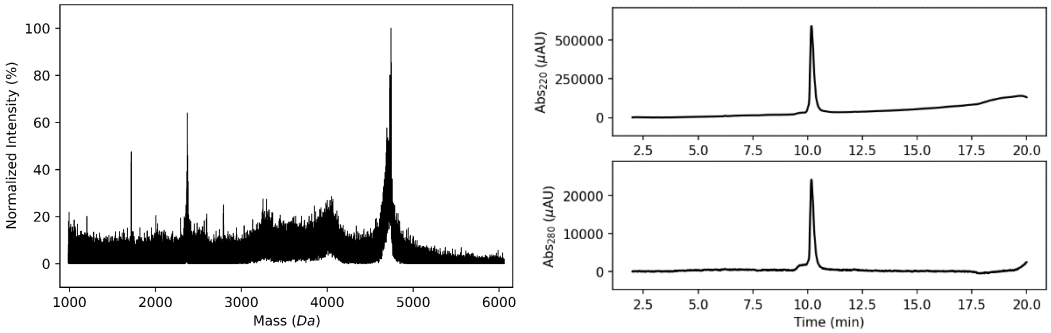

KLC1$^{104\text{-}141\ C114A}$ GQKLRAQVRRLAQENQWLRDELANTQQKLQKSEQSVAQLEG, Calculated Mass: 4818.33 Observed Mass: 4817.96. *HPLC plotted from 2 mins due to injection peak*

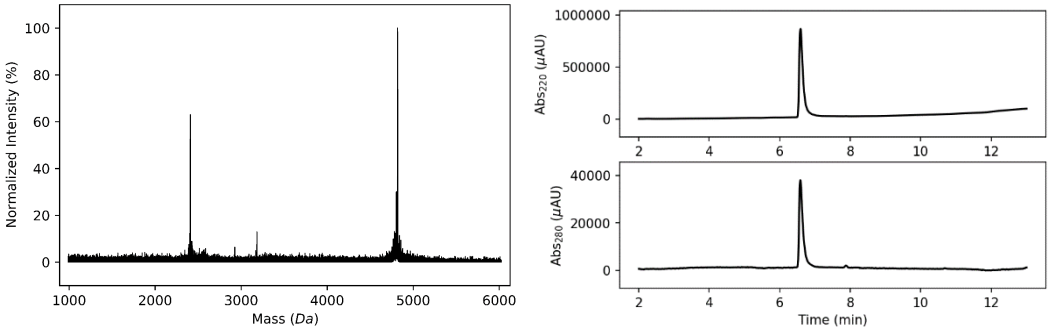

CCDi^{1}-KIF5C$^{777\text{-}804}$ GEIAALKQEREQAREDLKGLEETVSRELQTLHNLRKLWG, Calculated Mass: 4587.12 Observed Mass: 4588.50

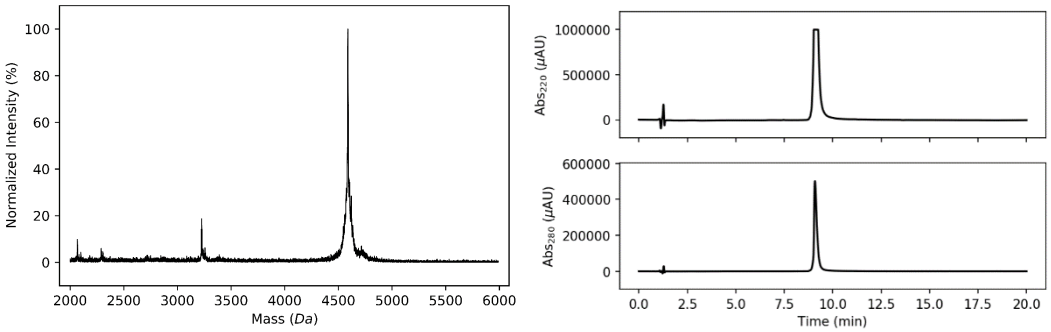

CCDi^{2}-KIF5C$^{777\text{-}804}$ GENAALKQEIAALKQEREQAREDLKGLEETVSRELQTLHNLRKLWG, Calculated Mass: 5341.95 Observed Mass: 5345.597

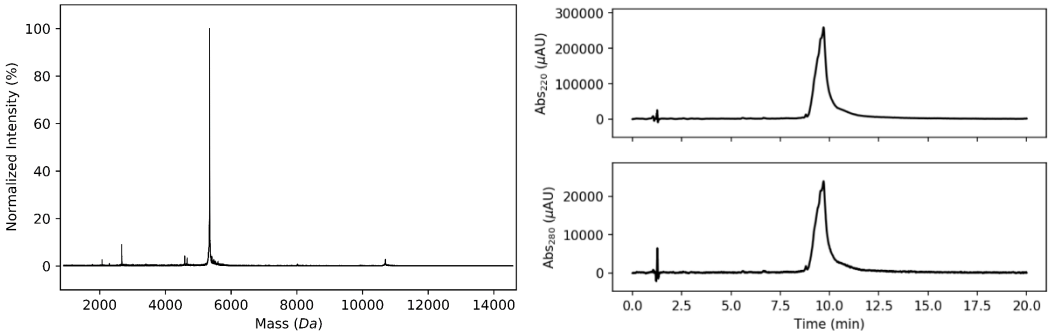

CCDi^{3}-KIF5C$^{777\text{-}804}$ GEIAALKQENAALKQEIAALKQEREQARED LKGLEETVSRELQTLHNLRKLWG, Calculated Mass: 6095.84 Observed Mass: 6099.66

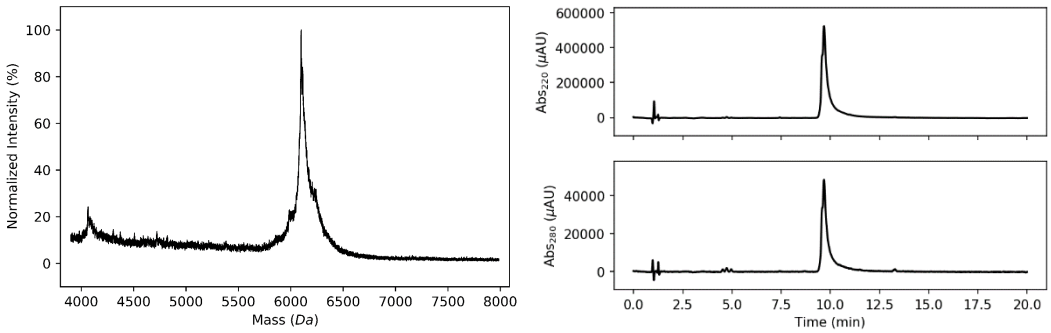

TAMRA-KIF5C^{IAK} EAVRAKNMARRAHSAQIAKPIRPGHY , Calculated Mass: 2970.43 Observed Mass: 2970.32. Two peaks in HPLC are TAMRA isomers

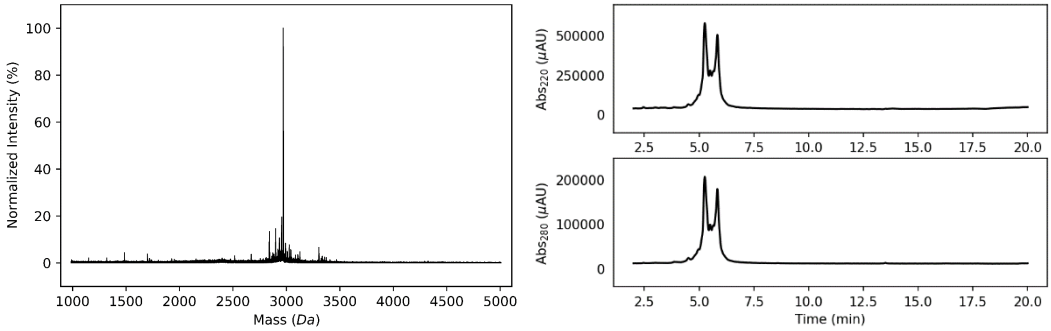

TAMRA-KIF5C$^{R\text{-}IAK\text{-}R}$ EAVRAKNMARRARSAQIAKPIRPGRY , Calculated Mass: 3008.52 Observed Mass: 3008.12. Two peaks in HPLC are TAMRA isomers

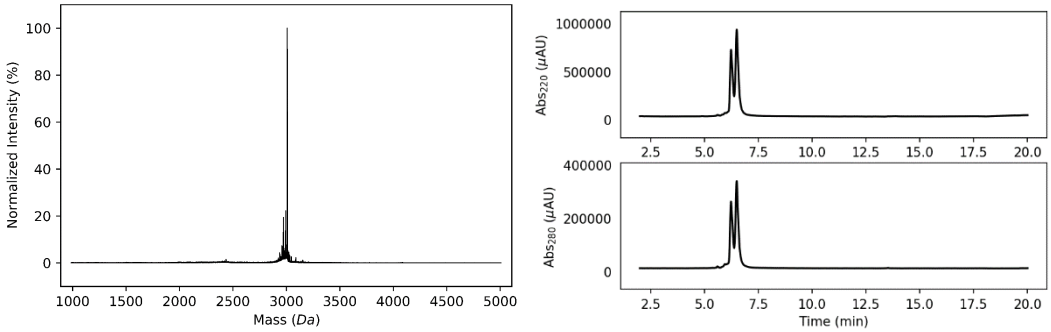

TAMRA-KIF5C$^{A\text{-}IAK\text{-}A}$ EAVRAKNMARRAASAQIAKPIRPGAY , Calculated Mass: 2838.3 Observed Mass: 2838.23. Two peaks in HPLC are TAMRA isomers

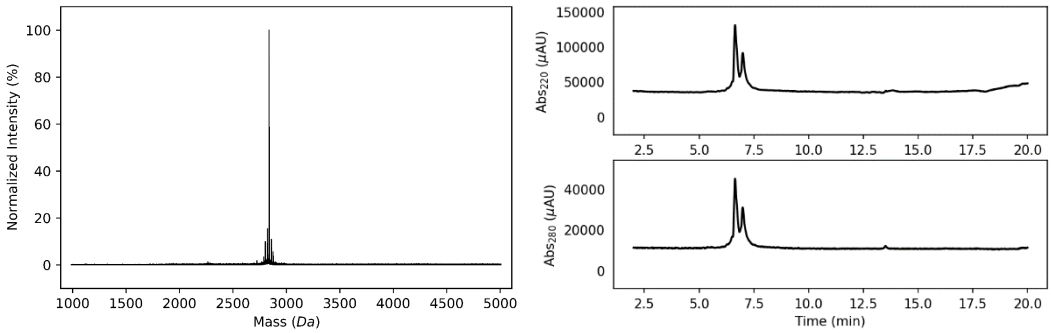

8.2 Protein purification

KLC2^{TPR}

Elution profiles from Ni affinity (left) and size exclusion (right) chromatography.

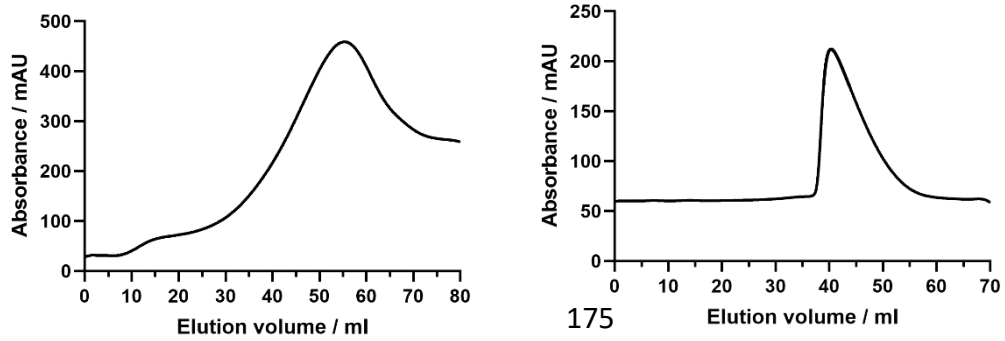

SDS PAGE

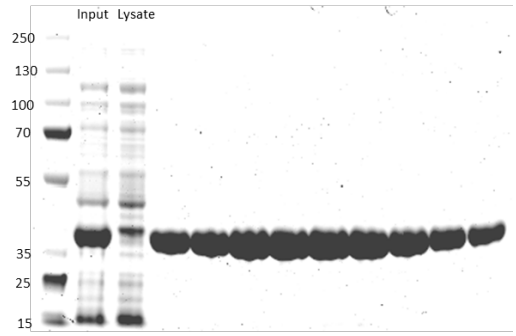

Analogous profiles were obtained for KLC1^{TPR}, KLC1ext^{TPR} and KLC2ext^{TPR}

CC-Di-G_5-KLC1$^{88-151}$ CC-Di-G_5-Kif5B$^{767-805}$.

SDS PAGE

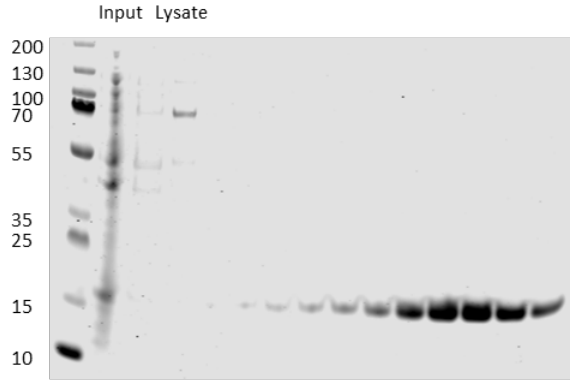

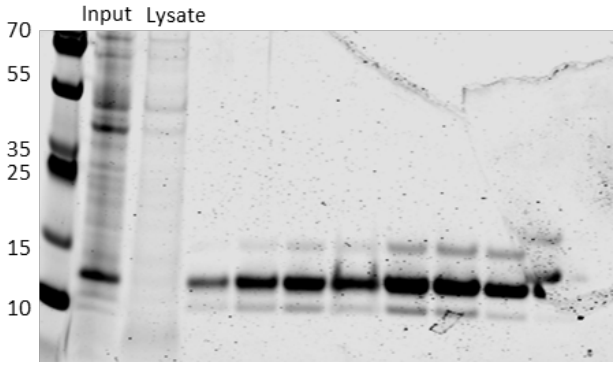

8.3 Crystallography tables

Table 8.1 *Data collection*

Data set	$KLC1^{TPR}$:KinTag
Beamline	I03 (DLS)
Wavelength (Å)	0.97625
Resolution range (Å) Highest res. bin (Å)	111.32-2.85 (2.90-2.85)
Space group	$P2_12_12_1$
Cell dimensions (Å)	101.73, 107.53, 222.65
Unique reflections	57529 (2758)
Overall redundancy	4.5 (4.4)
Completeness, (%)	99.3 (97.1)
$R_{merge,}$ (%)	11.4 (154.3)
R_{pim} (I), (%)	6.3 (88.9)
CC1/2*,* (%)	99.4 (36.5)
⟨I/σ(I) ⟩	8.0 (1.2)
Wilson *B* factor ($Å^2$)	46.7
Refinement	
PDB code	6SWU
R_{factor} (%)/R_{free}(%)	20.1 24.3
# non-H atoms	13791
rmsd bond lengths (Å)	0.008
rmsd bond angles (°)	1.421

Table 8.2

Data collection	
Data set	Kif5B$^{767\text{-}805\ Q780Y}$
Beamline	I03 (DLS)
Wavelength (Å)	0.9795
Resolution range (Å) Highest res. bin (Å)	45.31 - 1.75 (1.813 - 1.75)
Space group	$P2_12_12_1$
Cell dimensions (Å)	41.35, 44.99, 90.61
Unique reflections	17672 (1739)
Multiplicity	9.0 (9.3)
Completeness, (%)	99.93 (100.00)
$R_{merge,}$	0.07288 (0.6338)
R_{pim} (I)	0.02613 (0.2141)
CC1/2, (%)	0.999 (0.922)
⟨I/σ(I) ⟩	11.48 (0.43)
Wilson *B* factor (Å^2)	35.4
Refinement	
R_{work} R_{free}	0.2431 0.2961
# non-H atoms	1268
rmsd bond lengths (Å)	0.046
rmsd bond angles (°)	2.6

8.4 KinTag saturation mutagenesis

Table 8.3

		K_D/µM
SKIP	GSTNLEWDDSAI	7.33
J-S(Y)	GTEDIYEWDDSAI	1.05
J-S(L)	GTEDILEWDDSAI	2.91
T-J-S(Y)	GTVFTTEDIYEWDDSAI	0.26
T-J-S(L)	GTVFTTEDILEWDDSAI	1.27
	GTAFDVADAYEWDDEAI	0.80
	GTAFDVKDAYEWDDQAI	1.65
	GTAFDVADQYEWDDAAI	0.45
	GTAFDVKDQYEWDDEAI	0.97
	GTAFDVKDQYEWDDQAI	2.04
	GTVFTNEDIYEWDDSAI	0.56
	GTVFTTEDIYEWDDYAI	0.19
	GWVFTTEDIYEWDDSAI	0.30
	GTVFTWEDIYEWDDSAI	0.29
	GTVFTTEDIYEWWDSAI	2.76
	GTAFDVADAYEWDDQAI	0.96

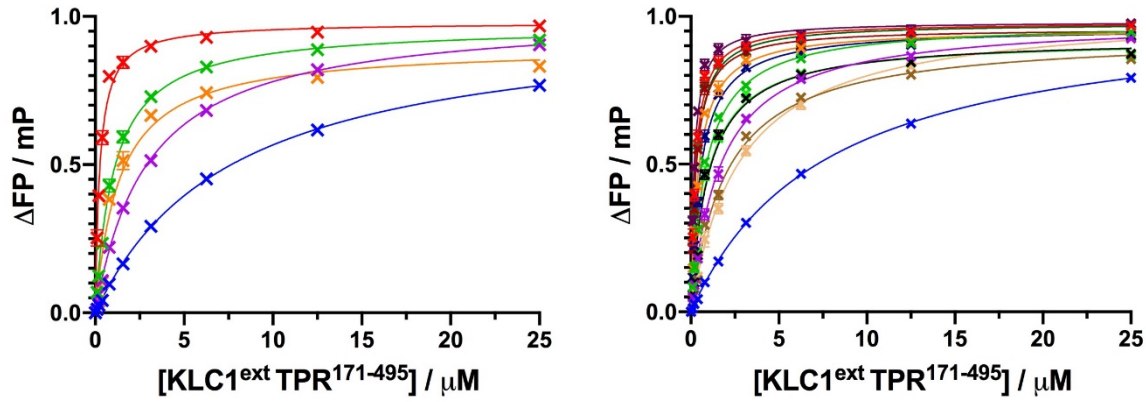

8.5 Publications